ANNUAL REPORT

2025

and list of publications

BGI

Bayerisches
Geoinstitut

Bayerisches Forschungsinstitut
für Experimentelle Geochemie und Geophysik
Universität Bayreuth

Bayerisches Geoinstitut
Universität Bayreuth
95440 Bayreuth
Germany

Telephone: +49-(0)921-55-3700
Telefax: +49-(0)921-55-3769
e-mail: bayerisches.geoinstitut@uni-bayreuth.de
www: https://www.bgi.uni-bayreuth.de

Editorial compilation by: Florian Heidelbach and Petra Buchert
Section editors: Andreas Audétat, Tiziana Boffa Ballaran, Audrey Bouvier,
Johannes Buchen, Dan Frost, Florian Heidelbach, Gregor Golabek,
Tomoo Katsura, Hans Keppler, Nobuyoshi Miyajima,
Gerd Steinle-Neumann, Tony Withers

Staff and guests of the Bayerisches Geoinstitut in **July 2025**:

Die Mitarbeiter und Gäste des Bayerischen Geoinstituts im **Juli 2025:**

first row, from left (1. Reihe, v. links) Wenyi Zhou, Laura Hahn, Danielle Silva Souza, Tiziana Boffa Ballaran, Cheng Qian, Xiaojun Hu, Anaëlle Antunes, Daniela Bubmann, Yuan Li, Sven Linhardt

second row, from left (2. Reihe, v. links) Ulrike Trenz, Xiaoshu Hao, Petra Buchert, Rebecka Matthäus, Dorothea Wiesner, Laurence Kreeger, Melanie Pöppelbaum, Yibo Qiao, Pedro Valdivia Munoz, Dave Rubie

third row, from left (3. Reihe, v. links) Erik Konrad, Olga Gaspert, Ye Wu, Matej Hlede, Nobuyoshi Miyajima, Tatjana Weiler, Pavlos Zampras, Dmitry Bondar

fourth row from left (4. Reihe, v. links) Holger Kriegl, Arne Spang, Gerald Bauer, Dan Frost, Tony Withers, Hiroaki Yokoyama, Oliver Rausch, Alexander Kurnosov

back rows, from left (hintere Reihen, v. links) Detlef Kraußе, Dapeng Zhu, Ibrahim Jemal, Yunke Song, Artem Chanyshev, Ran Zhao, Audrey Bouvier, Fei Wang, Hans Keppler, Johannes Buchen, Rémy Pierru, Denise Kelk-Huth, Raphael Njul, Gerd Steinle-Neumann, Sergius Dell, Andreas Audétat, Matteo Zippoli, Stefan Übelhack, Toni Puchtler, Florian Heidelbach

Absent (Es fehlten) Laura Czekay, Leonid Dubrovinsky, Tomo Katsura, Lianjie Man, Stephen Mojzsis, Sergey Ovsyannikov, Anke Potzel, Maximilian Schulze, Jinia Sikdar, Yuqing Yin

Contents

Foreword

Bayerisches Geoinstitut was originally founded to study Earth´s interior by high-pressure experiments in the laboratory. While this is still the main focus of our scientific activities today, the general advancement of science has opened up additional opportunities for research. Space probes have delivered detailed insights into the surface properties, composition and structure of neighboring planets in our solar system, most notably Mars. The interested reader will therefore find quite a few contributions in this annual report on material properties that may help to understand the interior structure of this planet. Moreover, thousands of exoplanets, planets in the orbit of distant stars, have now been discovered. Many of these exoplanets have bulk properties that are very different from anything seen in our solar system. At the same time, they open up the tantalizing opportunity that it may be possible to predict whether something similar to Earth may exist somewhere in the depths of the universe. This kind of information cannot come from observations alone, as the observable parameters for exoplanets are very limited. However, information about the composition of the host star allows predictions of likely compositions of the planets associated, and their evolution – including surface conditions and atmospheric composition – can then be predicted by geodynamic modelling. This is the background of the new ERC Synergy Grant "Geoastronomy" that was brought to Bayreuth by Prof. Stephen Mojzsis, who joined Bayerisches Geoinstitut in June 2025. Partners in this project are the LMU in Munich and CNRS in Orleans, France. We are very pleased that the partner group at CNRS Orleans is led by Fabrice Gaillard, who once himself was a postdoctoral fellow at our institute in Bayreuth.

In addition to research, supporting the career of young scientists has always had high priority at Bayerisches Geoinstitut. We are therefore very happy that Prof. Johannes Buchen secured an ERC Starting Grant that will allow him to study the stability and elastic properties of hydrous phases in Earth´s lower mantle. Moreover, within the framework of the recently approved DAAD graduate student program at BGI, we were able to welcome the first two Ph. D. students from India. As parts of our ongoing efforts to modernize the extensive experimental and analytical capabilities at BGI, we acquired a new FTIR spectrometer with microscope and two-dimensional focal plane array detector that will significantly expand our spectroscopic imaging capabilities.

Among the many scientific contributions in this annual report, it is naturally difficult to single out some studies that are particularly exciting. Nevertheless, as in every year, I would like to highlight two contributions from our young colleagues. On page 76 ff of this report, Apostolos Pantousas and coworkers describe new high-pressure polymorphs of calcium carbonates observed in laser-heated diamond anvil cells. These phases may be stable in the deep parts of the lower mantle. Unlike carbonates at lower pressure, the structures contain tetrahedrally coordinated carbon atoms and the CO_4^{4-} groups even form three-dimensional frameworks, qualitatively (but not in detail) similar to the three-dimensional frameworks that are common in silicates. Aside from its relevance for the deep storage of carbon, this observation nicely illustrates a principle that dates back to the very early days of high-pressure research: The behavior of an element at high pressure can often be roughly predicted by observing the behavior of the higher homologue of the element in the periodic table at lower pressure. Some phase transformations that are now well established in silicate systems were first observed in germanate analogues. Apostolos Pantousas now shows that at much higher pressures, even carbonates start to resemble silicates.

Multi anvil presses are one of our most important tools to study the deeper parts of Earth´s mantle. However, with conventional technology, they used to be limited to about 25 GPa, corresponding to just the uppermost layer of the lower mantle, while most of this reservoir was experimentally not accessible. Over many years, the group of Prof. Katsura has improved multi anvil technology such that now pressures up to 45 GPa can be routinely achieved. Not surprisingly, with these new experimental capabilities, it turns out that many material properties and chemical equilibria change drastically with depth in the lower mantle. The study of Dr. Wenyi Zhou and coworkers on page 53 ff of this annual report nicely illustrates this. The $CaSiO_3$ perovskite phase davemaoite is often considered to be the main host of incompatible trace elements, notably also heat-producing elements such as U, Th, or K in the lower mantle. However, it turns out that with increasing pressure, the partitioning of these elements into davemaoite very significantly decreases, which may have had a large effect on the primordial distribution of heat production inside the solidified mantle early in Earth´s history.

On the behalf of my colleagues, I would like to thank the *Free State of Bavaria* as represented by the *Bavarian State Ministry of Science, Research and Art*, as well as the *Advisory Board for High-Pressure Research in Geoscience of the Bavarian Academy of Sciences* for their continuing support and strong commitment to the Bayerisches Geoinstitut. I would further like to thank the *President and Leadership of the University of Bayreuth* for their high regard of our institute. We also gratefully acknowledge generous support from external funding agencies, in particular the *Alexander von Humboldt Foundation*, the *European Union*, the *German Science Foundation,* and the *Federal Ministry of Education and Research*, which continue to contribute greatly to the further development and success of the Geoinstitut.

Bayreuth, March 2026

Hans Keppler

Vorwort

Das Bayerische Geoinstitut wurde ursprünglich gegründet, um das Erdinnere mit Hilfe von Hochdruckexperimenten im Labor zu untersuchen. Dies ist auch heute noch der Hauptfokus unserer wissenschaftlichen Aktivitäten. Gleichzeitig hat aber der Fortschritt auf anderen Gebieten der Wissenschaft auch neue Tätigkeitsfelder erschlossen. Zahlreiche Raumsonden haben detaillierte Informationen über die Oberflächen-Beschaffenheit, Zusammensetzung und Struktur von Planeten in unserem Sonnensystem geliefert, insbesondere für Mars. Der interessierte Leser wird in diesem Jahresbericht daher etliche Beiträge finden, mit denen die innere Struktur dieses Planeten besser verstanden werden kann. Mittlerweile wurden aber auch bereits Tausende von Exoplaneten entdeckt, die fremde Sterne umkreisen. Viele dieser Exoplaneten haben Eigenschaften, die völlig verschieden sind von den Planeten in unserem Sonnensystem. Gleichzeitig eröffnen sie aber auch die Möglichkeit vorherzusagen, ob irgendwo in den Tiefen des Universums vielleicht Bedingungen existieren wie auf unserer Erde. Diese Information kann nicht allein aus astronomischen Beobachtungen kommen, da sich nur wenige Kenngrößen von Exoplaneten direkt messen lassen. Spektroskopische Daten des zugehörigen Sterns erlauben aber Vorhersagen über die wahrscheinliche Zusammensetzung der Planeten. Deren Struktur und Entwicklung, einschließlich der Oberflächenbedingungen und der Zusammensetzung einer Atmosphäre können dann mit Hilfe geodynamischer Modellierung vorhergesagt werden. Dies ist der wissenschaftliche Hintergrund des ERC Synergy-Projektes "Geoastronomy" von Prof. Stephen Mojzsis, der im Juni 2025 an unser Institut gekommen ist. Partner in diesem Verbundprojekt sind die LMU in München und das CNRS in Orléans. Wir freuen uns besonders, dass die Gruppe beim Kooperationspartner in Orléans von Fabrice Gaillard geleitet wird, der selbst einmal Postdoktorand bei uns in Bayreuth war.

Neben der Forschung hat die Unterstützung der Karriere junger Wissenschaftler stets hohe Priorität am Bayerischen Geoinstitut. Wir freuen uns daher sehr, dass Prof. Johannes Buchen ein ERC-Starting-Grant erhalten hat, um die Stabilität und elastischen Eigenschaften wasserhaltiger Phasen im unteren Erdmantel zu untersuchen. Im Rahmen des neu eingerichteten DAAD-Austauschprogramms am BGI konnten wir die ersten beiden Doktoranden aus Indien begrüßen. Als Teil unserer Anstrengungen, die experimentellen und analytischen Einrichtungen am BGI stets auf neuestem Stand zu halten, konnten wir ein neues FTIR-Spektrometer mit Mikroskop und zweidimensionalem Focal-Plane-Array-Detektor beschaffen. Dieses Gerät wird unsere Fähigkeiten zur spektroskopischen Bildgebung wesentlich verbessern.

Naturgemäß ist es schwierig, unter den zahlreichen Beiträgen in diesem Jahresbericht einzelne Arbeiten hervorzuheben. Trotzdem möchte ich gerne, wie in jedem Jahr, zwei Beiträge von unseren jungen Kollegen besonders erwähnen. Auf Seite 76 ff beschreiben Apostolos Pantousas und Kollegen neue Hochdruckformen von Calciumcarbonat, die in laserbeheizten Diamantstempelzellen synthetisiert wurden. Diese Phasen könnten eventuell auch in tiefen Teilen des unteren Mantels stabil sein. Im Gegensatz zu Carbonaten bei niedrigem Druck enthalten die

Strukturen tetraedrisch koordinierte Kohlenstoff-Atome und die CO_4^{4-}-Gruppen bilden sogar dreidimensionale Netzwerke, grundsätzlich (aber nicht im Detail) ähnlich den dreidimensionalen Netzwerken, die man aus Silikaten kennt. Abgesehen von der Bedeutung für die Speicherung von Kohlenstoff im tiefen Erdinnern illustriert diese Beobachtung sehr schön ein Prinzip, das zurückgeht auf die frühesten Tage der Hochdruckforschung: Das Verhalten von einem Element bei hohem Druck ähnelt oft dem des schwereren Elements, das im Periodensystem darunter steht bei niedrigerem Druck. Phasenumwandlungen, die mittlerweile bei Silikaten gut bekannt sind, wurden erstmals in Germanat-Systemen beobachtet. Apostolos Pantousas zeigt nun, dass bei wesentlich höheren Drücken selbst Carbonate anfangen, sich ähnlich wie Silikate zu verhalten.

Mehrstempel (Multi-Anvil)-Pressen sind eines unserer wichtigsten Werkzeuge, um die tieferen Teile des Erdmantels zu untersuchen. Konventionelle Pressen dieses Typs waren bisher stets auf etwa 25 GPa begrenzt. Hiermit konnte man gerade noch die alleroberste Lage des unteren Mantels untersuchen, während der größte Teil dieses Reservoirs experimentell nicht zugänglich war. Die Arbeitsgruppe von Tomo Katsura hat über viele Jahre technische Verbesserungen eingeführt, mit denen nun 45 GPa routinemäßig erreicht werden können. Mit Hilfe dieser neuen Technik zeigt sich nun, dass viele Materialeigenschaften und chemische Gleichgewichte im unteren Mantel sich mit der Tiefe drastisch ändern. Die Arbeit von Dr. Wenyi Zhou und Mitarbeitern auf Seite 53 ff dieses Jahresberichts illustriert dies sehr schön. Die $CaSiO_3$ Perowskit-Phase Davemaoit ist wahrscheinlich der Hauptträger vieler Spurenelemente im unteren Mantel, insbesondere auch von Elementen wie U, Th und K, die durch radioaktiven Zerfall Wärme produzieren. Es zeigt sich nun jedoch, dass mit steigendem Druck die Verteilung dieser Elemente in Davemaoit signifikant abnimmt. Dies könnte einen erheblichen Effekt auf die ursprüngliche Verteilung von Wärmequellen im Mantel zu Beginn der Erdgeschichte gehabt haben.

Meine Kollegen und ich möchten dem *Freistaat Bayern*, vertreten durch das *Bayerische Staatsministerium für Wissenschaft, Forschung und Kunst*, und dem *Beirat für Geowissenschaftliche Hochdruckforschung der Bayerischen Akademie der Wissenschaften* unseren Dank für ihre fortwährende Unterstützung des Bayerischen Geoinstituts aussprechen. Darüber hinaus möchten wir dem Präsidenten und der Hochschulleitung der Universität Bayreuth ausdrücklich für ihre zuverlässige und kontinuierliche Unterstützung unseres Instituts danken. Wir sind auch für die großzügige Förderung durch externe Geldgeber dankbar, insbesondere der *Alexander-von-Humboldt-Stiftung*, der *Europäischen Union* und der *Deutschen Forschungsgemeinschaft*, die ebenfalls wesentlich zur Entwicklung und zum Erfolg des Bayerischen Geoinstituts beigetragen haben.

Bayreuth, im März 2026 Hans Keppler

1. Advisory Board and Directorship

1.1 Advisory Board

The *Beirat für Geowissenschaftliche Hochdruckforschung der Bayerischen Akademie der Wissenschaften* advises on the organisation and scientific activities of the institute. Members of this board are:

Prof. Dr. Ulrich CHRISTENSEN	Emeritus, Max-Planck-Institut für Sonnensystemforschung, Göttingen
Prof. Dr. Rudolf GROSS (Chairman)	Walther-Meißner-Institut für Tieftemperaturforschung (WMI), Garching
Prof. Dr. Francois HOLTZ	Institut für Mineralogie der Leibniz Universität Hannover
Prof. Dr. Klaus MEZGER	Emeritus, Institut für Geologie der Universität Bern
Prof. Dr. Herbert PALME	Emeritus, Institut für Mineralogie und Geochemie der Universität zu Köln – Senckenberg Forschungsinstitut und Naturmuseum Frankfurt/M.
Prof. Dr. Markus RIEDERER (Vice Chairman)	Julius-von-Sachs-Institut für Biowissenschaften, Würzburg
Prof. Dr. Ekhard SALJE, FRS, FRSA († 24.02.2025)	Emeritus, Department of Earth Sciences, University of Cambridge
Prof. Dr. Christine THOMAS	Institut für Geophysik der Westfälischen Wilhelms-Universität Münster

1.2 Leadership

Prof. Dr. Hans KEPPLER (Director)
Prof. Dr. Dan FROST (Deputy Director)
Prof. Dr. Tomoo KATSURA
Prof. Dr. Audrey BOUVIER

2. Staff, Funding and Facilities

2.1 Staff

At the end of 2024 the following staff positions existed in the Institute:

Scientific staff:	**17**
Technical staff:	**14**
Administrative staff:	**2.5**
Administrative officer:	**1***

* The administrative officer is employed on 40 % of a full position provided by the central administration.

During 2025, 21 scientific positions (203 months) were funded by grants raised externally by staff members of the institute. In addition, 3 scientific positions (14.5 months) were funded by the resources of the BGI Visiting Scientists' Programme (see Sect. 8), which also supported short-term visits for discussing future projects or presenting research results (see Sect. 5). 10 student assistants (66 months) were funded by externally raised grants. 6 scientists and 11 PhD students (117 months) were supported by personal grants or stipends.
An additional position (72 months) for a tenure-track junior professorship was funded by BMBF and provided by courtesy of Bayreuth University.

2.2 Funding

In 2025, the following financial resources were available from the Free State of Bavaria:

Visiting Scientists' Programme:	164.000 €
Consumables:	595.000 €

The total amount of national/international external funding *("Drittmittel")* used for ongoing research projects in 2025 was 2.029.000 € (positions: 1.408.000 €; equipment, consumables and travel grants: 621.000 €).

	positions	**equipment, consumables, travel grants**	**total**
AvH	7.000 €	1.000 €	8.000 €
DFG	858.000 €	555.000 €	1.413.000 €
BMBF	94.000 €	20.000 €	114.000 €
EU	302.000 €	45.000 €	347.000 €
Others	147.000 €	0 €	147.000 €
	1.408.000 €	**621.000 €**	**2.029.000 €**

(AvH = Alexander von Humboldt Foundation; DFG = German Science Foundation; EU = European Union; BMBF = Federal Ministry of Science; Others: DAAD, Chinese Scholarship Council)

In the following list, only the BGI components of the funding are listed in cases where joint projects involved other research institutions. Principal investigators and the duration of the grants are listed in brackets. Total project funding refers to the funding over the entire duration of this project.

Funding institution	**Project, Funding**	**Total Project Funding**
AvH	Project SEPARATION (E. Kubik – 3/23-2/25) "Segregation efficiency of planetary cores addressed through the isotopes of nickel" Position: 24 months 70.000 € Consumables: 19.200 €	89.200 €
BMBF	05K25WC2 (L.S. Dubrovinsky – 7/25-6/28) SMSPRES: "Resonante Kernstreuung bei extrem hohen Drücken und Temperaturen. Teilprojekt 2" Total funding:	494.616 €
DAAD	Graduate School Scholarship Programme (A. Bouvier, H. Keppler – 2025-2026) on behalf of the doctoral programme "Experimental Geosciences" Positions: Four 4-year doctoral scholarships	800.000 €
DFG	AU 314/9-1 (A. Audétat – 6/24-6/27) "Das Verhalten volatiler Elemente und erzbildender Metalle während der Differentiation subduktionsgebundener Magmen unter hohen Drücken" Positions: E 13 (50 %), 36 months 115.200 € student assistant 20.700 € Consumables: 33.300 € Overhead: 37.200 €	206.400 €
DFG	FR 1555/14-1 (D.J. Frost) – 7/24-6/27 "Fluid permeability and speciation in subduction zones" Positions: E 13, 36 months 184.400 € student assistant 10.000 € Consumables and travel funding: 19.770 € Overhead: 47.118 €	261.288 €
DFG	INST 91/503-1 FUGG (H. Keppler – 2024-2025) Co-financing of a Fourier-transform infrared spectrometer with microscope. Total funding:	197.500 €

DFG	KA3434/19-1 (T. Katsura – 02/21-08/25) "Evaluation of the aspect ratio of ferropericlase under lower-mantle conditions" Positions: E13, 24 months 152.200 € Consumables: 50.000 € Overhead: 44.400 €	246.600 €
DFG	KA 3434/24-1 (T. Katsura – 10/23-9/26) "H_2O solubilities in Al-free and Al-bearing high-pressure silica polymorphs as a function of pressure and temperature: H_2O storage in the lower mantle" Positions: E13, 36 months 246.800 € student assistant 5.000 € Consumables: 78.000 € Overhead: 72.600 €	402.400 €
DFG	KA 3434/29-1 (T. Katsura – 9/25-8/28) "Experimentelle Untersuchung der Schmelzbeziehungen zwischen Bridgmanit und Davemaoit unter Bedingungen des unteren Erdmantels: Implikationen für die frühe Differenzierung der Erde" Positions: E13 (75 %), 36 months 189.100 € student assistant 8.000 € Consumables: 55.250 € Overhead: 55.517 €	307.867 €
DFG	KE 501/18-1 (H. Keppler – 1/23-5/26) "Stability of organic molecules in subduction zone fluids" Total funding:	259.555 €
DFG	KE 501/19-1 (H. Keppler – 7/24-12/27) "Subduction fluids and the source of metals in porphyry deposits" Total funding:	259.603 €
DFG	KE 501/20-1 (H. Keppler – 11/25-10/28) "Amphibol-Stabilität, Schmelzbildung und Wasser-Transport in Subduktionszonen" Total funding:	281.454 €
DFG	OV 110/3-3 (S.V. Ovsyannikov – 11/23-10/25) "High-pressure synthesis and properties of novel simple oxides with unusual stoichiometries" Position: E 13, 24 months: 159.900 € Consumables and travel funding: 36.000 € Overhead: 43.100 €	239.000 €

DFG	STE 1105/15-1 (G. Steinle-Neumann – 7/23-6/26) "The role of light elements at the core-mantle boundary – partitioning, demixing and transport " Positions: E 13 (75%), 36 months 172.100 € student assistant 7.000 € Consumables: 10.250 € Overhead: 41.657 €	231.007 €
DFG	TH 2076/8-1 (M. Thielmann – 11/21-10/25) "Identifizierung der Entstehungsprozesse tiefer Erdbeben" (Emmy-Noether-Programm) Positions: 670.913 € Consumables: 60.580 € Workshops: 5.000 € Overhead: 162.000 €	898.496 €
DFG	YU 358/1-1 (L. Yuan, G. Steinle-Neumann – 2/22-1/25) "Partitionierung flüchtiger Elemente im tiefen Magma Ozean der Erde" Positions: E 13, 36 months 232.900 € student assistant 10.000 € Consumables: 14.250 € Overhead: 56.600 €	313.750 €
EU	European Research Council (ERC) Grant No. 949 417 (R. Hin – 1/21-12/25) "The chemical consequences of vapour loss during planetary accretion (VapLoss)" ("HORIZON 2020") Positions: 756.169 € Travel funding: 44.781 € Consumables: 129.403 € Equipment: 153.802 € Internal Goods and Services: 173.235 € Overhead: 314.348 €	1.571.738 €
EU	European Research Council (ERC) Synergy Grant (S. Mojzsis, K. Heng, F. Gaillard – 2025-2031) "Exploring the chemical foundations for rocky exoplanets around Sun-like stars" ("GEOASTRONOMY") total funding: 10.073.000 € BGI share:	3.300.000 €

2.3 Laboratory and office facilities

The institute occupies an area of

ca. 1589 m^2	laboratory space
ca. 505 m^2	infrastructural areas (machine shops, computer facilities, seminar room, library)
ca. 622 m^2	office space

in a building which was completed in 1994.

2.4 Experimental and analytical equipment

The following major equipment is available at the Bayerisches Geoinstitut:

I. High-pressure apparatus

- 15 MN/1500 tonne Kawai-type multianvil high-pressure apparatus (50 GPa, 3000 K)
- 6 x 8 MN/6x800 tonne independently acting-anvil press (40 GPa, 3000 K)
- 50 MN/5000 tonne multianvil press (25 GPa, 3000 K)
- 12 MN/1200 tonne multianvil press (25 GPa, 3000 K)
- 10 MN/1000 tonne multianvil press (25 GPa, 3000 K)
- 5 MN/500 tonne multianvil press (20 GPa, 3000 K)
- 5 MN/500 tonne press with a deformation DIA apparatus
- 5 piston-cylinder presses (5 GPa, 2100 K)
- Cold-seal pressure vessels (700 MPa, 1100 K, H_2O), TZM vessels (300 MPa, 1400 K, Ar), rapid-quench cold-seal pressure vessels (400 MPa, 1200 K, H_2O)
- Magma fragmentation device (0.1 GPa, 1400 K)
- Internally-heated autoclave (1 GPa, 1800 K)
- High-pressure gas loading apparatus for DAC

II. Structural and chemical analysis

- 1 X-ray powder micro-diffractometer
- 1 X-ray powder diffractometer with furnace and cryostat
- 2 automated single-crystal X-ray diffractometers
- High-brilliance X-ray system
- Single crystal X-ray diffraction diffractometer with rotating anode coupled with a Brillouin scattering system
- Single crystal X-ray diffractometer with high-brilliance source
- 1 Mössbauer spectrometer (1.5 - 1300 K)
- 3 Mössbauer microspectrometers
- 3 FTIR spectrometers with IR microscope
- FEG transmission electron microscope (TEM), 200 kV analytical, with EDS

FEG scanning TEM, 80-200 kV analytical, with 4-SDDs EDS and post-column energy filter (EFTEM/EELS)
FEG scanning electron microscope (SEM) with BSE detector, EDS, EBSD and CL
Dual beam device, focused ion beam (FIB) and FEG SEM. In situ easy-lift manipulator, STEM, EDS and EBSD detectors, and beam deceleration option
3 Micro-Raman spectrometers with ultraviolet and visible lasers
Tandem-multipass Fabry-Perot interferometer for Brillouin scattering spectroscopy
2 electron microprobes; fully-automated with 14 resp. 12 crystals, 5 spectrometer configuration, EDX, capability for light elements, CL
193 nm Excimer laser-ablation quadrupole ICP-MS
Water content determination by Karl-Fischer titration
GC/MS-MS for organic analyses
Confocal 3D surface measurement system
1.4 Tesla sweepable ESR magnet
Isotope cosmochemistry & geochemistry laboratory ISO 6 cleanrooms equipped with ISO 2-4 exhaust laminar flow cabinets for sample preparation
1-500 Hz 193 nm Excimer laser-ablation system
Triple quadrupole ICPMS for solution or in-situ LA-isotopic analysis
Multi-collector ICPMS/MS for solution or in-situ LA-isotopic analysis

III. *In situ* determination of properties
Diamond anvil cells for powder and single crystal X-ray diffraction, Mössbauer, IR, Raman, Brillouin optical spectroscopy, electrical resistivity measurements over 200 GPa
Facility for in situ hydrothermal studies in DAC
Externally heated DACs for in situ studies at pressures to 100 GPa and 1200 K
1-atm furnaces to 1950 K, gas mixing to 1950 K, zirconia fO2 probes
1-atm high-temperature creep apparatus
Megahertz ultrasonic interferometer
2 freezing-heating stages for fluid inclusion analysis (80-870 K; 300-1900 K)
Impedance/gain-phase analyser for electrical conductivity studies
Apparatus for in situ measurements of thermal diffusivity at high P and T
Laser-heating facility for DAC
Portable pulsed laser heating system for DAC

The Geoinstitut maintains a well equipped machine shop, an electronic workshop and sample preparation laboratories. It has access to supercomputing resources at the University and Leibniz computer centres.

3. Forschungsprojekte

3.1 Struktur und Dynamik der Erde und Planeten

In diesem ersten Abschnitt untersuchen neun Beiträge sowohl Prozesse auf der Erde als auch auf anderen Planeten, von der Oberfläche bis zum Kern, in unserem Sonnensystem und darüber hinaus. Sie befassen sich mit der Zusammensetzung protoplanetarer Scheiben, der Entstehung von Mesosiderit-Meteoriten und der Zusammensetzung des Marskerns. Geodynamische Simulationen liefern Einblicke in die Entwicklung von gebundenen rotierenden Supererden. Ein weiterer Beitrag beschäftigt sich mit der seismischen Unruhe und Oberflächendeformation, die durch Magmazufluss unterhalb der Campi Flegrei verursacht werden.

Der erste Beitrag von Spaargaren und Kollegen untersucht, wie die Flüchtigkeit von Elementen während der Kondensation protoplanetarer Scheiben von der ursprünglichen Zusammensetzung der Scheibe abhängt. Tausend unterschiedliche Scheiben-Zusammensetzungen wurden auf der Grundlage beobachteter Elementhäufigkeiten in den Sternen modelliert. Es zeigt sich, dass die Zusammensetzung von Gesteinsplaneten stark vom C/O-Verhältnis abhängt, wodurch erdähnliche, graphitreiche oder Mg-Si-arme Planeten entstehen können. Damit wird eine große Vielfalt an Gesteinsplaneten vorhergesagt.

Im zweiten Beitrag verwendeten Bermingham und Kollegen die massenunabhängige Fraktionierung von Molybdän-Isotopen, um den Ursprung des spät auf der Erde akkretierten Materials einzugrenzen. Die letzten 10–20 % der Akkretion der Erde wurden von nicht-kohlenstoffhaltigem Material aus dem inneren Sonnensystem dominiert. Lediglich geringfügige Beiträge aus kohlenstoffhaltigen Quellen waren möglich, was frühere Diskrepanzen zwischen den Mo- und Ru-Isotopensignaturen beseitigt.

Zippoli und Mitarbeiter untersuchen den Ursprung von Mesosiderit-Meteoriten mithilfe von Petrographie, Spurenelement-Geochemie und Deformationsexperimenten. Ihre Ergebnisse stützen die Annahme, dass Mesosiderite durch große Einschlagereignisse entstanden sind, bei denen Metall aus dem Kern mit Silikaten aus der Kruste vermischt wurde. Dies führte zu charakteristischen Texturen, variablen Abkühlungsgeschichten und unvollständigem chemischem Gleichgewicht innerhalb eines einzigen differenzierten Mutterkörpers. Die Mesosiderite sind wahrscheinlich verwandt mit den Eukrit-Meteoriten und dem Asteroiden Vesta.

Der vierte Beitrag von Hu und Kollegen beschäftigt sich mit der Sm-Nd- und Lu-Hf-Isotopensystematik von drei Mars-Meteoriten, um die frühe chemische Entwicklung des Mars zu verstehen. Die drei Shergottite weisen unterschiedliche Seltenerd-Muster auf, wobei NWA 4468 und EETA 79001 jeweils mit der angereicherten und der intermediären Gruppe der Shergottite in Verbindung stehen. Die Seltenerd- und Isotopendaten zeigen, dass Teghaza 001 (Alter 4,2 Milliarden Jahre) eine unter den Shergottiten einzigartige Zusammensetzung aufweist, was auf eine Verbindung zu einem früh gebildeten Krustenreservoir und der polymikten Brekzie NWA 7034 hindeutet.

Im folgenden Beitrag untersuchen Pierru und Kollegen die physikalischen Eigenschaften von Silikatschmelzen bei Drücken relevant für die Kern-Mantel-Grenze des Mars. Diese Messungen sollen Aufschluss geben über die Entstehung und Stabilität einer basalen Schmelzschicht, die auf der Grundlage seismischer Beobachtungen postuliert wurde. Die Experimente liefern auch neue Erkenntnisse über die thermochemische Entwicklung des Planeten Mars.

Im sechsten Beitrag entwickeln Frost und Mitarbeiter ein thermodynamisches Modell zur Bestimmung des Sauerstoffgehalts im ansonsten Schwefel-reichen Marskern. Damit sollen die von der InSight-Mission gemessenen seismischen Geschwindigkeiten besser erklärt werden. Das Modell kann auch die Bedingungen der Kernbildung auf dem Mars besser eingrenzen und Aufschluss über die frühe Geodynamo-Aktivität auf dem Mars geben.

Im siebten Beitrag modellieren Meier und Kollegen die thermochemische Entwicklung der ultrakurz-periodischen, gebunden rotierenden Super-Erde K2-141 b. Das Modell erlaubt Vorhersagen über das tektonische Regime, über die Ausdehnung des Magmaozeans auf der Tagseite, die vulkanischen Aktivität auf der Nachtseite und die damit verbundenen Ausgasung einer Atmosphäre. Diese Vorhersagen können mit Hilfe hochauflösender Beobachtungen überprüft werden, wodurch die sonst unzugängliche Magmaozean-Phase junger terrestrischer Planeten untersucht werden kann.

Spang und Kollegen verwenden ein viskoelastisches numerisches 3D Modell, um das Eindringen von Magma in eine Magmakammer zu simulieren. Sie zeigen, dass die durch das heiße Magma verursachte thermische Schwächung der umgebenden Gesteine die Amplitude der Oberflächendeformation erhöht. Im letzten Beitrag verwenden Nardoni und Kollegen dieselbe Art von numerischen 3D Modellen, um den Magmazufluss unterhalb der Campi Flegrei in der Nähe von Neapel zu simulieren. Dieser Magmazufluss kann nur teilweise die in den letzten Jahren in dieser Region beobachtete Oberflächenanhebung erklären, so dass zusätzliche Ursachen erforderlich sind, um die Hebungsgeschichte vollständig zu erklären.

3.2 Geochemie

Die meisten chemischen Elemente, die schwerer sind als Wasserstoff und Helium, entstehen durch Nukleosynthese in Sternen. Bei einer Supernova gelangen diese Elemente zurück in das interstellare Medium, wo das angereicherte Material später kollabieren und neue Generationen von Sternen bilden kann. Galaktische Modelle der chemischen Evolution beschreiben, wie dieser sich wiederholende Zyklus aus Sternentstehung und Massenverlust die Galaxie im Laufe der Zeit allmählich mit chemischen Elementen anreichert. Wie im ersten Projekt dieses

Abschnitts beschrieben, werden einige Elemente, wie Phosphor und Kalium, in Sternen in höheren Konzentrationen beobachtet als von Standardmodellen der Sternentwicklung vorhergesagt. Eine mögliche Erklärung wäre, dass Vermischungsprozesse zwischen verschiedenen Schichten in massereichen Sternen die Produktion dieser Elemente verstärken. Während solcher Ereignisse vermischt sich Material aus unterschiedlichen Schalen und löst Kernreaktionen aus, die von Standardmodellen der Sternentwicklung nicht erfasst werden. Die Ergebnisse zeigen, dass kleine Unterschiede in der internen Vermischung zu großen Abweichungen in den vorhergesagten Elementhäufigkeiten führen können. Insbesondere die Produktion des langlebigen radioaktiven Isotops ^{40}K, einer wichtigen internen Wärmequelle von Gesteinsplaneten, kann um Größenordnungen variieren. Die thermische Entwicklung von Planeten kann daher je nach Geburtsort des Sterns sehr unterschiedlich sein.

Im folgenden Projekt wird die Erhaltung von Material aus dem frühen Sonnensystem in Kometen untersucht. Messungen der Edelgase aus dem Kometen 67P/Churyumov–Gerasimenko durch die ESA-Raumsonde Rosetta zeigen Isotopenzusammensetzungen, die sich von denen der Sonne unterscheiden. Dies deutet darauf hin, dass der Komet nur einen Teil der Edelgase enthält, die in der Gaswolke vorhanden waren, aus der die Sonne entstanden ist. Möglicherweise hat das Sonnensystem Material aus mehreren Quellen geerbt hat, wobei Kometen vorzugsweise die am frühesten entstandenen Bestandteile enthalten.

Die nächste Studie untersucht, wie Schwefel die Fraktionierung von Eisenisotopen beeinflusst, wenn sich Planetenkerne vom Silikatmantel trennen. Die Studie konzentriert sich hauptsächlich auf den Mars, der offenbar einen schwefelreichen Kern hat. Hochdruckexperimente zeigen, dass selbst bei einem hohen Schwefelgehalt die Kernbildung des Mars die Eisen-Isotopenverhältnisse nicht stark fraktionieren würde. Dies könnte erklären, warum Marsmeteoriten Eisen-Isotopensignaturen aufweisen, die denen des ursprünglichen Materials des Sonnensystems ähneln.

Die folgenden beiden Studien beschäftigen sich damit, wie sich die späteren Phasen der Akkretion der Erde und der Kernbildung auf die Zusammensetzung des Mantels ausgewirkt haben könnten. Die erste Studie untersucht mit laserbeheizten Diamantstempelzellen, wie sich chalkophile Elemente zwischen Mantel und Kern verteilen. Es wird vermutet, dass die Kernbildung in den späten Phasen der Erdakkretion mit einer Segregation einer Sulfidschmelze einherging. Diese Studie untersucht die Spuren, die ein solcher Prozess im Mantel hinterlassen hätte. Es wurde festgestellt, dass sich die meisten Elemente mit oder ohne Schwefel ähnlich verhalten, was eine Unterscheidung zwischen den Entstehungsszenarien erschwert. Die Ergebnisse deuten jedoch darauf hin, dass sich Silber durch eine Sulfidschmelze möglicherweise effizienter in den Kern abscheiden würde.

Es wird generell angenommen, dass hochsiderophile Elemente (HSEs) während der Planetenentstehung stark in den metallischen Kernen angereichert werden. Die Silikatmäntel der Erde, des Mars und des Mondes weisen jedoch unerwartet hohe und nahezu chondritische relative HSE-Häufigkeiten auf. Dies wird normalerweise durch die Hinzufügung einer "späten Deckschicht" (late veneer) aus chondritischem Material nach dem Ende der Kernbildung erklärt. Diese Interpretation stützt sich jedoch auf experimentelle Daten zur Verteilung der siderophilen Elemente, die bei unrealistisch hohen HSE-Konzentrationen gewonnen wurden. Ansonsten wäre es schwierig, die sehr geringen Konzentrationen zu messen, die in den Silikatschmelzen verbleiben. In der Studie von Li und Zhang wurden Metall-Silikat-Verteilungs-Experimente mit realistischeren HSE-Konzentrationen im flüssigen Metall durchgeführt. Dies ist dank Fortschritten in der Analysetechnik möglich, die die Messung extrem geringer HSE-Konzentrationen im Silikat erlaubt. Die Ergebnisse zeigen, dass Platin und Palladium bei den für einen planetarischen Magmaozean relevanten niedrigen Konzentrationen weitaus weniger stark in Metall- und Sulfidschmelzen angereichert werden. Eine 'late veneer' ist daher möglicherweise nicht erforderlich, um die Platin- und Palladiumkonzentrationen im Mantel zu erklären.

Mondgesteine, die von großen Meteoreinschlägen verändert worden sind, enthalten Spuren von Eisen-Nickel-Legierungen. Diese Legierungen sind Überreste der eingeschlagenen Meteorite. Sie enthalten damit Informationen über späte Akkretionsprozesse. In der folgenden Studie werden die HSE-Häufigkeiten in solchen Gesteinen mit Laserablations-Massenspektrometrie gemessen, um die Ursprünge dieser Impaktoren zurückzuverfolgen. Apollo-Proben enthalten demnach HSE-Signaturen, die mit nicht-kohlenstoffhaltigem Chondrit-Material aus dem inneren Sonnensystem übereinstimmen. Dieses Material hat daher offenbar zur späten Akkretion des Mondes und wohl auch der Erde beigetragen.

Die nächsten beiden Studien befassen sich mit der Kristallisation eines tiefen terrestrischen Magmaozeans. Um herauszufinden, ob die Kristallisation des Erdmantels zu einer Schichtung der Zusammensetzung geführt haben könnte, führten Chanyshev et al. Teilschmelzversuche bei 14–33 GPa an trockenem Peridotit durch. Hierzu wurden Probenumgebungen mit extrem geringen Temperaturgradienten in Vielstempelpressen verwendet. Texturuntersuchungen zeigen eine Aufwärtssegregation der partiellen Schmelzen, was bedeutet, dass Bridgmanit unter diesen Bedingungen dichter ist als die Silikatschmelze. Die Ergebnisse deuten darauf hin, dass sich während der Abkühlung und Kristallisation des unteren Mantels eine von Bridgmanit dominierte Schicht gebildet haben könnte. Die Entwicklung einer solchen Schichtung während der Kristallisation des unteren Mantels könnte die thermische Entwicklung und die interne Dynamik der Erde stark beeinflusst haben, je nach der Verteilung wärmeerzeugender Elemente wie U, Th und K während der Kristallisation des Magmaozeans. Um diese Frage zu untersuchen, bestimmten Zhou et al. die Verteilungskoeffizienten von Spurenelementen zwischen dem Mineral Davemaoit ($CaSiO_3$) und Silikatschmelze mithilfe von Experimenten mit Vielstempelpressen bei Drücken zwischen 20 und 33 GPa. Vorläufige Ergebnisse deuten darauf hin, dass die Davemaoit/Schmelze-Verteilungskoeffizienten für Seltenerd-Elemente mit steigendem Druck erheblich abnehmen. Wenn die Druckabhängigkeit für U, Th und K ähnlich ist, hätten Davemaoit-reiche Bereiche im unteren Mantel erheblich weniger radiogene Wärme erzeugt als bisher angenommen.

Archaische Kratone, die ältesten Kontinentalregionen der Erde, liegen auf Mantelgestein, das ungewöhnlich reich an Siliziumdioxid ist – eine Eigenschaft, die sich nicht durch einfaches Schmelzen von normalem Mantelmaterial erklären lässt. Die nächste Studie in diesem Abschnitt von Melai et al. untersucht die Hypothese, dass diese Gesteine durch die Wechselwirkung zwischen der frühen Lithosphäre und aufsteigenden Komatiit-Schmelzen entstanden sind. Hochdruckexperimente zeigen, dass Komatiit-Schmelzen, die mit Mantelgestein reagieren, Olivin-reiche Zonen und Orthopyroxen-reiche Reaktionsfronten erzeugen, die in ihrer Textur und Zusammensetzung den natürlichen archaischen kratonischen Peridotiten sehr ähnlich sind. Die Ergebnisse stützen ein Modell, nach dem intensiver Komatiit-Magmatismus die Zusammensetzung der frühen Kratonwurzeln verändert und möglicherweise zu ihrer langfristigen Stabilität beigetragen haben.

Einige seltene Diamanten enthalten Einschlüsse von (Mg,Fe)O-Ferroperiklas, einem Mineral, das aus dem unteren Mantel stammen könnte und daher oft als Beweis für einen tiefen Ursprung dieser Diamanten angesehen wird. Ein seit langem bestehendes Rätsel ist jedoch, warum diese Ferroperiklas-Einschlüsse extrem eisenreich sein können, weit mehr als für ein Gleichgewicht mit typischen Mantelgesteinen zu erwarten wäre. In der folgenden Studie untersuchen Hao et al. mithilfe von Hochdruckexperimenten, wie sich Eisen zwischen Ferroperiklas und Karbonatmineralien oder -schmelzen verteilt. Die Ergebnisse zeigen, dass sich während der teilweisen Reduktion von Karbonaten, die ursprünglich relativ wenig Eisen enthalten, sehr eisenhaltiger Ferroperiklas bilden kann. Eine solche teilweise Reduktion, die möglicherweise durch den Zufluss von stärker reduzierten Flüssigkeiten angetrieben wird, würde die lokale Bildung von Diamanten und eisenhaltigem Ferroperiklas ermöglichen, ohne dass ein Ursprung im unteren Mantel erforderlich wäre.

Die nächsten beiden Studien in diesem Abschnitt untersuchen anhand von Analysen einiger der ältesten Gesteine der Erde wichtige Aspekte früher tektonischer Prozesse. In der ersten Studie werden magmatische Gesteine aus dem Mantel aus dem frühen Archaikum (Eoarchaikum > 3,6 Milliarden Jahre alt) aus Nordkanada untersucht, die denen ähneln, die durch Vulkanismus in Inselbögen entstanden sind. Analysen von Schwefelisotopen zeigen eine Signatur, die nur in der frühen Erdatmosphäre entstanden sein kann. Diese Signatur wurde wahrscheinlich zusammen mit Sedimenten aus der frühesten kontinentalen Kruste in den Mantel transportiert in einem Prozess, der der heutigen Subduktion ähnelt. Die Ergebnisse liefern einen direkten Hinweis darauf, dass flüchtige Elemente vor mehr als 3,8 Milliarden Jahren von der Erdoberfläche ins Erdinnere transportiert wurden. Hierdurch wird der Beginn des durch Subduktion angetriebenen Kreislaufs flüchtiger Elemente im Vergleich zu einigen früheren Schätzungen um etwa eine Milliarde Jahre zurückdatiert. In der zweiten Studie werden Gesteine aus dem Eoarchaikum untersucht, die im Südwesten Grönlands und im Norden von Québec erhalten geblieben sind. Diese Gesteine waren ursprünglich sedimentär und enthalten daher Informationen über frühe Oberflächenbedingungen. Sie wurden jedoch später durch Metamorphose überprägt, deren Ausmaß und Zeitpunkt nur unzureichend bestimmt werden konnten. Durch die Kombination von Mineralthermometrie, Druckabschätzungen und Rutil-U-

Pb-Datierung wird die Geschichte der Versenkung, Erhitzung und Veränderung dieser Gesteine rekonstruiert. Metasedimente in beiden Regionen wurden während des Neoarchaikums (~ 2,7 Milliarden Jahre vor heute) unter Bedingungen der oberen Amphibolitfazies einer ähnlichen Hochtemperaturmetamorphose unterzogen. Dies deutet darauf hin, dass geografisch weit voneinander entfernte Teile der frühen kontinentalen Kruste im Neoarchaikum von vergleichbaren tektonischen Prozessen betroffen waren. In Grönland weisen die Gesteine auch eine spätere Episode einer geringeren Metamorphose während der kontinentalen Kollision im Proterozoikum auf, während diese jüngere Überprägung in den kanadischen Proben fehlt.

Skapolith gilt als seltenes magmatisches Mineral. Bei Fraktionierungsexperimenten mit oxidierten, schwefelhaltigen Inselbogen-Magmen stellten Qiao et al. jedoch fest, dass sich bei Drücken $\geq$ 0,7 GPa beträchtliche Mengen an Skapolith bildeten. Das Stabilitätsfeld von Skapolith wurde daher durch Gleichgewichts-Kristallisationsexperimente weiter eingegrenzt, Es erstreckt sich von 850 °C bei 0,7 GPa bis 750–950 °C bei 1,3 GPa. Skapolith könnte ein häufiges Mineral während der Magmafraktionierung bei hohem Druck sein, da es aber bei Druckentlastung und Abkühlung nicht mehr stabil ist, ist es in natürlichen Magmen selten erhalten geblieben.

Die nächsten beiden Beiträge befassen sich mit der Entstehung von porphyrischen Erzlagerstätten, die unsere Hauptquelle für Kupfer und Molybdän darstellen und auch eine wichtige Quelle für Gold sind. Um zu testen, ob einige der in porphyrischen Erzvorkommen enthaltenen Metalle aus subduzierten Sedimenten stammen könnten, untersuchten Hlede et al. die Verteilung von Cu, Mo, Zn und W zwischen wässrigen Fluiden und einer durchschnittlichen subduzierten Sedimentzusammensetzung (GLOSS). Die Experimente wurden bei 600–700 °C und 2,5–4,5 GPa in Stempel-Zylinder-Pressen unter Verwendung der Diamantfallen-Technik ausgeführt. Die Effizienz der Cu- und Zn-Extraktion aus Sedimenten steigt mit zunehmender Salinität, während für Mo und W ein solcher Effekt nur bei 4,5 GPa beobachtet wird. Insgesamt sind die Verteilungskoeffizienten hoch genug, um eine effiziente Mobilisierung aller Metalle zu bewirken. Dies bedeutet, dass anoxische, extrem Mo-reiche Sedimente eine potenzielle Quelle für die Bildung von Mo-reichen porphyrischen Erzen gewesen sein könnten.

Porphyrische Kupfer-Lagerstätten entstehen in der Regel nach Perioden tektonischer Kompression, wenn Restschmelzen nach umfangreicher Magmafraktionierung in der Tiefe in flache Krustenschichten aufsteigen konnten. Während die meisten porphyrische Kupfer-Lagerstätten aus dem Laramide-Zeitalter in Arizona diesem Modell entsprechen, ist die tektonische Lage der wenigen Lagerstätten, die weiter nördlich in Nevada, Utah und Idaho vorkommen, nicht genau bestimmt. Um diese Lücke zu schließen, bestimmten Bain et al. das Alter von Granaten in metamorphen Kernkomplexen dieser Region mittels Lu-Hf-Altersdatierung. Sie fanden Alter, die denen der Porphyr-Kupferlagerstätte Ely-Robinson ähneln. Diese besondere Lagerstätte entstand daher während der Periode der Krustenverdickung und nicht während der anschließenden Spannungsrelaxation.

In der letzten Studie dieses Abschnitts werden einige der ältesten Gesteine der Erde aus dem südlichen Westgrönland mit integrierten mineralogischen, chemischen und isotopischen Analysenmethoden untersucht. Demnach sind diese Gesteine als chemische Sedimente entstanden und nicht aus Vulkaniten oder klastischen Sedimenten. Trotz intensiver Verformung weisen die Gesteine charakteristische Silizium-, Sauerstoff-, Schwefel- und Seltenerdelement-Signaturen auf. Hierzu gehören Meerwasser-ähnliche Spurenelementmuster und massenunabhängige Schwefelisotope, die mit Ablagerungen aus oberflächennahen Fluiden in der Frühgeschichte der Erde übereinstimmen. Obwohl zuvor angenommen wurde, dass diese Gesteine die ältesten biologischen Strukturen der Erde beherbergen, zeigt die Studie, dass die beobachteten Merkmale später durch Verformung und Rekristallisation entstanden sind und keine Hinweise auf frühes Leben liefern.

3.3 Mineralogie, Kristallchemie und Phasenübergänge

Die Phasenbeziehungen und Kristallstrukturen von Mineralen bestimmen, wie sich chemische Elemente zwischen Phasen verteilen und über Skalen ausgetauscht werden, die von den atomaren Grenzflächen zwischen Mineralkörnern bis zu den geophysikalischen Untereinheiten des Erdinneren reichen. Schlüsselelemente, die oft nur in geringen Mengen oder sogar nur in Spuren vorhanden sind, können Verbindungen mit ungewöhnlichen Kristallstrukturen stabilisieren oder die Eigenschaften von gesteinsbildenden Mineralen verändern. Die Beiträge in diesem Abschnitt konzentrieren sich auf die Stabilitäten und kristallchemischen Eigenschaften von Mineralen und Hochdruckverbindungen, die relevant sind für Prozesse, die von der Akkretion und Differenzierung der Erde bis zur heutigen Subduktion und den Stoffkreisläufen von volatilen Elementen im Erdinneren reichen.

Die ersten vier Beiträge in diesem Abschnitt beleuchten die Vielfalt von Bor-, Kohlenstoff- und Wasserstoff-haltigen Mineralen und Verbindungen bei hohen Drücken und Temperaturen. Inspiriert durch Einschlüsse von Boraten in natürlichen Diamanten synthetisierten Antunes *et al.* eine neuartige Mg-Borat-Verbindung und beobachteten deren Kristallstruktur in Abhängigkeit vom Druck. Das Gerüst der Borat-Gruppen in der Kristallstruktur des neuen Mg-Borats, das bei niedrigeren Drücken sowohl planare BO_3-Gruppen als auch BO_4-Tetraeder aufweist, ordnet sich mit steigendem Druck allmählich zu einem rein tetraedrischen Gerüst um. Das organische Mineral Whewellit wurde als Einschluss in Zirkonen gefunden und enthält organische Oxalat-Anionen, die sich in den Fluiden von Subduktionszonen durch abiotische Prozesse bilden könnten. Um die Stabilitätsgrenze von Whewellit entlang dem geothermischen Gradienten einer typischen Subduktionszone zu bestimmen, führten Czekay und Keppler Experimente in Piston-Zylinder-Pressen durch und stellten fest, dass Whewellit selbst bei relativ niedrigen Drücken und Temperaturen zu einer Mischung aus Graphit, Karbonat-Mineralen und CO_2 zerfällt, was auf eine eingeschränkte Stabilität von Oxalat-Anionen in Subduktionszonen hindeutet. Bei deutlich höheren Drücken bildet Kohlenstoff tetraedrische $[CO_4]^{4-}$ Karbonat-Gruppen mit Sauerstoffatomen in vierfacher Koordination. Unter den

Produkten ihrer Experimente mit laserbeheizten Diamantstempelzellen fanden Pantousas *et al.* zwei neue Hochdruck-Karbonat-Phasen. Die Kristallstrukturen dieser Phasen basieren auf einem ausgedehnten dreidimensionalen Gerüst bzw. spiralförmigen Ketten von $[CO_4]^{4-}$ Karbonat-Gruppen. Diese Ergebnisse weisen auf eine bemerkenswerte strukturelle Vielfalt von tetraedrischen Karbonaten hin, die in gewisser Weise der strukturellen Vielfalt der Silikate ähneln könnte. Wie Kohlenstoff ist auch Wasserstoff ein volatiles Element, das in Hochdruckverbindungen eingebaut und so möglicherweise in den Materialien des tiefen Erdinneren gespeichert werden kann. Beim Erhitzen einer Reihe von eisenhaltigen Ausgangsmaterialien in laserbeheizten Diamantstempelzellen entdeckten Yuan *et al.* zwei neue Eisen-Oxyhydroxid-Phasen mit Eisen-Kationen in acht- und neunfacher Koordination. Angesichts ihrer hohen Dichte und thermischen Stabilität vermuten Yuan *et al.*, dass diese Oxyhydroxide aus einem Magmaozean an der Basis des Erdmantels auskristallisiert sein könnten. Sie könnten seitdem Wasserstoff im untersten Erdmantel gespeichert haben.

Der Phasenübergang in Ca-reichem Silikat-Perowskit, Davemaoit, kann die physikalischen Eigenschaften im tiefen Erdmantel von der Übergangszone bis zum unteren Erdmantel beeinflussen. Wu *et al.* untersuchten den Phasenübergang von $CaSiO_3$-$CaTiO_3$ Mischkristallen, um das Verhalten von Calciumsilikat-Perowskit im unteren Erdmantel mithilfe von Einkristall-Röntgendiffraktometrie und der Analyse möglicher Zwillingsbeziehungen zu verstehen. Verzwillingungen in Ti-haltigen Calcium-Perowskiten könnten auf eine Phasenumwandlung beim Abkühlen zurückzuführen sein, die mit einer Reduktion der Kristallsymmetrie einhergeht. Nicht nur Feststoffe, sondern auch Flüssigkeiten können unter extrem hohen Drücken Phasenübergänge erster Ordnung zeigen. Niu *et al.* untersuchten die Flüssig-Flüssig-Phasenumwandlungen von elementarem Schwefel, indem sie *in-situ*-Strukturmessungen bei hohen Drücken und hohen Temperaturen mittels Synchrotron-Röntgenbeugung in einer Vielstempel-Presse durchführten. Ihre neuen Schmelzkurven und Strukturdaten bieten einen hochpräzisen experimentellen Maßstab für das Verständnis der Thermodynamik und die Interpretation des Phasenverhaltens von schwefelhaltigen Systemen im Inneren von Planeten wie etwa dem Mars.

Die direkte Visualisierung von Atomketten ist eines der wirksamsten Werkzeuge zum Verständnis der atomaren Struktur von Mineralen. Jüngste Entwicklungen zur Korrektur der sphärischen Aberration in der Raster-Transmissions-Elektronenmikroskopie (STEM) erhöhen das Potenzial von Aufnahmen im High-Angle-Annular-Dark-Field-Modus (HAADF). Mithilfe moderner, für sphärischen Aberration korrigierter STEM und ergänzenden *ab-initio*-Berechnungen visualisierten Yao *et al.* Modulationen in der Fernordnung einer uranhaltigen Hämatit-Überstruktur. Ihr Modell einer relaxierten Überstruktur für Hämatit stimmt gut mit den STEM-HAADF-Beobachtungen überein. Mit einer ähnlichen Technik der hochauflösenden STEM untersuchten Miyajima *et al.* die Grenzfläche zwischen einem Diopsid-Kristall aus einem natürlichen Peridotit und einer Amphibol-Lamelle, die in den Kristall eingewachsen ist. Die hochauflösenden STEM-Bilder der Grenzfläche zeigen eine nur wenige Nanometer dicke Lage, die sich entlang der Grenzfläche erstreckt und eine atomare Struktur aufweist, die der des

Minerals Talk ähnelt. Die Struktur der Grenzfläche lässt sich durch eine topotaktische Abfolge von Pyroxen- und Glimmer-Modulen beschreiben, wie sie von J. B. Thompson für "Biopyribole" definiert wurden.

Um die Verteilung von Wasser im Erdinneren zu verstehen, sind präzise Messungen des Wassergehalts in anisotropen Mineralen erforderlich. Um die Genauigkeit der mittels Infrarot-Absorptions-Spektroskopie bestimmten Wassergehalte zu verbessern, stellen Withers und Zhang einen neuen Ansatz zur Analyse der anisotropen Absorption von Infrarotstrahlung durch Minerale mit unterschiedlichen Symmetrieklassen vor. Sie testeten ihr Modell, indem sie polarisierte und unpolarisierte Spektren von Olivin-Kristallen in verschiedenen Schnittlagen aufnahmen und die experimentellen Spektren mit den Modellvorhersagen verglichen. Das Modell sagt außerdem Unsicherheiten für unpolarisierte Messungen an Kristallen mit unterschiedlichen Symmetrieklassen und optischen Eigenschaften voraus.

Eisenmeteorite sind Teile der metallischen Kerne differenzierter Planetenkörper und liefern wichtige Informationen über die Entstehung von Planeten. Zhao *et al.* klassifizierten den komplexen Eisenmeteorit Wedel-IAB auf der Grundlage mineralogischer und chemischer Untersuchungen unter Verwendung der Elektronenstrahl-Mikroanalyse sowie der Laser-Ablations-Massenspektrometrie mit induktiv gekoppeltem Plasma (LA-ICP-MS). In dem Meteorit fanden sie das seltene Mineral Schreibersit, ein Eisen-Nickel-Phosphid, und bestimmten eine neue Kristallstruktur für dieses Mineral, die sich durch eine geordnete Verteilung von Ni-Atomen auszeichnet.

3.4 Physikalische Eigenschaften von Mineralen

Dank der jüngsten technologischen Fortschritte, wie sie in Kapitel 3.8 beschrieben werden, können nun Minerale unter Druck- und Temperaturbedingungen untersucht werden, die zuvor nur sehr schwer zu erreichen waren. Es überrascht daher nicht, dass die in diesem Kapitel vorgestellten Beiträge diese Innovationen nutzen, um neue Erkenntnisse über die Eigenschaften des Erdinneren zu gewinnen.

In den ersten beiden Beiträgen wurden der neu installierte MAR345-Detektor und das neue hochauflösende Rigaku-Diffraktometer verwendet, um jeweils die P-V-T-Zustandsgleichung eines Granats zu untersuchen. Diese Probe hatte eine Zusammensetzung, wie sie im Mantel von Mars erwartet wird. Mit den gleichen Geräten wurden auch die strukturellen Veränderungen untersucht, die bei steigendem Druck in einem Fe- und Al-haltigen Bridgmanit-Kristall auftreten. Der Fe-reiche Majorit-Granat scheint einen identischen Kompressionsmodul wie Pyrop zu haben. Dies liegt wohl am Fe^{3+} auf dem oktaedrischen Gitterplatz, das dem Effekt der Majorit- und Almandin-Substitutionen entgegenwirkt. Laufende Hochtemperaturmessungen zielen darauf ab, den Effekt der chemischen Zusammensetzung auf die thermische Ausdehnung unter Druck zu bestimmen. Der niedrigere Kompressionsmodul von Fe,Al-haltigem Bridgmanit im Vergleich zu Al-haltigem $MgSiO_3$ lässt sich durch die größere Kompressibilität der A-Position aufgrund der Fe^{3+}-Substitution erklären.

Im dritten Beitrag wurden dank der jüngsten Optimierungen der Vielstempel-Hochdruckpressen Ultraschalldaten für Bridgmanit in Synchrotronanlagen bei Drücken von bis zu 35 GPa und bei 1500 K gesammelt. Dies sind die ersten Ultraschalldaten unter solchen Bedingungen. Sie deuten darauf hin, dass bestehende thermodynamische Modelle die temperaturbedingte Verringerung der Schallwellengeschwindigkeiten in Bridgmanit wahrscheinlich unterschätzen.

In der Literatur besteht eine deutliche Diskrepanz zwischen den an polykristallinen Proben gemessenen Schallwellengeschwindigkeiten und denen, die aus dem vollständigen elastischen Tensor von Einkristallen berechnet wurden. Um die möglichen Ursachen dieser Diskrepanz aufzuklären, müssen die Eigenschaften von polykristallinen Proben gemessen werden, die hinsichtlich Korngröße und Porosität gut charakterisiert sind. Im vierten und fünften Beitrag wurden gesinterte Proben von Stishovit und Bridgmanit mittels Brillouin-Streuung untersucht, um den Einfluss der Korngröße und der Orientierungsverteilung auf die Schallwellengeschwindigkeiten in diesen Mineralien zu bestimmen. Die Brillouin-Spektren der Stishovit-Probe mit einer Korngröße im Nanometerbereich zeigen Scherwellen-Geschwindigkeiten, die für eine elastische Reaktion von Kornaggregaten charakteristisch sind. Dies steht im Gegensatz zum Verhalten der Bridgmanit-Probe, deren Korngrößenverteilung im Mikrometerbereich liegt.

Eine weitere Schwierigkeit bei der Messung von Brillouin-Spektren polykristalliner dichter Minerale besteht darin, dass die Signale der longitudinalen Schallwellen-Geschwindigkeit in der Regel unter den Scherwellen-Geschwindigkeiten der Diamantstempel verborgen sind. Im sechsten Beitrag wurde ein neues Diamant-Stempel-Design mit einer abgerundeten statt einer flachen Stempeloberfläche verwendet, um die Brillouin-Streuung einer polykristallinen Bridgmanit-Probe zu messen. Die Verwendung dieser Stempel verbesserte die räumliche Auflösung, so dass die Longitudinalwellen-Geschwindigkeit von Bridgmanit erstmals bei hohem Druck aus einer pulverförmigen Probe gemessen werden konnte.

Im siebten Beitrag werden Brillouin-Streuung und Röntgenbeugung in Verbindung mit einer CO_2-Laserheizung verwendet, um Einblicke in das Verhalten von Quarz bei hohen Temperaturen und hohem Druck zu gewinnen. Veränderungen der Elastizitätsmoduli über den α-β-Quarzübergang wurden bei 2 GPa kartiert und zeigten, dass sowohl die Kompressionswellengeschwindigkeit als auch der Kompressionsmodul von β-Quarz deutlich niedriger sind als von aktuellen thermodynamischen Modellen vorhergesagt.

Kubischer $CaSiO_3$-Perowskit, Davemaoit, ist nach wie vor ein sehr wenig erforschtes Mineral, da es aus Hochdruckversuchen nicht in kristalliner Form gewonnen werden kann. Analoga zu diesem Material sind typischerweise Ti-haltige $CaSiO_3$-Proben, die in einer verzerrten orthorhombischen Perowskitstruktur kristallisieren. Im vorletzten Beitrag wurden Brillouin-Spektren eines Perowskits mit einem Verhältnis Ti:Si = 1 gesammelt, um dessen vollständigen elastischen Tensor zu erhalten.

Das maschinelle Lernen entwickelt sich zu einem zentralen Werkzeug in der computergestützten Forschung. Im letzten Beitrag wurde ein bisher unbekannter Phasenübergang in ungeordnetem $CaCO_3$ unter lithosphärischen Bedingungen mit Hilfe einer DFT-basierten, durch maschinelles Lernen beschleunigten Molekulardynamik-Simulation entdeckt. Der Übergang führt zu einer signifikanten elastischen Erweichung, was den Ursprung einer lokalen mittel-lithosphärischen Diskontinuität erklären könnte.

3.5 Fluide, Schmelzen und ihre Wechselwirkung mit Mineralen

Die flüchtigen Elemente Kohlenstoff, Stickstoff und Wasserstoff bestimmen weitgehend die Bewohnbarkeit der Erdoberfläche. Das größte Reservoir dieser Elemente in unserem Planeten ist jedoch wahrscheinlich der Erdmantel. Untersuchungen zum Speichervermögen des Mantels für diese Elemente und über ihren Austausch mit der Erdoberfläche sind daher von entscheidender Bedeutung für das Verständnis der Evolution der Erde. Unter den flüchtigen Elementen war Stickstoff immer besonders rätselhaft. Aufgrund der Zusammensetzung der Reservoire nahe an der Erdoberfläche sowie des oberen Mantels scheint es, dass Stickstoff auf der Erde relativ zu Kohlenstoff und Wasserstoff um eine Größenordnung verarmt ist. Frühere Arbeiten am BGI haben aber bereits gezeigt, dass diese scheinbare Verarmung möglicherweise vorgetäuscht wird durch eine Anreicherung von Stickstoff in einem Reservoir des unteren Erdmantels, welches durch geologische Aktivität kaum beprobt wird. Der erste Beitrag in diesem Kapitel des Jahresberichts macht diese Vermutung noch plausibler. Neue experimentelle Daten zeigen, dass die Löslichkeit von Stickstoff in Eisen- und Aluminium-haltigem Bridgmanit, dem häufigsten Mineral des unteren Mantels, weit höher ist als bisher aufgrund von Experimenten im reinen $MgSiO_3$-System vermutet wurde.

Die Subduktion ozeanischer Kruste transportiert ständig leichte Elemente von der Erdoberfläche zurück in den Mantel. Wie effizient dieser Prozess ist, ist jedoch nicht genau bekannt. Einige frühere Studien hatten vorgeschlagen, dass Stishovit (eine Hochdruckphase von SiO_2) ein wichtiges Medium für den Transport von Wasser in den unteren Mantel sein könnte. Neue in-situ Röntgenbeugungs-Experimente in einer Multi-Anvil-Apparatur zeigen jedoch, dass die Wasser-Löslichkeit im Stishovit mit steigender Temperatur stark abnimmt, was die Effektivität des Transports einschränkt. Die Subduktion von Kohlenstoff ist vielleicht noch weniger gut verstanden als für Wasser. Seit einiger Zeit gibt es theoretische Vorhersagen, wonach zusätzlich zu CO_2 und CH_4 auch organische Kohlenstoff-Verbindungen in Fluiden von Subduktionszonen bei hohem Druck stabil sein könnten. Dies wurde mit Hilfe von Piston-Zylinder-Experimenten untersucht, bei denen Fluide unter hohem Druck als synthetische Flüssigkeitseinschlüsse in Quarz beprobt wurden. Die Ergebnisse zeigen, dass bei hohem Druck und hoher Temperatur Kohlenstoff im thermodynamischen Gleichgewicht nur als CO_2, CH_4 oder Graphit vorliegt. Einige organische Moleküle können allerdings auch metastabil bis zu erstaunlich hohen Temperaturen erhalten bleiben.

Die übrigen Beiträge in diesem Abschnitt des Jahresberichts untersuchen alle die Eigenschaften von Magmen und ihre Konsequenzen für die Evolution von Planeten und für vulkanische Prozesse. Wasser kann die Viskosität von Silikatschmelzen um viele Größenordnungen verringern und auch andere Eigenschaften drastisch verändern. Dies liegt teilweise an einer chemischen Reaktion des Wassers mit der Schmelze, gemäß dem Gleichgewicht $H_2O + O^{2-} = 2\ OH^-$. Dieses Gleichgewicht ist in SiO_2-reichen Schmelzen sehr gut bekannt, jedoch fehlen Daten für basaltische Magmen weitgehend. In einem neuen Projekt wird die Temperaturabhängigkeit des Lösungsmechanismus von Wasser durch langfristige Temperexperimente unterhalb der Glastransformations-Temperatur untersucht. Vorläufige Ergebnisse zeigen, dass die eine sinnvolle experimentelle Strategie sein könnte.

Die beiden folgenden Beiträge entwickeln Modelle für die Viskosität von Silikatschmelzen. Magmen auf dem Planeten Mars enthalten generell mehr Eisen als auf der Erde. In-situ Messungen entsprechender Peridotit-Schmelzen zeigen, dass die Viskosität der Fe-reichen Schmelzen auf Mars etwas geringer ist als für die entsprechenden Zusammensetzungen auf der Erde. Diese Daten werden verwendet werden, um die frühe Evolution von Mars zu modellieren. Auf der Erde sind wasserhaltige andesitische Schmelzen eine Hauptquelle vulkanischer Risiken. Ein neues Viskositätsmodell zeigt beispielsweise, dass die Magmen des Sakurajima-Vulkans in Japan etwa 45mal weniger viskos sind, als früher angenommen wurde.

Die letzten beiden Beiträge in diesem Abschnitt des Jahresberichts beschreiben Experimente, mit denen vulkanische Prozesse direkt im Labor simuliert werden: Die Keimbildung von Gasblasen in vulkanischen Schloten und die Fragmentierung von Magmen bei vulkanischen Explosionen. Technisch besonders eindrucksvoll ist die Zeit-aufgelöste, dreidimensionale Abbildung der Blasenbildung in einem Magma mit Hilfe von Synchrotron-Strahlung.

3.6 Rheologie

Seit ihren Anfängen ist die Erde ein dynamischer Planet, so dass die Rheologie von Gesteinen und Mineralen in ihrer Entwicklung bis heute ein wichtiger Faktor ist. Die Rheologie beschreibt die Verformung von Gesteinen aufgrund von deviatorischen (Scher-)Spannungen. Sowohl die Spannung als auch die Verformung beeinflussen die physikalischen Eigenschaften von Gesteinen und wirken sich auch auf chemische Prozesse wie metamorphe Mineralreaktionen aus. Insbesondere letzterer Effekt war Gegenstand der ersten beiden in diesem Kapitel vorgestellten experimentellen Studien. *Silva et al.* reproduzierten experimentell die P,T Bedingungen in subduzierenden ozeanischen Platten, in denen Serpentinit bei steigender Temperatur und steigendem Druck eine Dehydratisierungs-Reaktion zu Olivin, Orthopyroxen und Granat durchläuft. Es wird vermutet, dass diese Reaktion die ungewöhnlich tiefen Erdbeben verursacht, die in Subduktionszonen auf der ganzen Welt beobachtet werden. Die Ergebnisse zeigen, dass durch die gleichzeitige Verformung ein Netzwerk von Reaktionsprodukten entsteht und dass eine spröde (potenziell seismische) Verformung nur bei hohen Spannungen und Verformungsraten möglich wird. *Sieber et al.* untersuchten die Karbonatisierung von (ultra-)mafischen Gesteinen bei hohem Druck und hoher Temperatur durch eine fluidgetriebene Reaktion unter deviatorischen Spannungen. Die gleichzeitige Verformung verstärkte die Bildung von Karbonaten erheblich, indem sie in Olivin Risse und damit zusätzliche Wegsamkeiten für die Fluide erzeugte. Die statische Karbonatisierung führte zu einer Erniedrigung der Festigkeit des Wirtsgesteins, so dass die nachfolgende Verformung größtenteils durch die duktileren Karbonate aufgefangen wurde. Diese Prozesse sind auch für die potenzielle Speicherung von atmosphärischem CO_2 in (ultra-)mafischen Gesteinen von Bedeutung.

Da Deformationsexperimente oft eine technische Herausforderung darstellen, werden auch rechnerische Ansätze wie geodynamische Modellierungen oder ab-initio Berechnungen verwendet, um verschiedene Aspekte rheologischer Probleme zu untersuchen. Der dritte Beitrag nutzt einen rechnerischen Modellierungsansatz, um die mechanischen Konsequenzen unterschiedlicher Gesteinsrheologien in einer Subduktionszone zu untersuchen. *Weiler et al.* verwendeten dazu ein 2D-Modell mit einer nichtlinearen viskoelasto-plastischen Rheologie, um die potenzielle Quelle von Erdbeben mittlerer Tiefe in der Hindukusch-Region zu simulieren. Diese Erbeben hängen vermutlich mit der Ablösung der subduzierenden ozeanischen Erdplatte während der Subduktion zusammen. Das Viskositätsverhältnis zwischen der unteren Kontinentalkruste und der ozeanischen Lithosphäre sowie die Tiefe der unteren Kruste bestimmen offenbar die Tiefe, in der Seismizität und Plattenablösung auftreten. Im letzten Beitrag nutzen *Schulze & Steinle-Neumann* molekulardynamische Berechnungen, um den Diffusionskoeffizienten von Sauerstoff-Leerstellen im Kristallgitter des $CaSiO_3$-Perowskits (Davemaoit) unter den P,T-Bedingungen des unteren Mantels zu bestimmen. Diese ist ein entscheidender Faktor für die plastische Verformung dieses Minerals. Die Ergebnisse zeigen, dass Davemaoit unter den Mineralien des unteren Mantels die schnellste Diffusion von Sauerstoffleerstellen aufweist und somit die duktilste Komponente in diesem Bereich des Erdinneren darstellt.

3.7 Materialwissenschaften

Lange Zeit dominierten in diesem Abschnitt des Jahresberichts Forschungsberichte zu metallbasierten Oxiden, Karbiden und technischen Perowskiten mit relativ einfachen Strukturen. Dank Fortschritten bei der Röntgenbeugung und Datenverarbeitung sind jedoch auch wesentlich komplexere Strukturen zugänglich, zudem ermöglichen sie die Untersuchung von Elementen mit Röntgenstreufaktoren, die vor einem Jahrzehnt noch als zu gering für eine zuverlässige Strukturbestimmung galten. Dieser Trend spiegelt sich auch in den Beiträgen zu diesem Abschnitt des Jahresberichts wider, in dem fast alle vorgestellten Studien auf Experimenten in der Diamantstempelzelle basieren, um mit Hilfe verschiedener Röntgenquellen Hochdruckstrukturen zu charakterisieren.

Eine Ausnahme bildet das erste Projekt des Kapitels, das ein Thema aus dem letztjährigen Jahresbericht wieder aufgreift: das Verhalten von chiralen Halogenid-Perowskiten mit einer hybriden organisch-anorganischen Struktur unter hohem Druck in der Vielstempel-Presse. Trotz der hohen Kompressibilität der chiralen Perowskite und deren Amorphisierung bei 15–20 GPa sind wiedergewonnene Proben vollständig kristallin, zeigen aber geringfügige Unterschiede zur ursprünglichen Struktur. Metallhalogenide sind auch das Thema des zweiten Beitrags, in dem Eisenchlorid und Eisenbromid bei hohem Druck Strukturen bilden, die auf einer oktaedrischen Umgebung von Fe basieren. Bei zwei Chloriden (Fe_4Cl_9 und Fe_3Cl_8) sitzt Fe^{3+} und beim Bromid ($FeBr_2$) Fe^{2+} im Zentrum der Halogen-Oktaeder. Die Unterschiede zwischen den vom oktaedrischen Gerüst gebildeten Strukturen sind größer als erwartet und hängen mit der Wechselwirkung der Strukturen mit elektronischen und magnetischen Eigenschaften zusammen. In einem weiteren Beitrag zu Halogeniden wird die Synthese von Mg_3Cl_7 unter hohem Druck vorgestellt, einem seltenen Fall eines polaren Metalls, bei dem die freien Elektronen des Metalls die strukturellen Dipol-Dipol-Wechselwirkungen nicht (vollständig) abschirmen.

Die folgenden beiden Beiträge greifen Themen aus dem Vorjahr wieder auf, wobei der erste das Verhalten aromatischer Kohlenwasserstoffe unter Druck untersucht. Naphthalin ($C_{10}H_8$) und Anthracen ($C_{14}H_{10}$) zeigen bis zum erreichten Maximaldruck (~ 50 GPa) eine bemerkenswerte strukturelle Stabilität. In den letzten Jahren haben Forscher am BGI eine große Vielfalt an Stickstoffverbindungen entdeckt, die unter hohem Druck entstehen und fast die Vielfalt von Kohlenstoff-Strukturen aufzeigen. Hier wird über die Synthese einer Mischverbindung mit Cyclo-N_5^--Anionen und N_2-Dimeren berichtet, die bei Drücken von über 100 GPa einen Kristall mit Perowskit-Topologie bildet.

Seit Jahrzehnten wird in Diamantstempelzellen die Rubin-Druckskala verwendet, die auf der Lumineszenz von Cr^{3+}-dotiertem Al_2O_3 basiert. Unter nicht-hydrostatischen Bedingungen verbreitern sich jedoch die beiden Emissionslinien und beginnen zu überlappen, sodass alternative Druckskalen erforderlich sind. Im sechsten Beitrag wird die Lumineszenz in Al-Oxonitridoborat AlB_4O_6N, ebenfalls dotiert mit Cr^{3+}, als alternative Druckkalibrierung untersucht, mit vielversprechenden Ergebnissen bei niedrigem Druck, aber einer Aufspaltung des Fluoreszenzpeaks bei etwa 75 GPa, die seine Anwendbarkeit einschränkt.

Im letzten Beitrag dieses Abschnitts werden Ergebnisse aus Molekulardynamik-Simulationen vorgestellt, die zur Interpretation eines der ersten Experimente am European XFEL in Schenefeld bei Hamburg beitragen. Die Experimente deuten auf die Bildung von Goldhydrid bei hohem Druck und hoher Temperatur hin, wobei das Gold mit Kohlenwasserstoffen als Wasserstoffquelle in eine Diamantstempelzelle geladen wurde. Hoher Druck und hohe

Temperaturen werden in einer Freie-Elektronen-Laseranlage für Röntgenstrahlung durch eine Folge ultrakurzer, hochenergetischer Röntgenimpulse erreicht, die auch zur Röntgenbeugung verwendet werden. Die Simulationen stützen die experimentelle Hypothese zur Bildung von Goldhydrid und die daraus abgeleitete hexagonale Struktur und liefern eine plausible Erklärung für die Stabilisierung einer entropiegetriebenen Hochtemperaturphase durch die superionische Diffusionsfähigkeit des Wasserstoffs durch das Goldgitter.

3.8 Methodische Entwicklungen

Die Verbesserung der experimentellen und analytischen Techniken war seit den Anfängen der Forschung am BGI von entscheidender Bedeutung. Die experimentellen Entwicklungen konzentrierten sich auf die Erweiterung des zugänglichen Parameterraums für Hochdruck- und Hochtemperaturversuche, um die Bedingungen im Erdinneren oder im Inneren anderer Planeten nachzubilden. Da steigende Drücke und Temperaturen in Experimenten tendenziell zu immer kleineren Proben führen, müssen gleichzeitig auch die Analysetechniken an immer kleineren Probenvolumina mit einer höheren räumlichen Auflösung angepasst werden. Dieser Abschnitt umfasst vier Beiträge, die methodische Fortschritte bei der Erweiterung des experimentellen Parameterraums vorstellen, sowie vier Projekte, die die Analysemöglichkeiten verbessern oder Fortschritte bei der computergestützten Modellierung beschreiben.

Kurnosov et al. berichten über die Installation eines neuen Lasers zur Aufheizung kleiner Proben in der Diamant-Stempelzelle in einem System, mit dem die Dichte (mittels Röntgenbeugung) und die Elastizität (mittels Brillouin-Streuung) eines einzelnen Kristalls bei Drücken und Temperaturen für den gesamten unteren Mantel bestimmt werden können. Derartige Messungen werden dringend benötigt, um seismische Daten zur Aufklärung der Struktur des Erdinneren zu interpretieren. *Niu et al.* präsentieren eine signifikante Erweiterung des zugänglichen Druck-Bereichs in Experimenten mit Kawai-Vielstempelpressen. Während Standardpressen dieses Typs auf einen Druck von etwa 25 GPa begrenzt sind, gelang es ihnen mithilfe einiger technischer Fortschritte, Drücke von bis zu 45 GPa zu erreichen und dabei ein Probenvolumen von etwa 10 mm^3 beizubehalten.

Die Messung des Fluid-Überdrucks in einer experimentellen Vielstempelpresse bei hohem Druck und hoher Temperatur wird von *Pöppelbaum et al.* im dritten Bericht dieses Kapitels demonstriert. Dieses Phänomen tritt häufig in der tiefen Erde auf, wo Wasser aufgrund steigender Umgebungsdrücke und -temperaturen aus Kristallstrukturen freigesetzt werden kann. Dieser Vorgang führt zu einer Erniedrigung des Umgebungsdrucks und kann so Erdbeben in Tiefen verursachen, in denen normalerweise keine spröden Brüche mehr auftreten. *Kubik et al.* stellen einen Entwurf für einen Versuchsaufbau in einer Vielstempelpresse vor, der das gleichmäßige Erhitzen relativ großer Probenmengen mit geringen Temperaturgradienten ermöglicht. Dies wird durch den Einsatz eines kastenförmigen Ofens anstelle des üblicherweise verwendeten zylinderförmigen Ofens erreicht.

Minchenkova und Audétat stellen eine Strategie zur Messung experimentell erzeugter Diffusionsprofile mit Laserablations-ICP-MS vor. Diese Messmethode bietet im Vergleich zu anderen Methoden eine höhere Empfindlichkeit, benötigt dafür aber eine größere Menge an Probenmaterial. Anstatt die chemische Konzentration vertikal entlang eines Diffusionsprofils zu messen, bereiteten sie daher ihre Proben so vor, dass das erzeugte Profil fast horizontal liegt, und so bis zu 10-fach verlängert wird, wodurch größere Mengen an Probenmaterial pro Messpunkt gemessen werden können.

Die nächsten beiden Beiträge präsentieren Fortschritte bei der hochpräzisen Analyse von Isotopenverhältnissen unter Verwendung eines Neoma MC-ICP-MS/MS in Verbindung mit einem 193 nm Nanosekunden-Excimerlaser. *Zhu et al.* optimierten die Analyse von Sn-Isotopen, die häufig als Tracer für die Metallogenese, die Charakterisierung der magmatisch-hydrothermalen Entwicklung und die Geochemie der Erdkruste verwendet werden. *Chen et al.* entwickelten ein neues Protokoll zur Bestimmung des Alters von Mondgesteinen mit dem Rb/Sr-Isotopensystem. Hierdurch werden frühere Probleme überwunden, insbesondere die isobare Interferenz von ^{87}Rb auf ^{87}Sr, die die Messgenauigkeit beeinträchtigen kann.

Bei ihrer numerischen Modellierung von Lokalisierungsprozessen während der plastischen Gesteinsverformung stießen *Spang et al.* auf Probleme, die sich aus stark variierenden räumlichen und zeitlichen Skalen während der Simulation ergaben. Dadurch wurden die Resultate des Modells weitgehend von der zeitlichen und räumlichen Gitterskala und nicht von den tatsächlichen physikalischen Prozessen bestimmt. Als Lösung entwickelten sie einen Algorithmus, der sich dynamisch an die zeitliche Entwicklung des Verformungsprozesses anpasst. Außerdem prüften sie verschiedene Optionen, um die Variationen der räumlichen Skala im Modell zu begrenzen. Beide Ansätze verbesserten die Resultate der Modellierung deutlich.

3. Research Projects

3.1 Earth and Planetary Structure and Dynamics

In this first section, nine contributions investigate both Earth and planetary processes from surface to core in our Solar System and beyond. They investigate the composition of protoplanetary disks, the impact-related formation of mesosiderite meteorites and the composition of the martian core. Also, geodynamical simulations give insights into the evolution of tidally locked super-Earths and the seismic unrest and surface deformation caused by magma influx underneath the Campi Flegrei.

The first contribution by Spaargaren and colleagues examines how elemental volatility during protoplanetary disk condensation varies with initial disk composition. By modelling 1,000 disk compositions based on observed stellar abundances, they find that rocky planet compositions depend strongly on C/O ratios, producing Earth-like, graphite-rich, or Mg–Si-depleted planets. A greater diversity of rocky exoplanets is therefore predicted when accounting for a compositional dependence on condensation temperatures.

In the second contribution, Bermingham and colleagues used mass-independent Mo isotopic data to constrain the origin of Earth's late-stage building materials. Results suggest that the final 10-20 % of Earth's accretion was dominated by non-carbonaceous, inner Solar System material, with only minor possible contributions from carbonaceous sources, reconciling previous discrepancies between Mo and Ru isotopic signatures.

In the third contribution, Zippoli and colleagues investigate the origin of mesosiderite meteorites using petrography, trace-element geochemistry, and deformation experiments. Their findings suggest that mesosiderites may be related to eucrite meteorites and the asteroid Vesta through large impact events that mixed core-derived metal with crustal silicates, producing characteristic textures, variable cooling histories, and incomplete chemical equilibration within a single differentiated parent body.

The fourth contribution by Hu and colleagues investigates the Sm-Nd and Lu-Hf isotope systematics of three Martian meteorites to constrain the early chemical evolution of Mars. Three shergottites show distinct REE patterns, with NWA 4468 and EETA 79001 linked to the enriched and intermediate groups, respectively. The REE and isotopic data reveal that Teghaza 001 (4.2 Ga) has a unique composition among shergottites, suggesting a link to an early-formed crustal reservoir and the polymict breccia NWA 7034.

In the following contribution, Pierru and colleagues study the physical properties of silicate melts at martian core mantle boundary pressures to shed light onto the formation and stability of a basal melt layer located at the martian core mantle boundary that has been proposed based on seismic observations. These findings provide new insights into the thermochemical evolution of the planet Mars.

In the sixth contribution, Frost and colleagues develop a thermodynamic model to determine the oxygen content in the otherwise sulphur-rich martian core to better explain the seismic velocities as measured by the InSight mission seismic station. These results allow us to better constrain both the conditions of core formation on Mars and shed light on the early geodynamo activity of Mars.

In the seventh contribution, Meier and colleagues model the thermochemical evolution of tidally locked ultrashort-period super-Earth K2-141 b to make predictions on not only its tectonic regime, but also on the extent of its dayside magma ocean, its nightside volcanic activity and the related atmospheric outgassing. These predictions can be tested using the advent of high-resolution observations, thus allowing us to study the otherwise inaccessible magma ocean stage of young terrestrial planets.

In the eighth contribution, Spang and colleagues use a 3D visco-elastic model to simulate magma intrusion into a magma chamber and show that thermal weakening of the surrounding rocks caused by the hot magma affects the amplitudes of overpressure and surface deformation by up to one order of magnitude.

In the final contribution, Nardoni and colleagues use the same type of 3D numerical models to simulate the magma influx underneath the Campi Flegrei near Naples and demonstrate that this magma influx can only partly explain the surface uplift observed in this region over the last years, thus requiring additional contributions to fully explain the uplift history.

a. *Proto-planetary disk composition-dependent element volatility in the context of rocky planet formation (R. Spaargaren/Groningen, O. Herbort and P. Sossi/Zurich; H.S. Wang/ Copenhagen and S.J. Mojzsis)*

The inferred compositions of the solar System terrestrial (rocky) bodies are fractionated from that of the Sun, where elemental depletions in the bulk rocky bodies correlate with element volatility, expressed as their 50 % condensation temperature. However, because element volatility depends on disk gas composition, it is not mandated that elemental fractionation trends derived from the solar-terrestrial scenario apply to other planetary systems. In this work, we expanded upon previous efforts to quantify element volatility during disk condensation.

We first simulated condensation sequences for a sample of 1,000 initial disk compositions based on observed stellar abundances (Fig. 3.1-1). Based on these simulations, we presented parametrisations of how element 50 % condensation temperatures depend on disk composition, and applied element fractionation trends with appropriate element volatility to stellar abundances to simulate plausible compositions of a large population of rocky exoplanets.
We could show that Earth-like planets emerge from low-C/O disks (C/O less than or equal to 0.75) and graphite-bearing planets from high-C/O disks (C/O higher than 0.75). Furthermore, we identify an intermediate-C/O (0.84-1.04) class of planets characterised by Mg and Si

depletion, leading to relatively high abundances of Fe, Ca, and Al. We also show that devolatilization patterns could be adapted potentially with disk composition-dependent condensation temperatures to make predictions of rocky planet bulk compositions within individual systems. Although such patterns could be further modified by the dynamics of planetary accretion that remains under-constrained for most exoplanetary systems. The outcomes of our analysis suggest that accounting for disk composition-dependent condensation temperatures means that we can expect an even broader range of possible rocky planet compositions than has previously been considered.

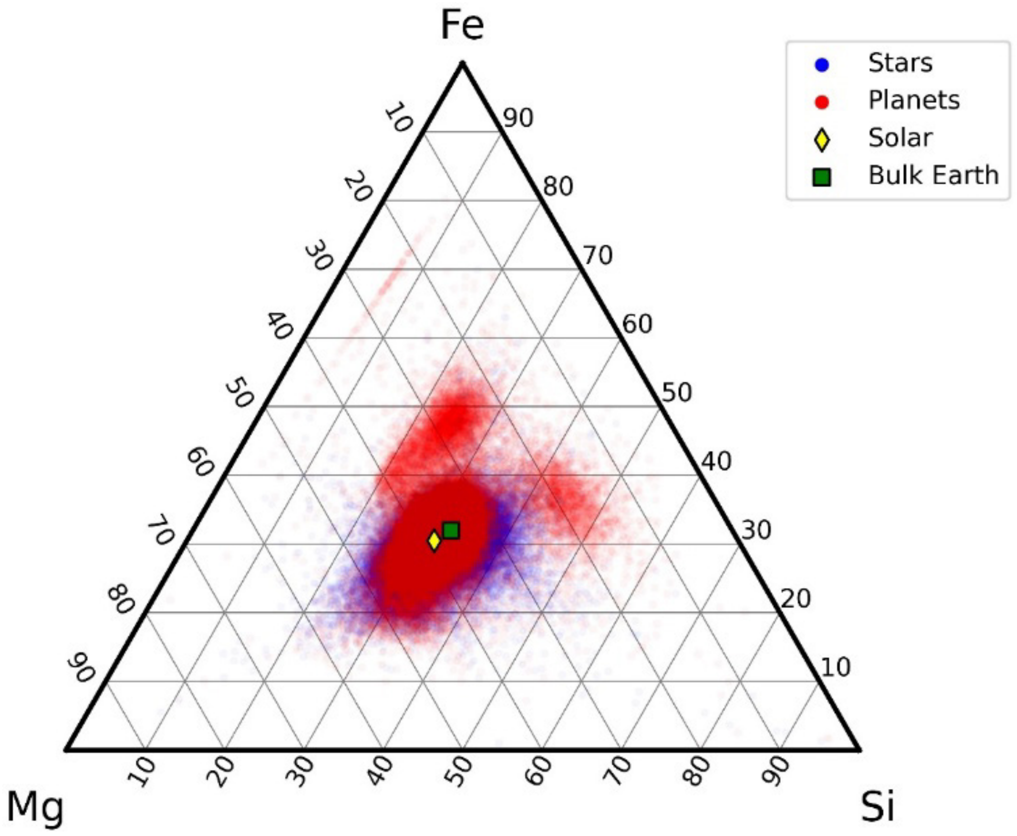

Fig.: 3.1-1: Stellar (blue) and planetary (red) Fe, Mg, and Si abundances normalised to the sum of these three elements. Solar abundances and Earth composition are plotted for comparison. While most planets and stars overlap, some systems show that Mg and/or Si are depleted.

b. *The non-carbonaceous nature of Earth's late-stage accretion (K. Bermingham, H.A. Tornabene and L.V. Godfrey/New Brunswick, R. Walker and R. Piccoli/College Park, B.S. Meyer/Clemson and S.J. Mojzsis)*

Constraining the origin of Earth's building blocks requires knowledge of the chemical and isotopic characteristics of the source region(s) where these materials accreted. The siderophile elements Mo and Ru are well suited to investigating the mass-independent nucleosynthetic (*i.e.*, "genetic") signatures of material that contributed to the latter stages of Earth's formation. Studies contrasting the Mo and Ru isotopic compositions of the bulk silicate Earth (BSE) with genetic signatures of meteorites, however, have reported conflicting estimates of the proportions of the non-carbonaceous type or NC (presumptive inner Solar System origin) and carbonaceous chondrite type or CC (presumptive outer Solar System origin) materials delivered to Earth during late-stage accretion (likely including the Moon-forming event and onwards). The present study reports new mass-independent isotopic data for Mo, which are presumed to reflect the composition of the BSE. A comparison of the new estimate for the BSE composition with new data for a select suite of NC iron meteorites is used to constrain the genetic characteristics of materials accreted to Earth during late-stage accretion. Results indicate that the final 10 to 20 wt. % of Earth's accretion was dominated by NC materials that were likely sourced from the inner Solar System, although the addition of minor proportions of CC materials, as has been suggested to occur during accretion of the final 0.5 to 1 wt. % of Earth's mass, remains possible. If this interpretation is correct, it brings estimates of the genetic signatures of Mo and Ru during the final 10 to 20 wt. % of Earth's accretion into concordance.

c. *Integrated analytical and experimental constraints on the petrogenesis of mesosiderites (M. Zippoli, A. Bouvier, R. Zhao and G.J. Golabek, in collaboration with N.P. Walte/Garching)*

Mesosiderites are complex stony-iron meteorites composed of nearly equal proportions of Fe-Ni metal and silicate fragments derived from crustal lithologies, recording extreme mechanical and thermal processes from the earliest Solar System. Although their petrogenesis remains debated, current hypotheses link their formation to asteroid 4 Vesta, whose extensively differentiated basaltic crust and subsequent large impacts could have excavated deep crustal materials, triggered partial remelting and facilitated mixing with core-derived metal. To investigate this scenario, we integrate analytical geochemistry and experimental petrology to reconstruct the formation and thermal evolution of mesosiderites.

Laser ablation LA-ICP-MS analyses of pyroxene, plagioclase and phosphate phases are used to characterise REE patterns and assess redox relations between metal and silicate phases, providing constraints on thermal conditions and impact-driven equilibration. Complementary high-strain deformation and partial-melting experiments on synthetic metal-silicate mixtures reproduce mesosiderite-like textures under controlled pressure-temperature conditions, allowing us to evaluate mechanical mixing processes and cooling rates.

Petrographic observations of Bondoc, Lamont, NWA 2932 and Vaca Muerta mesosiderite samples reveal a heterogeneous assemblage of pyroxene, plagioclase, phosphate and Fe-Ni metal in which brecciated silicates are embedded within metal networks. Pyroxenes show zoning and repeated re-equilibration, while phosphates preserve trace-element signatures indicative of high-temperature interaction with metal. The metal occurs as large nodules, intergranular veins and fine droplets infiltrating silicate domains. Features such as irregular metal blebs, metal-filled fractures and embayed silicate margins demonstrate injection of molten Fe-Ni metal into fractured silicates during large impact events, followed by variable cooling and incomplete chemical equilibration.

LA-ICP-MS data on the phosphate merrillite highlight systematic REE variations across lithologies (Fig. 3.1-2): NWA 2932 silicate matrix shows the lowest overall REE abundances, those in the Vaca Muerta gabbroic inclusions and the Bondoc pyroxenite nodule define intermediate patterns with pronounced Eu anomalies, whereas phosphates associated with the Bondoc metal nodule, Bondoc silicate matrix and the Lamont matrix are the most enriched and display relatively flat REE slopes. These variations are consistent with mixing between more primitive, deeper-sourced components and enriched, impact-modified crustal reservoirs on a single differentiated body. Deformation experiments (Fig. 3.1-3) show that high-strain rate deformation-driven fracturing, metal migration and subsequent annealing can reproduce the metal networks and textures characteristic of mesosiderites, providing a link between natural samples and impact-related processes.

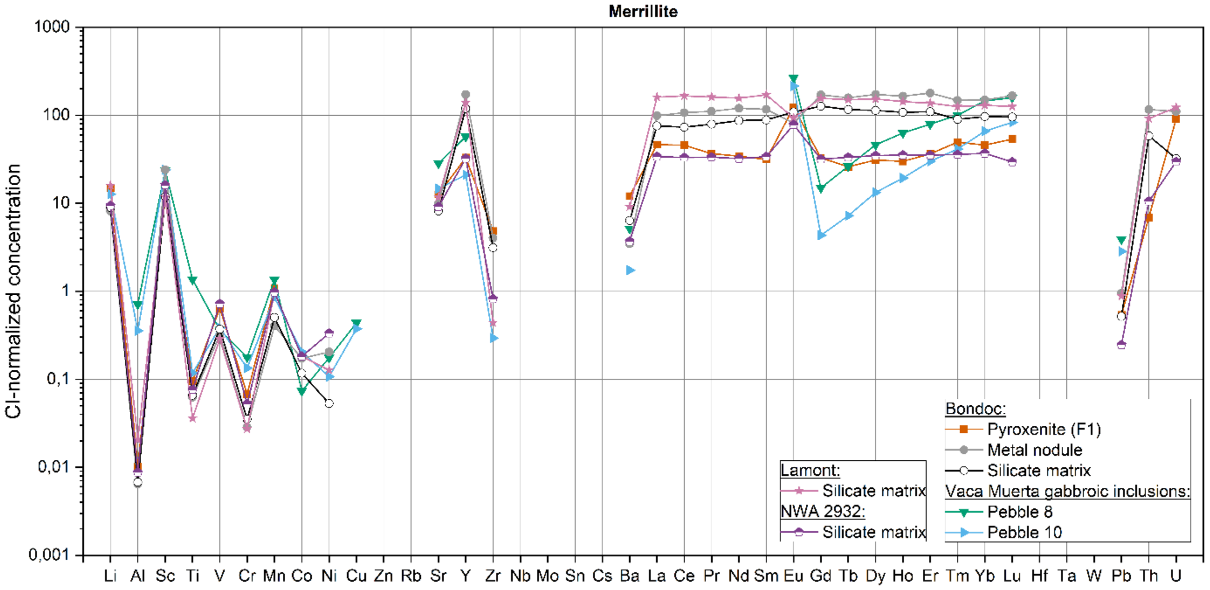

Fig.: 3.1-2: CI-normalised trace-element patterns of phosphate (merrillite) from mesosiderite samples Bondoc, Lamont, NWA 2932 and Vaca Muerta. Element data missing indicate measured concentrations below detection limits or values with analytical uncertainties exceeding the measured signal.

Combined together, petrography, trace-element geochemistry and experimental results reinforce an internal-origin model in which mesosiderites formed on Vesta through large scale impact-induced brecciation, mixing of core-derived metal with silicates and thermal re-equilibration within a single parent body that experienced a sub-catastrophic impact, ejecting significant material that was later reaccreted onto Vesta's crust.

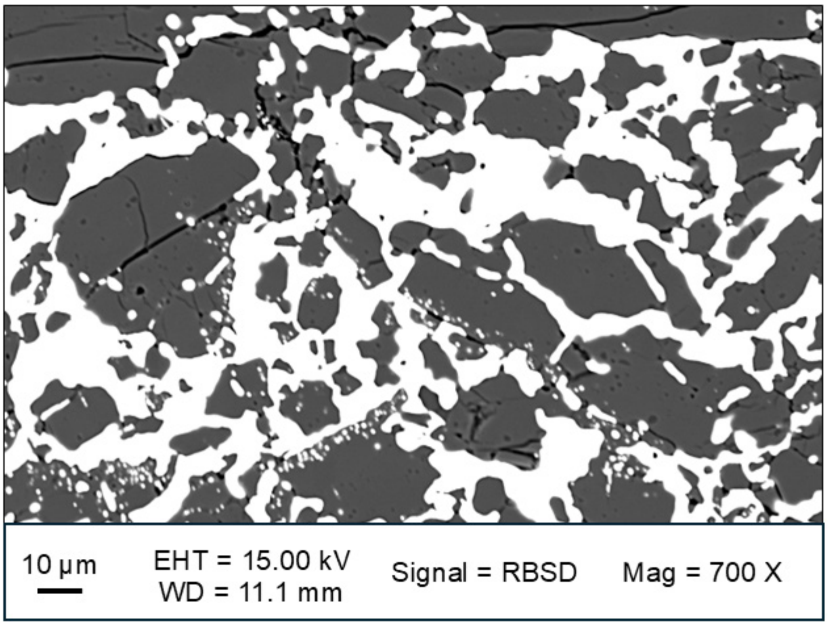

Fig.: 3.1-3: Backscattered-electron image showing fractured silicate grains surrounded by interconnected Fe-Ni metal, reflecting high-strain mixing and partial annealing during impact-related processes.

d. *Sm–Nd and Lu–Hf systematics and stable Hf isotope compositions of Martian shergottite meteorites (X.-J. Hu and A. Bouvier, in collaboration with M. Boyet and E. Grandhomme/ Clermont-Ferrand)*

Martian meteorites preserve essential information regarding the chemical evolution and mantle source heterogeneity of Mars. Radiogenic Sm–Nd and Lu–Hf isotope systems provide constraints on long-term rare-earth and high-field strength element fractionation and on the differentiation history of the Martian mantle. High-accuracy and high-precision analytical protocols using isotopic dilution for Sm–Nd and Lu–Hf systematics, and unspiked stable Hf and REE isotope measurements have been developed at the BGI isotope laboratory using the Thermo Neoma MC-ICPMS/MS. Three Martian shergottite meteorites were analysed in this study. Among these, the Martian shergottite Teghaza 001 (found in 2022) is the first igneous, non-brecciated (but shocked) Martian shergottite meteorite that is distinguished by its maskelynite-rich gabbroic diorite lithology with numerous accessory zircon grains. It has reported U-Pb zircon and Rb-Sr isochron ages at ~ 4.2 Ga. Together with shergottites EETA 79001 lithologies A (fine-grained), B (coarse-grained), and C (impact melt glass), and NWA 4468, these samples broaden the petrologic and isotopic diversity accessible for understanding Martian mantle reservoirs.

A sample chip or fragment of each meteorite between 0.15 and 0.72 g was ground to a fine bulk-rock powder in an agate mortar and pestle. Following dissolution protocol in Parr pressured vessels, each sample was fully dissolved and subsequently divided into three aliquots. Approximately 2 % to 5 % of each sample was used to determine whole-rock major, minor, and trace-element abundances with a Thermo Fisher iCAP TQ-ICP-MS. Whole-rock REE abundances provide a clear distinction between the enriched and intermediate shergottite groups (Fig. 3.1-4). Teghaza 001 and NWA 4468 display REE patterns characteristic of enriched shergottites, but with notably different profiles: Teghaza 001 shows strong LREE enrichment and pronounced REE fractionation ($(La/Yb)_N = 2.2$), whereas NWA 4468 exhibits a much flatter REE pattern (5-9 × CI) (Fig. 3.1-4). In contrast, EETA 79001 A, B, and C exhibit moderately sloping REE profiles consistent with intermediate shergottites (Fig. 3.1-4).

A second aliquot, representing ~ 10 % of each sample, was spiked with appropriate mixed ^{176}Lu–^{180}Hf and ^{149}Sm–^{150}Nd spikes and homogenised before ion exchange column protocols to separate each element from the rock matrices. The resulting purified solutions were analysed for Sm, Nd, Lu+Yb, and Hf isotope compositions using a Thermo Fisher Neoma MC-ICPMS/MS. The remaining ~ 85 % of each sample was treated for unspiked isotopic compositions after purifying Hf from the major and minor elements and the REE, which will be processed separately to measure Ce, ^{142,143}Nd, Sm and Eu isotopic compositions at LMV. The unspiked Hf solutions were analysed for stable ^{178}Hf/^{177}Hf (as a neutron capture monitor) and radiogenic ^{176}Hf/^{177}Hf isotope ratios.

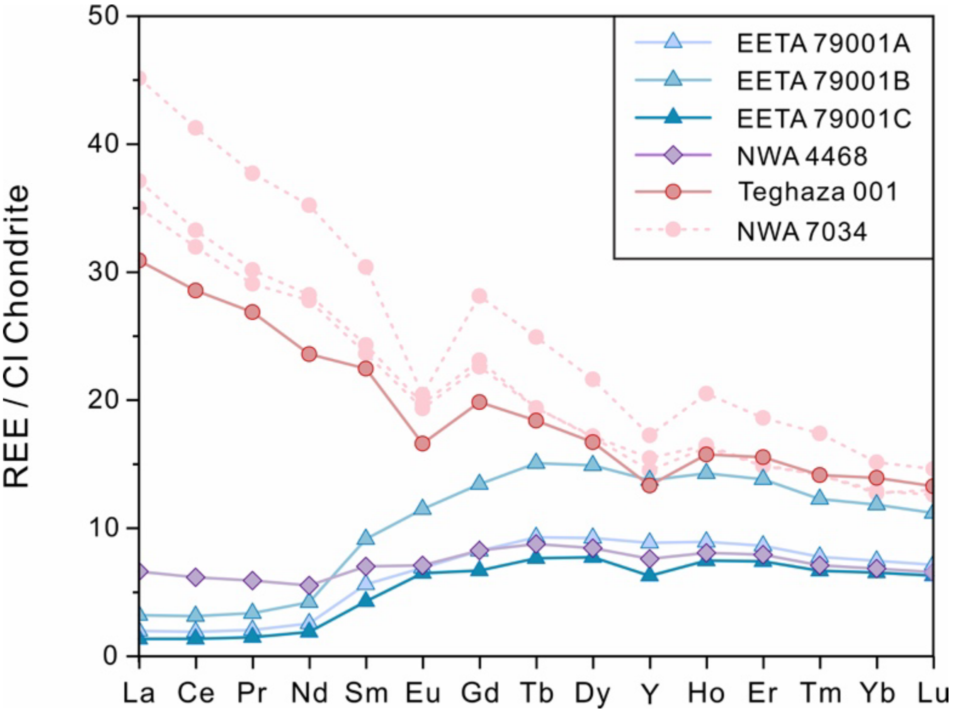

Fig. 3.1-4: CI Chondrite-normalised REE patterns of Martian shergottite samples and lithologies analysed in this study. Previously reported data for three separate bulk fragments of the polymict breccia NWA 7034 are also shown with dashed lines.

EETA 79001 A, B, and C have similar depleted Nd-Hf isotopic signatures corresponding to the intermediate shergottite group, while NWA 4468 is related to other enriched shergottites. Teghaza 001 is distinct from other shergottites with a strongly enriched composition (Fig. 3.1-4) and decoupled Hf-Nd isotopic evolution (initial εNd=-0.3 and εHf=-7.6 at 4.12 Ga). The calculated Sm–Nd and Lu–Hf source compositions clearly show these distinctions (Fig. 3.1-5), with Teghaza 001 notably plotting close to the unique polymict breccia NWA 7034, which is the oldest sample of the Noachian enriched crust with up to ~ 4.49 Ga zircon U-Pb ages. Together, these two meteorites derive from an early-formed crustal source reservoir, distinct from other martian meteorite lithologies.

The stable Hf isotope compositions do not show any variation with μ^{178}Hf of approximately 0 to 9 parts per million deviation from the JMC 475 Hf standard. Therefore, no significant neutron capture effects were produced due to exposure to cosmic rays since the launch and transfer of these meteorites from Mars to Earth.

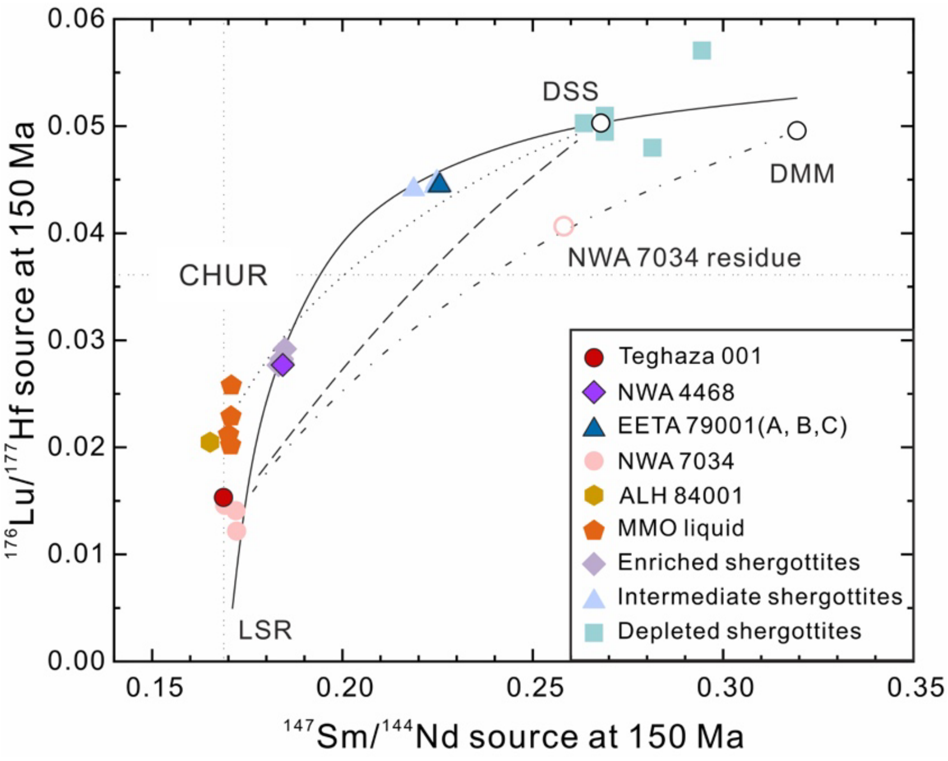

Fig. 3.1-5: Source ^{176}Lu/^{177}Hf versus ^{147}Sm/^{144}Nd calculated at 150 Ma. The LSR line is a least squares regression fit through all the plotted meteorite whole-rock data (with the exception of ALH 84001). DMM is the proposed depleted martian mantle composition, DSS is a depleted shergottite source composition, and MMO liquid is martian magma ocean liquid composition. The NWA 7034 residue composition was calculated based on the extraction of 4 % melt of a primitive mantle composition using a martian mantle mineralogy. The dashed and dotted–dashed lines represent binary mixing models between NWA 7034 and DSS or DMM, respectively. The dotted line is a calculated mix between the liquids after 98 % fractional crystallisation of a 1350 km deep magma ocean and DSS.

e. *Formation and stability of a basal magma layer on Mars (R. Pierru, L. Man, J. Monteux/Clermont-Ferrand, L. Henry/Paris, D. Bondar, S. Gao/Leuven, R. Farla/Hamburg, X. Feng/Hamburg and D.J. Frost)*

Recent interior models suggest that Mars may host, or may have hosted earlier in its evolution, a basal magma layer located directly above the core-mantle boundary (CMB). Such a molten or partially molten reservoir could profoundly influence the planet's thermochemical evolution by buffering heat transfer from the core, modifying deep mantle convection, and affecting the thermal state of the planet. Determining whether this layer can form and persist requires experimental constraints on the melting relations, liquid composition, viscosity and density of mantle materials under pressure-temperature conditions representative of the CMB. To explore these processes, we performed high-pressure multianvil experiments at the Bayerisches Geoinstitut (BGI) at approximately 19 GPa, which corresponds to the present-day pressure at the Martian CMB. The aim of these experiments was to determine melting temperatures, examine phase relations, and characterise the chemical properties of deep mantle melts in equilibrium with a core containing iron and sulphur. The samples were enclosed either in graphite capsules with or without FeS in order to assess the influence of a core-buffered redox environment on melting behaviour and metal-silicate exchange.

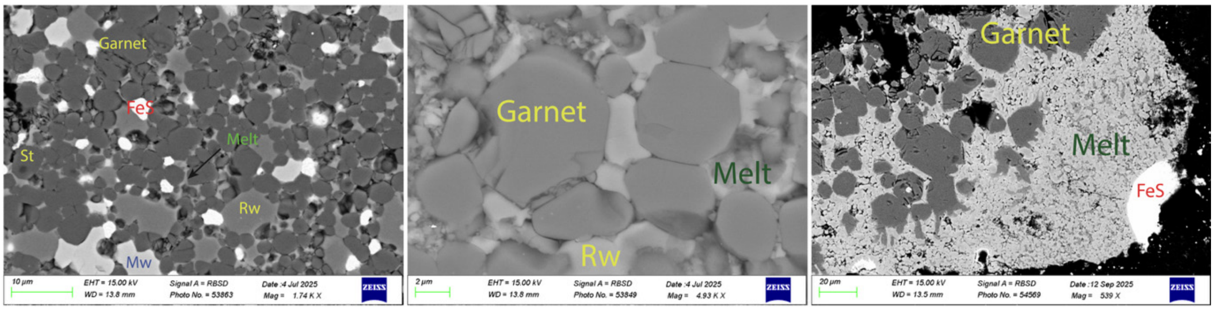

Fig. 3.1-6: Textures of high-pressure experiments performed at 19 GPa under FeS-buffered conditions. (Left): Solidus regime dominated by a crystalline assemblage of stishovite, magnesiowüstite, ringwoodite, and garnet. (Centre): Close-up view of a partially molten region where small fractions of silicate liquid are observed between garnet and ringwoodite grains at the onset of melting. (Right): Higher melt fraction showing residual garnet surrounded by silicate liquid, FeS melt, and minor magnesiowüstite. These textures illustrate the progressive transition from solidus to increasing degrees of partial melting at Martian core-mantle boundary conditions.

Preliminary analyses indicate that the silicate liquids produced at temperatures exceeding ~ 2000 °C exhibit a high FeO content, particularly near the solidus. The phase assemblage is complex and is characterised by the coexistence of stishovite, magnesiowüstite, garnet, and ringwoodite (Fig. 3.1-6). These petrographic and compositional constraints form the basis for describing the physical behaviour of deep Martian silicate melts. To complement these results, we directly measured the viscosity of some liquids produced at 19 GPa, using *in situ* experiments carried out at the DESY P61B beamline with X-ray radiography and sinking-sphere techniques. This setup enabled real-time tracking of tracer motion under the same pressure-temperature conditions as those explored at BGI. The resulting viscosities provide the first direct rheological constraints on Fe-rich Martian mantle melts at CMB pressures, and they are significantly lower than values typically estimated for bulk peridotitic mantle liquids. On the other hand, density estimates, based on phase proportions and endmember equations of state, further suggest that the melt remains sufficiently dense to percolate downward even at relatively low degrees of partial melting, a behaviour enhanced by its low viscosity. These results support the possibility that Fe-rich silicate liquids may have migrated and accumulated to form a basal magma layer above the Martian core.

The experimental results will be implemented in a two-dimensional geodynamical model designed to simulate the formation, evolution and possible longevity of a basal magma layer at the Martian CMB. The model incorporates the pressure and temperature dependence of melt viscosity and density, a parameterization of the solidus and liquidus for deep mantle compositions, and the heat flux across the core-mantle interface. The objective of this approach is to establish whether a basal magma layer can self-organise and persist as a long-lived reservoir of partially molten silicates, and to quantify its influence on core heat extraction, mantle differentiation, Fe–S chemical exchange, and possible seismic or tidal signatures relevant to InSight and future geophysical missions to Mars.

Some test simulations (Fig. 3.1-7) illustrate the effect of the density contrast between melt and crystals ($\Delta\rho$). The left panel shows the case $\Delta\rho = 1$ kg·m^{-3} and the right panel the case $\Delta\rho = 10$ kg·m^{-3}, both at t = 18,000 s. Colors represent the crystal volume fraction. For low $\Delta\rho$ (left)

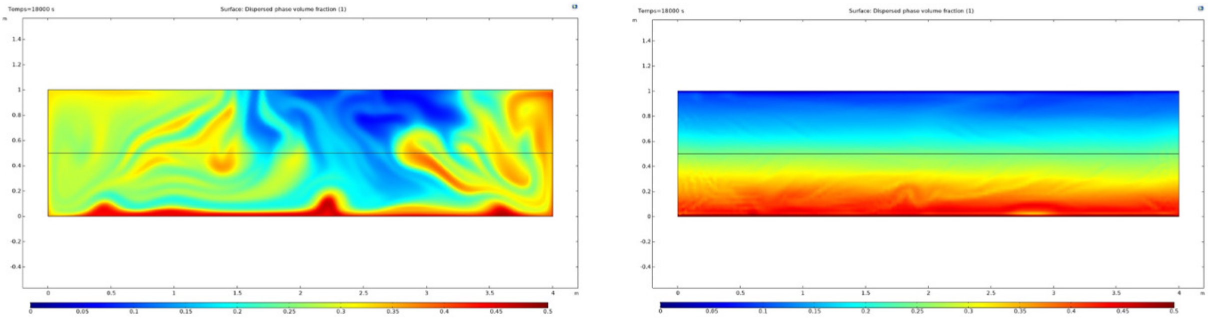

Fig. 3.1-7: Convection and crystal transport in a 4 m × 1 m magma reservoir located at Martian CMB conditions ($T = 2600$ K at the base, adiabatic heat flux at the top, $g = 3.4$ m s^{-2}). After establishing a thermal convection field, crystals are introduced with higher initial concentration in the upper half of the reservoir. Snapshots at $t = 18{,}000$ s show the crystal volume fraction for two density contrasts $\Delta\rho$: 1 kg m^{-3} (left) and 10 kg m^{-3} (right). Low $\Delta\rho$ leads to crystals remaining largely suspended and well mixed by convection, whereas high $\Delta\rho$ causes rapid sedimentation and the formation of a crystal-rich basal layer.

crystals remain largely suspended and are efficiently mixed by convection. For higher $\Delta\rho$ (right), crystals settle rapidly toward the base of the reservoir, producing a strongly stratified configuration with limited upward transport. This comparison highlights the strong control of crystal-melt density contrast on the efficiency of sedimentation and the potential formation of cumulate layers at the Martian CMB.

f. *The oxygen content of the Martian core (D.J. Frost, L. Man and R. Pierru)*

Geodetic constraints on the bulk density and internal density distribution of Mars, together with recent seismic measurements from the InSight lander, indicate that Mars has a relatively low-density, liquid core, consistent with it containing, in addition to iron and nickel, a substantial concentration of light elements. Identifying the nature of these light elements is crucial for understanding how terrestrial planets form, the materials from which they accrete and the conditions under which their cores segregate from silicate mantles. Sulphur is often proposed as the likely dominant light element in the Martian core. However, recent core density estimates would require sulphur concentrations so high that they imply very little volatile-element depletion in Mars, which is inconsistent with the clear depletions of other non-core-forming volatile elements. Furthermore, estimates for the P-wave velocity (V_p) of the core, which appears similar to that of pure liquid iron, are also inconsistent with very high sulphur concentrations, implying that at least one other light element must be present in significant proportions.

Recently, evidence of seismic waves that appear to have passed through the solid inner core of Mars was found in the InSight data. The inner core is proposed to have a radius of approximately 600 km and a density consistent with FeO. If this is correct, it implies that the outer core must contain significant oxygen in addition to sulphur, iron, and nickel. Furthermore, it allows the O content of the outer core, at least at the inner core boundary, to be constrained for a given S content.

We have developed a thermodynamic model that allows the O content of an Fe–S liquid in equilibrium with FeO to be calculated. This model is constrained using many different types of experimental data, including melting phase relations, liquid immiscibility observations and partitioning data between solid (Mg,Fe)O and Fe–S–O liquids, in addition to physical measurements of liquid densities and P-wave velocities. These data are fitted to a single, internally consistent, thermodynamic model that can be used to calculate both liquid compositions and elastic properties in the Fe–S–O system.

In Figure 3.1-8, this model is used to calculate the Fe–FeO melting phase diagram at a pressure consistent with the Martian inner core boundary (35 GPa), with further curves calculated for the FeO liquidus as a function of liquid S content. In the absence of S, the Fe–FeO eutectic contains approximately 4 wt. % O, but the temperature of the eutectic is much higher than the range proposed for the Martian core (indicated by the shaded region). Upon the addition of S to the system, however, the eutectic temperature drops rapidly and becomes consistent with core temperatures. If S contents were between 11 and 15 wt. %, as proposed in many cosmochemical models for the Martian core, then the O solubility would reach levels between 5-7 wt. % at the inner core boundary. At lower pressures within the core, the relative behaviour of O depends on temperature, as shown for the curves calculated for 15 wt. % S at 35 and 20 GPa. However, for an adiabatic temperature drop across the outer core of approximately 250 K, the O solubility would be expected to decrease by approximately 1.5 wt. %, which would cause FeO to crystallise within the liquid core. This implies a so-called "snowing core" scenario, where FeO dissolved in upwelling liquid reaches saturation as it rises and crystallises FeO, which then sinks.

If Mars indeed has an inner FeO core, then a plausible scenario is that its outer core contains 11-15 wt. % S but then must also contain 5-7 wt. % O. Our thermodynamic model indicates that this composition would satisfy the density of the outer core, but the model lacks sufficient constraints to verify the effect of this composition on V_P. The model can be used to calculate the conditions of core-mantle equilibration required to produce this core O content, for which we calculate an average equilibration temperature of approximately 3000 K.

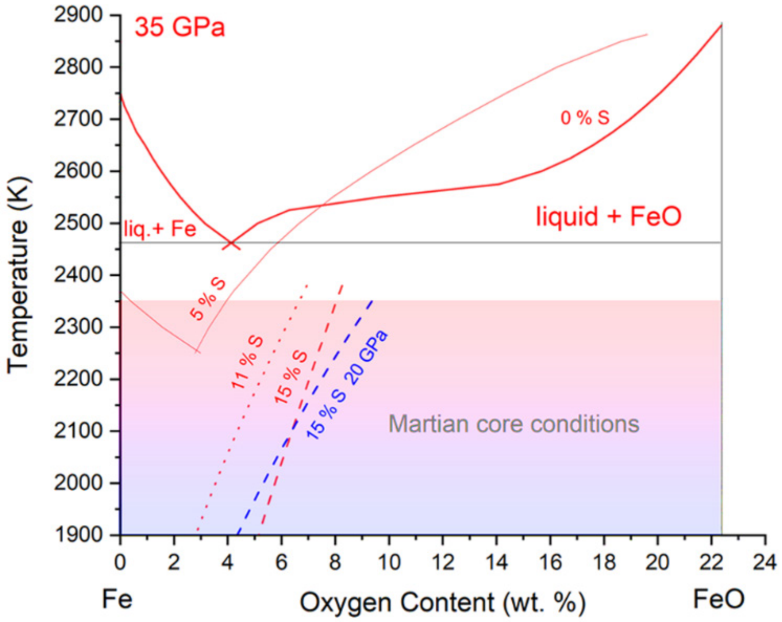

Fig. 3.1-8: The Fe–FeO phase diagram at conditions proposed for a Martian inner core boundary (35 GPa). Further liquidus curves (in red) are calculated for the sulphur contents indicated in wt. %. Only sections of the liquidus curves in equilibrium with solid FeO are shown for S contents of 11 and 15 wt. %. An FeO liquidus for a composition containing 15 wt. % S is also calculated for conditions near the top of the core (20 GPa; blue curve). Proposed Martian core temperatures at 35 GPa are indicated by the shaded region.

g. *Mantle convection and nightside volcanism on Lava World K2-141 b (T.G. Meier, C.M. Guimond, R.T. Pierrehumbert, J. Birkby, R.D. Chatterjee, C.E. Fisher, M. Hammond, T.D. Komacek, A. McGinty, E. Meier Valdés, H. Nicholls and L.T. Parker/Oxford, T. Lichtenberg and R.J. Spaargaren/Groningen, P.J. Tackley/Zurich and G.J. Golabek)*

Ultra-short period lava worlds offer a unique window into the coupled evolution of planetary interiors and atmospheres under extreme irradiation. We investigate the mantle dynamics, nightside volcanism, and volatile outgassing on lava world K2-141 b (1.54 R_{Earth}, 5.31 M_{Earth}) using two-dimensional convection models with volatile tracking. We explore a range of interior configurations, including models with and without plastic yielding, basal versus mixed heating, core cooling, and melt intrusion. In models with a strong lithosphere, we find that mantle upwellings form at the substellar and antistellar points, while downwellings form near the day-night terminators at the boundary between the magma ocean and the cold, solid nightside. These downwellings represent a form of asymmetric, single-lid tectonics. The resulting magma ocean thickness corresponds to about 2-3 % of the planet's radius. Continuous nightside volcanism produces a basaltic crust and gradually depletes the mantle of volatiles. We show that even relatively large volcanic eruptions on the nightside produce thermal emission signals that remain below the current detectability threshold in thermal phase curves. However, for most models, outgassing rates are increased near the day-night terminators and future studies should assess whether such localised outgassing could lead to atmospheric signatures in transmission spectroscopy.

h. *Intrusion of compressible magma in thermally weakened visco-elastic crust (A. Spang, A. Piccolo/Leeds, M. Gerbault/Toulouse, B. Kaus/Mainz and M. Thielmann/Bonn)*

Surface deformation is one of the most widely available observables for volcanic activity, and uplift is commonly interpreted as the result of magmatic intrusion into the shallow crust. The most frequently used approach to model this process is a fully elastic crust hosting an expanding cavity. While this approach yields quick results and facilitates inverting for depth, overpressure or intruded volume, it is associated with several significant simplifications. Most notably, the host rock surrounding an existing magma body is expected to be hot enough to deform visco-elastically. Furthermore, the properties and dynamics of the ascending and intruding magma are entirely ignored.

In this study, we use three-dimensional (3D) thermomechanical numerical models to investigate surface deformation due to intrusion into a pre-existing magma body. We accomplish this by connecting the magma body to the bottom boundary of the model and imposing an inflow of material there. This pressurises the feeding system, the magma body, and the surrounding crust which results in uplift of the free surface (Fig. 3.1-9a). We use a visco-elastic host rock rheology where the viscous component is an experimentally constrained dislocation creep flow law for quartzite. The magma is approximated as a compressible visco-elastic fluid. We also test different crustal temperature structures to account for different levels of thermal maturity of the magmatic system.

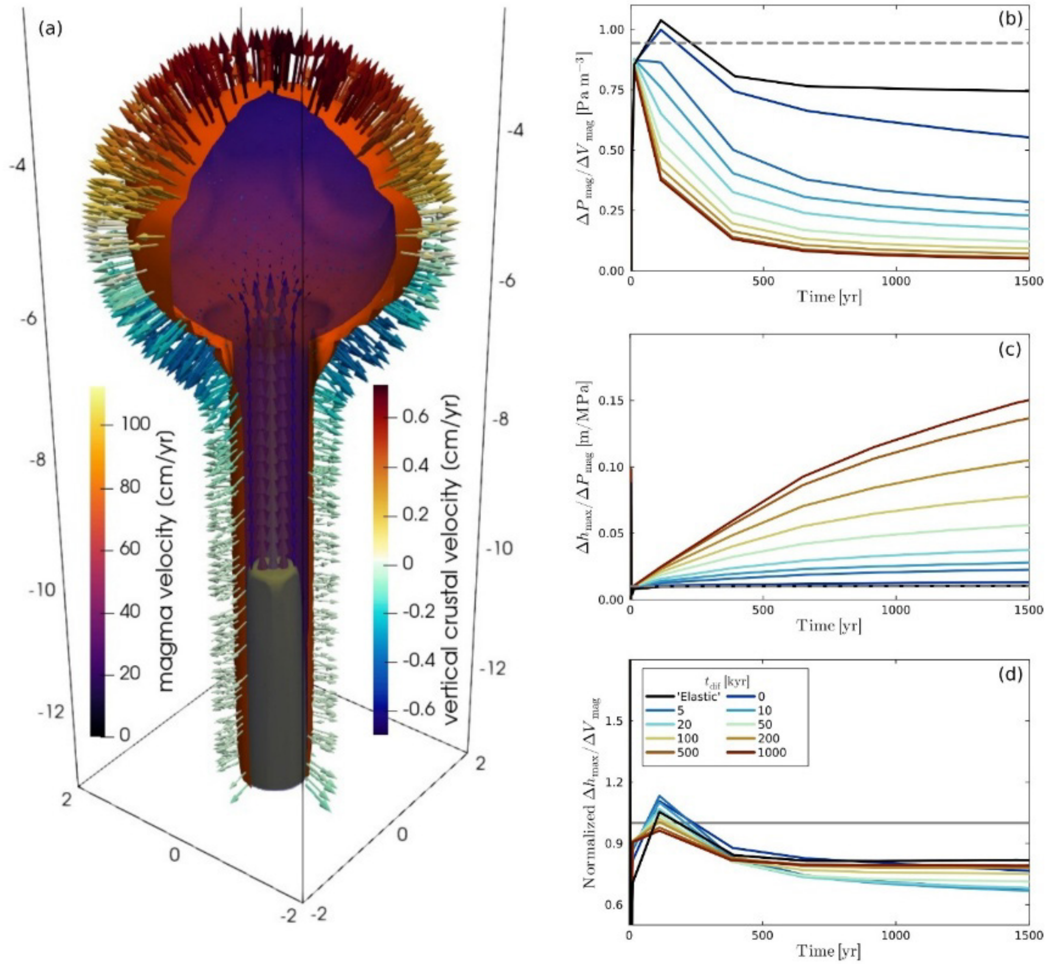

Fig. 3.1-9: (a) 10 MPa overpressure contours after 20 years (yellow), 200 years (blue), and 1000 years (orange). Arrows along the orange contour show velocities that are induced in the crust by the influx of magma. (b) – (d) Time series for different states of thermal maturity. Colors denote how long the host rock was heated up by the magmatic system. (b) Ratio between overpressure and intrusion volume. (c) Ratio between surface deformation and overpressure. (d) Ratio between surface deformation and intruded volume, normalised by the analytical elastic solution (grey line).

With increasing thermal maturity of the magmatic system, the host rock surrounding the magma body undergoes thermal weakening. This has two effects: (i) as the walls of the magma body can deform quicker, intruding magma causes about one order of magnitude less overpressure than assumed by the traditional elastic model (Fig. 3.1-9b). (ii) as the weakened host rock is easier to deform, the same amount of overpressure leads to about one order of magnitude more uplift than an elastic crust would (Fig. 3.1-9c). These two effects almost cancel out, resulting in overall less uplift per intruded volume for thermally weakened crust (Fig. 3.1-9d). If a realistic magma compressibility ($2 \cdot 10^{-10}$ Pa^{-1}) is considered, effect (i) outweighs effect (ii). Ignoring the effects of thermal maturity and compressibility results in an overestimation of magma overpressure and an underestimation of intrusion volume when these quantities are derived from surface deformation.

i. *Quantifying the contribution of magma to the current unrest at Campi Flegrei caldera through thermomechanical modelling (C. Nardoni/Bologna, A. Spang and L. De Siena/Bologna)*

The Campi Flegrei caldera has experienced a critical increase in uplift rates over the past 20 years. Recent geodetic and seismic observations have shown large ground deformation (~ 18 cm in 2024) and an increase in both seismicity rates and magnitudes further prompting the ongoing debate about the underlying causes. While shallow magma transport is often invoked to explain the deformation, other studies point to the accumulation of fluids in the shallow crust as primary drivers of overpressure and surface displacement. Disentangling the contribution of these processes remains a key challenge. In this study, we aim to quantify the uplift resulting from potential shallow magma migration and determine whether the deformation can be attributed mainly to this migration.

To address this, we integrate constraints from seismic imaging and rock physics into a thermomechanical model which involves visco-elasto-plastic rheologies. Thermomechanical modelling has been guided by recent tomographic studies and allows the estimation of magma-driven deformation in the current unrest. Employing this available structural information on the caldera, the model features a deep magma influx originating at 8 km depth, feeding a shallow reservoir centred at around 5 km. Including the effects of magma expansion, we test the contribution of magma upward migration to the main uplift anomaly located in the centre of the caldera, considering an influx of $4.5 \cdot 10^{-4}$ km^3/yr. We evaluate how a shallow, mechanically weak tuff layer and the presence of a hydrothermal system modulate the effects of deeper magmatic inputs, as shown in Figure 3.1-10a. Visco-elastic parameter variation has been further investigated as well as an increased inflow velocity. The thermomechanical model reproduces only a small part (~ 8 %) of the observed surface deformation rate (Fig. 3.1-10b)

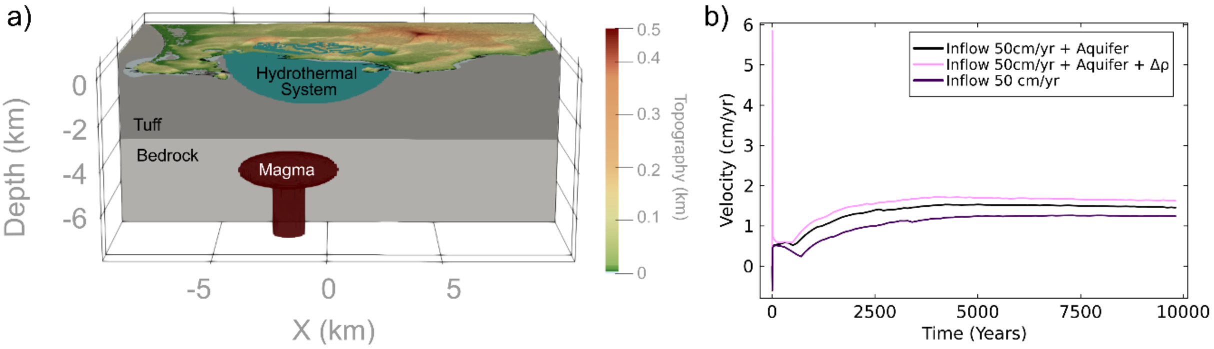

Fig. 3.1-10: (a) Crustal model of the Campi Flegrei caldera, including the bedrock, a weaker tuff layer, an aquifer and the magma sill fed by an influx from below. (b) Surface uplift rate above the sill centre for three models: (purple line) without aquifer, (black line) with aquifer, and (magenta line) including density contrasts between crustal layers, the sill, and the aquifer.

suggesting additional pressure sources, such as gas formation or hydrothermal pressurization - which are not explicitly modelled here - may play a significant role. These results are crucial for improving our comprehension of the deformation sources at Campi Flegrei and their interactions with shallow structures for seismic modelling purposes.

3.2 Geochemistry

Most chemical elements heavier than hydrogen and helium are produced by nucleosynthesis in stars. When stars go supernova, these elements are returned to the interstellar medium, where the enriched material can later collapse to form new generations of stars. Galactic chemical evolution models describe how this repeated cycle of star formation and mass loss gradually enriches the galaxy in chemical elements over time. As described in the first project in this section, some elements, such as phosphorus and potassium, are observed in stars at higher abundances than predicted by standard stellar evolution models. One solution explored in this project is that mixing events between different nuclear fusion layers, called shells, in massive stars enhance the production of these elements. During such events, material from different shells mixes rapidly, triggering nuclear reactions not captured by standard stellar models. The results show that small differences in internal mixing can lead to large variations in predicted element abundances. In particular, the production of the long-lived radioactive isotope ^{40}K, an important source of internal heat for rocky planets, can vary by orders of magnitude, implying that early planetary thermal evolution may differ substantially depending on stellar birthplace.

In the following project, the preservation of material from the early Solar System in comets is studied. Measurements by the ESA Rosetta spacecraft of noble gases from the comet 67P/Churyumov–Gerasimenko reveal isotopic compositions that differ from those found in the Sun. This indicates that the comet contains only a subset of the noble-gas material present in the molecular cloud that collapsed to form the Sun. It is proposed that this reflects the fact that the Solar System inherited material from multiple sources, with comets preferentially retaining the earliest-formed components.

The next study examines how sulphur affects the way that iron isotopes are fractionated as planetary cores separate from silicate mantles. The study is mainly focused on Mars, which appears to have a sulphur-rich core. High-pressure experiments show that even with significant sulphur, Mars' core formation would not strongly fractionate iron isotope ratios. This helps to explain why Martian meteorites preserve iron isotope signatures similar to those of primitive Solar System material.

The following two studies investigate how proposed later stages of Earth's accretion and core formation may have affected the composition of the mantle. The first study uses laser-heated diamond anvil cell experiments to examine how chalcophile elements, *i.e.*, those that preferentially partition into sulphide liquid, would have been distributed between the mantle and core. During the late stages of Earth's accretion, core formation has been proposed to involve segregation of a sulphide liquid (the so-called Hadean matte), rather than partitioning into iron-rich metal, and this study explores the mantle signature such a process would produce. Most elements are found to behave similarly with or without sulphur, making it difficult to distinguish between formation scenarios. However, the results suggest that silver may have been more efficiently stripped into the core by a sulphide liquid.

Highly siderophile elements (HSEs) are expected to be strongly partitioned into metallic cores during planet formation, yet the silicate mantles of Earth, Mars, and the Moon retain unexpectedly high and near-chondritic relative HSE abundances. This is normally explained by the addition of a "late veneer" of chondritic material to planetary mantles to restore HSEs after their removal at the end of core formation by the aforementioned Hadean matte. However, this interpretation relies on partitioning data obtained at unrealistically high HSE concentrations, due to the difficulty in analysing the otherwise very small concentrations remaining in the silicate melts. In the study by *Li and Zhang*, metal-silicate partitioning experiments are performed employing more realistic metallic liquid HSE concentrations. This is possible due to advances in analytical techniques that allow extremely small silicate HSE concentrations to be measured. The results show that platinum and palladium partition far less strongly into metal and sulphide melts at the low concentrations relevant to a planetary magma ocean. The results, therefore, indicate that a late veneer may not be required to account for mantle platinum and palladium budgets.

Metallic Fe–Ni alloys in lunar rocks affected by large impacts preserve traces of the meteorites that originally struck the Moon, providing a direct record of late accretion processes. In the following study analysis of HSE abundances in such rocks, using laser ablation inductively coupled plasma mass spectrometry (ICP-MS), is employed to trace the origins of these impactors. Results show that Apollo samples contain HSE signatures consistent with non-carbonaceous chondrite material from the inner Solar System, which therefore appears to have contributed to the Moon and, by extension, also the Earth's late accretion.

The next two studies address the process of crystallization in a deep terrestrial magma ocean. To find out whether the crystallization of Earth's mantle could have caused compositional layering, *Chanyshev et al.* performed partial melting experiments at 14-33 GPa on dry peridotite, using "nearly-zero temperature gradient" assemblies in multianvil presses. Textural evidence reveals upward segregation of the partial melts, implying that bridgmanite is denser than the silicate melt at these conditions. The results suggest that during the cooling and crystallization of the lower mantle, a bridgmanite-dominated layer may have developed. The development of such compositional layering during lower-mantle crystallisation may have strongly influenced Earth's thermal evolution and internal dynamics, depending on the distribution of heat-producing elements such as U, Th, and K during magma-ocean crystallization. To examine this issue, *Zhou et al.* determined trace-element partition coefficients between the lower-mantle $CaSiO_3$ mineral davemaoite and silicate melt using multianvil experiments at pressures between 20 and 33 GPa. Preliminary results indicate that davemaoite–melt partition coefficients for rare-earth elements decrease substantially with increasing pressure. If a similar pressure dependence applies to U, Th, and K, davemaoite-rich domains in the lower mantle would have generated considerably less radiogenic heat than previously assumed.

Archean cratons, Earth's oldest continental regions, are underlain by mantle rocks that are unusually enriched in silica, a feature that cannot be explained by simple melting of normal mantle material. The next study in this section by *Melai et al.* tests the idea that these rocks formed through interaction between the early lithosphere and ascending komatiite melts. High-pressure experiments show that komatiite melts reacting with mantle rocks produce olivine-rich zones and orthopyroxene-rich reaction fronts that closely mimic the textures and compositions of natural Archean cratonic peridotites. The results support a model in which high komatiite melt fluxes modified the composition of early craton roots and may have contributed to their long-term stability.

Some rare diamonds contain inclusions of (Mg,Fe)O ferropericlase, a mineral commonly associated with the lower mantle and therefore often taken as evidence for a deep origin of these diamonds. A long-standing puzzle, however, is why these ferropericlase inclusions can be extremely iron-rich, far more so than expected for equilibrium with typical mantle rocks. In the following study, *Hao et al.* use high-pressure experiments to investigate how iron partitions between ferropericlase and carbonate minerals or melts. The results show that very iron-rich ferropericlase can form during partial reduction of carbonates that initially contain relatively little iron. Such partial reduction, potentially driven by the influx of more reduced fluids, would allow localised formation of diamonds and iron-rich ferropericlase without requiring a lower-mantle origin.

The next two studies in this section use analyses of some of the oldest rocks on Earth to investigate key aspects of early tectonic processes. In the first of these, mantle-derived magmatic rocks of early Archean age (Eoarchean > 3.6 billion years old) from northern Canada are examined that resemble those produced by arc volcanism. Sulphur isotope analyses show that these rocks contain a chemical signature that could only have formed in Earth's early atmosphere. This signature was likely transported into the mantle with surface sediments derived from the earliest continental crust, in a process similar to modern subduction. The results provide direct evidence that volatile elements were being recycled between Earth's surface and interior more than 3.8 billion years ago, pushing the onset of subduction-driven volatile cycling back by about one billion years compared to some previous estimates. In the second study, Eoarchean rocks preserved in southwest Greenland and northern Québec are examined. These rocks were originally sedimentary and therefore provide rare records of early surface environments, but they were later overprinted by metamorphism, the extent and timing of which have been poorly constrained. By combining mineral thermometry, pressure estimates, and rutile U–Pb dating, the burial, heating, and modification history of these rocks is reconstructed. The results show that metasediments in both regions experienced similar high-temperature metamorphism during the Neoarchean (~ 2.7 billion years ago), under upper amphibolite-facies conditions, indicating that geographically distant parts of the early continental crust were affected by comparable Neoarchean tectonic processes. In Greenland, the rocks also record a later episode of lower-grade metamorphism during Proterozoic continental collision, whereas this younger overprint is absent in the Canadian samples.

Scapolite is considered a rare magmatic mineral. However, during fractionation experiments of oxidised, sulphur-bearing arc magmas, *Qiao et al.* noticed the formation of considerable amounts of scapolite at pressures ≥ 0.7 GPa. The stability field of scapolite was thus further constrained by equilibrium crystallization experiments, and it was found that it extends from 850 °C at 0.7 GPa to 750-950 °C at 1.3 GPa. The results suggest that scapolite may be a common mineral during magma fractionation at high pressure, but because it readily breaks down during depressurization and cooling it is rarely preserved in natural arc magmas.

The next two contributions deal with the formation of porphyry-type ore deposits, which provide our main source of Cu and Mo, as well as being a major source of Au. To test whether some of the metals contained in porphyry-type ore deposits could be derived from subducted sediments, *Hlede et al.* studied the partitioning of Cu, Mo, Zn and W between aqueous fluids and an average subducted sediment composition (GLOSS) at conditions of 600-700 °C and 2.5-4.5 GPa in piston cylinder experiments using the diamond trap technique. The results show that the efficiency of Cu and Zn extraction from sediment increases with increasing fluid salinity, whereas for Mo and W such an effect is observed only at 4.5 GPa. Overall, the partition coefficients are high enough to result in an efficient mobilization of all metals, which means that anoxic, Mo-rich sediments could have been a potential source for producing Mo-rich porphyries.

Porphyry copper deposits usually form after periods of tectonic compression, when residual melts were able to ascend to shallow crustal levels after extensive magma fractionation at depth. Whereas most of the Laramide-age porphyry copper deposits in Arizona conform to this model, the tectonic setting of the few deposits occurring further north in Nevada, Utah and Idaho is not well constrained. To fill this gap, *Bain et al.* determined the ages of garnets in metamorphic core complexes of that region by Lu-Hf age dating. They found ages that are similar to that of the Ely-Robinson porphyry copper deposit, which suggest that this particular deposit formed during the period of crustal thickening rather than during subsequent stress relaxation.

In the final study in this section, integrated mineralogical, chemical, and isotope analyses of some of Earth's oldest rocks from southern West Greenland are used to show that they formed as sedimentary chemical precipitates, rather than from volcanic rocks or clastic sediments. Despite intense deformation, the rocks preserve distinctive silicon, oxygen, sulphur, and rare earth element signatures, including seawater-like trace-element patterns and mass-independent sulphur isotopes, that are consistent with deposition from surface-derived fluids early in Earth's history. Although these rocks were previously proposed to host Earth's oldest biological structures, the study shows that the observed features formed later through deformation and recrystallization and do not provide evidence for early life.

a. *3D macro physics and light odd-Z element production in O-C shell mergers: Implications for 40K production and radiogenic heating inventories of rocky exoplanets (J. Issa and F. Herwig/Victoria, S.J. Mojzsis and M. Pignatari)*

The abundances of light odd-atomic number (Z) elements phosphorus, chlorine, potassium, and scandium are systematically underestimated by galactic chemical evolution models when compared with spectroscopic abundance measurements of stars in the Milky Way. A plausible explanation for this discrepancy is that some massive stars undergo oxygen–carbon (O–C) shell mergers late in their evolution, which can substantially enhance the production of these elements through dynamic, convective-reactive nucleosynthesis. To investigate this process, this study examines how variations in convective macrophysics, determined through three-dimensional hydrodynamic simulations, influence nucleosynthesis in the oxygen-burning shell by post-processing a MZAMS = 15 M⨀, Z = 0.02 stellar model from the NuGrid dataset.

Four key aspects of convective behaviour are explored: a downturn in mixing efficiency near convective boundaries, boosted convective velocities, reduced ingestion rates of carbon-rich material, and partial convective quenching. Across 24 distinct mixing cases that span these assumptions, the resulting pre-explosive abundance ratios relative to iron, expressed on a base-10 logarithmic scale (dex), vary over a wide range. Specifically, the predicted changes in [P/Fe], [Cl/Fe], [K/Fe], and [Sc/Fe] span [−0.33, 0.23] dex, [−0.84, 0.64] dex, [−0.78, 1.48] dex, and [−0.36, 1.29] dex, respectively, where each bracketed pair denotes the minimum and maximum values obtained across the full set of models.

The largest abundance enhancements are found in cases that combine a convective downturn with the fastest ingestion rates where production is found to be non-monotonic with boosted velocities. Furthermore, the dominant nuclear reaction pathways responsible for producing these elements differ between mixing cases, emphasizing that nucleosynthesis during shell mergers is highly sensitive to the details of the convective flow.

The production of the long-lived radioactive isotope ^{40}K ($t_{1/2}$ = 1.248 Gyr), which is a key internal heat source for rocky planets forming within the last 2-3 Gyr, is additionally parameterised. The predicted ^{40}K yields are found to vary by more than three orders of magnitude across the explored mixing cases (Fig. 3.2-1). Such a wide range of initial ^{40}K abundances implies that the early thermal and geodynamic evolution of silicate mantles in rocky exoplanets may differ substantially from that of Earth. Overall, these results demonstrate that a predictive understanding of the origin and variability of the light odd-Z elements, as well as the stellar ^{40}K/K ratio, requires explicit consideration of the three-dimensional macro physics governing convection during shell-merger events.

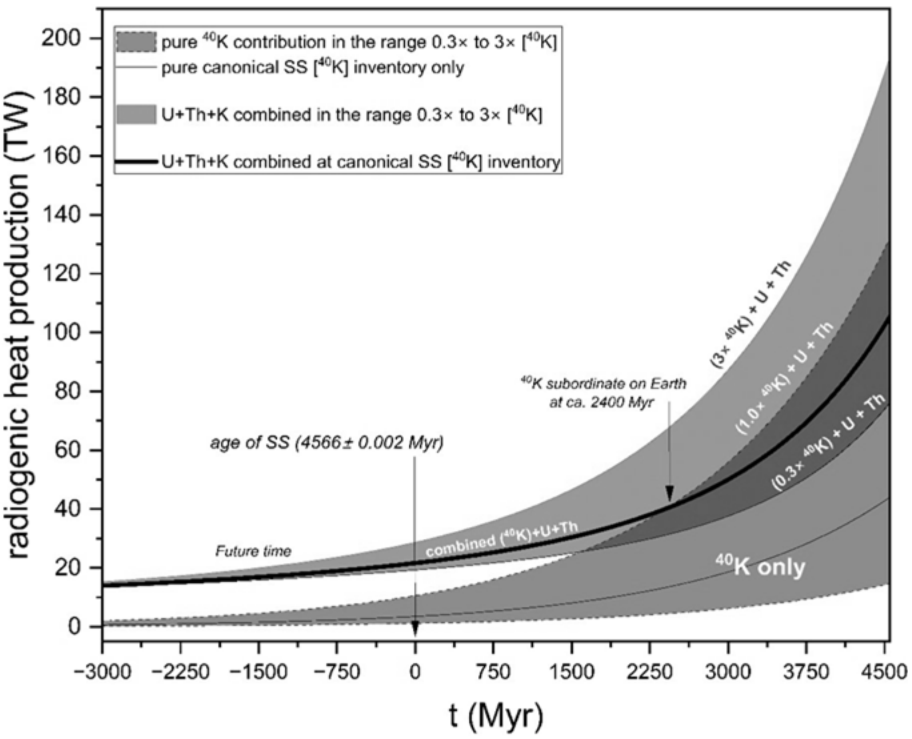

Fig. 3.2-1: The evolution over time of radioactive heat production is shown for an Earth-like planet, where 40K abundances are increased and decreased by a factor of 3 compared to the typical Earth values. The combined total heat productions by ^{40}K, ^{232}Th, ^{235}U, and ^{238}U are also shown. Time on the x-axis is in Gyr before present and so moves from right to left.

b. *The astrophysical birth environment of the Solar System inferred from cometary noble gases (W. Cassata/Berkeley, M. Lugaro/Budapest, B. Wehnmeyer/Wroclaw, R. Trappitsch/Lausanne, S.J. Mojzsis and M. Pignatari)*

The stellar sources that contributed to the chemical and isotopic composition of the Solar System, their mixing in the galactic environment, and the evolution and longevity of the molecular cloud from which our Solar System formed can be probed using isotopic measurements of presolar grains, meteorites, and comets. The isotopic compositions of cometary xenon and krypton measured in the coma of 67P/Churyumov–Gerasimenko (67P/C-G)—the diffuse cloud of gas released from the comet's icy nucleus and sampled *in situ* by the ESA Rosetta spacecraft—are distinct from those of the Sun.

As noble gases preserved in cometary ices are thought to record material inherited from the same molecular cloud that formed the Sun, the non-solar isotopic compositions observed in 67P/C-G indicate that the comet sampled only a subset of the noble-gas reservoirs present in the presolar molecular cloud. Comparison with the solar isotopic composition therefore implies that an additional, compositionally distinct noble-gas reservoir must have existed in the presolar cloud but is not preserved in 67P/C-G.

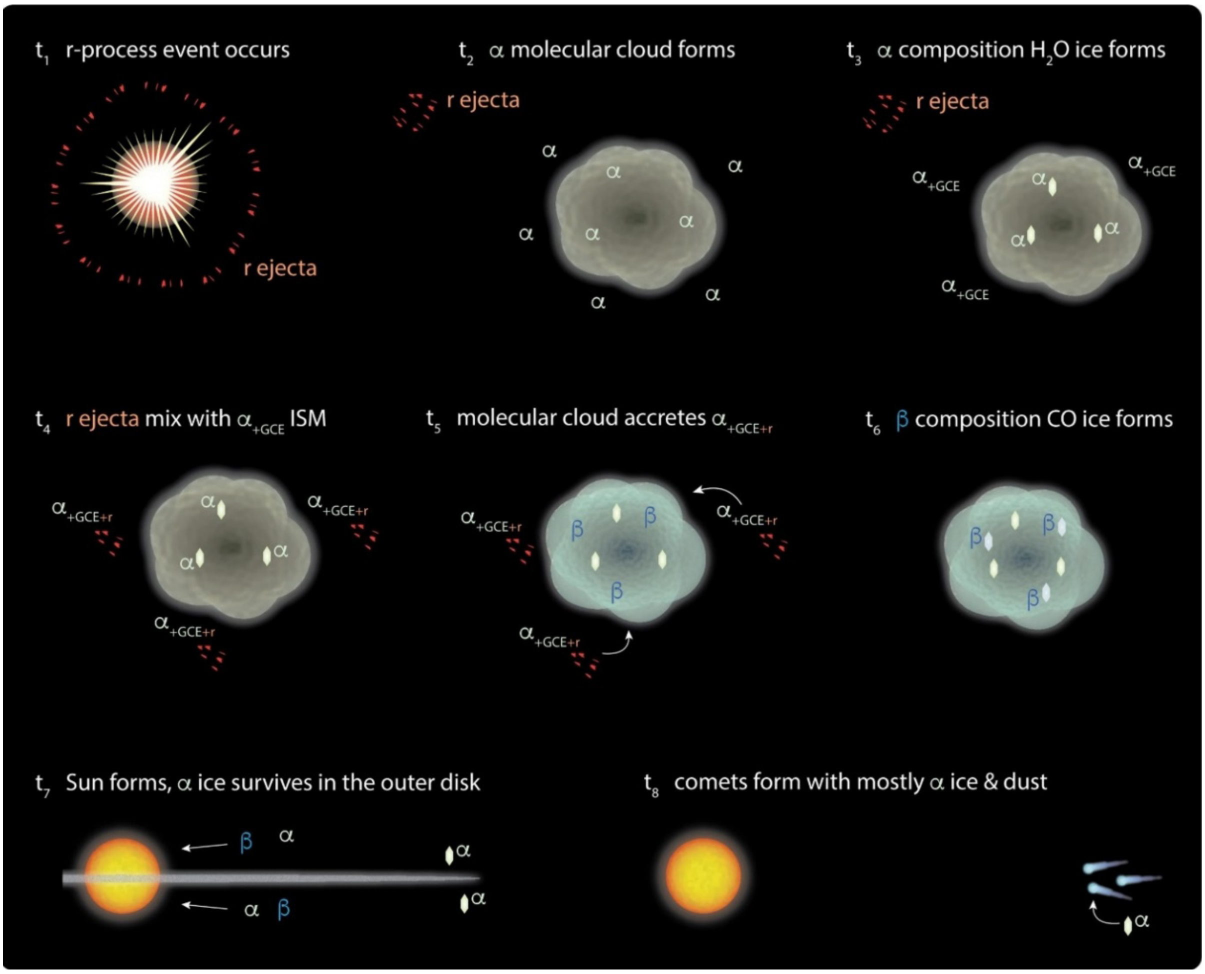

Fig. 3.2-2: Proposed sequence of events leading to distinct isotopic compositions of solar and cometary Xe and Kr. t_1: An r-process event occurs at some distance from the eventual presolar molecular cloud. t_2: The presolar molecular cloud forms from the local inter stellar medium (ISM) with a Xe and Kr composition denoted as α. The r-process ejecta are still in the halo or not yet mixed with the local ISM. t_3: Water ice begins to form in the molecular cloud, trapping α composition Xe and Kr. More volatile ices that crystalise later at lower temperatures may also form. The r-process ejecta are still in the halo or not yet mixed with the local ISM. t_4: The r-process ejecta mix with the local ISM. t_5: The molecular cloud accretes the modified ISM composition (or acquires it from a cloud-cloud collision). The cloud has then the β composition. Water ice with the α composition is not destroyed in this process. t_6: Predominantly more volatile β composition ices form in the cloud. t_7: The Sun forms with a mixture of α and β compositions and volatile ices throughout the protoplanetary disk vaporise. More refractory α composition water ices survive in distal regions of the protoplanetary disk. t_8: Comets form in the outer Solar System from dust mixed with ices that predominantly bear α composition Xe and Kr.

This absence most likely reflects selective loss: a noble-gas component that was originally co-trapped in more volatile ice was subsequently destroyed or removed during processing within the protoplanetary disk, prior to comet accretion. In this study, it is shown that this inferred, now-missing component was enriched in r-process and potentially p-process isotopes relative to the solar composition, and that these isotopes formed more than one hundred million years before the coalescence and cosmochemical isolation of the Solar System.

A scenario is developed in which this component was accreted by the presolar molecular cloud after the formation of water ice containing co-trapped xenon and krypton with the composition preserved in 67P/C-G. Such material may have been derived from a diffuse, heterogeneous molecular component of the interstellar medium accreted by the presolar molecular cloud, or incorporated through cloud–cloud collision (Fig. 3.2-2). These observations further imply that at least two distinct r-processes contributed to the overall solar r-process abundance pattern.

c. *Experimental determination of the effect of S on Fe isotopic fractionation during core formation up to 14 GPa (E. Kubik, in collaboration with S. Rabin/Brussels)*

In this project, the effect of sulphur (S) on the isotopic fractionation factor of iron (Fe) was investigated under conditions relevant to core formation on fully grown terrestrial planets, particularly Mars, for which core-mantle equilibration likely occurred in the pressure range 12-20 GPa. The composition and structure of Mars' interior constitute critical knowledge for deciphering its accretion process and genetic history within the inner Solar System. One key feature of Mars' interior is a core enriched in light elements, more so than Earth's. That S is a major element in the Martian core is supported by numerous recent studies using different approaches, including seismic measurements from the InSight mission.

Previous metal–silicate experimental studies reported a significant effect of S alloy content on the Fe isotopic fractionation factor at 1 GPa. However, this effect has never been tested under conditions directly relevant to core formation on Mars. In this study, four experiments were performed at 8-14 GPa under superliquidus conditions ranging from 2200 to 2500 K using the Zwick 5000-ton multianvil press. The starting material was a mixture of natural MORB and synthetic metal in a 70:30 ratio, with the metal composed of pure Fe and FeS to achieve approximately 15 wt. % S. The starting powder was loaded into a single-crystal MgO capsule housed in custom "box furnace" assemblies, compressed, and subsequently heated for 3-7 minutes at the target temperature.

The quenched equilibrated metal and silicate from each run were mechanically separated, and their Fe isotopic compositions were measured at Ghent University using a Neptune multi-collector ICPMS. Prior to measurement, the Fe fraction was purified at Vrije Universiteit Brussel. Moderate fractionation factors ($\Delta^{56}\mathrm{Fe}_{\mathrm{metal–silicate}}$) from -0.07 to 0.12 ‰ were obtained (Fig. 3.2-3), indicating that core formation between 8 and 14 GPa with a S-rich core is unlikely to significantly fractionate Fe isotopes. This result differs from the effect measured in previous low-pressure studies, possibly due to (1) differences in the structure of silicate melts and molten alloys affecting the Fe bonding environment, or (2) temperatures that were too high to resolve isotopic fractionation.

We estimate that the $\Delta^{56}Fe_{metal–silicate}$ measured at low pressure and 1923 K in the literature would correspond to approximately 0.19‰ at our experimental temperature of 2200 K, which is significantly larger than the average factor of 0.04 ± 0.06‰ measured in our experiments. Our new dataset is also slightly offset relative to previous S-free experiments performed using the same technique (Fig. 3.2-3), which show elevated fractionation factors between 8 and 14 GPa. Overall, these results demonstrate that Martian core-forming metal could contain relatively high S concentrations while maintaining a chondritic Fe isotopic composition of the mantle, in agreement with Fe isotopic signatures measured in Martian meteorites.

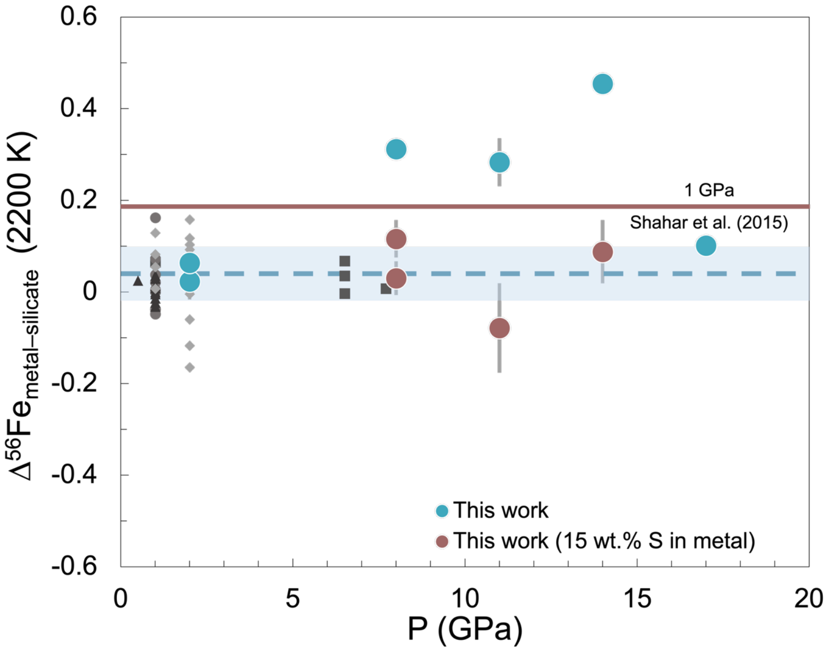

Fig. 3.2-3: Iron isotope fractionation factor between metal and silicate in multianvil experiments as a function of pressure. Literature data are indicated by the smaller grey and black symbols and the value proposed by Shahar *et al.* (2015; Geochim. Cosmochim. Acta 150, 253) at 1 GPa is shown by the horizontal red line.

d. *Testing the Hadean matte scenario: Experimental LH-DAC sulphide–silicate chalcophile element partitioning (E. Kubik, O. Lord/Bristol, L. Man, A. Minchenkova, I. Blanchard/Paris, E.-M. Rogmann/Bristol and D.J. Frost)*

The sulphide matte, or Hadean matte, is a phase of core formation hypothesised to occur at the end of Earth's accretion and involves the formation of an immiscible sulphide liquid that equilibrated with the mantle before merging into the metallic core. It was first invoked to explain the elevated sulphur depletion observed in the bulk silicate Earth (BSE). This hypothesis is further supported by the fact that sulphur is only moderately siderophile at the high pressures relevant to Earth's core formation (40-60 GPa), as reported by recent laser-heated diamond anvil cell experiments. The Hadean matte scenario has also been proposed to play a crucial role in establishing the abundances of highly siderophile elements in the BSE. However, recent experiments have shown that sulphur solubility in a magma ocean is very high, rendering sulphur saturation and the formation of an immiscible sulphide liquid less likely.

In this project, laser-heated diamond anvil cell experiments (LH-DAC) were performed at the University of Bristol to determine the partitioning behaviour of four chalcophile elements—Cd, Mn, Cr, and Ag—between sulphide (stoichiometric FeS) and silicate. These results were used to assess whether the BSE signatures of these elements were established by FeS segregation or by segregation into a Fe-dominated metallic alloy. Two diamond anvil cells were loaded with a sandwich consisting of two pyrolitic glass discs enclosing a piece of FeS doped with the four chalcophile elements and were subsequently laser heated at 40 and 44 GPa. Lamellae extraction was carried out using a focused ion beam at the Bayerisches Geoinstitut (Fig. 3.2-4).

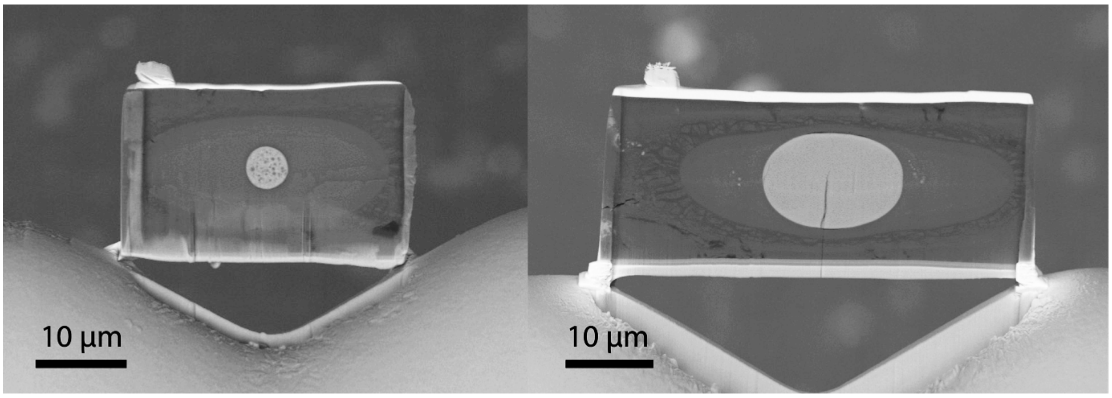

Fig. 3.2-4: Backscattered electron images of LH-DAC samples extracted with the focused ion beam. In the centre, a sphere of iron-sulphide melt (light) is surrounded by quenched silicate melt (light grey) encased in a darker, unmolten silicate.

The results show that, for Cd, Mn, and Cr, sulphide–silicate partitioning is nearly identical to metal–silicate partitioning under similar conditions (Fig. 3.2-5). This indicates that these data cannot be used to distinguish between different chalcophile element segregation scenarios during Earth's accretion and core formation. In contrast, the Ag results indicate that Ag partitions more strongly into the alloy when FeS is present compared to a Fe-dominated alloy. This suggests that the Hadean matte could have been an efficient mechanism for transporting Ag into the core, potentially explaining its observed depletion in the mantle. However, this conclusion is based on a limited number of experiments, and no metal–silicate partitioning measurements exist from diamond anvil cell studies at comparable pressures. As a result, the present data can only be compared with a small number of low-pressure literature studies extrapolated to the pressure conditions of these experiments. Consequently, further experiments are required to better characterise the partitioning behaviour of chalcophile elements between metal and silicate, as well as between sulphide and silicate, in order to robustly test the Hadean matte scenario.

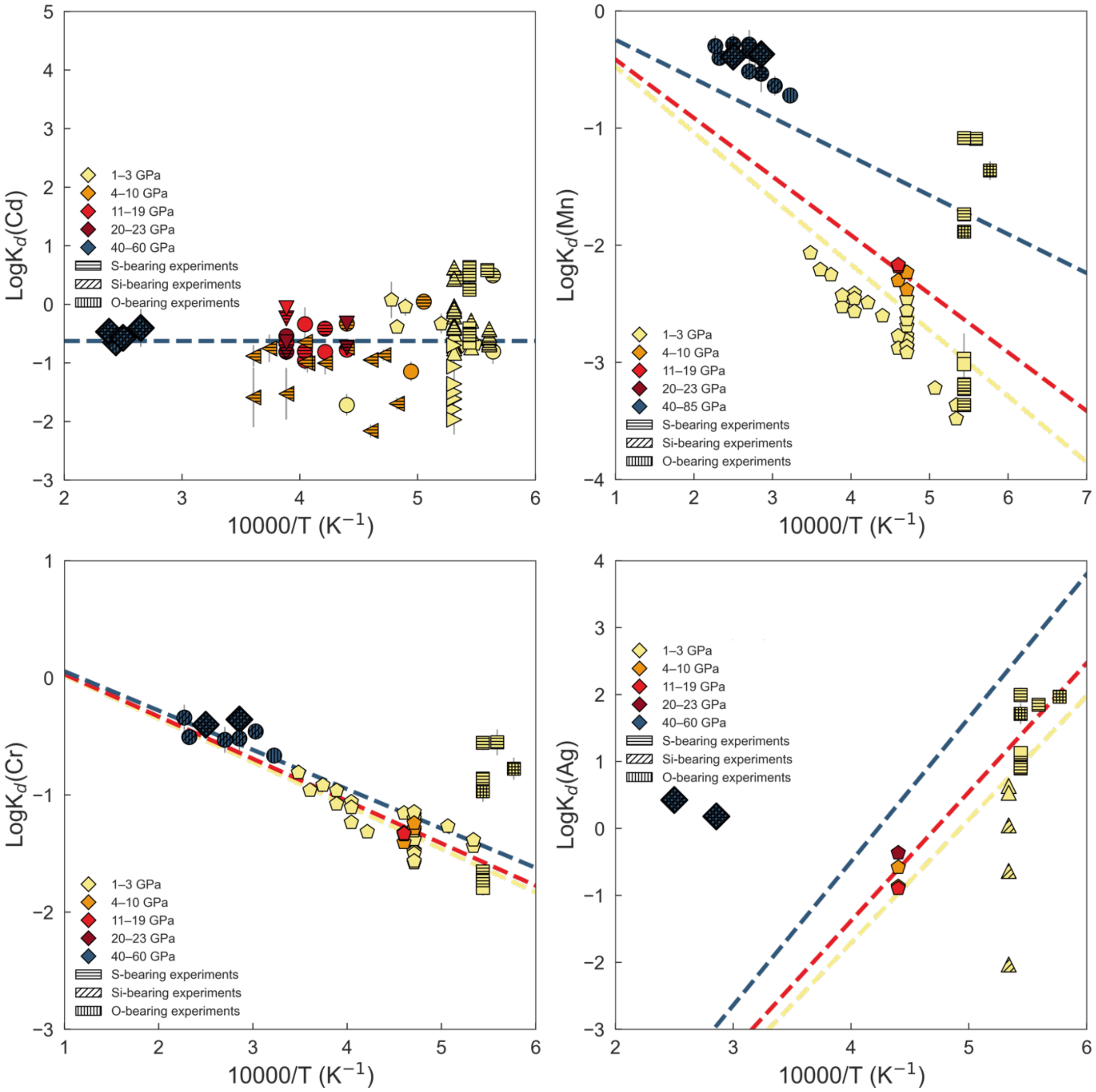

Fig. 3.2-5: Experimental partitioning data for Cd, Mn, Cr and Ag obtained in this study (diamond symbols) and compared to literature data (all other symbols). The partitioning is expressed as the logKd as a function of reciprocal temperature. Experiments are colour coded by pressure range and patterns on the symbols indicate the presence of significant (> 1 at. %) light elements in the metal alloy.

e. *Concentration-dependent partitioning of platinum and palladium does not support a late veneer in planetary mantles (Y. Li and M. Zhang)*

Platinum-group elements (PGEs: Os, Ir, Ru, Rh, Pt, and Pd) are classified as highly siderophile elements, making them powerful tracers for planetary accretion and core–mantle differentiation. Geochemical studies show that the silicate mantles of Earth, Mars, the Moon, and several differentiated asteroids are strongly depleted in PGEs relative to chondritic abundances, yet retain near-chondritic relative PGE patterns. Absolute PGE abundances in these mantles are typically depleted by factors of ~ 10^2-10^4 compared with their original solar or chondritic concentrations. Both 1-bar solubility experiments and high-pressure metal–silicate partitioning experiments demonstrate that PGEs have a strong, though element-specific, affinity for Fe-rich metal. Consequently, core–mantle segregation is expected to generate non-chondritic relative PGE abundances in silicate mantles. For small rocky planets, such as the Moon and asteroids, which experienced core–mantle segregation at relatively low pressures and temperatures, experimentally determined metal–silicate PGE partition coefficients ($D_{PGE}^{Met/Sil}$) of 10^6 to 10^{11} predict silicate mantle PGE abundances that are several orders of magnitude lower than those actually observed and non-chondritic in terms of relative PGE abundances. Although the effective siderophile behaviour of PGEs may be reduced in the deep magma oceans of larger planetary bodies, significant discrepancies remain. Even under such conditions, predicted abundances in Earth's mantle for elements such as Ir and Ru are still up to three orders of magnitude lower than observed values. Therefore, the near-chondritic relative PGE abundances recorded in planetary mantles could so far not be fully explained by core–mantle segregation alone.

The concept of late accretion of chondritic material following planetary core–mantle segregation—commonly referred to as the late veneer—has long been proposed and widely accepted as a solution to this discrepancy. In this framework, silicate mantles are expected to have been severely depleted in, or nearly devoid of, PGEs immediately after core formation because of the exceptionally high $D_{PGE}^{Met/Sil}$. Subsequent accretion of chondritic material, amounting to approximately 0.01-0.6 wt. % of the silicate mantle, would then have replenished PGEs and re-establish near-chondritic relative PGE abundances, consistent with those observed in the silicate mantles of Earth, Mars, the Moon, and certain differentiated asteroids. For Earth, however, core formation occurring during a deep magma-ocean stage may have resulted in an overabundance of Pt and Pd in the silicate mantle, while the overall PGE pattern remained distinctly non-chondritic. Reconciling this outcome with the late veneer hypothesis requires an additional depletion mechanism operating prior to late accretion. Specifically, efficient removal of PGEs via segregation of sulphide melts into the core from the silicate mantle has been proposed, driven by the high sulphide–silicate partition coefficients ($D_{PGE}^{Sul/Sil}$= 10^3 to 10^6). Such sulphide segregation would have reduced mantle PGE abundances to sufficiently low levels, allowing subsequent chondritic addition to restore near-chondritic relative PGE ratios.

Although the late veneer model provides an elegant explanation for the near-chondritic PGE abundances in planetary mantles, we noticed that previous determinations of $D_{PGE}^{Met/Sil}$ and $D_{PGE}^{Sul/Sil}$ were primarily based on weight percent (wt. %) levels of PGEs in the metal or sulphide phases. In this study, we thus conducted new experiments to determine $D_{Pt,Pd}^{Met/Sil}$ and $D_{Pt,Pd}^{Sul/Sil}$ as a function of Pt and Pd concentration at 1.5-14 GPa and 1600-2150 °C, from 7 wt. % down to 100 μg/g, in order to better understand the behaviour of PGEs in planetary systems. Starting materials included Fe-FeS mixtures and silicates of MORB to peridotite composition. At pressures ≤ 4 GPa, coexisting metallic, sulphide, and silicate melts were produced, and the silicate melts were quenched into glasses. At 7 GPa, coexisting sulphide and silicate melts were generated, while at 14 GPa, coexisting metallic and silicate melts were formed. The silicate melts were quenched into dendritic texture at 7-14 GPa. Pt and Pd concentrations in all run products were measured by LA-ICP-MS, with detection limits of ~ 5 ng/g.

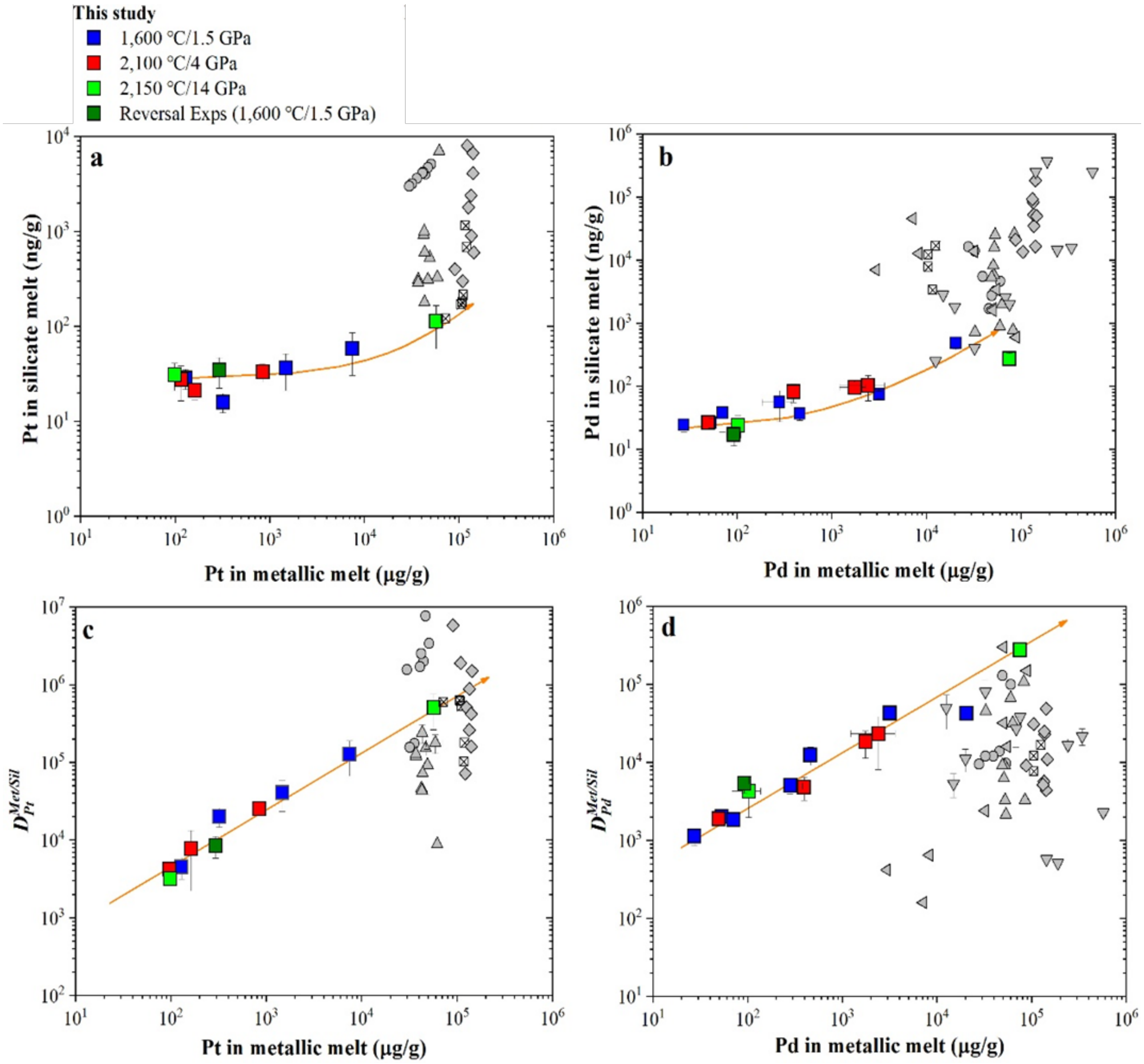

Fig. 3.2-6: The Pt and Pd concentrations in silicate melts and the $D_{Pt,Pd}^{Met/Sil}$ as a function of the Pt and Pd concentrations in metallic melts. Data from this study are shown as coloured squares at the conditions indicated, all other symbols are from the literature.

Partition coefficients $D_{Pt,Pd}^{Met/Sil}$ and $D_{Pt,Pd}^{Sul/Sil}$ were calculated from the weight proportions of Pt and Pd in the metallic, sulphide, and silicate melts (Fig. 3.2-6 and -7). Figure 3.2-6 shows that

$D_{Pt,Pd}^{Met/Sil}$ range from 1100 to 0.5 × 10^6, and Figure 3.2-7 shows that $D_{Pt,Pd}^{Sul/Sil}$ range from 550 to 0.9 × 10^5. Importantly, $D_{Pt,Pd}^{Metal/Sil}$ show a strong positive dependence on $C_{Pt,Pd}^{Met}$ (Pt and Pd concentration in the metallic melt), and $D_{Pt,Pd}^{Sul/Sil}$ a strong positive dependence on $C_{Pt,Pd}^{Sul}$ (Pt and Pd concentration in the sulphide melt). Our $D_{Pt,Pd}^{Met/Sil}$ values at high Pt and Pd concentrations are broadly consistent with those obtained in previous studies at similar concentration levels (Fig. 3.2-6). Also the $D_{Pt,Pd}^{Sul/Sil}$ and $C_{Pt,Pd}^{Sil}$ values reported in previous studies are consistent with the systematics observed in the present study (Fig. 3.2-7). In Figure 3.2-6, the large scatter observed in previous $D_{Pd}^{Met/Sil}$ values at high Pd concentrations in the metals has been attributed to variations in pressure, temperature, composition, and oxygen fugacity conditions; however, our $D_{Pt,Pd}^{Met/Sil}$ obtained at 1.5-14 GPa and 1600-2150 °C seem to be controlled dominantly by $C_{Pt,Pd}^{Met}$, rather than by pressure and/or temperature.

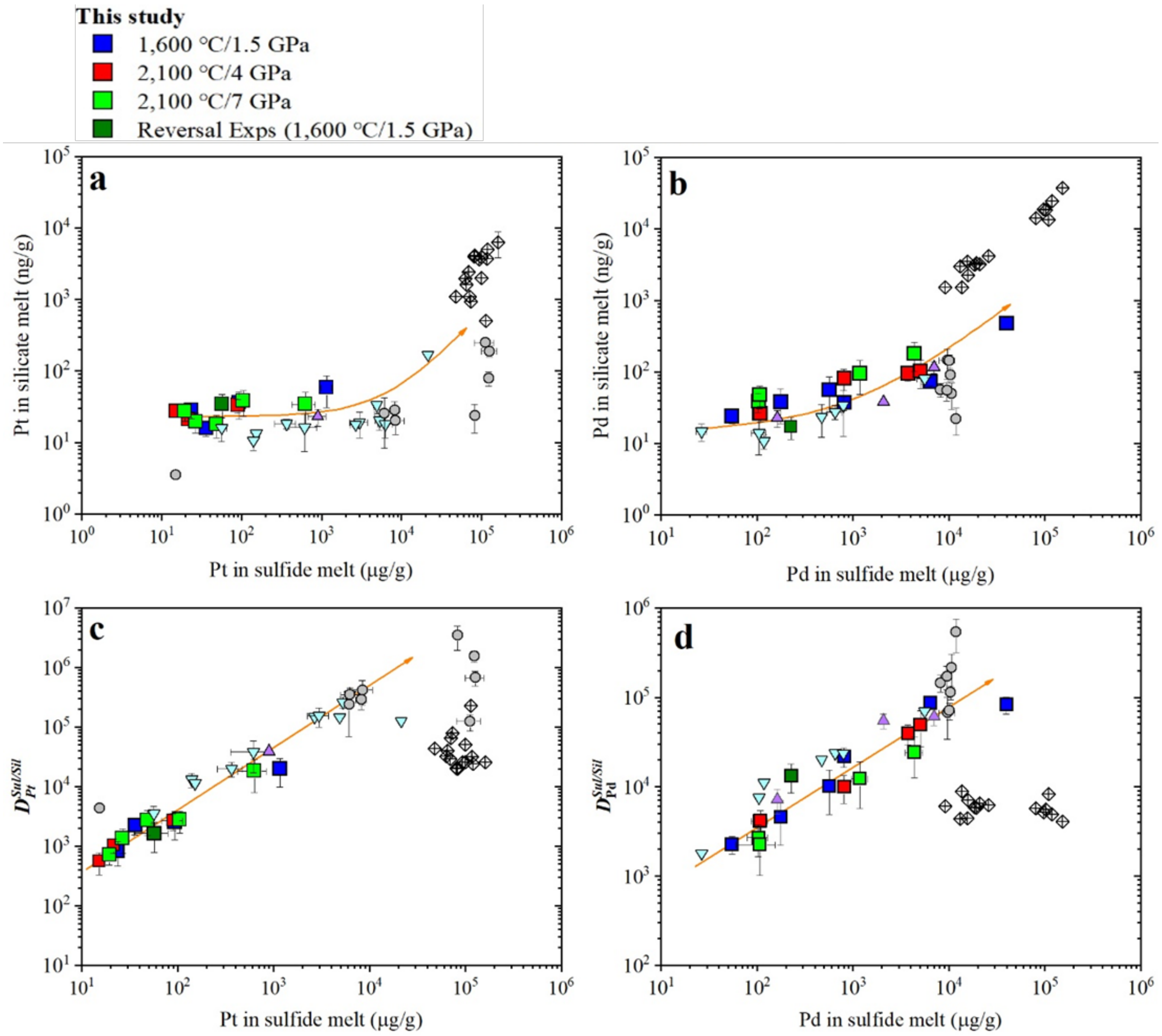

Fig. 3.2-7: The Pt and Pd concentrations in silicate melts and the $D_{Pt,Pd}^{Sul/Sil}$ as a function of the Pt and Pd concentrations in sulphide melts. Data from this study are shown as coloured squares at the conditions indicated, all other symbols are from the literature.

The concentration-dependence of $D_{Pt,Pd}^{Met/Sil}$ and $D_{Pt,Pd}^{Sul/Sil}$ suggests that previously determined $D_{Pt,Pd}^{Met/Sil}$ and $D_{Pt,Pd}^{Sul/Sil}$ from experiments with wt. % Pt and Pd concentrations are not suitable for modelling planetary core–mantle segregation or constraining the delivery of a late veneer. The observed relatively low $D_{Pt,Pd}^{Met/Sil}$ and $D_{Pt,Pd}^{Sul/Sil}$ values (< 10^3-10^4) at $C_{Pt,Pd}^{Met}$ and $C_{Pt,Pd}^{Sul}$ between 10 and 100 µg/g (Fig. 3.2-6 and -7) indicate that Pt and Pd are far less siderophile and chalcophile in natural magmatic systems than previously assumed. In Figure 3.2-8, we demonstrate that $D_{Pt,Pd}^{Met/Sil}$ values of < 10^3-10^4 align closely with the values needed to explain the Pt and Pd abundances in the silicate mantles of both Earth and Mars through core–mantle equilibrium partitioning. The PGE abundances of the lunar mantle are about two orders of magnitude lower than those in Earth's mantle. If we assume the bulk Moon shares a similar terrestrial mantle composition in terms of PGEs, then the lunar mantle Pt and Pd abundances can also be explained by partitioning into the core (Fig. 3.2-8). This interpretation of Pt and Pd abundances in the mantles of Earth, Mars, and the Moon, based on the concentration-dependence of $D_{Pt,Pd}^{Met/Sil}$, suggests that a late veneer is not required.

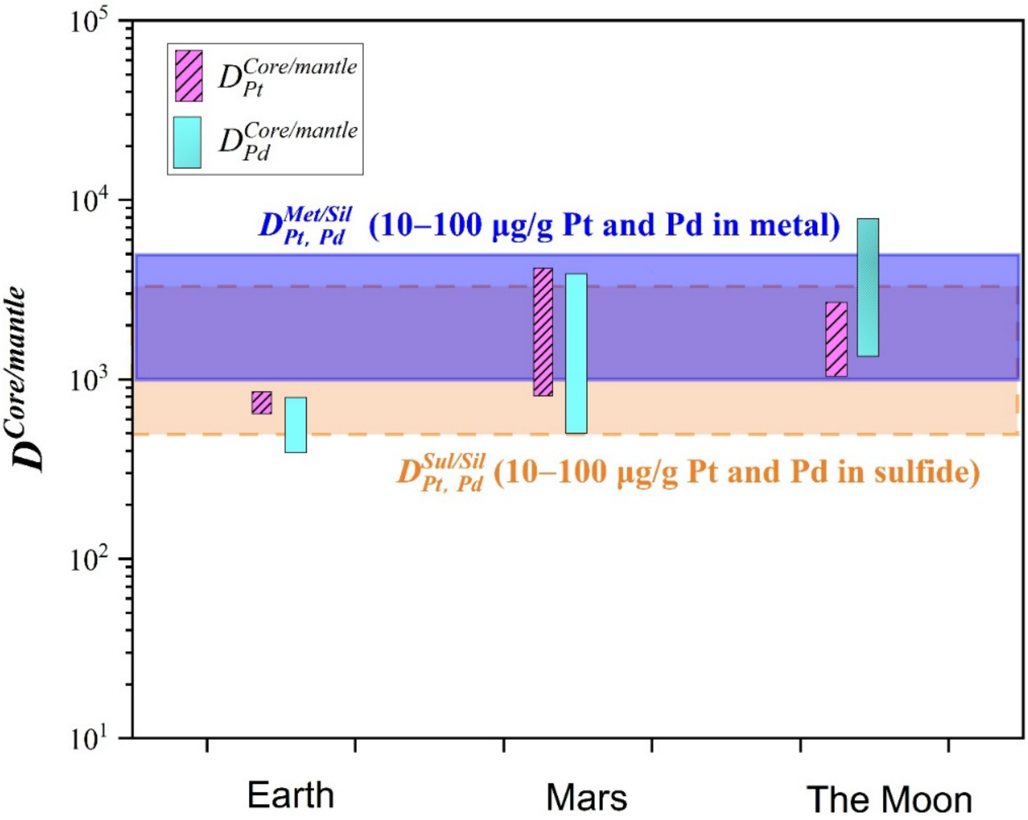

Fig. 3.2-8: The core–mantle partition coefficients ($D^{Core/mantle}$) required to explain the Pt and Pd contents in the silicate mantles of Earth, Mars, and the Moon. Note that we used previously estimated minimum to maximum Pt and Pd values of the silicate mantles to calculate a range of $D^{Core/mantle}$ values. The presently obtained $D_{Pt,Pd}^{Met/Sil}$ and $D_{Pt,Pd}^{Sul/Sil}$ values at Pt and Pd concentrations between 10 and 100 µg/g overlap with the required $D^{Core/mantle}$ values.

f. *Origin of metal in lunar impactites using siderophile element abundance analysis (R. Zhao and A. Bouvier, in collaboration with R. Brasser/Budapest)*

Metallic iron-rich alloys are abundant phases in chondrite and achondrite meteorites. The abundances of highly siderophile elements (HSE) in Fe–Ni metal of meteorites offer an effective tracer of the nature of the impactors that have collided with the Moon and other planetary bodies. *In situ* analysis of HSE abundances in metals using laser ablation ICP-MS offers higher analytical efficiency than INAA, and our previous work has demonstrated that this approach is not significantly affected by matrix mismatch between standard materials (NIST SRM 610 glass) and Fe–Ni metal, allowing robust investigation of impactor sources involved in late accretion processes of the Earth–Moon system.

The glass reference material NIST SRM 610, along with the iron meteorites Hoba (IVB) and North Chile (IIAB), was used before and after measurements of unknown samples for calibration. All measurements were performed using an ESL NWR 193 nm laser ablation system coupled with a Thermo iCap TQ ICPMS system at BGI. ^{31}P, ^{52}Cr, ^{57}Fe, ^{59}Co, ^{61}Ni, ^{63}Cu, ^{71}Ga, ^{72}Ge, ^{75}As, ^{95}Mo, ^{99}Ru, ^{103}Rh, ^{105}Pd, ^{120}Sn, ^{121}Sb, ^{182}W, ^{185}Re, ^{189}Os, ^{193}Ir, ^{195}Pt and ^{197}Au were analysed. The laser ablation spot analyses consisted of 20s of blank measurement, followed by a burst of 500 laser pulses of sample ablation at 15 Hz, using spot sizes of 75 to 100 µm, and a fluence of 5 J/cm^2. The Co concentration obtained using EPMA was used for internal normalization. For external normalization, NIST SRM 610 glass was used for Cr, Ga, Ge, As, Sn, Sb and Au and Hoba for the other elements. The detection limit and reproducibility (2SE) performance for low-abundance HSE such as Re, Os, Ir, Pt and Au are ~ 0.03 and ~ 0.02 ppm, respectively.

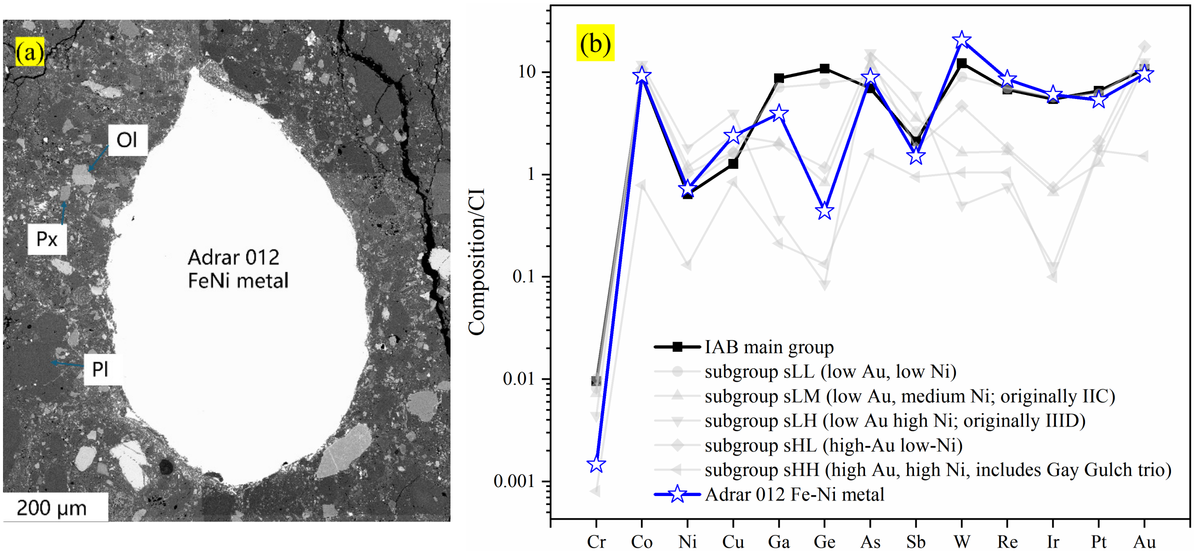

Fig. 3.2-9: BSE image and normalised elemental composition of Lunar meteorite Adrar 012 compared to IAB main and sub-groups.

Lunar feldspathic breccia Adrar 012 contains abundant glassy spherules and basaltic impact melt rock clasts along with lithic olivine, pyroxene, and anorthite enclosed within a clastic to glassy matrix. A large Fe-Ni grain (790 × 490 µm), lacking troilite and schreibersite inclusions, was found in the matrix (Fig. 3.2-9a). The composition of the Fe-Ni grain is $Fe_{91.8\pm0.1}Ni_{7.7\pm0.1}Co_{0.4\pm0.1}P_{0.1\pm0.1}$ (wt. %) using EPMA. The HSE abundances (with the exception of Ga and Ge) of the Adrar 012 Fe-Ni grain match those of the main group of IAB iron meteorites (Fig. 3.2-9b). The precursor of the metal found in Adrar 012 experienced approximately 55 wt. % Ga and 96 wt. % Ge depletion that may be related to impact remelting and rapid cooling. Evaporation experiments on Fe-Ni liquid indicate that Ga and Ge depletion in IAB metal can occur over a range of temperatures and evaporation durations during impacts. Ir, Au, and Pt in Apollo samples 67915, 67955, and 76055 are consistent with iron meteorite groups IIAB and IIE, both of which formed in the inner Solar System (Fig. 3.2-10). Meanwhile, the Co and Ni compositions more strongly suggest an impactor source from the IIAB group. Similarly, Apollo 67935 shows affinities with the IAB iron meteorite group, which also originated in the inner solar system. However, Ge and Ga are depleted in all Apollo samples and Co is enriched relative to Ni due to impact-related mixing with indigenous lunar components characterised by high Co/Ni ratios.

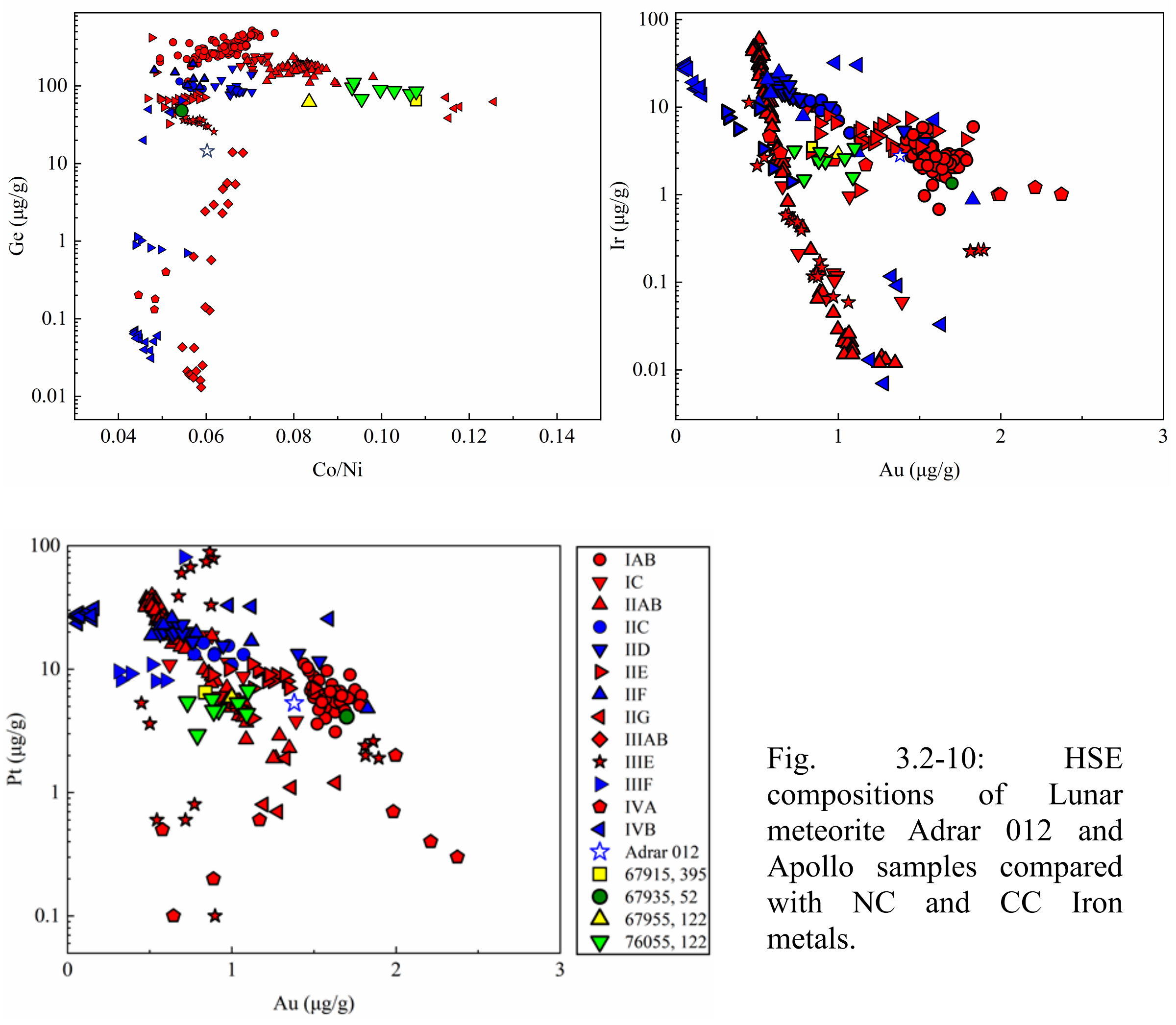

Fig. 3.2-10: HSE compositions of Lunar meteorite Adrar 012 and Apollo samples compared with NC and CC Iron metals.

Fe-Ni metals in the Apollo samples with impact ages of ~ 4.15 to 3.90 Ga have both lunar and impactor origins. HSE compositions are consistent with non-carbonaceous (NC) iron meteorite sources in the inner solar system. Our results from metal-bearing lunar impact melt breccias indicate that non-carbonaceous (NC) iron meteorite-like impactors in addition to other NC chondrite-like materials from the inner Solar System contributed to the HSE reservoir of the Moon and Earth during late accretion.

g. *Determination of melting relations of dry KLB-1 peridotite to 33 GPa using multianvil technique (A. Chanyshev, N. Martirosyan, H. Fei and T. Katsura)*

The Earth's mantle likely experienced extensive melting early in its history, resulting in the formation of a terrestrial magma ocean in which minerals crystallised as cooling progressed. Dense minerals would have sunk, while minerals with neutral buoyancy would have accumulated at their equilibrium depths. This settling process would have produced chemical differentiation, shaping the initial structure of the mantle. However, reconstructing this early structure remains difficult because it depends on whether solidification occurred through fractional or batch crystallization. Fractional crystallization would create compositional layering, whereas batch crystallization would result in a more homogeneous mantle. Depending on melting sequences and density contrasts, layers enriched in either bridgmanite or iron-rich ferropericlase may have formed in the deep lower mantle. The key factor governing this chemical stratification is the melting behaviour of peridotite under lower-mantle conditions.

Melting relations of peridotite at deep-mantle pressures have been widely studied, but previous experiments faced difficulties such as steep temperature gradients and limited pressure–temperature conditions. To address these limitations, we developed multianvil cell assemblies with "nearly zero-gradient" furnaces and employed hard tungsten carbide anvils to achieve higher pressures. Using this approach, we conducted multianvil experiments at pressures between 14 and 33 GPa to determine the solidus and liquidus of anhydrous KLB-1 peridotite.

The results (Fig. 3.2-11) show that the solidus and liquidus at 14-23 GPa are consistent with previous findings, whereas results at 25-33 GPa differ significantly from earlier laser-heated diamond anvil cell experiments. We observe a much narrower melting interval (≤50 K), indicating a sharp solid-liquid transition. Textural evidence reveals vertical segregation between melt and bridgmanite, implying that bridgmanite is denser than the coexisting melt at these conditions. This density contrast would have promoted efficient melt expulsion during magma-ocean cooling. These findings suggest that solidification occurred over a narrow temperature range and followed a fractional crystallization pathway. Consequently, the deep lower mantle likely crystallised as a compositionally distinct, bridgmanite-dominated layer, contributing to the early chemical stratification of Earth's mantle.

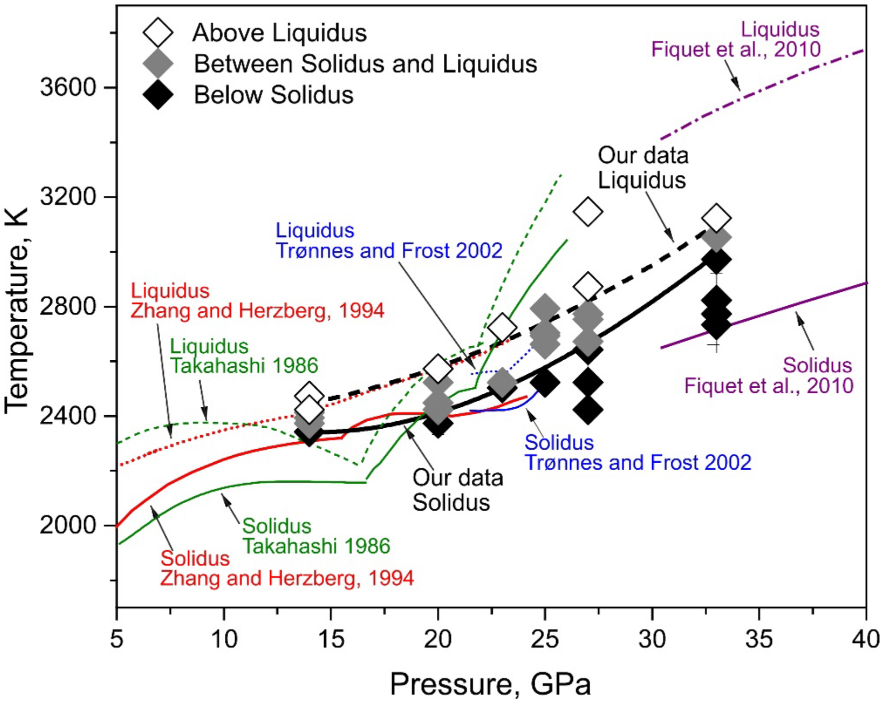

Fig. 3.2-11: Solidus and liquidus of anhydrous KLB-1 peridotite, combined with data from the literature. Previous data are from Takahashi (1986; J. Geophys. Res. 91: 9367), Zhang and Herzberg (1994; J. Geophys. Res. 99:17729), Trønnes and Frost (2002; Earth Planet. Sci. Lett. 197: 117-131), Fiquet et al. (2010; Science 329: 1516)

h. *Trace element partitioning between davemaoite and silicate melt (W.-Y. Zhou, A. Chanyshev, F. Wang, Y. Song, R. Zhao, A. Bouvier, A. Audétat, D.J. Frost and T. Katsura)*

Earth's lower mantle constitutes ~ 56 % of the planet's volume and hosts a major proportion of Earth's heat-producing and lithophile trace elements, making it critical for understanding the planet's thermal and chemical evolution. Approximately half of Earth's U and Th and ~ 20 % of K are expected to reside in the lower mantle, and Earth's internal heat budget is mainly generated by radioactive decay of ^{238}U, ^{235}U, ^{232}Th, and ^{40}K. Rare earth elements (REEs), along with Th and U, are key tracers of Earth's chemical evolution because they are refractory, lithophile, and highly sensitive to mineral–melt partitioning. Therefore, the distribution of REEs, Th, and U in the lower mantle provides critical insights into the chemical layering, thermal state, and long-term dynamics of Earth's interior.

A popular hypothesis is that davemaoite-rich domains in the lower mantle, such as large low-shear-velocity provinces, act as geochemical reservoirs of REEs, Th, and U. Multianvil press (MAP) element partitioning experiments at ~ 25 GPa between major lower mantle minerals and melts suggested REE, Th and U are primarily stored in davemaoite. Davemaoite has a perovskite structure (ABO_3) in which Ca^{2+} occupies the large 12-fold coordinated A sites and Si^{4+} occupies the small 6-fold coordinated B sites, making it relatively easy to accommodate cations with different sizes and valences. However, all previous MAP experiments on this topic were limited to < 27 GPa. These results have been widely extrapolated to the entire lower mantle, predicting that davemaoite may dominate the deep storage of REEs, U, and Th. The limited pressure ranges and different starting materials used in previous studies make it difficult to isolate the effect of pressure. A later study by Tateno *et al.* (2018; J. Geophys. Res. 123: 5515) investigated a wider pressure range (31-69 GPa) using laser heated diamond anvil cells, but only Sm and Nd, K, and Na partitioning between davemaoite and melt was studied. Their results suggested that D_{Sm} and D_{Nd} decrease with increasing pressures; however, how pressure affects partitioning of other trace elements remains underexplored.

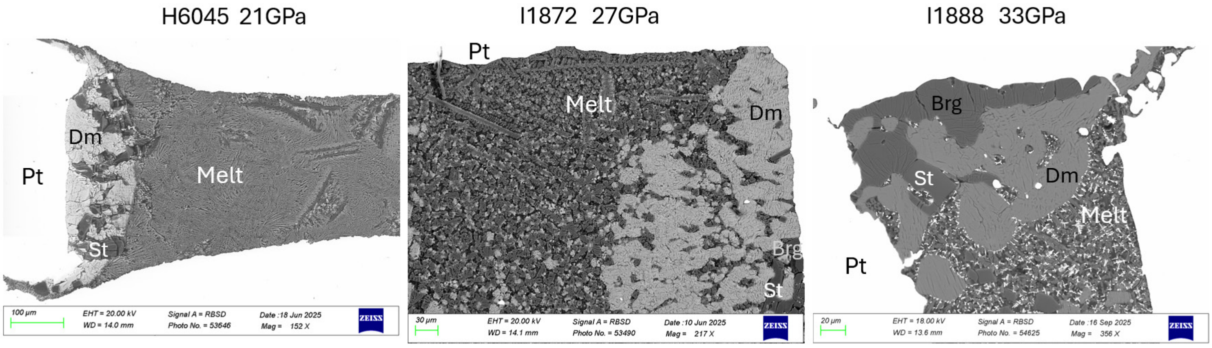

Fig. 3.2-12: SEM-BSE (Scanning Electron Microscopy-Backscattered Electron) images of the three representative run products.

Here, utilizing MAP, SEM, EPMA, and LA-ICPMS facilities at BGI, we conducted partial melting experiments in an ultracalcic system from 20 GPa to 33 GPa (Fig. 3.2-12), and determined the effect of pressure on trace element partitioning between davemaoite and silicate melt. Our preliminary results suggest that the partition coefficients of REEs decrease systematically with increasing pressure (Fig. 3.2-13), possibly because REE^{3+} are relatively incompressible compared to the A site in the davemaoite crystal structure. These partition coefficients in combination with D_{Th} and D_U will provide new constraints on the capacity of davemaoite to host trace elements throughout the mid-lower mantle, enabling evaluation of deep-mantle trace element storage.

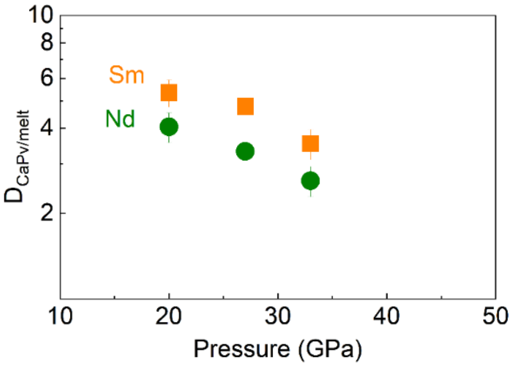

Fig. 3.2-13: Effect of pressure on Sm and Nd partitioning between davemaoite and melt.

i. *Experimental investigation of the role of komatiite-peridotite interaction in generating silica enrichment in the cratonic lithosphere (C. Melai/Dublin, A.C. Withers, P. Guyett/Dublin and E.L. Tomlinson/Dublin)*

A longstanding problem in understanding Archean mantle processes is the origin of silica-rich, orthopyroxene-rich cratonic peridotites, that have MgO/SiO_2 ratios that lie below those produced by simple high-pressure melting of fertile peridotite. These silica-rich peridotites are found particularly in the lithosphere below the Kaapvaal and Siberian cratons. Their enrichment in orthopyroxene and their narrow $\delta^{18}O$ range, indistinguishable from that of the upper mantle, implicate interaction with a mantle-derived, Si-bearing melt rather than involvement of crustal fluids. Given the abundance of komatiites during craton formation in the Archean and the likelihood of variably depleted sources, a compelling scenario is that ascending aluminium-depleted komatiite (ADK) melts reacted with the overlying lithospheric mantle. The ultramafic, low-Al character of ADK melt would avoid stabilising new garnet while preserving high Mg# in the residue, making it an ideal agent of silica addition. Recent thermodynamic modelling has shown that komatiite-peridotite interaction can theoretically produce silica-rich peridotite with little change to the other major elements. However, the paucity of relevant experiments means that the effect of komatiite-peridotite interaction on the composition of the Archaean lithosphere and of the reacting melt remains poorly constrained, despite increasing recognition of the importance of such processes in generating variability in mantle composition.

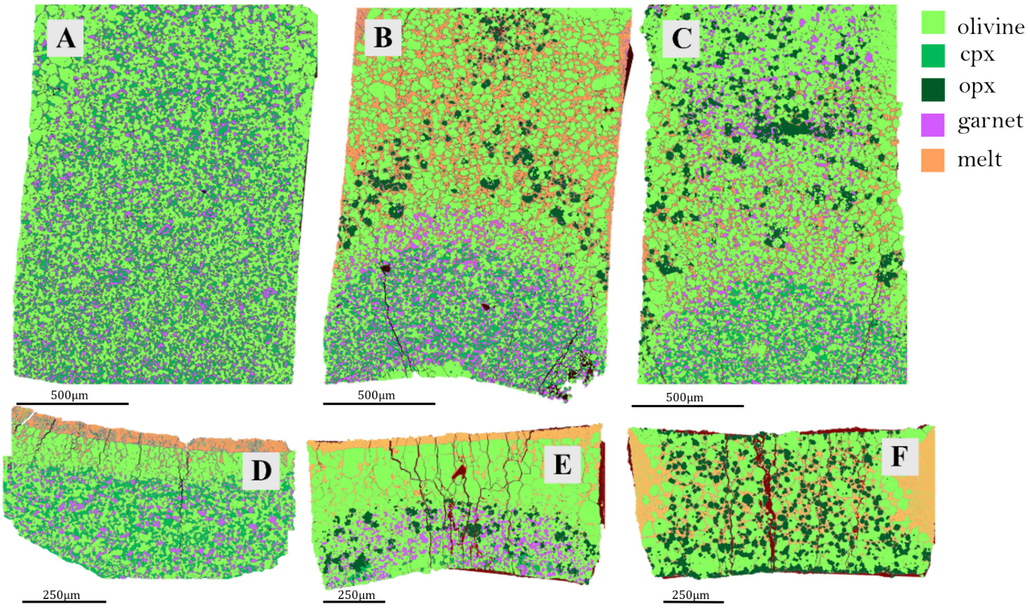

Fig. 3.2-14: Representative energy-dispersive X-ray spectroscopy maps from each experimental setup. (A) Cylinder synthesis experiment; (B) Hybrid experiment; (C) Reaction couple experiment; (D) Layered powder experiment; (E) Partial melting of depleted peridotite; (F) Partial melting of komatiite. In all phase maps, garnet appears in purple, clinopyroxene (cpx) in dark green, olivine in lime green, orthopyroxene (opx) in forest green, and melt in orange.

Our high-pressure experimental study directly tests this hypothesis using a suite of reaction-couple, hybrid, and layered experiments (Fig. 3.2-14) at 5 GPa and high temperature (1600-1690 °C), involving fertile and depleted peridotites juxtaposed with an ADK-type komatiite melt. The experiments reveal a two-stage reaction process: at the highest temperatures, komatiite melt undergoes an olivine-saturated reaction, precipitating large volumes of high-Mg# olivine and yielding an increasingly SiO_2-rich melt. As this modified melt migrates into cooler portions of the capsule, it crosses into orthopyroxene saturation, driving the peritectic replacement of olivine by large poikilitic orthopyroxene crystals. The result is a transition within the experimental capsule from olivine-rich dunite-like zones to orthopyroxene-rich reaction fronts, mimicking the textural characteristics observed in natural cratonic peridotites. Melt compositions range from komatiitic to high-SiO_2 komatiite and picritic liquids, demonstrating that ADK melts diversify during ascent as a consequence of reactive porous flow.

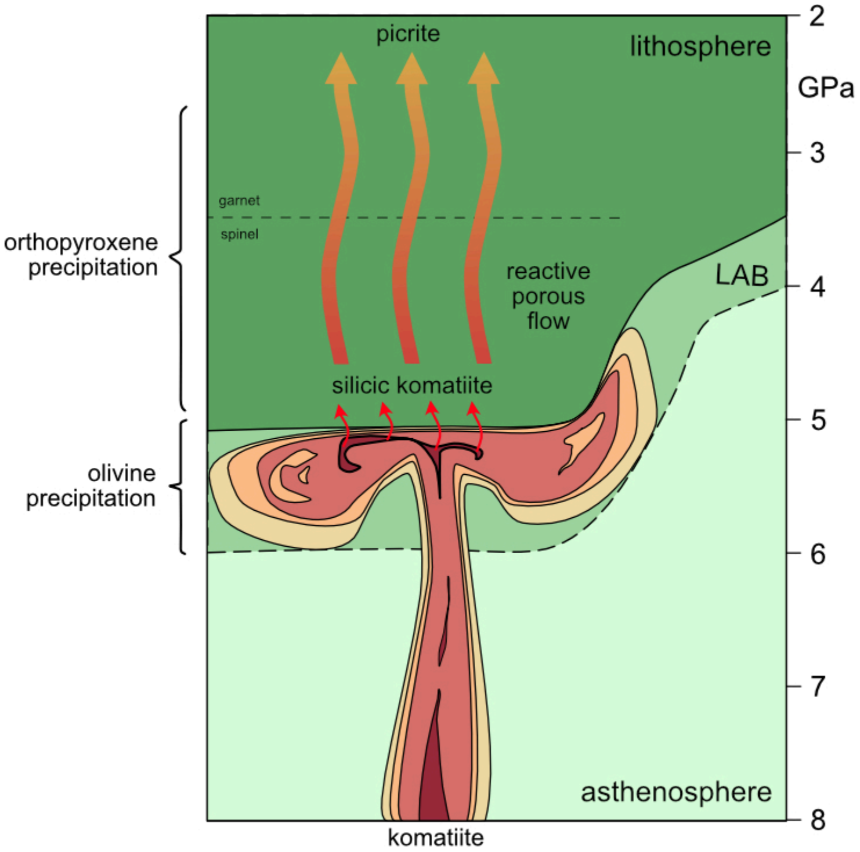

Fig. 3.2-15: Schematic model showing effect of reactive porous flow of komatiite through depleted cratonic lithosphere. LAB = Lithosphere–Asthenosphere Boundary.

The residues produced in our experiments reproduce the key features of natural Archean peridotites: the olivine-rich zones match cratonic dunites, whereas the orthopyroxene-rich zones replicate the silica-enriched harzburgites characteristic of the mid-lithospheric cratonic mantle. These results provide the first experimental evidence that silica-excess in cratonic mantle can arise from open-system interaction with ascending komatiite melt rather than melt extraction alone. They support a model in which Archaean craton roots were modified by high melt fluxes of komatiite, linking komatiite volcanism, lithospheric strengthening, and the chemical structure of cratonic mantle (Fig. 3.2-15).

j. *Iron partitioning between carbonate and ferropericlase (X. Hao, L. Man and D.J. Frost)*

It is quite plausible that at least some diamonds are formed through the reduction of carbonate liquids in the Earth's mantle, as carbonate minerals are occasionally found as inclusions inside diamonds. Ferropericlase, (Fe,Mg)O, is also found as an inclusion in some diamonds, which has often been linked with formation in the lower mantle. However, it is also possible that ferropericlase forms through the reduction of carbonates as some diamonds form. One outstanding issue concerning ferropericlase inclusions in diamonds is why compositions extend up to nearly 90 % FeO, as such compositions should be far from equilibrium with mantle rocks. It is possible that this results from strong partitioning of iron into ferropericlase as carbonates undergo reduction, however, to date, no experimental studies have measured the Fe-Mg exchange between ferropericlase and carbonate minerals or melts.

In this study, multianvil experiments were performed to examine this Fe-Mg exchange in the Fe-Mg-C-O system. Starting compositions were prepared by mixing $MgCO_3$ with four different ferropericlase compositions, with Fe/(Fe+Mg) ratios of 0.15, 0.20, 0.40 and 1.00. All four compositions were loaded into two duel-chamber graphite capsules, which were then both placed in each experiment on either side of a radially inserted thermocouple. The samples were equilibrated at 6 GPa and 1673, 1873 and 2073 K and one experiment was performed at 15 GPa and 1873 K. Recovered samples were sectioned and polished for analysis with the electron microprobe.

At 6 GPa and 1673 K, all samples contained solid carbonate coexisting with ferropericlase but at 1873 K and above, the samples contain melt and ferropericlase (Fig. 3.2-16). Chemical inhomogeneities due to the coarse quench-melt texture lead to larger analytical uncertainties. Fig. 3.2-17 shows Fe/(Fe+Mg) ratios for carbonate minerals and coexisting ferropericlase. For solid carbonates there is no detectable difference in the partitioning between the two pressures studied. The results of a thermodynamic model describing solid carbonate-ferropericlase Fe-Mg exchange are shown to be in excellent agreement with the experimental data, even though the thermodynamic data for ferropericlase and carbonate were taken from independent studies. Iron partitions very strongly into ferropericlase relative to solid carbonate but once the carbonate melts, this tendency is reduced and continues to decrease with increasing temperature. However, with increasing temperature, the melt compositions also shift away from being $(Mg,Fe)CO_3$-rich and become more (Mg,Fe)O bearing. It is very likely that this compositional shift causes the observed change in Fe-Mg partitioning, as moves the system towards the simpler MgO-FeO system, in which the liquid is always more Fe-rich than coexisting solid ferropericlase.

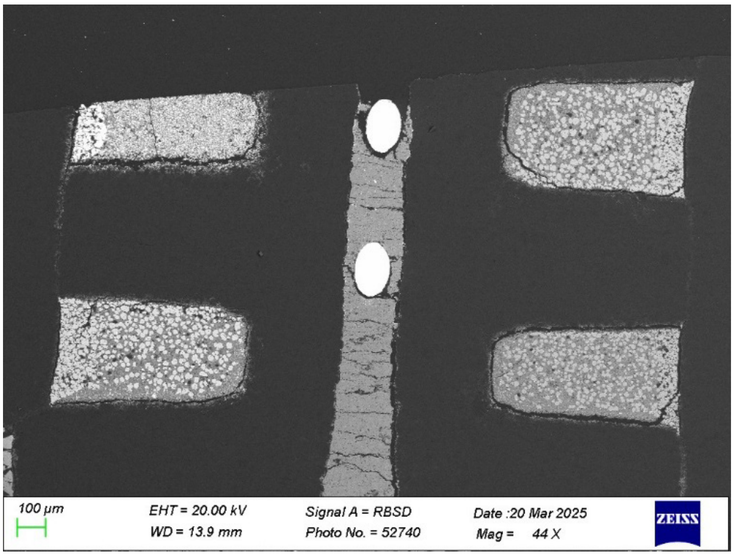

Fig. 3.2-16: A back-scattered electron image of a sample from 6 GPa and 2073 K. Two graphite capsules each containing two samples are placed either side of a radially inserted thermocouple (the two bright spots in the centre of the image). Each sample contains bright ferropericlase grains surrounded by carbonate melt.

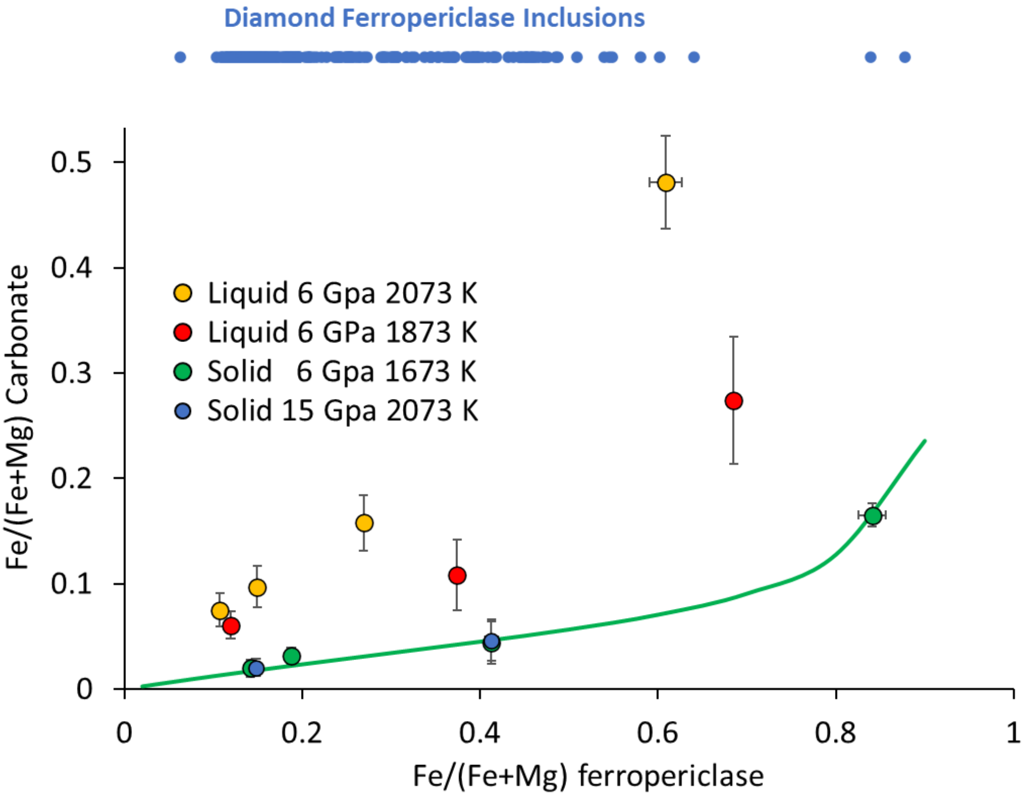

Fig. 3.2-17: Fe/(Fe+Mg) molar ratios of carbonate minerals and melts versus the coexisting ferropericase ratio. The solid line is a calculation from a thermodynamic model for solid carbonate at 6 GPa and 1673 K. The range of ferropericlase Fe/(Fe+Mg) ratios from inclusions in natural diamonds is plotted above the graph.

In this study so far, only Mg-rich carbonates have been equilibrated with ferropericlase, which requires unusually high temperatures to exceed the solidus, resulting in melts with excess (Mg,Fe)O. These temperatures are higher than those expected in the mantle, where Na is likely to depress the carbonate solidus. Investigating the role of Na on the solidus and partitioning will form the next phase of this project, to see whether Fe-Mg partitioning for such melts approaches that of solid carbonate found in this study. If this is the case, then as seen in Figure 3.2-17, the formation of very Fe-rich ferropericlase inclusions in natural diamonds would be consistent with the reduction of initially Fe-poor carbonates, which could have been in equilibrium with mantle rocks.

k. *Early Archaean onset of volatile cycling at subduction zones (G. Caro, G. Paris, P. Bourgeois and P. Bouilhol/Nancy, T. Grocolas/Lausanne and S.J. Mojzsis)*

The subduction of pelagic sediments and altered oceanic crust modulates the global cycle of volatile elements. Sulphate and carbonate fluids released when one plate descends beneath another modify the redox state of the mantle, and generate the return of water and reactive gases to the atmosphere and hydrosphere via arc volcanism, affecting planetary habitability over geologic timescales. However, the timing of the onset of subduction remains uncertain, hindering our understanding of how deep geochemical cycles operated on the early Earth.

Fig. 3.2-18: Field photograph of mafic and ultramafic rocks of the *ca.* 3.8 Ga Innuksuak Complex, northern Quebec, Canada. (S.J. Mojzsis at right; with G. Caro, D. Trail, N. Cates, E. Bell, and S. Davie).

In this work, our team measured sulphur and neodymium isotope data on Eoarchaean mantle-derived rocks of the Innuksuac Complex in northern Québec, Canada (Fig. 3.2-18), with petrological characteristics of arc magmas. These rocks exhibit anomalous sulphur isotopic compositions originally produced by photochemical reactions in the atmosphere more than 3.8 Gyr ago. Combined sulphur and neodymium isotope data suggest that these signatures were transferred to the Innuksuac mantle through devolatilization and partial melting of terrigenous sediments derived from a Hadean (4.3-4.4 Gyr ago) continental source, providing a record of an early continental margin subduction environment.

This result pushes back direct evidence of a subduction-driven volatile cycle to the onset of the terrestrial rock record, approximately 1 Gyr earlier than previously inferred from diamond inclusions.

l. *Geothermobarometry and rutile petrochronology of Neo-Archaean metamorphism in the Eo-Archaean metasediments from Akila and Innersuartuut (SW Greenland) and the southern Inukjuak domain, Québec (Canada) (P. Tropper and J. Peine/Innsbruck, A.K. Schmitt/Heidelberg, S.J. Mojzsis and C.E. Manning/Los Angeles)*

The oldest supracrustal belts are our best archives of early surficial processes; two well-known ancient examples occur in southern West Greenland (Færinghavn terrane) and northern Quebec (Inukjuak domain). Despite their widespread interest, the metamorphic histories of these rocks are little constrained. Previous work on the Akilia and Innersuartuut islands Færinghavn supracrustal enclaves (Fig. 3.2-19) reported minor anthophyllite-garnet rocks with rare metamorphic zircons yielding common U–Pb core ages of *ca.* 3650 Ma and rim ages at *ca.* 2700 Ma. The main mineral assemblages comprise garnet + anthophyllite + hornblende + biotite + plagioclase + K-feldspar + quartz. Secondary biotite and plagioclase with diffusive modification of the garnet compositions along fractures points to a later metamorphic overprint. We reported new phase equilibrium calculations of the main matrix assemblage yield average P-T conditions (± 1σ) of 580 ± 40 °C and 0.6 ± 0.1 GPa for both Akilia and Innersuartuut. Zr-in-rutile geothermometry of rutile inclusions in garnet from an Akilia sample (GR114) shows increasing T from 610 ± 30 °C (core) to 670 ± 30 °C (rim). Rutile U–Pb geochronology yields discordant ages (± 1σ) ranging from 2410 ± 56 Ma to 1383 ± 78 Ma: the upper intercept age of 2542 ± 214 Ma overlaps with uncertainties previously reported U–Pb zircon rim ages around 2700 Ma and a lower intercept at 1014 ± 237 Ma points to a Grenville/Sveconorwegian orogen overprint. An Inukjuak domain coarse-grained quartzite contains several different zircon age populations; the oldest (detrital) zircons have a weighted average ^{207}Pb/^{206}Pb age of 3736 ± 5 Ma. Two younger, smaller, zircon populations cluster around 3650 Ma and *ca.* 2700 Ma. The main mineral assemblage is anthophyllite + muscovite + quartz + rutile. Former biotite is replaced by stilpnomelane, and anthophyllite is replaced by chlorite + talc. Pervasive greenschist-facies retrogression of the sample prevents the calculation of P-T conditions using phase equilibrium calculations. Zr-in-rutile geothermometry limits T at an assumed pressure (0.6 GPa) to 670 °C ± 20 °C (± 1σ). Rutile U–Pb geochronology yielded 2538 ± 10 Ma, an age which correlates well with the youngest zircon age cluster, consistent with the lower closure T for Zr diffusion in rutile (< 600 °C).

Fig. 3.2-19: Field photograph of common mafic amphibolites from the southwestern peninsula of Akilia, southern West Greenland (yellow hammer handle in the centre of the picture is approximately 1 m).

The Færinghavn and Inukjuak supracrustal rocks experienced synchronic Neoarchean metamorphism at analogous upper amphibolite-facies conditions (580-670 °C). Our P-T data agree very well with intermediate thermal dT/dP gradient from the literature that are typical for the Neoarchean geodynamic setting of paired metamorphic belts. Evidence for a high-greenschist-lower amphibolite-facies overprint during the Late Proterozoic Grenville/Sveconorwegian event is present in the Færinghavn terrane, but not the Inukjuak domain.

m. *Scapolite as a major fractionating mineral phase in deep-seated arc magmas (Y. Qiao and A. Audétat)*

Scapolite is a volatile-bearing silicate mineral capable of incorporating CO_3, SO_3, and/or Cl into its crystal structure. It occurs mostly in calc-silicate rocks and lower crustal granulites. The origin of scapolite in the latter rocks is debated. Possible scenarios include (1) conversion of pre-existing sulphides or sulphates to scapolite during high-grade metamorphism, (2) scapolite formation through addition of external fluids, in the lower crust, and (3) scapolite crystallizing as a primary igneous phase. Because primary igneous scapolite is rarely observed in natural samples, many researchers favor the first two hypotheses. Here, we demonstrate by means of high P-T experiments that scapolite can be a major fractionating phase in arc magmas fractionating at high pressure.

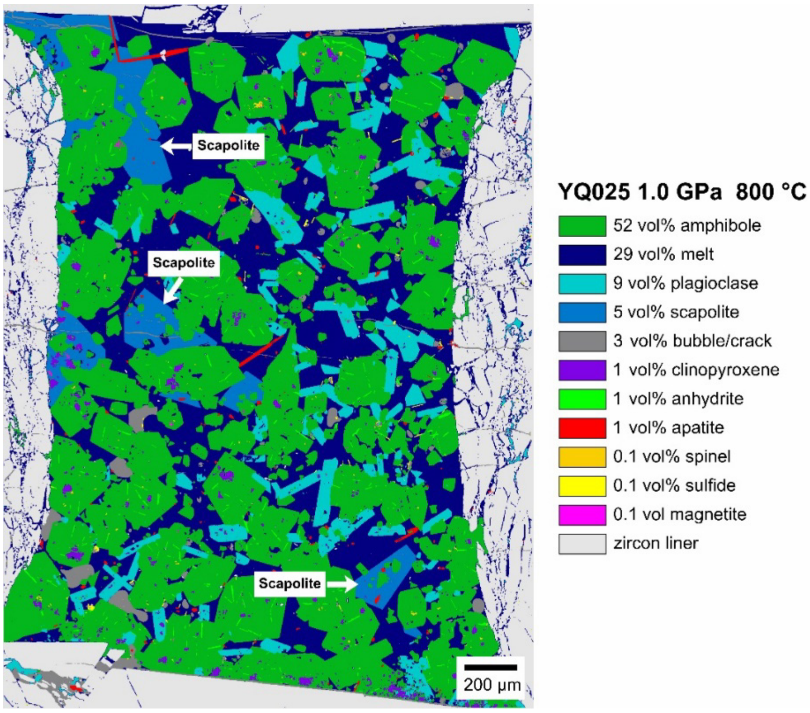

Fig. 3.2-20: Quantitative SEM-EDS map of experiment YQ025, which was slowly cooled from 1100 °C to 800 °C at 1.0 GPa within 15 days.

We conducted piston-cylinder experiments at 0.4, 0.7, 1.0, and 1.3 GPa and 700-1200 °C using both slow-cooling and equilibrium crystallization methods. The starting material was a natural basaltic rock powder doped with volatiles and trace elements at geologically realistic concentrations, having the following composition: 50.3 wt. % SiO_2, 17.4 wt. % Al_2O_3, 9.9 wt. % FeO_{tot}, 9.3 wt. % CaO, 5.8 wt. % MgO, 3.0 wt. % Na_2O, 1.0 wt. % K_2O, 3.5 wt. % H_2O, 0.50 wt. % CO_2, 2200 µg/g S, 1000 µg/g Cl, and 200 µg/g Cu. The sulphur was added in the form of anhydrite. Oxygen fugacity was buffered internally at $\log_{10} fO_2 \approx$ FMQ + 2.0 by the partial reaction of anhydrite to monosulphide solid solution.

Scapolite was first discovered in slow-cooling experiments conducted at 1.0 GPa and 800-900 °C (Fig. 3.2-20). The stability field of scapolite was subsequently explored in seeded equilibrium crystallization experiments, in which the stability of scapolite could be unambiguously determined by the presence or absence of newly-grown, Ca- and S-rich scapolite (Fig. 3.2-21). A total of 22 slow-cooling and 11 equilibrium crystallization experiments yielded consistent limits of the scapolite stability field: at 1.3 GPa, scapolite is stable at 750-950 °C, at 1.0 GPa, it is stable at 800-900 °C, and at 0.7 GPa, it is stable only at 850 °C (Fig. 3.2-22). Quantitative phase maps of the 1.0 GPa slow-cooling experiments demonstrate that scapolite accounts for ~ 38 vol. % of the minerals that formed within the temperature interval of 900-800 °C.

The experimental results are supported by the presence of primary, igneous scapolite in natural, hornblende-rich lower crustal rocks found in Fiordland, New Zealand, and Mercaderes, southwestern Colombia, which formed under conditions of 850-1050 °C, 0.9-1.2 GPa, and 720-850 °C, 1.0-1.4 GPa, respectively. These conditions agree well with the stability field of igneous scapolite determined in the present study. Taken together, the available evidence suggests that scapolite could be a common mineral phase in arc magmas differentiating within the lower crust. This would explain why scapolite is common in lower crustal granulites, and why the S and C isotopic signature of these rocks is similar to that of mantle rocks rather than of sediments. The restricted P–T–X stability of scapolite implies that it readily decomposes during the delamination of scapolite-bearing arclogites into the mantle and thus may contribute to the generation of unusually oxidised, sulphur-rich mantle melts.

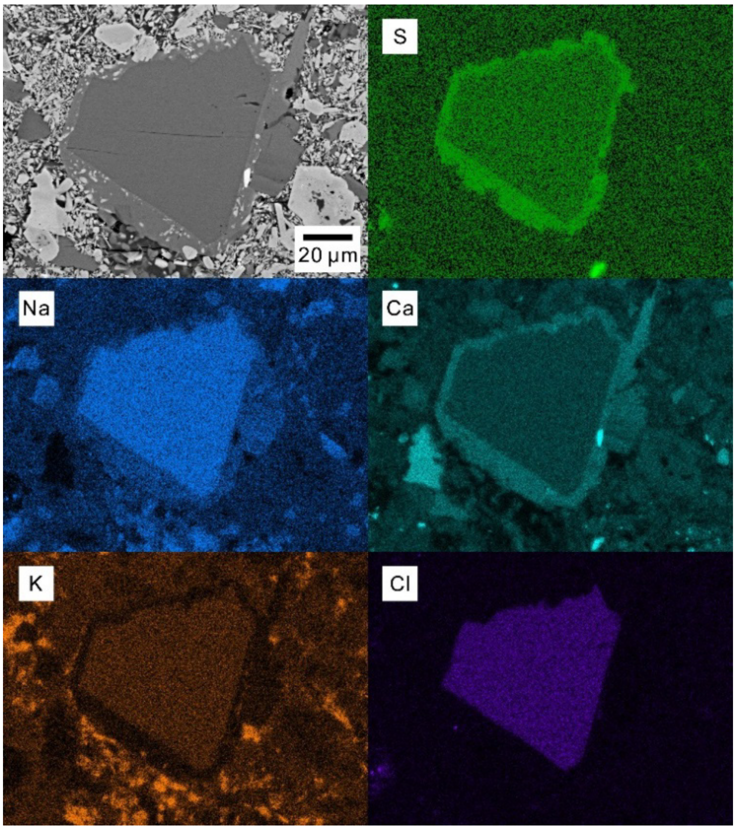

Fig. 3.2-21: BSE image and SEM-EDS element distribution maps of a scapolite overgrowth structure in experiment YQscp09. The core represents a Cl-rich scapolite seed, and the rim corresponds to newly formed, S-rich scapolite.

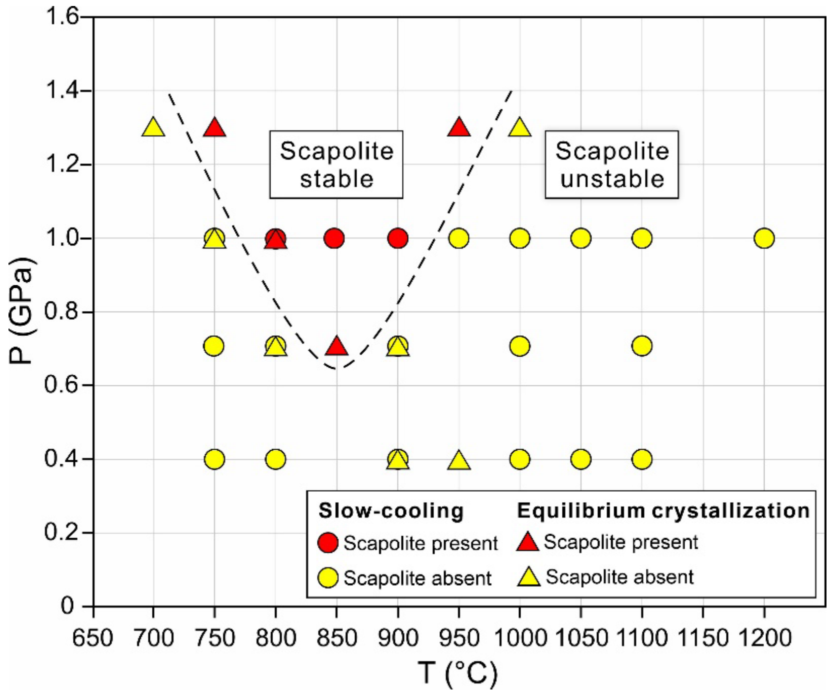

Fig. 3.2-22: P–T stability field of scapolite in the investigated arc basalt composition.

n. *From subducted sediments to arc magmas: Experimental insights on Cu, Zn, Mo and W mobility in subduction zone fluids (M. Hlede, A. Audétat and H. Keppler)*

Many of the geochemical signatures found in arc magmas are sourced from the subducting slab. However, the mechanisms involved in this transport are still being debated. Slab melting was often proposed as a main cause. However, slabs may not reach temperatures high enough for melting to occur, and recent studies at BGI have shown that geochemical slab signatures can be mobilised by saline dehydration fluids. In the field of mineral exploration, the spatial and chemical association between subduction zones and porphyry copper deposits has long been known. However, the primary source of the metals in these large-scale deposits is still debated. One promising candidate are the oceanic sediments that get subducted together with the slab. These sediments are enriched in many of the metals found in porphyry deposits, with a particular strong enrichment of Mo in reduced black shales. In this study we explore whether saline fluids that result from the dehydration of the slab are capable of mobilizing trace metals (Cu, Zn, Mo and W) found in the subducted sediments, resulting in an enrichment in the arc magmas.

The goal of these experiments was to equilibrate a starting material of subducted sediment composition (a glass of GLOSS composition, doped with trace amounts of Cu, Zn, Mo and W) and saline solutions at slab-dehydration conditions (600 - 700°C, 2.5 - 4.5 GPa), and to determine the fluid/sediment partitioning coefficients ($D^{fluid/sediment}$) for the studied metals. Experiments were carried out with automated end-loaded piston cylinder presses to precisely control the compression, decompression and heating of the charges. We employed Pt capsules with an inner liner of Cu foil to avoid partitioning of the trace metal into the walls. Capsules were loaded with a charge consisting of the GLOSS powder, the solution and a central layer of diamond powder. This highly porous layer served to trap the fluid during the experiment, allowing us to freeze it afterwards and to analyse it separately from the solid. For the piston cylinder experiments, ½” MgO-NaCl assemblies were used. Compression and decompression were programmed to occur automatically and very slowly to avoid fracturing of the capsule and loss of the fluid. Furthermore, a temperature cycling around the target temperature was implemented to enhance crystal growth via the effect of Ostwald ripening. After the experiments, the retrieved capsules were weighed to check for fluid loss and stored in a freezer until the analysis day. They were then cut in half and the diamond trap layer was analysed by LA-ICP-MS to recover the fluid composition. Afterwards, SEM mapping was performed, which helped to better navigate the sample during mineral analysis via EMPA (for major elements) and LA-ICP-MS (for trace elements). The individual $D^{fluid/mineral}$ were then combined into a single bulk $D^{fluid/sediment}$ by calculating the mineral fractions using a mass-balance least-square calculation. In addition, some reversed experiments with trace metals doped into the fluid were performed at key salinities to check whether chemical equilibrium was really achieved.

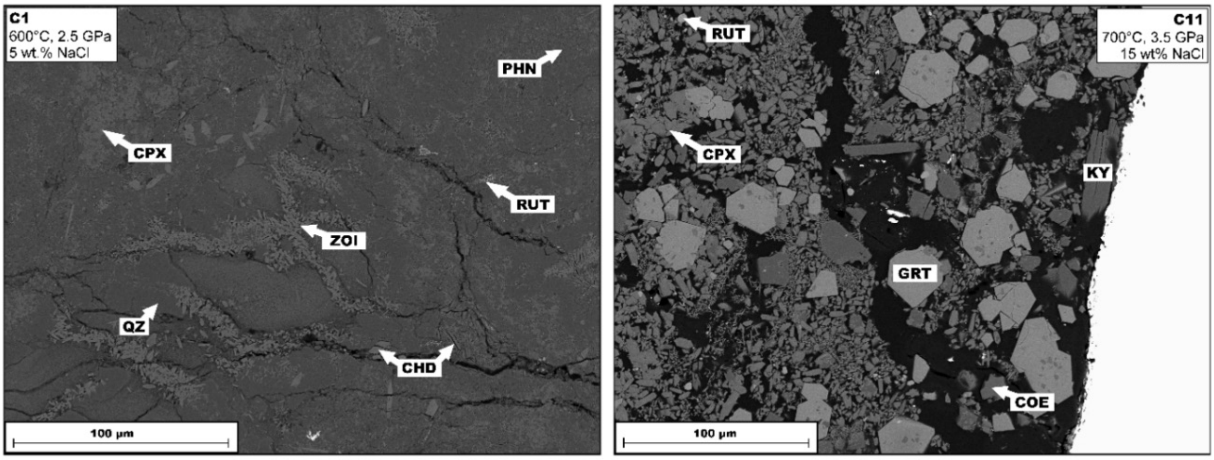

Fig. 3.2-23: Representative backscattered electron images of the phase assemblage at different conditions. Abbreviations: Cpx – clinopyroxene, phn – phengite, qz – quartz, zoi – zoisite, chd – chloritoid, rut – rutile, grt – garnet, coe – coesite, ky – kyanite.

The post-experiment mineral assemblage reflected that of a metasomatised sediment. At 600 °C and 2.5 GPa, the resulting phases were quartz, clinopyroxene, zoisite, chloritoid and phengite. At higher pressures, the assemblage turned to coesite, clinopyroxene, garnet, lawsonite/kyanite, phengite (Fig. 3.2-23). In addition, most of the samples contained minor amounts of accessory rutile, and some of them showed the formation of scheelite and, in one case, staurolite. The results show that the fluid/melt partitioning of Cu and Zn is always enhanced by salinity, while for Mo and W, such an effect is only seen at the highest pressure of 4.5 GPa (Fig. 3.2-24). There are some prominent outliers from these general trends. For zinc, we note the formation of staurolite at 700 °C, 4.5 GPa and 15 wt. % NaCl. Since staurolite very effectively incorporates Zn (up to 3 wt. %), this results in the bulk fluid/sediment partitioning coefficient being unusually low for this particular experiment (see Fig. 3.2-24). Similarly, we observed the formation of Mo-rich scheelite, $Ca(W_{1-x}Mo_x)O_4$, in two experiments at 600 °C, 2.5 GPa, 15 wt. % NaCl, and 700 °C, 3.5 GPa, 15 wt. % NaCl. This resulted in the sequestration of most of the Mo and W contained in the sample (see Fig. 3.2-24). Both the formation of staurolite and of scheelite may have been induced by the relatively high Zn and W concentrations in the starting materials and therefore, these "abnormal" runs may not be representative for natural sediments. Overall, our results show that saline subduction fluids are highly efficient in mobilizing metals, suggesting that during the subduction history of the slab, some ore-forming metals will be leached from the sediments and transported to the melting zone in the mantle. In particular for elements such as Mo that are strongly enriched in sediments, subducted sediments may indeed serve as a primary source for metal enrichment in arc magmas.

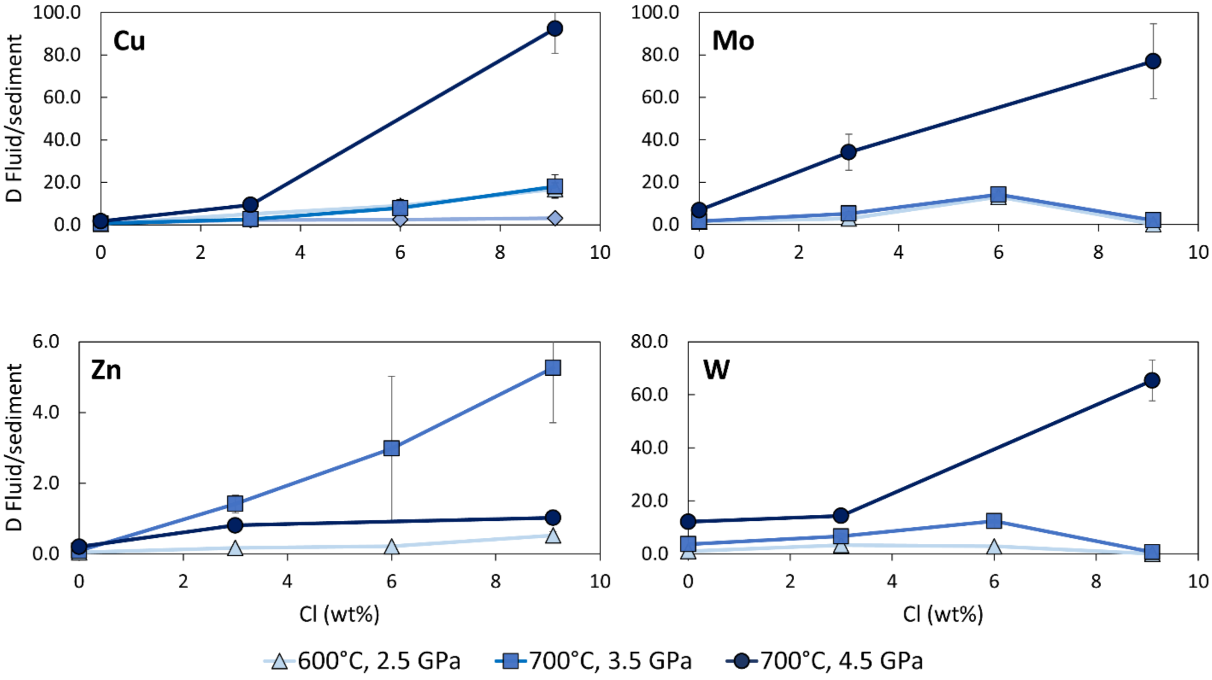

Fig. 3.2-24: Summary of bulk fluid/sediment partitioning coefficients for Cu, Zn, Mo and W at different P-T conditions plotted against the Cl concentration in the fluid. Uncertainties are given as one standard deviation.

o. *Garnet dating to constrain the tectonic setting of porphyry copper deposit formation (H. Bain/Bristol, F. Cooper/London, A. Bouvier and N. Roberts/Keyworth)*

Copper is primarily sourced from porphyry copper deposits (PCDs), which are magmatic-hydrothermal systems typically formed above subduction zones within compressional arcs.

However, the tectonic controls on precisely where and when they form within an arc are poorly understood. Clustering of PCDs in space and time implies that tectono-magmatic controls play an important role. If better constrained, these controls could be valuable to guide exploration efforts, particularly during preliminary, terrane-scale investigations.

In the copper-rich Laramide Porphyry Province (LPP) of Arizona, most PCDs are thought to have formed over a 20 Myr period (~ 75-54 Ma), synchronous with a relaxation of contractional stress that was produced at the onset of flat-slab subduction. However, in the adjacent Northern Great Basin (NGB: Nevada-Utah-Idaho), a lower copper endowment and longer, episodic history of PCD formation (~ 170-24 Ma) suggests the tectonic controls must have been different. To explain this difference and resolve the tectonic settings of PCD formation in the NGB, we compare the spatial-temporal history of crustal contraction, relaxation, and extension, to the distribution of PCDs. To avoid the widespread post-Laramide Basin and Range extension that overprinted much of the earlier deformational history, we focus on the pre-extensional deformation fabrics and metamorphic assemblages preserved within two exhumed metamorphic core complexes.

The two core complexes expose metapelites of upper-greenschist to amphibolite facies, which often contain metamorphic garnet. As garnet typically grows during burial and prograde metamorphism, the age of garnet growth can be used to constrain the timing of crustal contraction. As garnets grow, they incorporate rare earth elements into their structure, hence the decays of ^{176}Lu to ^{176}Hf, and ^{147} Sm to ^{143}Nd can be used to date garnet growth.

Three samples were selected for garnet dating: two from the Northern Snake Range (NSR), FEM113 and FHe253, and one from the Raft River – Albion – Grouse Creek Mountains (RAG), HB-ID22HC3.

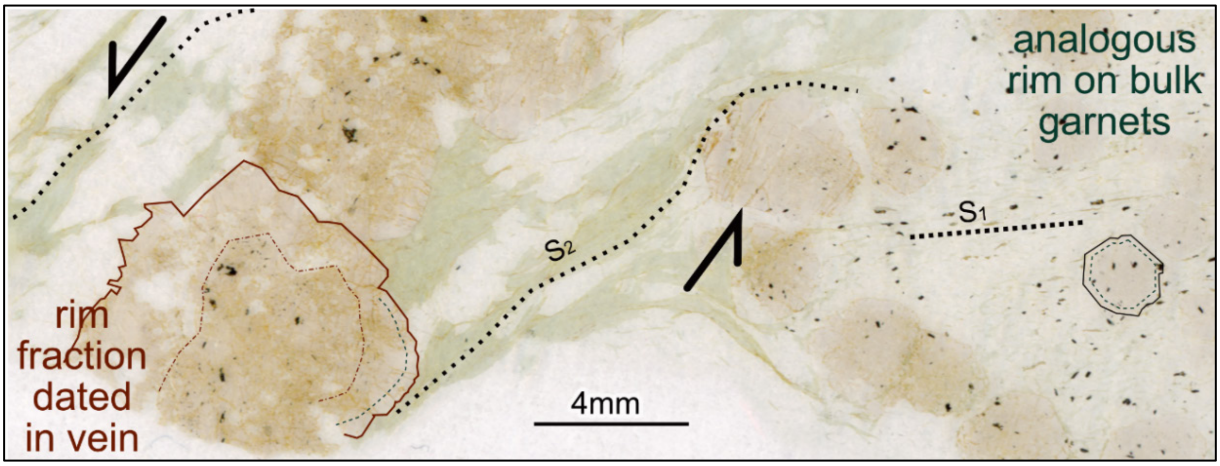

Fig. 3.2-25: Scan of thin section of sample ID22HC3 showing vein garnets on the left and wall-rock garnets on the right. Annotations show the rims on the garnets, and the fabrics in the wall rock (S1) and vein (S2).

Garnets previously dated to 138-132 Ma in the RAG have a distinct core-rim texture, and it is not clear whether the previous dates are the timing of burial, or an average of garnet core and rim ages (of *e.g.*, 150 Ma and 85 Ma). Sample ID22HC3 contains garnets of analogous texture and chemistry to those previously dated, along with large hydrothermal vein garnets (Fig. 3.2-25).

Crushed garnet mineral separates and garnet-free whole rock fractions were prepared at the University of Bristol. *In situ* trace element concentration profiles for the garnets were previously collected by LA-ICPMS at the British Geological Survey in Keyworth. Sample dissolution, column chemistry and measurement were performed at the BGI, following an established isotope dilution protocol using mixed enriched spikes ^{176}Lu-^{180}Hf added to garnet and whole-rock samples. Isotopic measurements of Sm, Nd, Lu+Yb and Hf were carried out on the Neoma MC-ICPMS/MS with an Apex Omega nebulisation system for sample introduction.

All three garnets did not have a sufficient spread in Sm/Nd to provide a significant isochron age. This is likely due to monazite and xenotime inclusions and/or limited Sm/Nd fractionation in dissolved garnet fractions. The two NSR samples, FEM113 and FHe253, both give garnet growth Lu-Hf ages within error: 105.6 ±3.9 Ma and 104.6 ±0.83 Ma respectively (Fig. 3.2-26). The ~ 105 Ma age likely represents the age of the midpoint of continuous garnet growth.

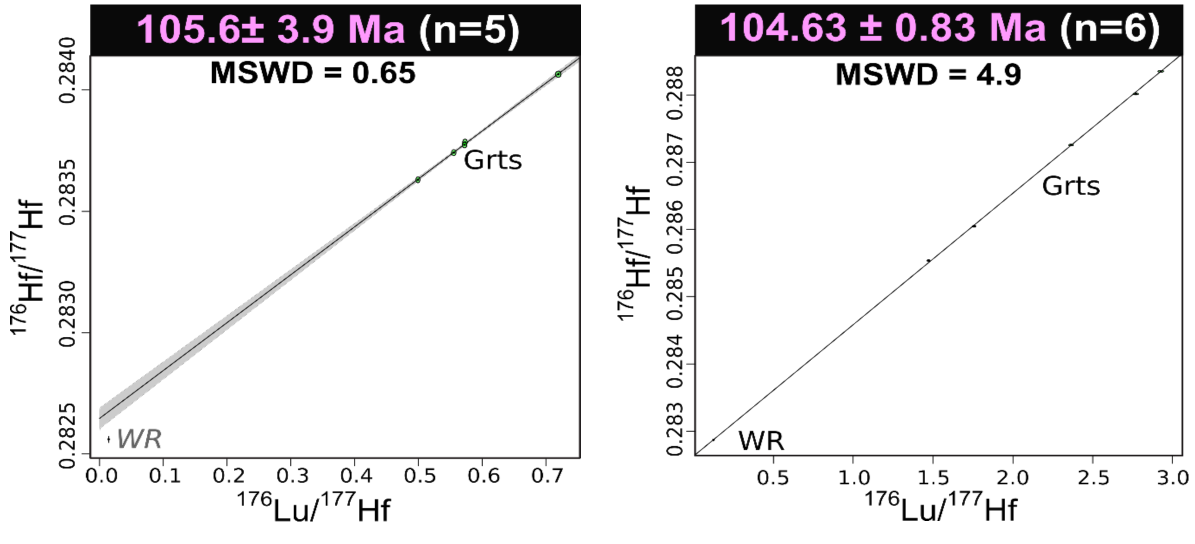

Fig. 3.2-26: Lu-Hf isochrons for the NSR samples. Left, FEM113 including garnet fractions G1-5 only and showing how the WR fraction falls below the line: Right, FHe253 including WR and G1-5.

The Lu-Hf date of RAG ID22HC3 is 125.3 ±12.6 Ma (MSWD=25), which is interpreted as the age of garnet rim growth. The lower precision within this sample likely comes from the mixing between the two clear rim phases: (a) the orange "inner rim" which is high in Ca and Mn, and low in REE, and (b) the bright pink "outer rim" which has higher Fe and Mg, and is high in

REE. This result supports the suggestion that the ~ 138-132 Ma garnet dates are an average of an older core and younger rim.

The garnet ages in the NSR suggest contraction-related burial of samples FEM113 and FHe253 at 105 Ma. This age fits well with published geochronology, to date the whole metamorphic cycle: (1) the start of burial at ~ 120 Ma as constrained by the timing of initiation of xenotime breakdown, (2) continued burial and garnet growth between 105 and 88 Ma (3) peak metamorphism at the end of burial, represented by ~ 78 Ma U-Pb dates of metamorphic monazite and zircon.

The timing of contraction these garnet dates constrain in the NSR is coincident with the timing of slip on the Willard thrust fault, which is along-strike northwards from the fold-thrust belt proposed to have formerly overlain the NSR. Low-temperature thermochronology constrains slip on this fault to be mainly between 125-90 Ma. This is also the age of the formation of the Ely-Robinson PCD, which is dated by K-Ar to between 123-109 Ma. Our new garnet ages therefore suggest that this PCD may have formed during crustal contraction. This is unusual for PCDs in the NGB, as most are seen to form synchronous with extension in the metamorphic core complexes, or synchronous with peak metamorphism associated with relaxation of contractional stresses. If the Ely PCD formed early during crustal thickening, it is a tectonic outlier amongst PCDs, and therefore very interesting.

p. *Marine chemical sedimentary protoliths determined for* ca. *3.71 Ga calc-silicate schists and quartzites from the Isua Supracrustal Belt (M. Zawaski and N. Kelly/Boulder, J. Marin-Carbonne, A. Ulianov and A.-S. Bouvier/Lausanne, and S.J. Mojzsis)*

Foliated calc-silicate schists and quartzites (Fig. 3.2-27) from a *ca.* 3.71 Ga domain within the northeastern part of the Isua Supracrustal Belt (southern West Greenland) may be interpreted as either deformed layered "metasedimentary" rocks, or the metasomatic fluid alteration products of a deformed mafic igneous precursor (*i.e.*, basaltic protolith). One important reason for protolith assignment in this case stems from the debated claim that these are originally clastic sedimentary rocks which host the oldest interpretable bio-mediated sedimentary structures (cf. "stromatolites"). To determine the protolith, we used correlated mineralogical, outcrop- and regional-scale structural, and *in situ* major-, minor- and trace-element geochemical analyses coupled with high spatial resolution Si, O, and S isotope measurements. We conclude the protoliths were sedimentary chemical precipitates with a minor detrital clay fraction. This interpretation is bolstered by the low levels of generally immobile elements (Zr, Cr, Y, Ti, and P), which rule out either a purely igneous or clastic sedimentary origin. Further evidence for a sedimentary origin includes heterogeneous Si and O isotopes and mass-independent S isotope values (Δ33S > 0, S-MIF), along with rare earth element (REE + Y) signatures that show light REE-depletion in PAAS normalised REE patterns and seawater-like Y/Ho. Pervasive deformation has masked or obliterated most if not all primary sedimentary structures, such that no chemical or physical features can be reliably used as indicators for (shallow) water depth at time of deposition. Although we conclude these rocks are of sedimentary origin we reiterate that the nabla-shaped (∇) features found within them are not biogenic stromatolites. Instead, evidence points towards their formation as products of local and regional strain and recrystallization, long after deposition.

Fig. 3.2-27: Outcrop photograph of complexly folded and foliated calc-silicate schists and quartzites from the *ca.* 3.8 Ga Isua Supracrustal Belt in southern West Greenland. (yellow field notebook is approximately 8 x 10 cm).

3.3 Mineralogy, Crystal Chemistry, and Phase Transformations

The phase relations and crystal structures of minerals determine how chemical elements are distributed and exchanged over length scales that range from the atomic interfaces between mineral grains to the geophysical subunits of the Earth's interior. Key elements that are often only present in minor or even trace amounts may stabilise compounds with uncommon crystal structures or alter the properties of rock-forming minerals if incorporated into their crystal structures. The contributions in this section focus on the stabilities and crystal-chemical properties of minerals and high-pressure compounds that may have affected the distribution of such key elements in the Earth's interior by processes that span from the Earth's accretion and differentiation to modern-day subduction and deep recycling of volatiles.

The first four contributions in this section highlight the diversity of boron, carbon, and hydrogen-bearing minerals and compounds at high pressures and temperatures. Inspired by inclusions of borate minerals in natural diamonds, Antunes *et al.* synthesised a novel Mg-borate compound and determined the crystal structure of this compound as a function of pressure. Featuring both planar BO_3 groups and BO_4 tetrahedra at lower pressures, the framework of borate groups in the crystal structure of the new Mg-borate gradually rearranges into a purely tetrahedral framework with increasing pressure. The organic mineral whewellite has been found as an inclusion in zircon and contains organic oxalate anions that may form in subduction zone fluids by abiotic processes. To determine the stability limit of whewellite along a typical subduction geotherm, Czekay and Keppler performed experiments in piston-cylinder presses and found whewellite to decompose into a mixture of graphite, carbonate minerals, and CO_2 even at relatively low pressures and temperatures, which may indicate a limited stability of oxalate anions at the pressures and temperatures of the experiments. At much higher pressures, carbon forms tetrahedral $[CO_4]^{4-}$ carbonate groups with four coordinating oxygens. Among the products of their experiments with laser-heated diamond anvil cells, Pantousas *et al.* found two new high-pressure carbonate phases. The crystal structures of these phases are based on an extended three-dimensional framework and helical chains of $[CO_4]^{4-}$ carbonate groups, respectively. These findings point to a remarkable structural diversity of tetrahedral carbonates that may, to some extent, resemble the structural diversity of silicate minerals. Like carbon, hydrogen is a volatile element that may be incorporated into high-pressure compounds and, in this way, stored in materials of the Earth's deep interior. When heating a range of iron-bearing starting materials in laser-heated diamond anvil cells, Yuan *et al.* discovered two new iron oxyhydroxide phases with iron cations in eight and nine-fold coordination. Given their high densities and thermal stabilities, Yuan *et al.* suggest that these oxyhydroxides may have crystallised from a basal magma ocean and have since then retained hydrogen in the Earth's lowermost mantle.

The phase transition in Ca-rich silicate perovskite, davemaoite, may affect the physical properties in the deep mantle from the transition zone to the lower mantle. Wu *et al.* studied the phase transition of the $CaSiO_3$-$CaTiO_3$ solid solution to understand the behaviour of calcium silicate perovskite in the Earth's lower mantle with single crystal X-ray diffraction and the analysis of possible twinning relations. Twinning in Ti-bearing calcium perovskites may originate from a phase transformation upon cooling that is accompanied by a reduction in crystal symmetry. Not only solids but also liquids may show first-order phase transitions under extreme high-pressure conditions. Niu *et al.* investigated liquid-liquid phase transformations of elemental sulphur by conducting *in situ* structural measurements at high pressures and high temperatures using synchrotron X-ray diffraction in a multianvil press. Their refined melting curve and structural data offer a high-precision experimental benchmark for understanding thermodynamics and interpreting the phase behaviour of sulphur-bearing systems in the interiors of planets such as Mars.

The direct visualisation of atomic columns is one of the most powerful tools to understand the atomic structure of minerals. Recent developments to correct for spherical aberration in scanning transmission electron microscopy (STEM) raise the potential of high-angle annular dark field (HAADF) imaging. Using advanced STEM corrected for spherical aberration and complementary *ab initio* calculations, Yao *et al.* visualised long-range modulations in a uranium-bearing hematite superstructure. Their model of a relaxed superstructure of hematite yields good agreement with the STEM-HAADF observation. Using a similar technique of high-resolution STEM, Miyajima *et al.* inspected the interface between a diopside crystal from a natural peridotite and an amphibole lamella that is intergrown into the crystal. The high-resolution STEM images of the interface reveal a layer with a thickness of only a few nanometres that extends along the interface and has an atomic structure similar to the mineral talc. The structure of the interface can be described by a topotactic sequence of pyroxene and mica modules as defined by J. B. Thompson for 'biopyriboles'.

Precise measurements of water contents in anisotropic minerals are required to understand the distribution of water in the Earth's interior. To improve the precision of water contents determined by infrared absorption spectroscopy, Withers and Zhang propose a new approach to analyse the anisotropic absorption of infrared radiation by minerals with different symmetry classes. They tested their model by collecting polarised and unpolarised spectra of a non-principal plane of olivine and compared the experimental spectra with model predictions. The model further predicts uncertainties for unpolarised measurements on crystals with different symmetry classes and optical properties. Iron meteorites sample the metallic cores of differentiated planetary bodies and provide important information on planetary formation. Zhao *et al.* classified the Wedel IAB complex iron meteorite based on mineralogical and chemical investigations using electron probe microanalysis and laser ablation inductively coupled plasma mass spectrometry (LA-ICP-MS) analyses. In the meteorite, they found the rare iron-nickel-phosphide mineral schreibersite and determined a new crystal structure for this mineral that is characterised by an ordered distribution of Ni.

a. *Synthesis and structural characterisation of high-pressure Mg and Ca borates (A. Antunes, Y. Yin, A. Chanyshev, T. Boffa Ballaran and L.S. Dubrovinsky)*

Boron is known to exist in the Earth's deep interior as evidenced by the presence of B-doped blue diamonds. Recently, inclusions of borate minerals, ludwigite and kotoite, have been discovered in natural diamonds, representing the first observation of such inclusions. Since carbonates are well-known carriers of carbon into the mantle, down to depths where diamonds are formed, this discovery raises an important question: Can reactions between carbonates and boron lead to the formation of borates at mantle depths? In this study, we investigated the potential reactions between carbonates and boron under high-pressure conditions. Using single-crystal X-ray diffraction (SCXRD), we identified the reaction products and characterised their crystal structures. In total, we synthesised 19 phases, including 15 new compounds, among which ten are novel high-pressure borate structures.

The compounds were synthesised using both multianvil (MA) and diamond anvil cell (DAC) techniques. Two BX90-type screw-driven DACs equipped with 250-µm culet diamonds were employed. The sample chambers were prepared by pre-indenting rhenium gaskets to a thickness of approximately 20 µm and laser-drilling a hole of 100 µm in diameter. DACs were loaded with $MgCO_3$ or $CaCO_3$ powders together with pure boron to explore possible reactions between magnesite or calcite and boron. Pressures up to 80 GPa (Mg system) and 60 GPa (Ca system) were achieved, and temperatures reached ~ 2000 K using an in-house laser-heating system. For the MA experiments, a mixture of $MgCO_3$ and boron in a 1:1 molar ratio was used. These runs were performed at 11 GPa and 20 GPa using 18/11 and 10/4 assemblies, respectively.

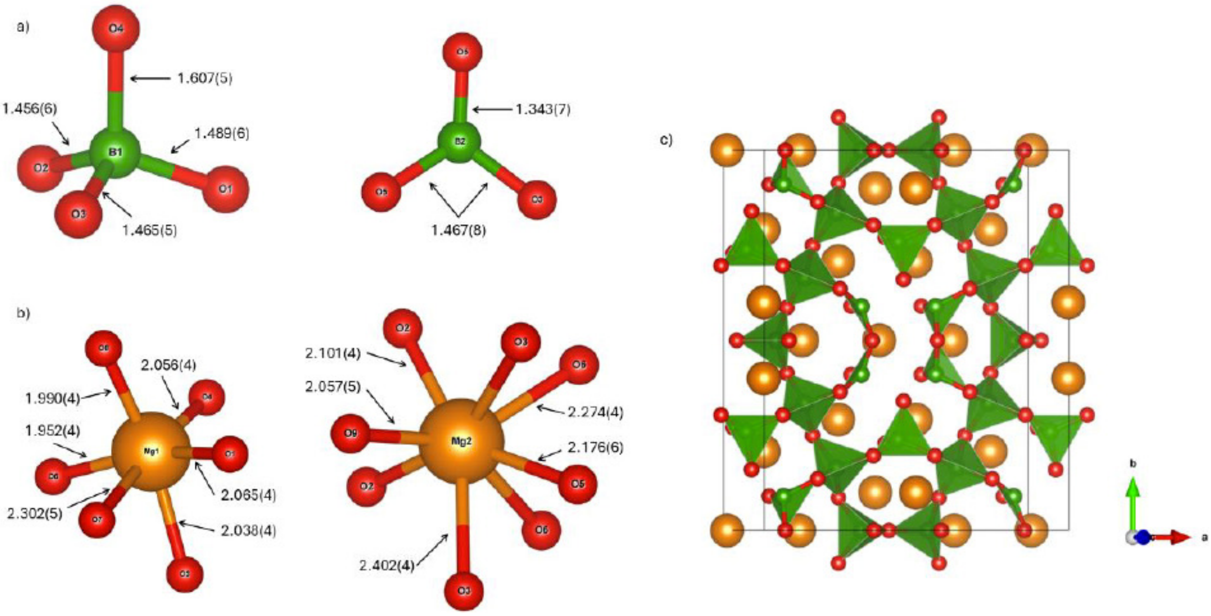

Fig. 3.3-1: Structure of *Cmm*2-$Mg_3B_4O_9$ at 20 GPa. (a) Boron atoms coordinated by four oxygen atoms forming tetrahedra (left) and by three oxygen atoms forming triangles (right). (b) Mg atoms in sixfold (left) and eightfold (right) coordination. Numbers indicate interatomic distances (Å). (c) Unit cell viewed along the *c*-axis.

SCXRD measurements on the recovered MA run products were conducted at the BGI, while synchrotron SCXRD measurements for the DAC experiments were carried out at the ESRF. Diffraction data were processed using our methodology for multi-grain, multi-phase samples with the DaFi program. Among the ten newly discovered structures, we identified $Mg_3B_4O_9$ crystallising in the orthorhombic system, space group *Cmm*2 (#35)**,** stable between 20 and 35 GPa. At 20 GPa, boron atoms exhibit two coordination environments, forming both BO_3 triangles (with B–O distances of 1.343(7) and 1.467(8) Å) and BO_4 tetrahedra (1.348(9) to 1.465(9) Å) (Fig. 3.3-1). Upon compression to 35 GPa, the BO_3 groups transform into BO_4 tetrahedra, with B–O bond lengths of 1.589(14), 1.354(4), 1.464(18), and 1.419(19) Å (Fig. 3.3-2). Consequently, only tetrahedrally coordinated boron remains at high pressure.

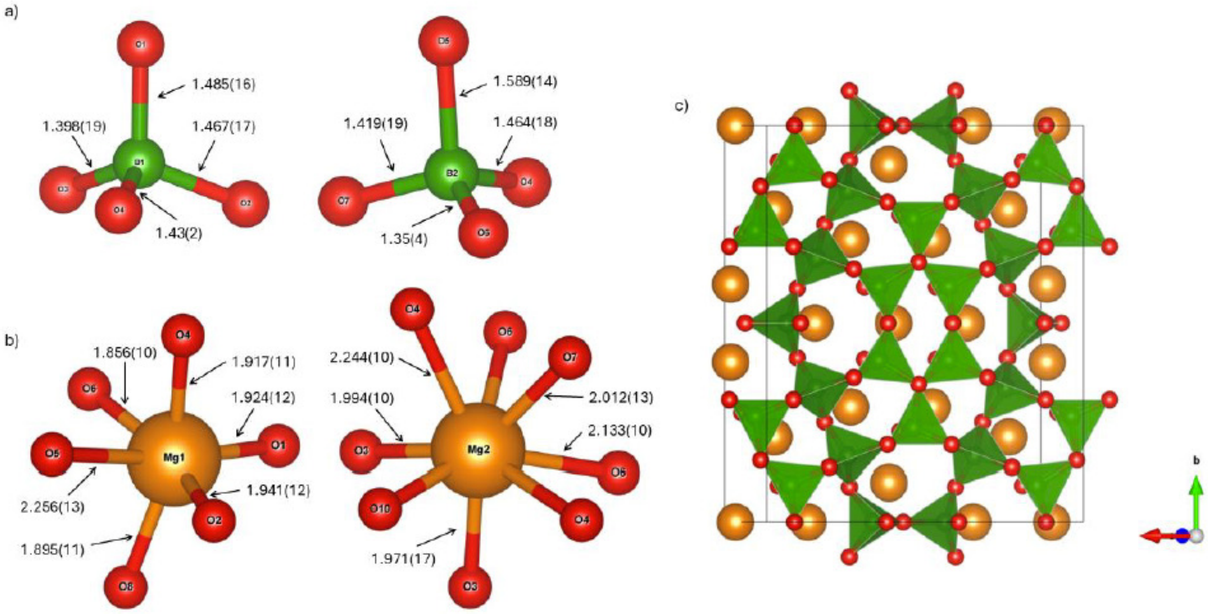

Fig. 3.3-2: Structure of *Cmm*2-$Mg_3B_4O_9$ at 35 GPa. (a) Boron atoms coordinated by four oxygen atoms forming tetrahedra. (b) Mg atoms in sixfold (left) and eightfold (right) coordination. Numbers indicate interatomic distances (Å). (c) Unit cell viewed along the *c*-axis.

b. *Piston cylinder experiments on the stability of whewellite, an organic mineral, in subduction zones (L. Czekay and H. Keppler)*

Recent theoretical studies have proposed that organic anions may be abundant in high-pressure subduction zone fluids. Moreover, whewellite ($CaC_2O_4{\cdot}H_2O$), an organic mineral, has been identified as an inclusion in zircon from high-pressure metamorphic rocks related to subduction. Its stability under high-pressure and high-temperature conditions is of great interest as it may support the abiotic formation of carbon-bearing compounds and affect the deep carbon cycle. To test these predictions, we performed both *in situ* Raman spectroscopic experiments in an externally heated diamond cell and *ex situ* piston-cylinder experiments at temperatures up to 600 °C and pressures up to 3.5 GPa.

Our previous experiments using an externally heated diamond anvil cell at temperatures up to 500 °C and pressures up to 1.5 GPa first demonstrated that whewellite crystals may persist, potentially as a metastable phase, up to 300 °C and 1.5 GPa. However, Raman spectra indicated the presence of graphitic carbon in the sample chamber. The graphite must have formed through the partial decomposition of whewellite, indicating that the experimental conditions were close to the stability limit of this phase.

Building on this observation, piston cylinder experiments were conducted along a typical subduction geotherm in order to further investigate the stability of whewellite. For this purpose, powdered whewellite synthesised by hydrothermal annealing of amorphous calcium oxalate monohydrate was loaded with water in a gold capsule. The experiments were conducted at 2 to 3.5 GPa and 300 to 600 °C with run durations of up to 26 days. The gold capsules were used to minimise chemical reactions between the sample and the capsule material. This contrasts with Pt capsules, where the capsule material may form alloys with carbon. Gold also provides a slower diffusion pathway for hydrogen, allowing the redox state within the capsule to be maintained over a longer duration. This ensured that the internal experimental conditions remained as stable as possible throughout the run, with oxygen fugacity being intrinsically buffered by the whewellite itself. In some experiments, outer Pt-Rh capsules were used to stabilise the soft inner gold capsule.

After opening the capsules, gas and liquid were released and the originally white whewellite powder had been transformed into a grey to dark grey powder. The colour of the sample suggested the presence of graphitic carbon. Even at the lowest temperatures and pressures, the escape of gases and liquids from the capsule upon opening indicated that the conversion of the starting material had already occurred under these conditions. This observation suggests that the whewellite decomposition begins at relatively low *P-T* conditions. The obtained samples were analysed using Raman spectroscopy. As illustrated in Figure 3.3-3, the resulting spectrum reveals whewellite to have decomposed into aragonite and graphite as the predominant phases. In addition, small amounts of calcite were detected in some samples. No further phase change was observed at higher temperatures and pressures. Additionally, powder diffraction analysis confirmed the presence of aragonite as the main crystalline phase.

These findings indicate that whewellite underwent decomposition according to the reaction 2 CaC_2O_4 = 2 $CaCO_3$ + CO_2 + C (graphite). The decomposition of whewellite releases a substantial amount of CO_2. It is possible that some of the $CaCO_3$ dissolved in the CO_2-containing water under high pressure and subsequently precipitated as calcite when the capsules were opened and the sample was dried at room temperature. This could explain the presence of small amounts of calcite together with the abundant aragonite, which is the stable phase of $CaCO_3$ at run conditions.

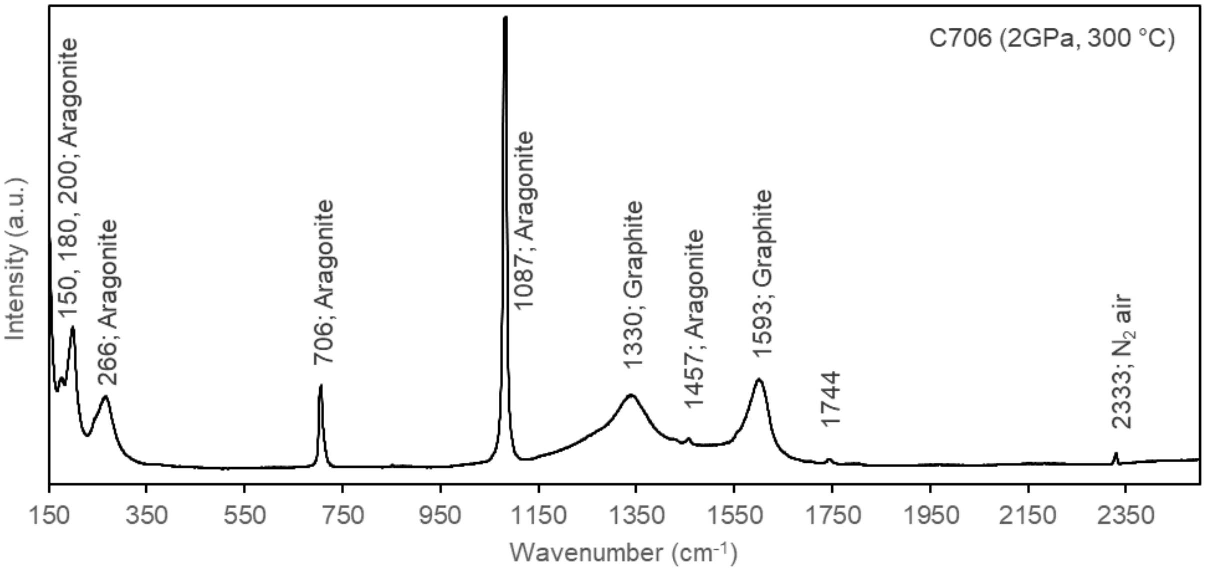

Fig. 3.3-3: Raman spectrum of the run product from a piston cylinder experiment at 300 °C and 2 GPa. The spectrum shows that whewellite decomposed to form aragonite, CO_2 gas, and graphite.

c. *Tetrahedral frameworks and helical chains: oP32–CaC_2O_5 and mP80–$CaCO_3$ calcium carbonates above 100 GPa (A. Pantousas, G. Aprilis/Grenoble, A. Aslandukova/Frankfurt a. M., I. Kupenko/Grenoble, X. Li/Münster, S. Müller/Münster, W. Zhou, P. Leveque/Nantes, M. Hanfland/Grenoble, L.S. Dubrovinsky and A. Pakhomova/Grenoble)*

Recent advances in the exploration of carbonates have established their high-pressure crystal chemistry as mainly based on carbon in the sp^3 configuration. Such carbonates, built upon isolated or vertex-sharing CO_4 tetrahedra, reveal striking structural diversity. Despite extensive research, synthesis of layered or framework carbonates remained a long-standing challenge. Herein, we report on the synthesis and full structural characterization of a novel carbonate, oP32 CaC_2O_5, obtained at 122 GPa and 2800 K in a laser-heated diamond anvil cell. The crystal structure of oP32 CaC_2O_5 is based on a vertex-sharing tetrahedral framework. In addition, mP80 $CaCO_3$ was obtained at the same conditions, featuring pyroxene-like chains of vertex-sharing tetrahedra. In contrast to previously reported experimentally observed or theoretically proposed $CaCO_3$ phases, our single-crystal X-ray diffraction data revealed that the structure of mP80 $CaCO_3$ features both clockwise and counterclockwise helical chirality of the pyroxene-like chains. *Ab initio* calculations support our experimental findings and indicate the thermodynamic stability of oP32 CaC_2O_5 and mP80 $CaCO_3$ in the megabar pressure range.

In the Ca-C-O system a variety of sp^3-carbonates has been proposed in the literature to exist at elevated pressures based on *ab initio* simulations and with different stoichiometries, *i.e.*, $CaCO_3$, Ca_2CO_4, Ca_3CO_5, and CaC_2O_5, and arrangements of CO_4 tetrahedra. These predictions inspired us for the experimental re-investigation of the Ca-C-O system at high pressures using cutting-edge experimental techniques. The experiments were performed at high pressure (122(2) GPa) and high temperature (2800(100) K) using a laser-heated diamond anvil cell. A crystal of FeO, sandwiched between pellets of a $CaSiO_3$–$CaCO_3$ mixture served as starting material. *In situ*, multi-grain, single-crystal X-ray diffraction at the beamline ID15b of the European Synchrotron Radiation Facility allowed the identification of products of the reaction and the resolution of their crystal structures. Two new compounds of calcium carbonates were identified in the process.

The novel CaC_2O_5 compound crystalises in the orthorhombic space group $Pna2_1$ (#33) with a = 3.8643(9) Å, b = 13.342(3) Å, c = 3.6790(5) Å, and V = 189.68(7) Å^3 at 122 GPa. The carbon atoms are tetrahedrally coordinated, making it a prime example of a high-pressure sp^3-carbonate. The striking feature of the CaC_2O_5 crystal structure is the polymerization of the CO_4 tetrahedra into a three-dimensional framework in which each tetrahedron shares three vertices with adjacent tetrahedra (Fig. 3.3-4a). Topological analysis of the network of carbon atoms demonstrates that it is built on linked 10-membered loops as previously described in the literature for the silicon framework in the $ThSi_2$ structure. Therefore, the architecture of the carbon-based framework can be classified as a THS net.

Along with the oP32 CaC_2O_5, another novel sp^3-carbonate was synthesised in the same experiment. It has monoclinic symmetry with space group $P2_1/c$ (#14) and lattice parameters a = 3.2989(4) Å, b = 10.877(4) Å, c = 14.224(4) Å, β = 90.162(16)°, and V = 510.4(2) Å^3. The prominent feature of the mP80 $CaCO_3$ crystal structure are pyroxene-like chains of corner-sharing CO_4 tetrahedra that expand along the c-axis. The here-discovered novel phases of oP32 CaC_2O_5 and mP80 $CaCO_3$ advance our knowledge of the high-pressure crystal chemistry of carbonates.

Another interesting aspect of the current work is the stoichiometry of oP32 CaC_2O_5 as we present the successful synthesis of a new compound of high carbon content that incorporates two equivalents of carbon per formula unit. This allows for more efficient storage of carbon under high-pressure conditions with potential implications for the geochemistry of the Earth's lower mantle. When it comes to the mP80 $CaCO_3$ phase, the racemic model of the mP80 $CaCO_3$ phase allows us to accurately describe the conformation of the tetrahedral chains and points towards a structural complexity of chemically simple compounds in the megabar pressure range.

To summarise, the successful synthesis and characterization of the first framework metal carbonate oP32 CaC_2O_5 provide new ground on which the chemistry and high-pressure behaviour of carbon may be studied and constitutes an example of a high-carbon-content compound at extreme conditions. This phase may further host other metal cations with similar radii and coordination chemistry as Ca^{2+} such as Sr^{2+}, Ba^{2+}, or solid solutions of such cations. Together with previously reported predictions of similar structures and the interesting chiral polymorph mP80 $CaCO_3$, the here-discovered phases demonstrate that further study of carbonate systems at extreme conditions is warranted.

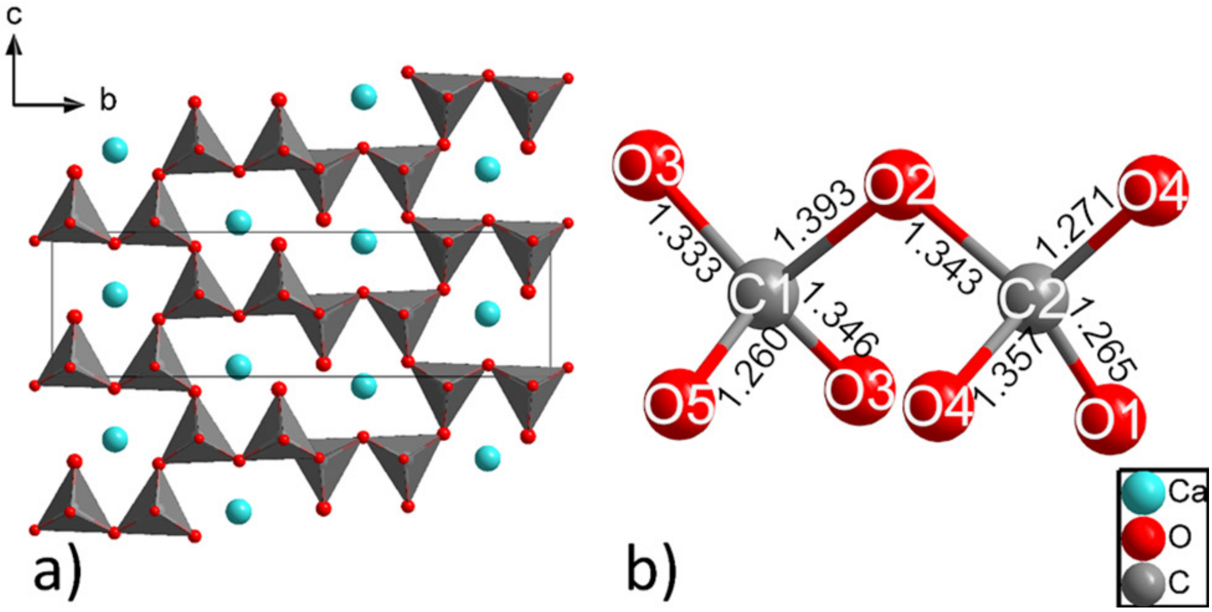

Fig. 3.3-4: (a) The crystal structure of the oP32 CaC_2O_5 carbonate at 122 GPa obtained from single-crystal structure solution. The framework of vertex-sharing CO_4 tetrahedra (shown in grey) is viewed along the *a*-axis. (b) The geometry of vertex-sharing $C1O_4$ and $C2O_4$ tetrahedra. Notably, the C–O bonds that do not participate in the formation of C–O–C bridges are quite shorter than the rest.

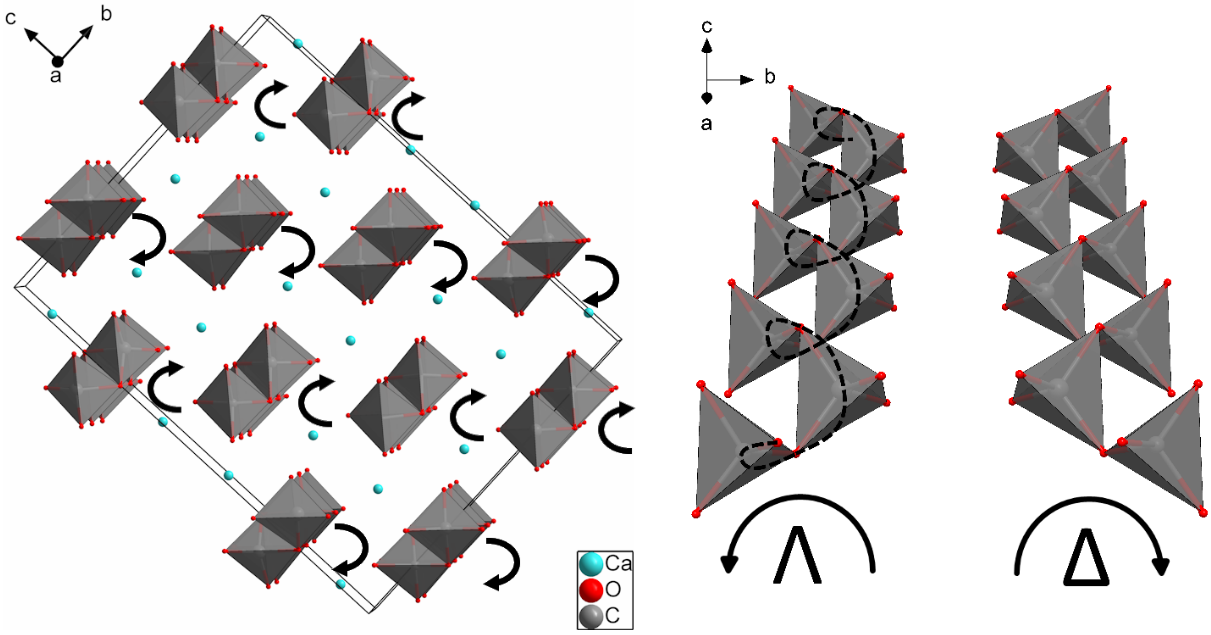

Fig. 3.3-5: The crystal structure of the mP80 $CaCO_3$ phase at 122 GPa obtained from single-crystal structure solution. The vertex-sharing CO_4 tetrahedra form spiraling chains along the *a*-axis. These chains extend along the C–O–C bonds and display helical chirality. The chains are grouped into alternating layers of clockwise (Δ) or counterclockwise (Λ) helices that expand along the $(01\bar{1})$ crystallographic plane.

d. *Deep-mantle iron oxyhydroxides as reservoirs of primordial and recycled water (H. Yuan and Q. Hu/Shanghai, L. Man, Y. Yin, R. Pierru, D.J. Frost and L.S. Dubrovinsky)*

Water profoundly influences the structure, dynamics, and chemical evolution of the Earth's mantle. However, identifying stable water-bearing phases under the extreme pressure-temperature conditions of the deep mantle remains a fundamental challenge. Conventional candidates face significant limitations: dense hydrous magnesium silicates require substantial alumina to survive at ambient mantle temperatures while hydrous silica phases may rise upwards due to their low density. Furthermore, the cubic FeO_2H_x phase is restricted by its requirement for highly oxidizing conditions and by its thermal instability in the hot lowermost mantle.

Here, we report the synthesis and characterization of two novel hexagonal iron oxyhydroxides, $Fe_5O_{12}H_x$ and $Fe_7O_{12}H_x$. Using laser-heated diamond anvil cell experiments at pressures of 78 to 198 GPa and temperatures of 2400 to 2800 K, these phases were synthesised from diverse starting materials ranging from synthetic orthopyroxene and FeO-enriched peridotite glass to simple oxides mixed with hydrous silica or retaining adsorbed moisture. Crystal structures were determined *in situ* via high-pressure single-crystal X-ray diffraction at synchrotron radiation sources (ESRF and DESY) while scanning transmission electron microscopy coupled with energy dispersive X-ray spectroscopy of recovered samples was employed to constrain chemical composition. Structural analysis revealed that both compounds feature rigid frameworks of hyper-coordinated FeO_8 or FeO_9 polyhedra that create large channels partially occupied by iron where oxygen atoms provide favorable sites for significant hydrogen incorporation (Fig. 3.3-6). Indeed, stoichiometric constraints based on charge balance and a thermodynamic volume additivity model establish lower bounds of $x \geq 9$ for $Fe_5O_{12}H_x$ and $x \geq 3$ for $Fe_7O_{12}H_x$. Crucially, these iron oxyhydroxides are stable in coexistence with all major minerals of a pyrolitic lower-mantle assemblage, including bridgmanite, post-perovskite, ferropericlase, and davemaoite.

The high density and thermal stability of these phases suggest that they may potentially play a role in the Earth's deep water cycle. We hypothesise that if such dense Fe-O-H phases crystallise during the solidification of a basal magma ocean, they might segregate from residual melts and chemically anchor primordial water at the base of the mantle. Gravitational accumulation of these phases could theoretically contribute to the formation of dense structures, such as the roots of ultralow-velocity zones. Furthermore, the introduction of iron and water via subducted lithologies might provide a pathway to stabilise these oxyhydroxides to the present day. These findings extend our understanding of deep-mantle water storage beyond the limits of nominally anhydrous minerals, offering a potential mineralogical candidate for deep volatile reservoirs.

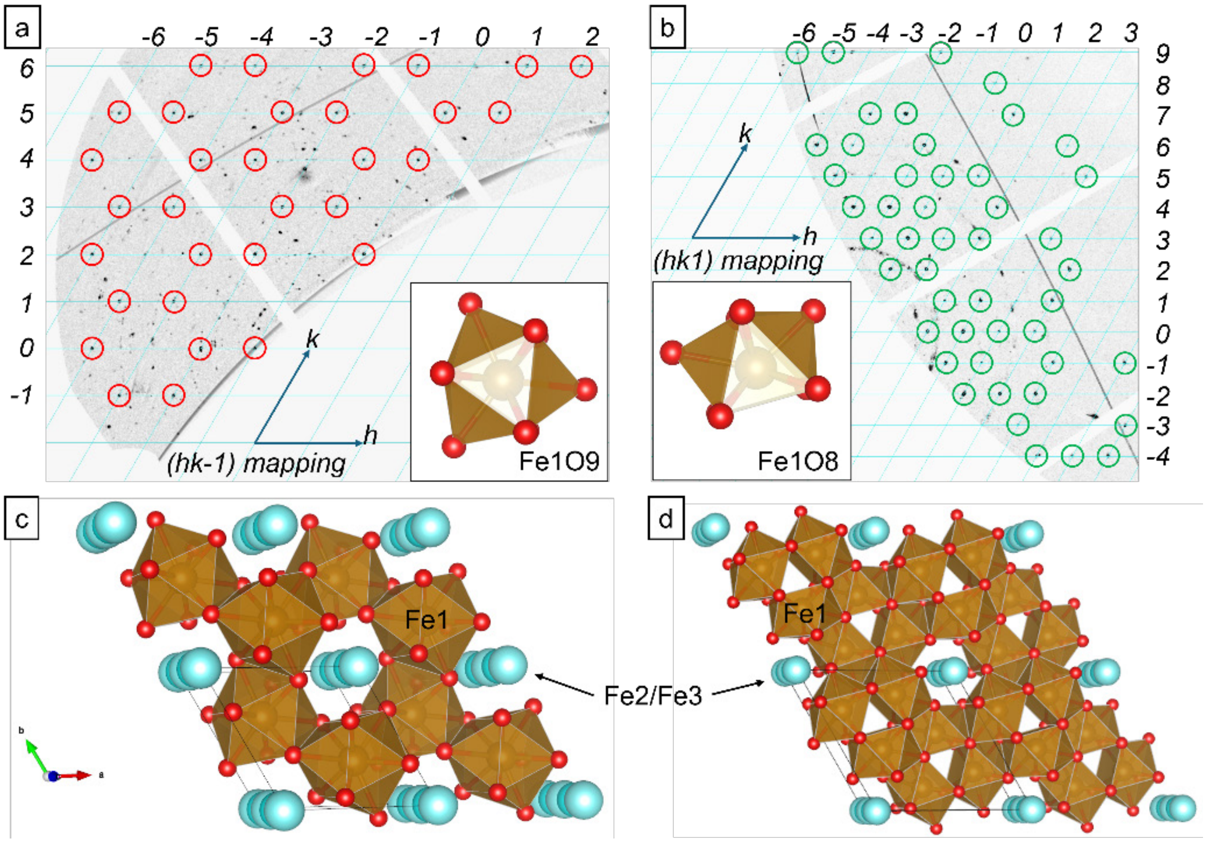

Fig. 3.3-6: *In situ* crystal structure determination of hexagonal iron oxyhydroxides synthesised at high pressures. (a) Reconstructed reciprocal layers of the ($hk\bar{1}$) reflections for $Fe_5O_{12}H_x$. (b) Reconstructed reciprocal layers of the ($hk1$) reflections of $Fe_7O_{12}H_x$. (c) $Fe_5O_{12}H_x$ (space group $P6_3/m$ at 100 GPa; $a = 5.0960(11)$ Å, $c = 2.81490(13)$ Å) featuring FeO_9 tricapped prisms (brown). (d) $Fe_7O_{12}H_x$ (space group $P6_3/m$ at 170 GPa; $a = 7.2784(15)$ Å, $c = 2.6688(6)$ Å) featuring FeO_8 distorted square antiprisms (brown). In both structures, Fe1 atoms are shown in brown and O atoms in red while Fe2 and Fe3 atoms, which partially occupy the channels, are shown in varying shades of blue.

e. *Crystal structures and microstructures of Ti-bearing calcium silicate perovskites (Y. Wu/Wuhan, T. Boffa Ballaran and N. Miyajima, in collaboration with B. Zhao and T. Ishii/Misasa)*

The $CaSiO_3$-$CaTiO_3$ solid solution has been the focus of several studies, given that it may help to understand the behaviour of calcium silicate perovskite in the Earth's lower mantle. $CaSiO_3$ and $CaTiO_3$ form a continuous perovskite solid solution at high-pressure and -temperature conditions. Ti-bearing calcium silicate perovskites can be quenched to ambient conditions for compositions containing up to 75-80 mol. % of $CaSiO_3$. Beyond this threshold, the recovered materials tend to exhibit amorphous characteristics. With increasing $CaSiO_3$ content, the structure of the quenchable perovskites gradually evolves from an orthorhombic symmetry toward a pseudo-cubic structure. Previous studies have indicated that samples with 50:50

compositions, *i.e.*, $CaSi_{0.5}Ti_{0.5}O_3$, crystallise in a double cubic perovskite structure, featuring alternating SiO_6 and TiO_6 octahedra. However, some extra reflections in the electron diffraction pattern of these samples indicated violation of the F-centered symmetry. As the ordering/disordering process has a significant effect on the elastic properties of a material, we have decided to undertake a careful study aimed at better understanding the nature of such extra reflections.

Three quenchable Ti-bearing calcium silicate samples, $CaSi_{0.53}Ti_{0.47}O_3$, $CaSi_{0.58}Ti_{0.40}Al_{0.02}O_3$, and $CaSi_{0.59}Ti_{0.41}O_3$, with a perovskite structure were synthesised at high-pressure and -temperature conditions using a multianvil apparatus. Their crystal structures and microstructures were investigated by single-crystal X-ray diffraction, transmission electron microscopy, and Raman spectroscopy, respectively. Structure refinements revealed that they crystallised in the orthorhombic perovskite structure (space group *Pbnm*). Twinning was observed in all samples, with {112} reflection twins identified via single-crystal X-ray diffraction (Fig. 3.3-7) and precession selected area electron diffraction in transmission electron microscopy. Such merohedral twinning is responsible for mimicking the high-symmetry double cubic perovskite lattice, which however cannot be indexed with a F-centered lattice due to the presence of several reflections violating such symmetry. Twinning in Ti-bearing calcium perovskites may originate from a phase transformation from a high-temperature cubic or tetragonal symmetry to a low-temperature orthorhombic symmetry during temperature quenching at high pressure.

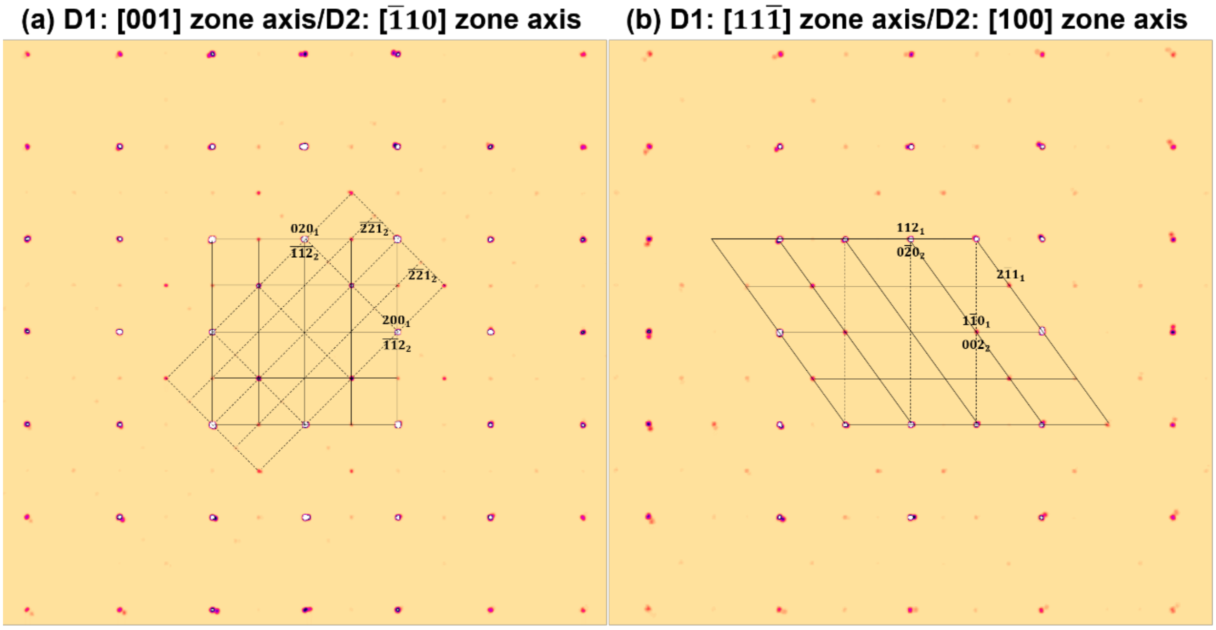
(a) D1: [001] zone axis/D2: [$\bar{1}$10] zone axis

(b) D1: [11$\bar{1}$] zone axis/D2: [100] zone axis

Fig. 3.3-7: Diffraction patterns of Ti-bearing calcium silicate perovskite ($CaSi_{0.53}Ti_{0.47}O_3$) containing two twin components (D1 and D2). Solid and dashed lines represent reciprocal lattice grids of D1 and D2, respectively. Miller indices with subscripts 1 and 2 stand for crystal planes of D1 and D2, respectively.

f. *Probing liquid-liquid phase transformations of elemental sulphur under high-pressure and high-temperature conditions (G. Niu/Beijing, L. Man, R. Pierru, D.J. Frost and H. Gou/Beijing)*

Despite its seemingly simple composition, elemental sulphur exhibits complex chemical behaviour under high-pressure and high-temperature (HP-HT) conditions. Liquid sulphur displays abrupt changes in thermodynamic properties at elevated pressures, marked by several plausibly first-order liquid-liquid phase transitions (LLPTs); however, definitive experimental confirmation remains lacking. In our previous ultrasonic interferometry studies of liquid sulphur under pressure, preliminary results revealed a pronounced elastic anomaly: the sound velocity of liquid sulphur increases rapidly with pressure at 1-7 GPa and reaches a plateau from approximately 7 GPa to 10.5 GPa, then turns to increase again above 10.5 GPa. This non-monotonic pressure dependence suggested underlying microscopic structural transformations in the liquid, motivating direct, *in situ* structural investigations to clarify the microscopic mechanisms responsible.

To directly probe the structural evolution of liquid sulphur under HP–HT conditions, we conducted *in situ* HP-HT structural measurements using synchrotron X-ray diffraction (XRD) in a multianvil press. *In situ* X-ray diffraction (XRD) experiments were conducted at the PSICHE beamline (SOLEIL) using a multianvil press in combination with the newly optimised CEASAR (combined angle and energy-dispersive structural analysis and refinement) method. The investigation covered a broad P-T range up to 22 GPa and 1573 K, employing highly X-ray-transparent assemblies based on boron–epoxy octahedral pressure media developed in this study, which significantly reduced background scattering and enabled high-quality *in situ* XRD measurements of the liquid structure. As illustrated in Figure 3.3-8a, the sulphur sample was loaded in a single crystal MgO capsule to avoid melt leakage. Figure 3.3-8b shows the investigated P-T conditions, compared with the phase boundaries (S-L and L-L) reported before. A representative Intensity (I)-2θ-energy profile (upper) and the corresponding projected I (Q) (lower) are shown in Figure 3.3-8c, which display the characteristic diffuse scattering signature of the liquid phase. Additionally, the melting curve of sulphur is also determined up to 22 GPa, which shows good consistency with previous works at relatively low pressure (< 10 GPa) and measurable deviations at higher pressures, suggesting the need for revised phase boundaries.

The systematic characterization of sulphur structures in this study provides critical experimental constraints for the long-debated LLPT in sulphur. By establishing a direct correlation between atomic-scale structural evolution and the previously identified elastic anomalies, this work will elucidate the microscopic origins of macroscopic thermodynamic discontinuities. Furthermore, the refined melting curve and structural data offer a high-precision experimental benchmark for understanding thermodynamics and interpreting the phase behaviour of sulphur-bearing systems in planetary interiors.

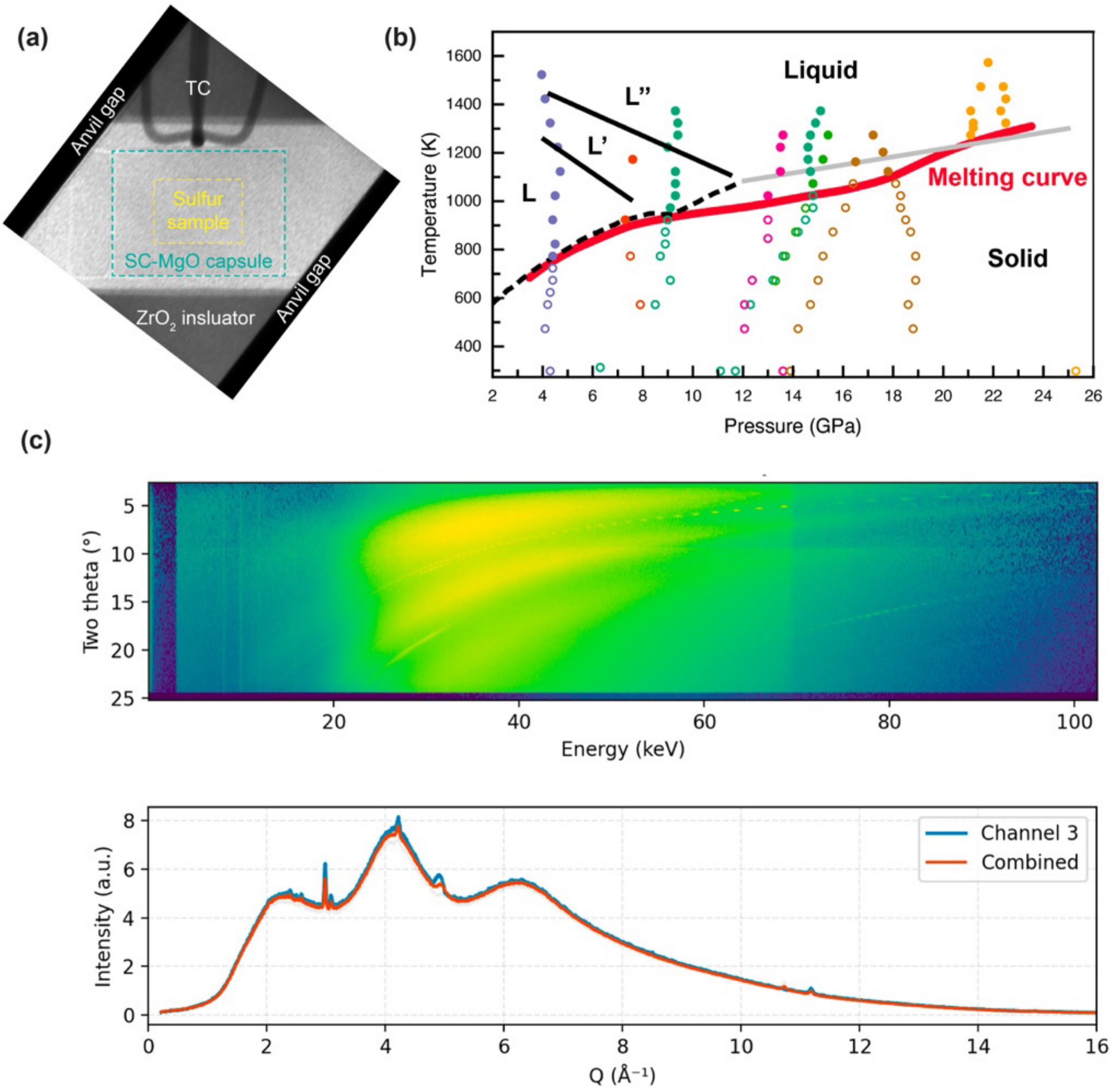

Fig. 3.3-8: (a) X-ray image of the assembly at ambient condition. (b) P-T conditions where X-ray diffraction is conducted, each color of the circles represents one run, and open circles and solid circles represent solid and melt samples, correspondingly. (c) Upper: The representative CAESAR profiles collected at 4.7 GPa and 1123 K. Lower: The corresponding projected *I* (Q) displays the characteristic diffuse scattering signature of the liquid phase.

g. *Long-range modulation in uranium-bearing hematite superstructure constrained from STEM analysis and* ab initio *calculations (J. Yao, C.L. Ciobanu, N.J. Cook, K. Ehrig and A.D. Slattery/Adelaide, E.S. Ilton/Richland, N. Miyajima and G. Steinle-Neumann)*

Natural hematite from the Olympic Dam Cu-U-Au-Ag deposit, South Australia, contains pentavalent uranium in hematite, with an average composition of $Fe_{1.982}U_{0.014}Pb_{0.005}O_3$, for which high-angle annular dark field STEM imaging revealed a 12-fold, long-range modulation (periodicity of 17.4 Å) and blocks of six lines each with bright and dark contrast (Fig. 3.3-9), which requires comparison to simulated electron diffraction patterns for an understanding of the underlying structure.

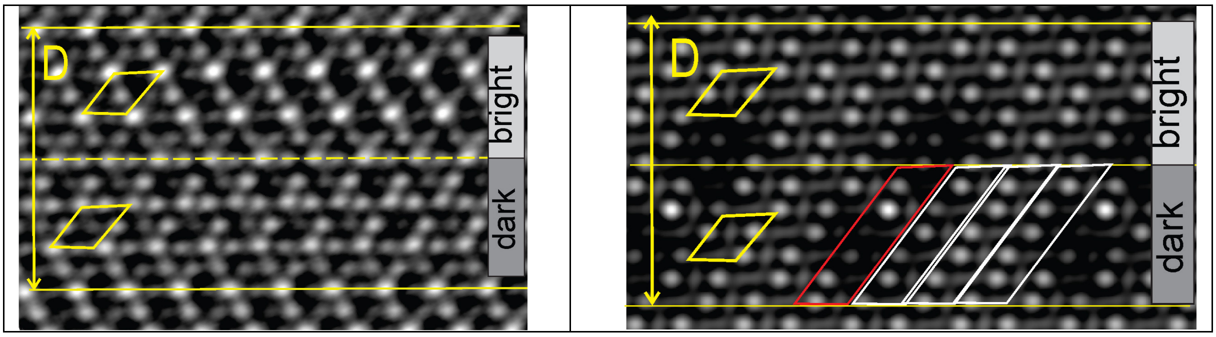

Fig. 3.3-9: Comparison between analytical STEM image (left) and simulated STEM image of the 4 x 4 x 4 hematite superstructure with U incorporation (right). The *D* interval shows a 17.4 Å repeat unit of one dark and one bright block. The rhombus-shaped motifs (in yellow) highlight comparable atomic arrangements on the images. The model shows further heterogeneity (red and white stripes) introduced by Fe and O vacancies, in the vicinity of the U sites (red stripe).

Hematite consists of a set of O and Fe layers, and anions form a hexagonally close packing lattice, and Fe^{3+} cations occupy two-thirds of the octahedral sites, with twelve FeO_6 octahedra forming the unit cell. The unit cell contains 3 layers of Fe along the hexagonal *a*- and *b*-axis, 6 layers along the *c*-axis. Supercells of hematite are required to model the observed modulations and the incorporation of high-valence cations such as U. The repeat pattern of 12 layers makes a 4 x 4 x 1 superstructure ($a = b$) of hematite the simplest supercell to possibly obtain a match between simulated and observed electron diffraction pattern.

Indeed, the observed modulation is reproduced by simulated electron diffraction patterns with an empirical model of a 4 x 4 x 1 hematite superstructure with variable Fe occupancy over 12 layers. Additional analytical data, however, require the expansion of the superstructure to a 4 x 4 x 4 supercell. Its large size ($Fe_{768}O_{1152}$ for stoichiometric hematite) prohibits Kohn-Sham density functional theory-based calculations to constrain a model with variable Fe and O occupancies and U incorporation, and a simplified Fe and O vacancy scheme is explored, educated by the results on the 4 x 4 x 1 cell. The bright blocks are simulated with stoichiometric Fe_2O_3, in the dark block, U is incorporated via a double-corner Fe vacancy environment and an associated O vacancy (Fig. 3.3-10), with additional Fe (and O) vacancies in the dark block for partial occupancy (and charge balance). The relaxed superstructure of $Fe_{756}U_4O_{1144}$ yields good agreement with the STEM observation (Fig. 3.3-9). Calculated Bader charges and magnetic moments for the U atoms support the inference of its incorporation as a pentavalent cation into the hematite superstructure, based on a comparison to prior work on uranium oxide U_2O_5.

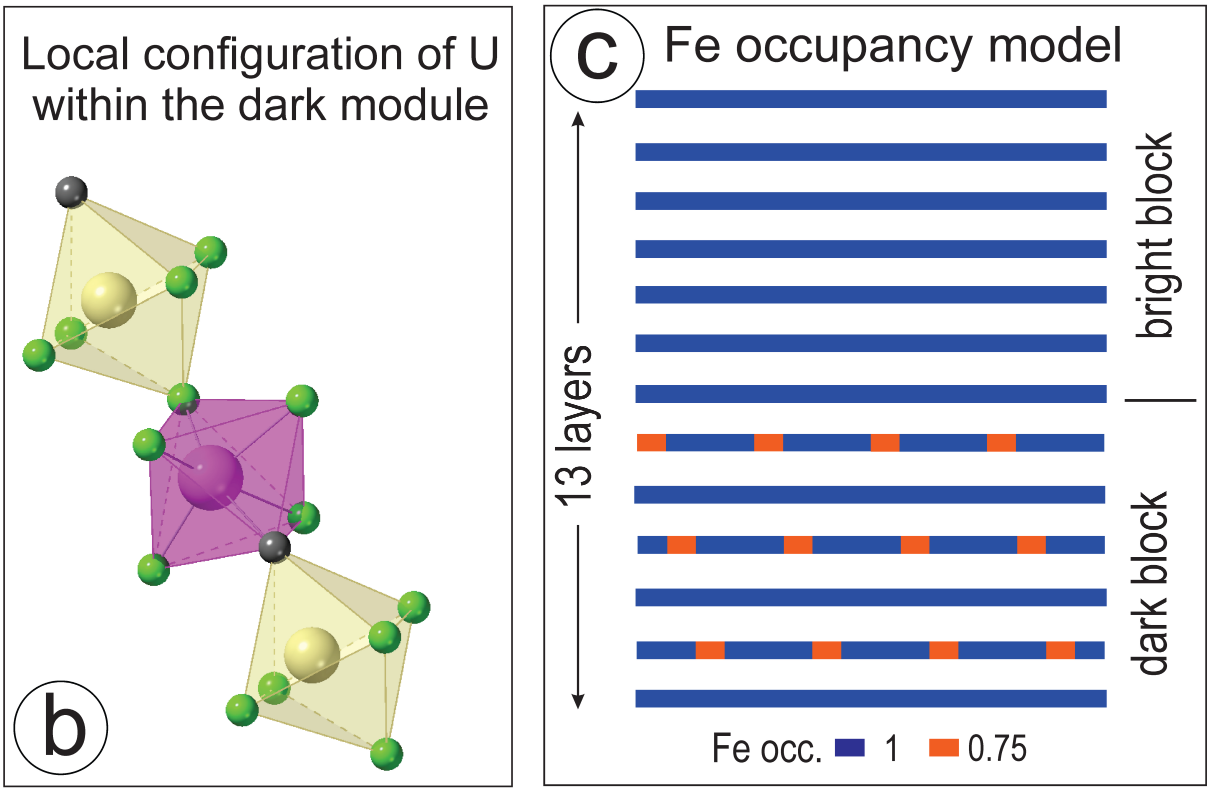

Fig. 3.3-10: (left) Local atomic configuration for uranium incorporation in an octahedral Fe environment, sharing two corners with vacant octahedra. Oxygen vacancies are placed at one vortex of the U octahedra. (right) Iron occupancy scheme for the 4 x 4 x 4 hematite superstructure featuring six layers with alternating occupancy, 0.75 (requiring additional Fe and O vacancies) and 1.00 in the dark block, and six fully occupied layers in the bright block.

h. *High-resolution scanning transmission microscopy of an amphibole-talc-diopside interface: the microscopic visibility of modular structures according to Thompson's parity rule (N. Miyajima; S.C. Tarantino, A. Zanetti and M. Zema/Pavia and F. Heidelbach)*

Topotaxial intergrowth of amphibole in clinopyroxene in mantle rocks is of interest for the structural evolution from single to double-chain silicate minerals during magmatic and metasomatic processes involving fluid migration. Current high-resolution scanning transmission microscopy (STEM) can not only identify topotaxy between amphibole and diopside but also visualise nanometre-sized impurities at the interface. Here, we characterised the topotaxial interface in a natural sample of diopside from the subcontinental mantle peridotite body of Balmuccia (Ivrea-Verbano Zone, Italy) in order to clarify the formation mechanisms of the topotactic relationships and the talc-forming fluid migration process.

A petrographic thin-section of a natural diopside (Di) crystal containing kaersutite-amphibole (Amp) lamellae was thinned to electron transparency by the Ar-milling method for STEM. At the end of the milling process, the surface damaged layer was cleaned with a gentle Ar plasma at a low voltage for 0.5 to 1 hour. High-angle annular dark-field scanning transmission electron microscopy (HAADF-STEM) was performed at BGI by using a none-aberration corrected scanning transmission electron microscope equipped with a thermal Schottky emitter in a field emission gun and an aberration of $C_S = 1.3$ mm in the condenser lens. The theoretical spatial resolution of the scanning electron microscope is 0.16 nm, but after careful alignment of the illumination lens system the resolution was improved to 0.136 nm, resulting in the visibility of silicon dumbbells in the [110] zone axis HAADF images of crystalline silicon (Fig. 3.3-11). Noisy contrast in the HAADF images was removed by a noise filtering technique.

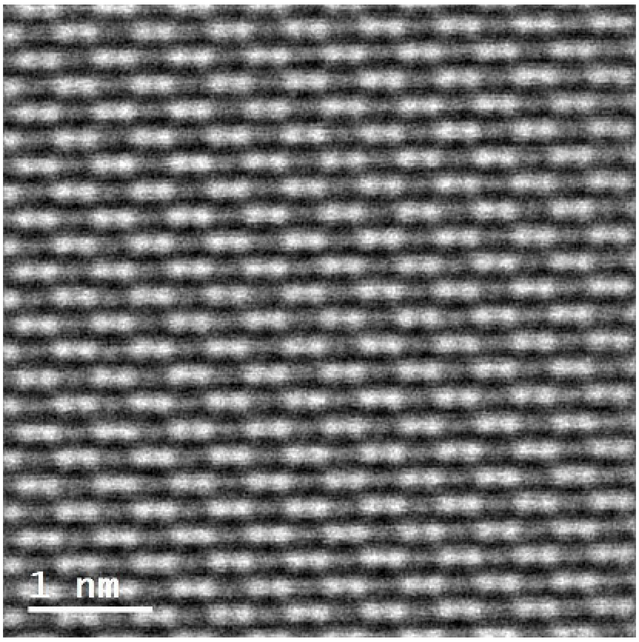

Fig. 3.3-11: A filtered high-angular annual dark-field (HAADF)-STEM image of crystalline silicon along the [110] zone axis. The visible dumbbell structure is made of Si–Si pairs separated by 0.136 nm.

The HAADF-STEM image of an interface between Amp and Di (Fig. 3.3-12) displays the existence of a talc-structured phase (Tlc) consisting of two tetrahedral cation sites (T) and one octahedral site (O) and forming a TOT layer in the vertical direction. The visibility of individual cation columns in the Z-contrast image reveals the modular structure of a polysomatic series of the minerals Amp, Tlc, and Di, consisting of pyroxene (Py) modules and mica (M) modules according to Thompson's "biopyriboles" criteria (inset in Fig. 3.3-12). In the HAADF image, the Amp structure is visible as the sequence …PyMPy… while Di and Tlc are indicated by the sequences …PyPyPy… and …MMM…, respectively. As illustrated in J.B. Thompson's drawing (inset in Fig. 3.3-11), the Amp structure can be visually divided into mica (M) and pyroxene (Py) modules along the vertical (010) boundaries in the experimental HAADF-STEM image. The discovery of Tlc at the interface between Di and Amp implies a selective fluid migration through the misfit dislocations on the (010) plane.

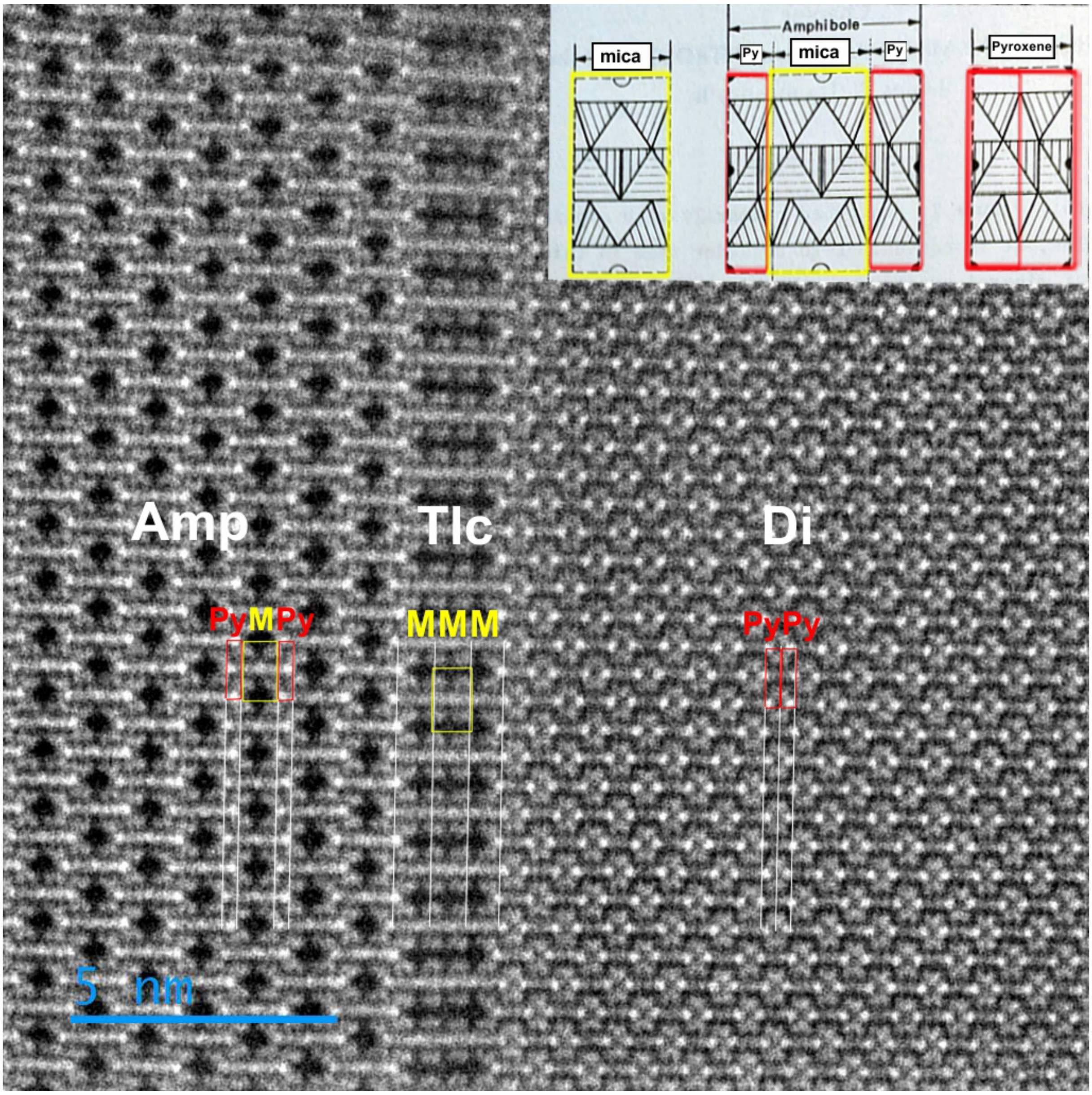

Fig. 3.3-12: A filtered HAADF-STEM image of an amphibole (Amp)-talc (Tlc)-diopside (Di) interface along the [001] zone axis of Amp and Di and the [100] zone axis of Tlc. The inset shows the idealized **I-beam**-modules of mica (M), amphibole (PyMPy) and pyroxene (Py) according to Thompson's parity rule.

i. *The anisotropy of infrared absorption in minerals of different symmetry classes (A.C. Withers and Z. Zhang/Beijing)*

Infrared spectroscopy can be used to quantify the concentrations of absorbing species in isotropic materials such as glass and cubic crystals by application of the Beer-Lambert law. When infrared light passes through anisotropic crystalline material with some arbitrary incident direction, however, the incident light is split into two rays that each have a distinct absorbance that depends on the vibration direction of the ray and the orientation of the absorbing dipole. Consequently, the Beer-Lambert law cannot be directly applied without some correction for the effects of anisotropy. For this reason, quantitative infrared spectroscopy of minerals is ideally done using polarised infrared light with vibration directions parallel to the principal axes of the indicatrix. In this special case, the total absorbance of a dipole can be retrieved by summing the principal absorbances.

The general case, where the incident direction of light is arbitrary, is of interest for both fundamental and practical reasons. For many samples of interest, especially those produced in high-pressure experiments, polarised measurements of oriented crystals are challenging, so it is much more practical to make unpolarised measurements of unoriented crystals. In this case, the average absorbance will be biased, and measurements will have scatter arising from differences in orientation. To quantify the uncertainties arising from bias and scatter it is necessary to have a good description of the absorbance, as a function of incident light direction and polarization state. Unfortunately, even though the physics of absorption of infrared light is well understood, existing formulations in the geoscience literature include simplifying assumptions that limit their applicability. In particular, these models are framed in terms of polarization direction without reference to the direction of incidence, which means that the vibration directions are unknown, which is a significant shortcoming. In addition, existing models do not have provision to account for the effects of differing crystal symmetry. Here we aim to develop a new model that improves upon existing models by removing some of those simplifications.

As the starting point for our calculation, we consider a dipole of a given orientation, described by vector **D**, and with total absorbance A. The vibration directions $\mathbf{P}_1$ and $\mathbf{P}_2$ are calculated for a given incident direction, based on the principal refractive indices for visible light for a given mineral. The total absorbance of the dipole is divided over family of n symmetry-equivalent dipoles, whose orientations depend on the symmetry of the crystal. The dipole absorbances are then projected onto the vibration directions and summed. Finally, Malus' law is used to determine the absorbance that will be measured:

$$A_{\mathrm{pol}} = -\log_{10}[10^{-\sum_{i=1}^{n}\frac{A}{n}(\hat{\mathbf{D}}_i\cdot\hat{\mathbf{P}}_1)^2}\cos^2\theta + 10^{-\sum_{i=1}^{n}\frac{A}{n}(\hat{\mathbf{D}}_i\cdot\hat{\mathbf{P}}_2)^2}\sin^2\theta] \tag{1}$$

$$A_{\mathrm{unpol}} = -\log_{10}\{[10^{-\sum_{i=1}^{n}\frac{A}{n}(\hat{\mathbf{D}}_i\cdot\hat{\mathbf{P}}_1)^2} + 10^{-\sum_{i=1}^{n}\frac{A}{n}(\hat{\mathbf{D}}_i\cdot\hat{\mathbf{P}}_2)^2}]/2\} \tag{2}$$

where A_{pol} and A_{unpol} are, respectively, polarised and unpolarised absorbance, and θ is the polariser orientation measured from vibration direction $\mathbf{P}_1$.

We tested our model by collecting polarised and unpolarised spectra in a non-principal plane of olivine and comparing these with model predictions. For this we used a gem-quality olivine crystal from Sapat, Pakistan. The olivine crystal was oriented optically and cut to create a 2 mm cube whose faces are perpendicular to the principal axes of the optical indicatrix, the axes of which consequently run parallel to the edges of the cube. Two opposing corners of the cube were truncated to form triangular faces perpendicular to the Cartesian (1, 1, 1) direction of the indicatrix (Fig. 3.3-13a).

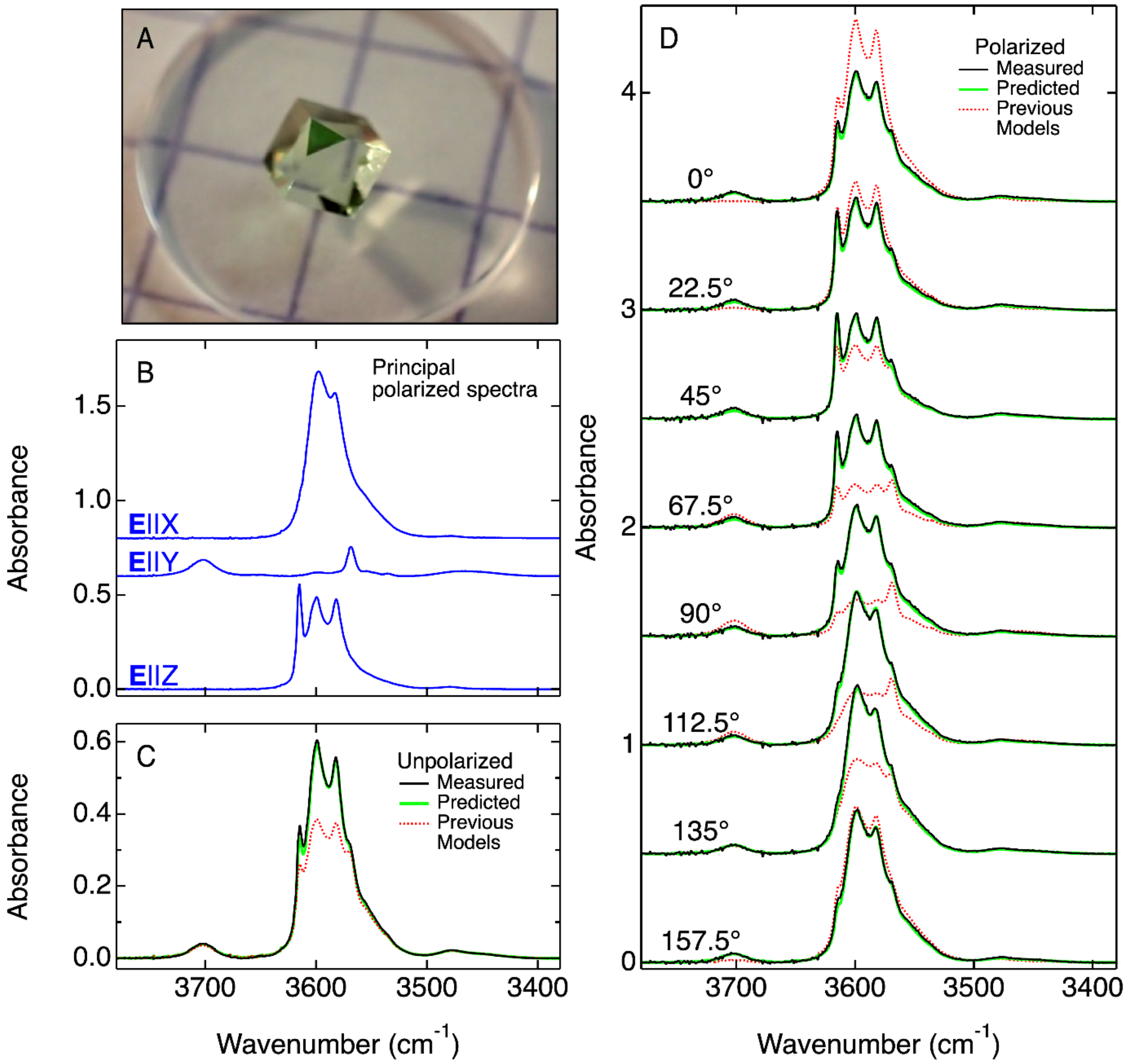

Fig. 3.3-13: (a) Photograph of the olivine that was used as a test for the model. The path length between triangular truncated faces of the 2 mm cube is 2.67 mm. The X, Y and Z axes of the optical indicatrix are parallel to the edges descending from the corners of the triangular face toward the top left, bottom left, and right sides, respectively, of the image. (b) Principal polarised spectra. (c) Unpolarised and (d) polarised infrared spectra with light incident in the (1, 1, 1) direction of the optical indicatrix. Angles denote polariser orientation.

Polarised and unpolarised infrared spectra were collected using the newly installed Bruker Vertex 80 Fourier transform infrared spectrometer and Hyperion II microscope at BGI. Unpolarised measurements are averages of two unpolarised spectra in which the sample is rotated by 90° between measurements, which corrects the effects of partial polarization in the optical path. Principal polarised spectra were analysed with incident directions parallel to X and Y indicatrix directions (Fig. 3.3-13a). The cube was then arranged so that the incident direction was parallel to the (1, 1, 1) direction of the optical indicatrix, with polariser orientation measured from a direction perpendicular to the projection of the Y axis in a clockwise direction as viewed from (-1, -1, -1). Using refractive indices for olivine, the calculated vibration directions correspond to polariser orientations of 43.8° and 133.8°. When viewed with an optical microscope under cross-polarised light, we observed extinction with a stage rotation of 42-43°. With the sample placed over a CaF_2 window in the infrared microscope, the maximum and minimum absorbances for the range of frequencies in the OH stretching region were observed with the infrared polariser oriented at 45° and 135°. The excellent agreement between calculated and observed vibration directions with both visible and infrared light sources shows that our model can be usefully applied using known refractive indices for visible light. Figures 3.3-13c and 3.3-13d show unpolarised and polarised spectra measured over a range of polariser orientations. Based on the measured principal spectra (Fig. 3.3-13b), we can use our model to predict the infrared spectrum for any polariser orientation. Ideally, the principal spectra should be decomposed by peak fitting to determine the contribution from each dipole. Here, however, we make the simplifying assumption that the principal absorbances at any frequency arise from a single family of symmetry-multiplexed dipoles. This is not the case, since absorbance peaks overlap in the spectra and absorbances arising from dipoles with different orientations are not additive. Nevertheless, using the measured principal spectra as input, together with the refractive indices, the predicted spectra show excellent agreement with the measured spectra. In contrast, spectra predicted using the previously optimal models are a poor match for spectra measured in this non-principal plane.

Having verified that our model offers an improved predictive power over previous models, the model can be used to predict uncertainties for unpolarised measurements for crystals with different symmetry classes and optical properties.

j. *Mineralogical and chemical investigations of the Wedel IAB complex iron meteorite (R. Zhao, A. Bouvier, L.S. Dubrovinsky and N.A. Dubrovinskaia)*

Iron meteorites sample the metallic cores of differentiated planetary bodies. They are commonly classified into thirteen major chemical groups based on the bulk concentrations of siderophile elements (those that have a strong affinity for iron), including Ni, Co, Au, As, Sb, W, Ga, Ge, Ir, and Cu. Traditionally, the bulk chemical compositions of iron meteorites were determined using instrumental neutron activation analysis (INAA). However, this technique has largely been replaced by mass-spectrometric methods. In this study, we determined the bulk composition of the Wedel iron meteorite, which was found in the federal state of Schleswig-Holstein, Germany in 2024. We measured the elemental chemical compositions of individual metal and phosphide mineral phases in a polished section of ~ 90 mm² (Fig. 3.3-14) to calculate a bulk composition using their corresponding modal abundances. A grid-based point-counting method in SEM images was implemented using the software JMicroVision. The Wedel meteorite consists predominantly of kamacite (96.7 vol. %), with minor schreibersite (2.3 vol. %) and trace amounts of taenite (< 1.0 vol. %). Schreibersite occurs as grains 80-200 µm in size. Taenite grains were too small (< 20 µm) to be subsequently analysed by LA-ICP-MS. Major elements (Fe, Ni, and Co) were first analysed by electron probe microanalysis (EPMA). The composition of kamacite and schreibersite are $Fe_{93.1(3)}Ni_{6.3(3)}Co_{0.48(4)}$ (N = 29), and $Fe_{51.1(25)}Ni_{34.3(25)}P_{14.5(2)}$ (N = 12) in wt. %, respectively. Cobalt was subsequently used as an internal standard for laser ablation inductively coupled plasma mass spectrometry (LA-ICP-MS) analyses of trace siderophile elements. All LA-ICP-MS measurements were performed at the BGI using an ESL NWR 193 nm excimer nanosecond laser ablation system coupled to a Thermo Scientific iCAP TQ ICP-MS. We used the NIST SRM 610 glass, as well as the North Chile and Hoba iron meteorites as reference materials for calibration and quality control. Analytical conditions for Fe–Ni metal and schreibersite were optimised by comparing line-scan and spot-analysis modes.

Elements measured in line mode, including Au, Cr, Cu, Ga, Ge, and Mo, show relatively large variations when reported in bulk compositions owing to spatial heterogeneity between kamacite and schreibersite measurements. If using the average composition measured by spot mode, the Au concentration is 1.4(1) ppm, which is more precise and consistent with the average value reported for the IAB main group (1.5 ppm), but lower than the reported value of 1.8 ppm obtained by LA-ICPMS on the repository specimen (Meteoritical Bulletin). Although the IAB main group and the sLL subgroup overlap in their abundances of many elements, they can be distinguished using a small number of diagnostic elements, notably As, Ni, Co, and Ge. The concentrations of these elements in Wedel are consistent with the IAB main group rather than the sLL subgroup.

The classification type specimen contains coarse-grained kamacite and taenite crystals that can reach several centimetres in size. In contrast, taenite is only a minor phase in the analysed section of our sample. This difference in modal mineralogy likely accounts for the observed discrepancies between our results and the previously published bulk compositions. The reported variations in mode and bulk compositions of these two sample chips, however, do not affect the classification.

Schreibersite in the Wedel meteorite occurs between coarse kamacite grains as thin layers approximately 20-30 µm thick and up to ~ 500 µm in length, locally thickening to ~ 40-50 µm to form irregularly shaped pockets. In addition, needle-like schreibersite inclusions were observed within individual kamacite grains. Owing to their small size and irregular geometry, mechanical extraction of schreibersite from the meteorite proved impractical. To overcome this limitation, we employed focused ion beam (FIB) techniques to isolate two plates from schreibersite-bearing regions, each with approximate dimensions of 20 × 10 × 2 μm^3. These fragments were too small for data collection using an in-house X-ray diffractometer; therefore, they were mounted on a diamond anvil in a BX90-type diamond anvil cell (DAC) and transferred to the Extreme Brilliant Source of the European Synchrotron Radiation Facility (EBS-ESRF) for further investigation.

Synchrotron X-ray diffraction experiments were conducted at the ID15B beamline using a wavelength of $\lambda = 0.4099$ Å. The X-ray beam was focused to 2 × 1 μm^2, and diffraction data were collected using an Eiger2 X CdTe 9M detector. Full X-ray diffraction mapping was performed for each sample. Single-crystal diffraction data were acquired using step scans of 0.5° over an angular range from -38° to +38°. The CrysAlis^{Pro} software package was used for the analysis of the single-crystal XRD data (peak hunting, indexing, data integration, frame scaling, and absorption correction). To calibrate an instrumental model in the CrysAlis^{Pro} software, *i.e.*, the sample-to-detector distance, the detector's origin, offsets of the goniometer angles, and rotation of both the X-ray beam and detector around the instrument axis, we used a single crystal of orthoenstatite [$(Mg_{1.93}Fe_{0.06})(Si_{1.93},Al_{0.06})O_6$, *Pbca* space group, $a = 8.8117(2)$ Å, $b = 5.18320(10)$ Å, and $c = 18.2391(3)$ Å]. The DAFi program was used for the search of reflections groups belonging to the individual single crystal domains. Using the OLEX2 software package, the structures were solved with the ShelXT structure solution program using intrinsic phasing and refined with the ShelXL refinement package using least-squares minimization. Crystal structure visualization was made with the VESTA software.

Both schreibersite samples extracted from the meteorite were found to be monodomain single crystals. The high quality of the diffraction data ($R_{int} \approx 2$ %, resolution 0.57 Å, completeness ≈ 65 %, redundancy ≈ 3, ~ 450 independent reflections, and more than nine reflections per refined parameter) enabled an accurate crystal structure solution and refinement.

Although the chemical composition of schreibersite, $(Fe,Ni)_3P$, is relatively simple, its crystal structure is quite complex (Fig. 3.3-15). The mineral crystallises in the non-centrosymmetric space group $I\bar{4}$ and contains phosphorus in a single crystallographic site, while metal atoms are distributed over three distinct sites (M1, M2, and M3). All structural sites have equal multiplicity, corresponding to eight formula units per unit cell.

Published data are inconsistent regarding whether iron and nickel are distributed over all metal sites or are restricted to specific positions, and whether terrestrial (natural and synthetic) and meteoritic schreibersite differ in their metal-site occupancies. In our structural refinements, all crystallographic sites were assumed to be fully occupied, consistent with electron microprobe (EMPA) analyses. Using standard ShelXL procedures, the metal sites were initially tested for mixed Fe/Ni occupancy. When the occupancy of the minor substituent (Ni, in this case) at a given site exceeded 3σ, the site was refined with mixed metal occupancy.

We found that the distribution of Ni in the studied schreibersite samples is ordered: within the precision of the refinement, Ni is absent from the M1 site, present at the M2 site, and dominant at the M3 site. Refined compositions of two samples are $Fe_{1.87(15)}Ni_{1.13(15)}P$ and $Fe_{1.80(13)}Ni_{1.20(13)}P$, in good agreement with EMPA data – $Fe_{1.713(79)}Ni_{1.299(85)}P_{1.000(55)}$.

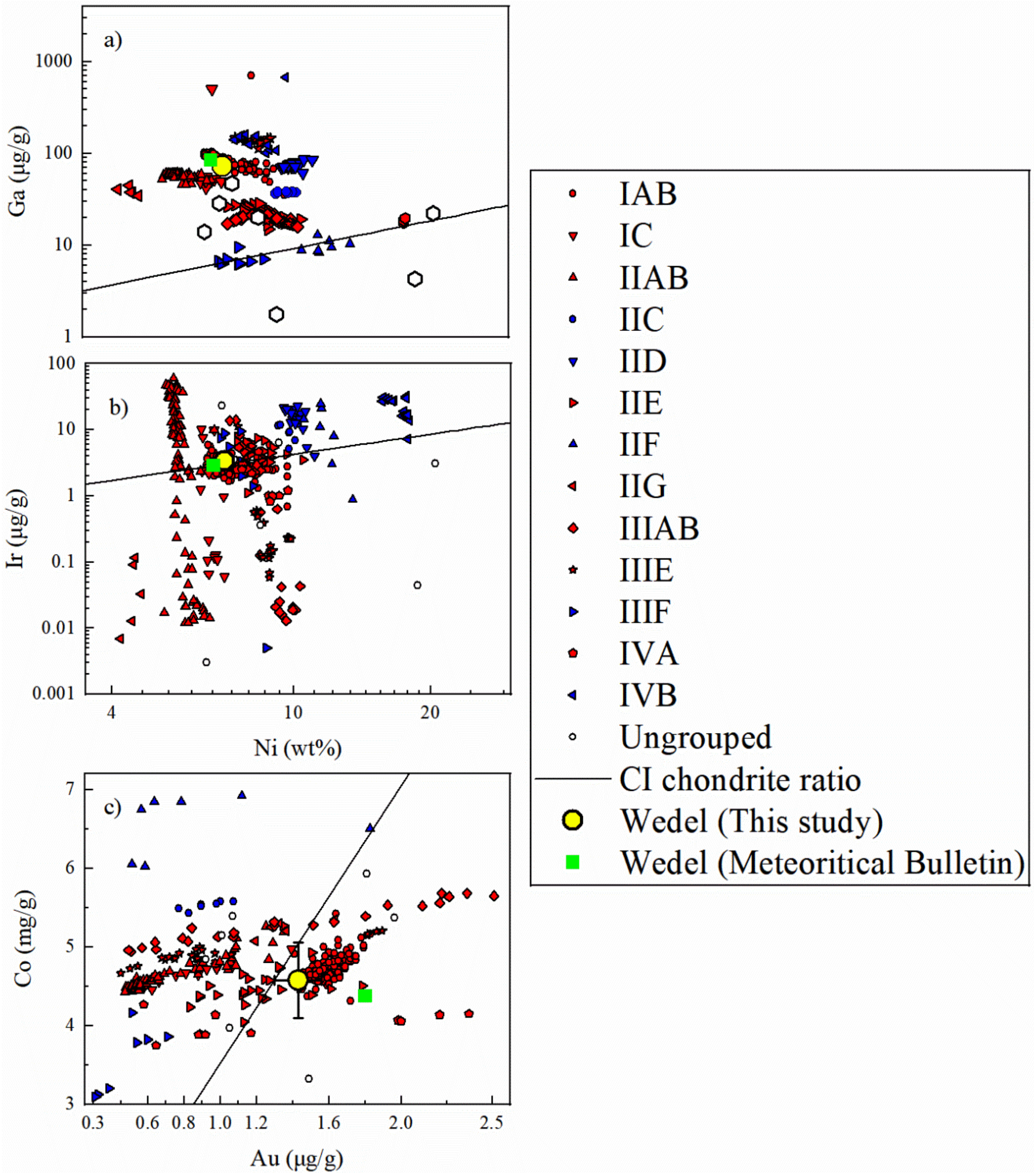

Fig. 3.3-14: Elemental composition of the Wedel iron meteorite compared with grouped and ungrouped iron meteorites. Shown are bivariate plots of (a) Ga versus Ni, (b) Ir versus Ni, and (c) Co versus Au. For Ge, Ir, and Ni, analytical uncertainties are smaller than the symbol sizes in panels (a) and (c). Red symbols represent non-carbonaceous iron meteorites, whereas blue symbols represent carbonaceous iron meteorites, classified based on nucleosynthetic isotope anomalies (*e.g.*, Mo and Ru).

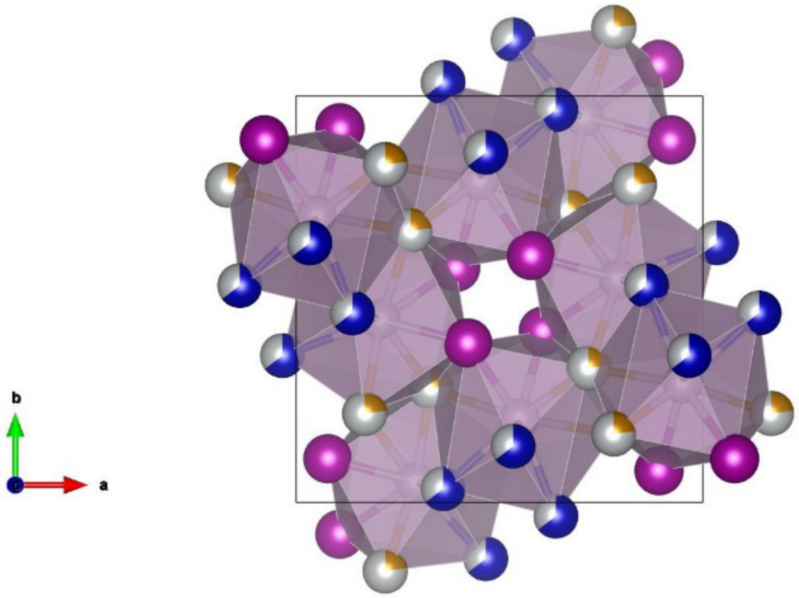

Fig. 3.3-15: Crystal structure of schreibersite with composition $Fe_{1.87(15)}Ni_{1.13(15)}P$, as determined by single-crystal X-ray diffraction of a sample from the Wedel meteorite. Phosphorus atoms (pink) are located at the centers of three-capped triangular prisms formed by Fe/Ni atoms occupying the M1 (magenta), M2 (blue), and M3 (yellow) sites. Partial occupancy of the M2 and M3 sites by Ni is visualised in silver, with the cross-sectional area proportional to the nickel occupancy at these positions.

3.4 Physical Properties of Minerals

Recent technological advances, such as those described in Chapter 3.8, now allow scientists to investigate minerals under pressure and temperature conditions that were previously very difficult to achieve. It is therefore unsurprising that the contributions presented in this chapter make use of these innovations to shed new light on the properties of Earth's interior.

In the first two contributions, the newly installed MAR345 detector and the new high-brilliance Rigaku diffractometer have been used to study, respectively, the *P-V-T* equation of state of a garnet with Martian composition and the structural changes occurring with increasing pressure in an Fe,Al-bearing bridgmanite crystal. The Fe-rich majoritic garnet appears to have a bulk modulus identical to pyrope, due to the presence of Fe^{3+} at the octahedral site counteracting the majoritic and almandine substitutions, and ongoing high-temperature measurements aim at determining the effect of thermal expansion at pressure. The lower bulk modulus of Fe,Al-bearing bridgmanite with respect to Al-bearing $MgSiO_3$ can be explained by the larger compressibility of the A- site due to the Fe^{3+} substitution.

In the third contribution, ultrasonic data for bridgmanite have been collected at synchrotron facilities at pressures as high as 35 GPa and at 1500 K, thanks to recent optimisations of the multianvil assembly. These are the first ultrasonic data at such conditions and indicate that existing thermodynamic models likely underestimate the temperature-induced reduction of the acoustic wave velocities in bridgmanite.

There is a clear discrepancy in the literature between acoustic wave velocities measured on polycrystalline samples, and those calculated from the full elastic tensor obtained from single-crystals of the same material. In order to shed light on the potential causes of this discrepancy, the properties of polycrystalline samples that are well-characterised in terms of grain size and porosity need to be measured. In the fourth and fifth contributions, sintered samples of stishovite and bridgmanite were investigated by means of Brillouin scattering in order to determine the effect of grain size and orientational distribution on the acoustic wave velocities of these minerals. The Brillouin spectra of the nanometre-sized stishovite sample show shear wave velocities that are characteristic of an elastic response of aggregates of grains, in contrast to the shear waves generated within individual grains with different orientations in the micrometre-sized bridgmanite sample.

Another difficulty encountered when collecting Brillouin spectra of polycrystalline dense minerals is that the longitudinal acoustic wave velocity signals are usually hidden below the shear wave velocities of the diamond anvils. In the sixth contribution, a new diamond anvil design with a rounded table instead of a flat one was used to measure Brillouin scattering from a polycrystalline sample of bridgmanite. The use of these anvils improved spatial resolution, allowing the longitudinal wave velocity of bridgmanite to be measured for the first time at high pressure from a powdered sample.

In the seventh contribution, Brillouin scattering and X-ray diffraction coupled with CO_2 laser heating are used to provide insight into the behaviour of quartz at high temperature and high pressure. Changes in the elastic moduli across the α - β quartz transition were mapped at 2 GPa, showing that both the compressional wave velocity and the bulk modulus of β-quartz are significantly lower than those predicted by current thermodynamic models.

Cubic $CaSiO_3$ perovskite, davemaoite, remains a very understudied mineral due to the fact that it cannot be recovered from high-pressure experiments in crystalline form. Analogues to this material are typically Ti-bearing $CaSiO_3$ samples, which crystallise in a distorted orthorhombic perovskite structure. In the second-to-last contribution, Brillouin spectra of a 50:50 Ti:Si perovskite composition were collected in order to obtain its full elastic tensor.

Finally, among the latest methodological advances, machine learning is emerging as a central tool in computational research. In the last contribution, a previously unknown phase transition in disordered $CaCO_3$ has been observed at mid-lithospheric conditions using a DFT-based machine learning-accelerated molecular dynamics simulations approach. The transition produces significant elastic softening, which may explain the origin of the mid-lithospheric discontinuity.

a. *The effect of Fe and Ca substitution on the elastic properties of majoritic garnets (A. Kurnosov, T. Boffa Ballaran, G. Criniti/Munich, A. Antunes and D.J. Frost)*

Garnet minerals occur in a variety of petrologic processes and as such are a major rock forming mineral of planetary interiors. In the Earth's lower crust and upper mantle, garnet is principally a solid solution between pyrope ($Mg_3Al_2Si_3O_{12}$), grossular ($Ca_3Al_2Si_3O_{12}$), and almandine ($Fe_3Al_2Si_3O_{12}$), but with increasing pressure the majoritic component ($Mg_4Si_4O_{12}$) becomes increasingly important. These complex cation substitutions can be described using the crystal-structural formula $^{VIII}X_3{}^{VI}Y_2{}^{IV}Z_3O_{12}$ with large cations, like Mg, Ca, Fe^{2+}, occupying the 8-fold coordinated X sites, medium sized cations, like Al, Fe^{3+}, Cr, occupying the octahedral Y sites, whereas the tetrahedral Z site is occupied mainly by Si. At pressures above 5 GPa, the coupled substitution of Si and Mg at the Y site gives rise to the majoritic substitution. Several studies have investigated the effect of cation substitutions on the elastic properties of garnet having both end-member and mixed compositions and have shown that the compression of the octahedral site dominates the bulk compressibility of this mineral, although Fe^{2+} at the X site appears also to slightly stiffen the garnet structure. At present, however, it is not clear whether the Ca and Fe (both Fe^{3+} and Fe^{2+}) substitutions affect the compressibility of majoritic garnet, given that, in these minerals, the Y site can be occupied by a mixture of Si, Mg, Al, and Fe^{3+}. Such complex compositions are particularly important since they represent garnets forming in the Martian mantle and therefore play an important role in determining the seismic profile of that planet.

In this study, the compressibility of a single-crystal of an Fe-rich majoritic garnet having a composition similar to that expected to be stable in the Martian mantle has been studied up to 12.5 GPa at room temperature using single-crystal X-ray diffraction. The bulk modulus of this garnet is identical to that of pyrope, in spite of the presence of 40 % of majoritic component at the octahedral site and 23 % of Fe^{2+} at the X site. This indicates that the presence of 10 % of Fe^{3+} at the octahedral site is counteracting the effect of the majoritic and almandine substitution, increasing the compressibility of the garnet structure with respect to that expected.

The effect of these different substitutions at high pressures and high temperatures is at the moment under investigation. To this end, we are using the newly installed MAR345 detector on the Huber diffractometer coupled with a CO_2 laser heating system. The garnet single-crystal loaded in a diamond anvil cell has been currently heated up to 2000 K at 12 GPa (Fig. 3.4-1). Analysis of the collected intensity data will allow us to constrain the *P-V-T* equation of state of this material at conditions relevant for the Martian mantle.

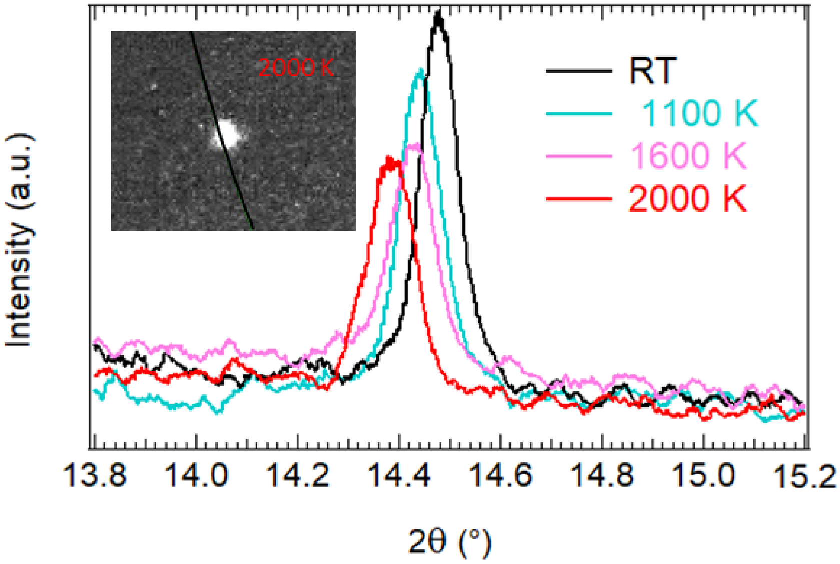

Fig. 3.4-1: Evolution with temperature of the *400* reflection of the majoritic garnet investigated in this study at 12 GPa. The detector image of the same reflections at 2000 K is shown in the inset. The black curve in the inset represents the 2θ position of the same reflection at room temperature and it is used as a guide to the eye to show the visible 2θ shift due to temperature.

b. *Effect of Fe^{3+} and Al incorporation on the structure and equation of state of bridgmanite at high pressure (C. Qian, T. Boffa Ballaran, A. Kurnosov and D.J. Frost)*

$(Mg,Fe,Al)(Si,Al)O_3$ bridgmanite is the most abundant mineral in Earth's lower mantle. The incorporation of Fe and Al in bridgmanite significantly affects its crystal structure, elastic behaviour, and density, thereby influencing seismic interpretations and models of the Earth's lower mantle. A previous study on Al-bearing bridgmanite has suggested that Al has little effect on the bulk modulus. In contrast, iron exerts a more complex influence: whereas Fe^{2+} is restricted to the A site, Fe^{3+} can be incorporated into bridgmanite through charge-coupled substitution with Al, leading to complex site occupancy and modifications of both A-site and B-site polyhedra. The Fe^{3+}-Al charge-coupled substitution ($Fe^{3+}AlO_3$) does not induce a spin transition but has been suggested to cause a substantial increase in compressibility of the bridgmanite structure. However, the specific structural mechanism responsible for this softening remains unclear due to the lack of high-pressure crystal structural determinations. Here we performed laboratory-based X-ray diffraction on a single-crystal Fe^{3+}- and Al-bearing bridgmanite sample to investigate the combined effect of Fe^{3+} and Al on the structure and equation of state of bridgmanite up to 50 GPa.

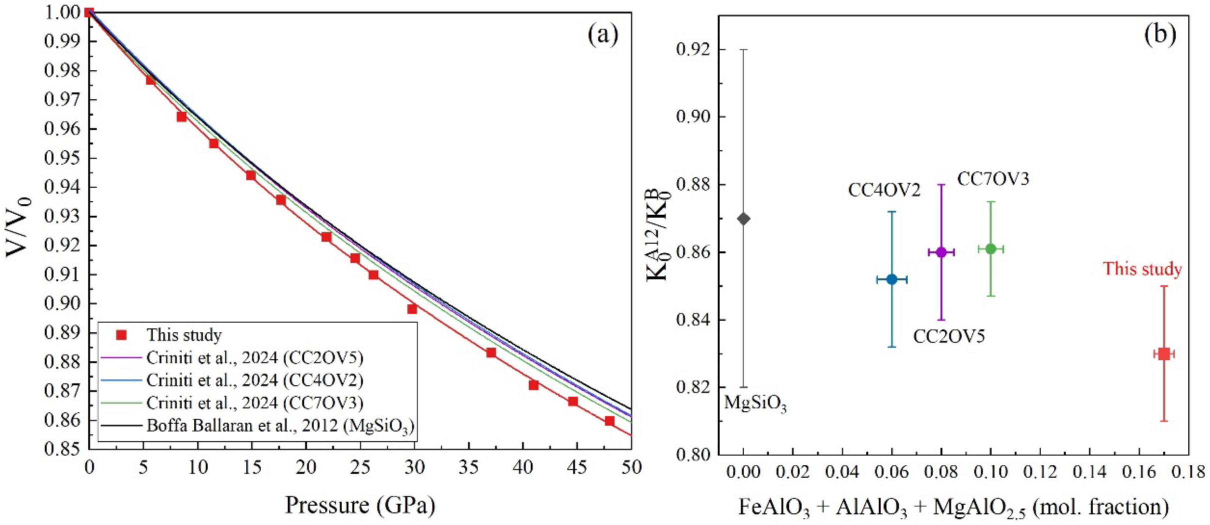

Fig. 3.4-2: (a) Linear compression of the unit-cell volume of several bridgmanite samples normalised with respect to their room pressure values. Solid lines represent 3rd-order Birch-Murnaghan equations of state. Previous studies are: Boffa Ballaran *et al.*, 2012, EPSL, 333-334, 181-190; and Criniti *et al.*, 2024, JGR Solid Earth, 129, e2023JB026879; (b) Variation of the A-site and B-site incompressibility ratio K_0^{A12}/K_0^{B} as a function of the trivalent cation substitution.

High-quality single crystals of Fe^{3+}- and Al-bearing bridgmanite were synthesised using a multianvil press at 25 GPa and 1800 K. The recovered sample was mounted in epoxy resin, polished, and characterised by SEM and EPMA, revealing grain sizes of ~ 30 µm and a homogeneous composition with an average formula of $Mg_{0.87}Fe_{0.13}Si_{0.83}Al_{0.17}O_3$. The $Fe^{3+}/\sum Fe$ ratio in the sample was determined using synchrotron Mössbauer spectroscopy, which indicates that iron is present exclusively as Fe^{3+}. A single-crystal grain (~ 30 µm in length and < 10 µm thick) from the recovered sample was selected for single-crystal X-ray diffraction. A diamond anvil cell (DAC) was used to generate high-pressure conditions. Helium and a ruby sphere were loaded as pressure-transmitting medium and pressure standard, respectively. High-pressure single-crystal X-ray diffraction experiments were performed up to 50 GPa using a Rigaku XtaLAB Synergy single-crystal diffractometer in BGI equipped with a rotating anode Mo X-ray source.

The refined unit-cell volume of this sample decreases smoothly with increasing pressure, showing no indication of structural phase transitions within the investigated pressure range. The pressure-volume data were fitted using a third-order Birch-Murnaghan equation of state, yielding a significantly lower bulk modulus than that of $MgSiO_3$ bridgmanite (Fig. 3.4-2a). The increased compressibility can be attributed to the coupled substitution of Fe^{3+} and Al. By comparing the incompressibility of the A-site and B-site of our sample with $MgSiO_3$ bridgmanite and Al-bearing bridgmanite samples, it appears that substitution of Fe^{3+} at the A-site increases the compressibility of the A-polyhedra with respect to that of Al-bearing bridgmanite (Fig. 3.4-2b).

c. *Acoustic velocity measurement of bridgmanite under mid-lower mantle conditions (L. Man, R. Pierru, C. Qian, A. Kurnosov, A. Chakraborti, W. Zhou, T. Boffa Ballaran and D.J. Frost, in collaboration with R. Farla/Hamburg, G. Niu/Beijing, Z. Liu/Jilin and C. Zhou/Shanghai)*

Fe- and Al-bearing $MgSiO_3$ bridgmanite is the most predominant mineral in the lower mantle, accounting for an estimated 75 % to 93 % of its volume. Given the lack of direct access to the Earth's deep interior, the composition and mineralogy of the lower mantle are primarily estimated by comparing compressional- (v_P) and shear-wave velocity (v_S) profiles determined from seismological observations with those calculated for candidate mineral assemblages, under pressure and temperature conditions that correspond to those of the lower mantle. The elastic properties required for this, including the density (ρ), the bulk (K) and the shear modulus (G) are determined through either laboratory experiments or theoretical calculations. Nevertheless, our current understanding of the elastic properties of lower mantle minerals remains insufficient to interpret the detailed insights and enigmas uncovered by rapidly advancing modern seismology. First and foremost, whether the chemical composition of the lower mantle is consistent with that of the upper mantle – *i.e.*, is aligned with the classic pyrolite model – is still a topic of considerable debate. This controversy primarily arises from the limited and insufficient direct measurements of acoustic velocities in mantle minerals, especially at simultaneous high-pressure and -temperature conditions and over ranges of compositions plausible for the mantle.

In this study, we conducted ultrasonic interferometry experiments on $MgSiO_3$ and $(Mg,Fe)(Si,Al)O_3$ bridgmanite at the synchrotron-based multianvil beamlines (P61B, DESY and BL12SW, SSRF) to determine their acoustic velocity under high pressure and high temperature. Benefiting from recent technical advances in multianvil assembly optimization, we successfully extended these measurements to conditions of up to 35 GPa and 1500 K, corresponding to the mid–lower mantle. Figure 3.4-3 shows an example of the measurement at BL12SW. Our room-temperature results are in good agreement with previous Brillouin scattering measurements on single-crystal $MgSiO_3$ bridgmanite. However, the high-temperature data reveal that existing thermodynamic models, largely constrained by sparse high-temperature measurements, systematically underestimate the temperature-induced reduction of both v_P and v_S in bridgmanite. Based on these new data, we will construct an integrated thermoelastic model for bridgmanite, providing improved constraints for the interpretation of lower-mantle seismic observations.

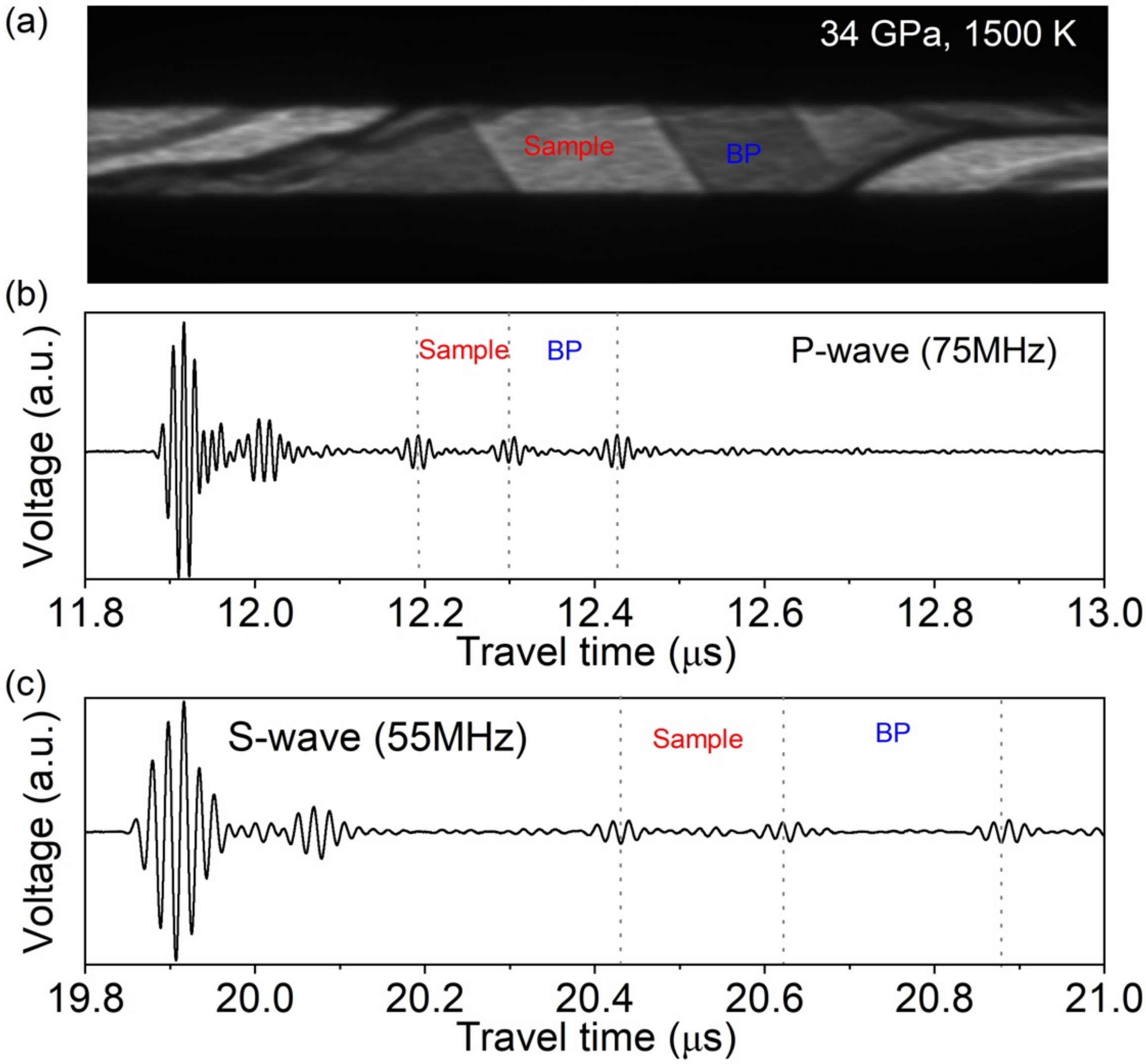

Fig. 3.4-3: Ultrasonic interferometry measurements on bridgmanite at 34 GPa and 1500 K in a multianvil press. (a) X-ray image of the assembly under high pressure and temperature. BP indicates backing plate. (b) Reflections of P-wave at 75 MHz. (c) Reflections of S-wave at 55 MHz.

d. *Brillouin scattering measurements on polycrystalline stishovite at high pressures (J. Buchen, A. Chaudhari, A. Kurnosov, H. Marquardt/Oxford and S. Speziale/Potsdam)*

In metabasaltic rocks with sufficient SiO_2, the mineral stishovite may form as a polymorph of SiO_2 at pressures above 10 GPa and contribute to the mineral assemblage of such rocks in the mantle transition zone and in the Earth's lower mantle. Stishovite may also form in very iron-rich compositions of the Earth's lower mantle if the solubility of the component $FeSiO_3$ in bridgmanite is exceeded. In addition, SiO_2 may exsolve from the Earth's core. The resultant SiO_2-rich domains may be dispersed in the lower mantle by convection, and their mineral assemblage will be dominated by high-pressure SiO_2 polymorphs, including stishovite.

At pressures of the lower mantle, the tetragonal crystal structure of stishovite distorts to the orthorhombic crystal structure of $CaCl_2$-type SiO_2. At room temperature and for pure SiO_2, this ferroelastic phase transition takes place at a pressure of about 55 GPa and causes a substantial reduction of the elastic shear resistance of stishovite and $CaCl_2$-type SiO_2 over an extended pressure interval centred at the phase transition pressure. The resulting softening of the elastic shear modulus of these two SiO_2 polymorphs may impose unique seismic properties on SiO_2-rich rocks in the lower mantle, potentially enabling their detection by seismological observations. While the reduction of the elastic shear modulus has been predicted by Landau theory and observed on measurements on single crystals, it remains unclear to which extent the elastic softening will affect the elastic behaviour of a polycrystalline aggregate of stishovite.

Here, we measured the shear wave velocities of a sintered polycrystal of stishovite at pressures of the lower mantle by means of Brillouin scattering. The sintered polycrystal had a grain size of 165 nm and was polished to a final thickness of 13 µm before being cut and loaded into a diamond anvil cell (DAC). Neon was added to the pressure chamber of the DAC as the pressure-transmitting medium, and pressures were determined by ruby luminescence spectroscopy. Brillouin spectra were recorded at pressures between 0 and 60 GPa at the Brillouin scattering setup at DESY in Hamburg. Figure 3.4-4a shows an example of a Brillouin spectrum recorded on the sintered polycrystal of stishovite. To extract the shear wave velocities from the Brillouin spectra, we fitted peak functions with Gaussian profiles to the background-corrected spectra. Figure 3.4-4b compares the intensity distribution in the Brillouin spectrum as approximated by the fitted peak with the distributions of shear wave velocities in a single crystal of stishovite. The distributions of shear wave velocities were generated by calculating the propagation velocities of both shear modes (S1 and S2) for 1,000 randomly oriented propagation directions within a single crystal of stishovite. In addition, Figure 3.4-4b shows the shear wave velocities of a polycrystalline aggregate of stishovite calculated by averaging the single-crystal elastic properties according to the Voigt (V) and Reuss (R) approximations. The centre of the fitted peak is close to the shear wave velocity of the Voigt average while the shape of the fitted peak does not seem to approximate the velocity distribution of either shear mode within a single crystal of stishovite. This observation indicates that the shear waves that were sampled by Brillouin scattering were characterised by the elastic response of aggregates of grains as opposed to shear waves within individual grains with different orientations. Based on the scattering angle of the setup, the Brillouin spectra sampled shear waves with wavelengths of about 640 nm and with frequencies of approximately 12.4 GHz. Since the wavelength of the shear waves is several times longer than the average grain size of the sintered polycrystal, the periodic strain imposed by the shear waves will be distributed over several grains. Therefore, the propagation velocities of the shear waves will be controlled by the combined elastic response of a collection of grains. The similarity of the experimentally observed shear wave velocity to the shear wave velocity of the Voigt average may hence be explained by the relative size of the wavelength of the shear waves to the grain size of the sintered polycrystal. The relatively high frequencies of the shear waves sampled by Brillouin scattering leave little time for the material to relax elastic stresses by anelastic, viscous, or plastic deformation. Consequently, the elastic response of the sintered polycrystal at such high frequencies is closer to the Voigt approximation of uniform strain than to the Reuss approximation of uniform stress.

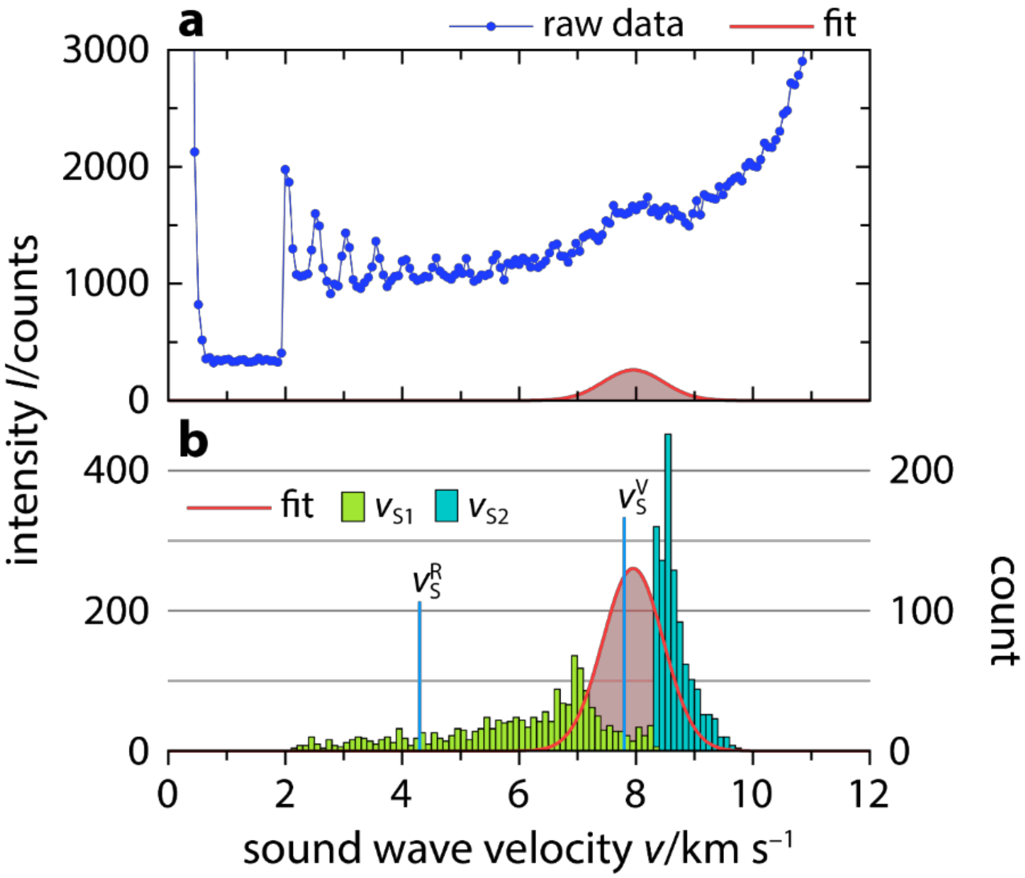

Fig. 3.4-4: Experimental Brillouin spectrum (a) and modelled shear wave velocity distributions (b) of stishovite at a pressure of 50 GPa and room temperature. The spectrum in (a) was recorded on a sintered polycrystal of stishovite. The velocity distributions in (b) for both shear modes (S1 and S2) and the shear wave velocities for the Voigt (V) and Reuss (R) approximations were modelled using the single-crystal elastic properties of stishovite as reported in the literature. Red lines and shadings show the peak function that was fitted to the experimental Brillouin spectrum.

Our analysis of Brillouin spectra suggests that the grain size of a polycrystalline sample is critical when interpreting sound wave velocities derived from Brillouin spectra of polycrystalline samples. For the sintered polycrystal of stishovite, the average grain size was significantly smaller than the wavelength of the shear waves sampled by Brillouin scattering and therefore allowed the measurement of shear wave velocities that reflect the elastic response of aggregates of grains. Interestingly, however, the shear wave velocities did not show a strong reduction as expected based on the predicted elastic softening of stishovite at pressures close to the ferroelastic phase transition. Further measurements are needed to confirm whether the shear wave velocities of polycrystalline aggregates of stishovite may follow the predicted reduction, for example, at frequencies that are closer to those of seismic waves and at high temperatures.

e. *Sound wave velocities of sintered polycrystalline bridgmanite at high pressures (I. Jemal, J. Buchen, C. Qian, A. Kurnosov and T. Boffa Ballaran)*

Bridgmanite is predicted to be the most abundant mineral in the Earth's lower mantle. Among the various endmembers of bridgmanite, the $MgSiO_3$ component has been shown to be the most abundant. Accurate determinations of the elastic properties of $MgSiO_3$ bridgmanite are thus essential as input parameters for synthetic mineral-physics models of the Earth's lower mantle that can be compared with seismic observations to derive accurate estimates of the composition and mineralogy of the Earth's lower mantle. At high pressures, the elastic properties of minerals can be derived from sound wave velocity measurements by means of Brillouin scattering. Previously, sound wave velocities, and thus elastic properties, of $MgSiO_3$ bridgmanite have been determined on single crystals and on powder samples. The results of these measurements, however, contradict each other. The potential reasons for such discrepancy have so far not been studied in-depth. Moreover, no sound wave velocity measurements have been performed on a sintered polycrystal of $MgSiO_3$ bridgmanite. Grain-grain interactions in a sintered polycrystal may result in sound wave velocities that deviate from those derived from measurements on powder and single-crystal samples. Realistic estimates of the sound wave velocity of $MgSiO_3$ bridgmanite in polycrystalline samples thus require analysing the effects of grain size and grain-grain interactions.

In this study, the shear (S) wave velocities of a sintered polycrystal of $MgSiO_3$ bridgmanite were measured at eight pressure points between 31.5 and 62.2 GPa using a diamond anvil cell (DAC) and Brillouin scattering. At each pressure, twelve spectra were collected by rotating the sample in 30° increments around the compression axis of the DAC. Moreover, the distributions of shear wave velocities in a single crystal of $MgSiO_3$ bridgmanite were modelled at each experimental pressure by calculating both shear wave (S1 and S2) velocities for 10,000 randomly oriented propagation directions using literature data. The histograms of the resulting velocity distributions are compared with the measured spectra in Figure 3.4-5a. In Figure 3.4-5b, the measured shear wave velocities of a sintered polycrystal of $MgSiO_3$ are compared with the shear wave velocities of an ideal polycrystal of $MgSiO_3$ bridgmanite, characterised by a perfectly random distribution of grain orientations. The shear wave velocities of an ideal polycrystal were calculated from previously reported single-crystal elasticity data according to the Voigt and Reuss bounds as well as their Voigt–Reuss–Hill average.

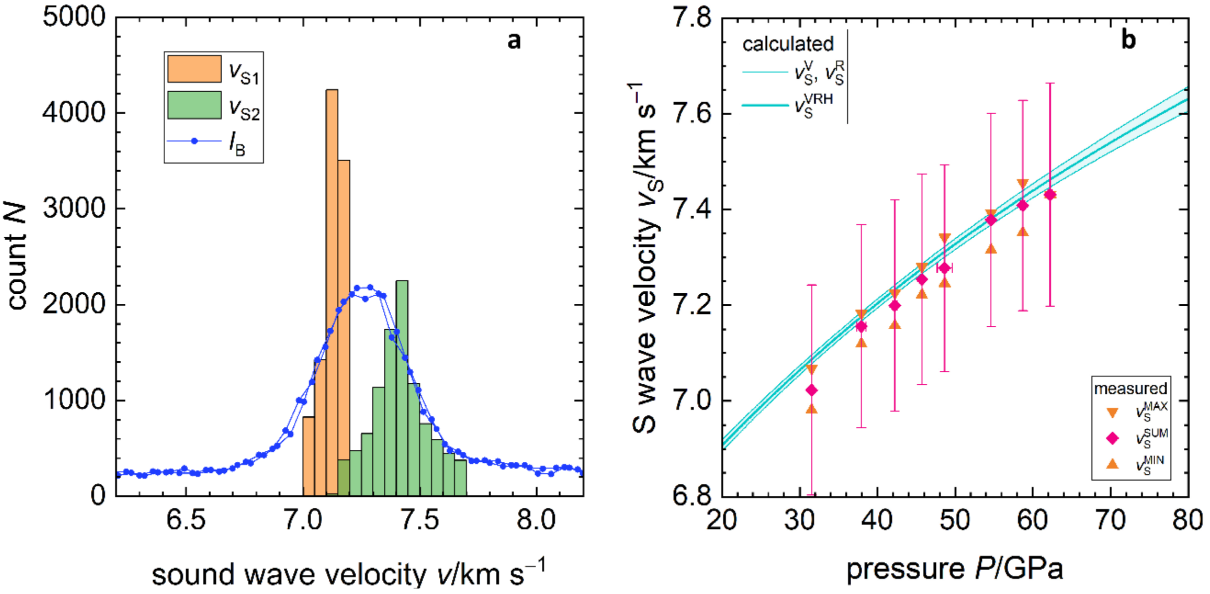

Fig. 3.4-5: (a) Modelled distributions of S1 and S2 velocities within a single crystal of $MgSiO_3$ bridgmanite at 45.7 GPa sampled for 10,000 randomly oriented propagation directions. Blue circles show the sum of Brillouin spectra collected at the same pressure. (b) Modelled and measured shear wave velocities of $MgSiO_3$ bridgmanite as a function of pressure. V_S^{MAX}, V_S^{SUM} are shear wave velocities of a sintered polycrystal of $MgSiO_3$ bridgmanite obtained in this study, representing extrema of the twelve shear wave velocities measured at a given pressure and the velocity derived from the sum of all twelve spectra at a given pressure, respectively. Vertical and horizontal bars represent uncertainties in velocity and pressure, respectively. All calculated velocities were modelled using single-crystal elastic properties reported by Criniti *et al.*, 2021, JGR Solid Earth, 126, e2020JB020967. V_S^V, V_S^R, and V_S^{VRH} represent shear wave velocities of an ideal polycrystal of $MgSiO_3$ bridgmanite calculated using Voigt and Reuss bounds on the shear modulus and their Voigt–Reuss–Hill average, respectively.

The measured shear wave velocities of a sintered polycrystal of $MgSiO_3$ bridgmanite were found to be slightly lower than the modelled shear wave velocities of an ideal polycrystal of $MgSiO_3$ bridgmanite (Fig. 3.4-5b). Previous Brillouin measurements on a polycrystalline sample of $MgSiO_3$ bridgmanite (which was not sintered) yielded shear wave velocities that show a much more pronounced reduction. While the modelled distributions of shear wave velocities in a single crystal of $MgSiO_3$ bridgmanite showed two S-wave maxima (S1 and S2), only one broad S-wave peak was observed in the measured Brillouin spectra (Fig. 3.4-5a). The average wavelength of acoustic phonons probed in this study was calculated to be smaller than the average size of grains in our sintered polycrystal sample, indicating that Brillouin scattering events in our measurements likely took place within individual grains.

Based on the comparison of modelled and measured shear wave velocities of $MgSiO_3$ bridgmanite (Fig. 3.4-5), the systematic reduction of measured polycrystal shear wave velocities of $MgSiO_3$ bridgmanite from modelled polycrystal velocities was inferred to result from the combined effects of the photoelastic effect and the uneven sampling of grains and their acoustic phonons during Brillouin measurements on polycrystalline samples. An additional contribution to the observed reduction of shear wave velocities may arise from elastic softening and acoustic phonon scattering at grain boundaries in polycrystalline samples.
Fully resolving the effect of grain size on the shear wave velocities of $MgSiO_3$ bridgmanite as determined by Brillouin scattering on polycrystalline samples will require additional measurements on polycrystalline samples with a range of different grain sizes.

f. *High-pressure measurement of longitudinal wave velocity in polycrystalline bridgmanite using Brillouin scattering and round table diamond anvils (C. Qian, A. Kurnosov, T. Boffa Ballaran, L. Man and D.J. Frost)*

It is widely accepted that bridgmanite is the primary constituent of the Earth's lower mantle, therefore knowledge of its elastic properties at lower mantle conditions is necessary for constraining the structure of the Earth's deep interior. Bridgmanite single-crystal acoustic velocities have been measured at BGI up to 80 GPa at room temperature, providing a well-constrained set of elastic parameters at high pressure. However, due to the overlap between the longitudinal wave velocity (V_P) of bridgmanite and the shear wave velocity (V_S) of diamond at high pressure, measurements of these velocities were not possible in a large pressure region of the Earth's lower mantle. For polycrystalline materials the situation is even more critical due to the broad and weak V_P signal so that when Brillouin scattering is collected for powdered samples of bridgmanite, no V_P acoustic velocity can be measured at any pressure.

Diamond Anvils with a Round Table (DART-anvils) provide several advantages over conventional diamond anvil. They allow a substantial enlargement of the sample image (approximately a factor of 2.4), thereby improving spatial resolution. Importantly, DART-anvils act as solid lenses that focus the laser beam during Brillouin scattering experiments, simultaneously reducing the contribution of Brillouin signals originating from the diamond, enabling reliable observation of the V_P signal of bridgmanite.

In this study, polycrystalline $MgSiO_3$ bridgmanite samples with an average grain size of ~ 1 µm were synthesised at 24 GPa and 1700 K and prepared as thin disks (10 µm in thickness and 30 µm in diameter) using focused ion beam. Acoustic wave velocities were measured at high pressure using Brillouin scattering combined with DART-anvils (Fig. 3.4-6), providing the first measurements of V_P from powdered samples. Both acoustic velocities are systematically lower than the aggregate velocities calculated from the elastic tensor determined for the bridgmanite single-crystals in a previous study conducted here at BGI, which may be attributed to multiple scattering events between the incident Brillouin light and the polycrystalline grains when the optical wavelength is comparable to the grain size. Future work will include finite-element simulations to quantify these scattering effects, as well as Brillouin scattering experiments combined with DART-anvils and laser-heating systems to obtain elastic parameters of bridgmanite under simultaneous high-pressure and high-temperature conditions, thereby improving constraints on the composition of the Earth's lower mantle.

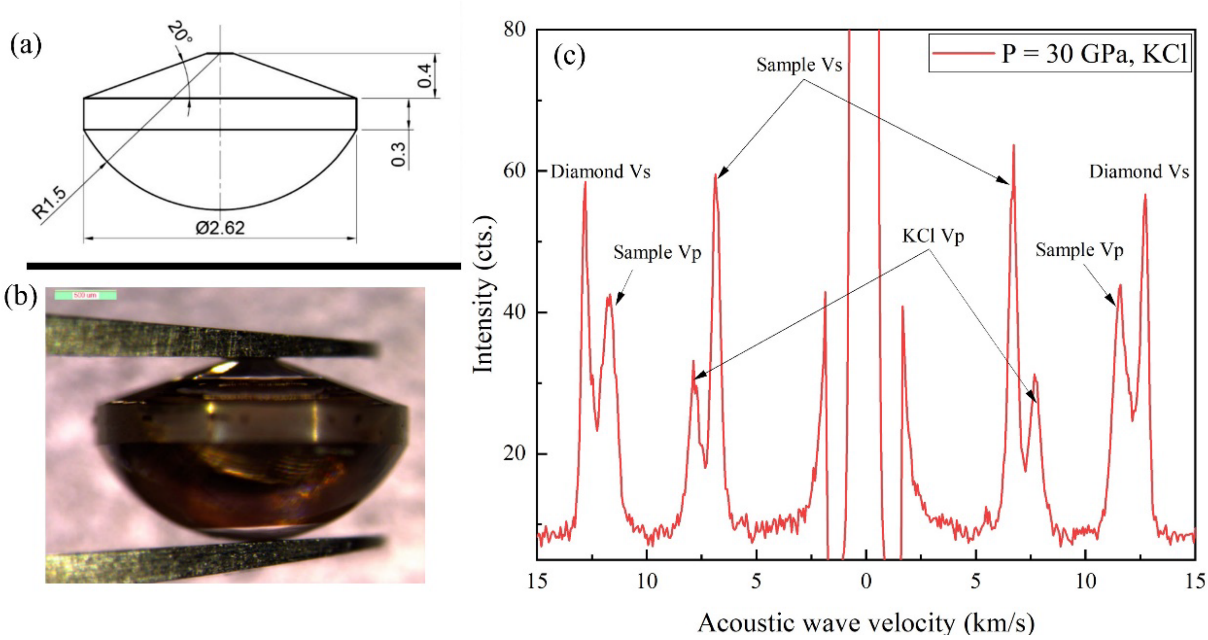

Fig. 3.4-6: (a) schematic and (b) microscope image of the DART-anvil; (c) Brillouin spectrum collected at 30 GPa and room temperature where strong V_S and V_P signals of bridgmanite are observed, together with a weaker signal due to the pressure-transmitting medium (KCl) and to the diamond anvils.

g. *New data for the elasticity of quartz (G. Mingardi/Paris, R.J. Angel/Padova, A. Kurnosov and T. Boffa Ballaran)*

At the pressure and temperature conditions of the lower crust quartz undergoes a displacive phase transition from its trigonal α-phase to a hexagonal β-phase. At room pressure, the α-β quartz transition occurs at 574.1 °C and it is associated with large changes in thermodynamic and elastic properties. In particular, the bulk modulus K drops from approximately 70 GPa to nearly zero over a narrow temperature range of just 10-15 K. While the transition has been extensively studied at ambient pressure, the elasticity of β-quartz under high-pressure and high-temperature conditions (relevant to Earth's lower crust) were unknown until our own recent ultrasonic wave velocity measurements on polycrystalline β-quartz in a multianvil press at the

ESRF. These suggested that the compressional wave velocities (V_p) of β-quartz and *K* are significantly lower than those predicted by current models (Fig. 3.4-7).

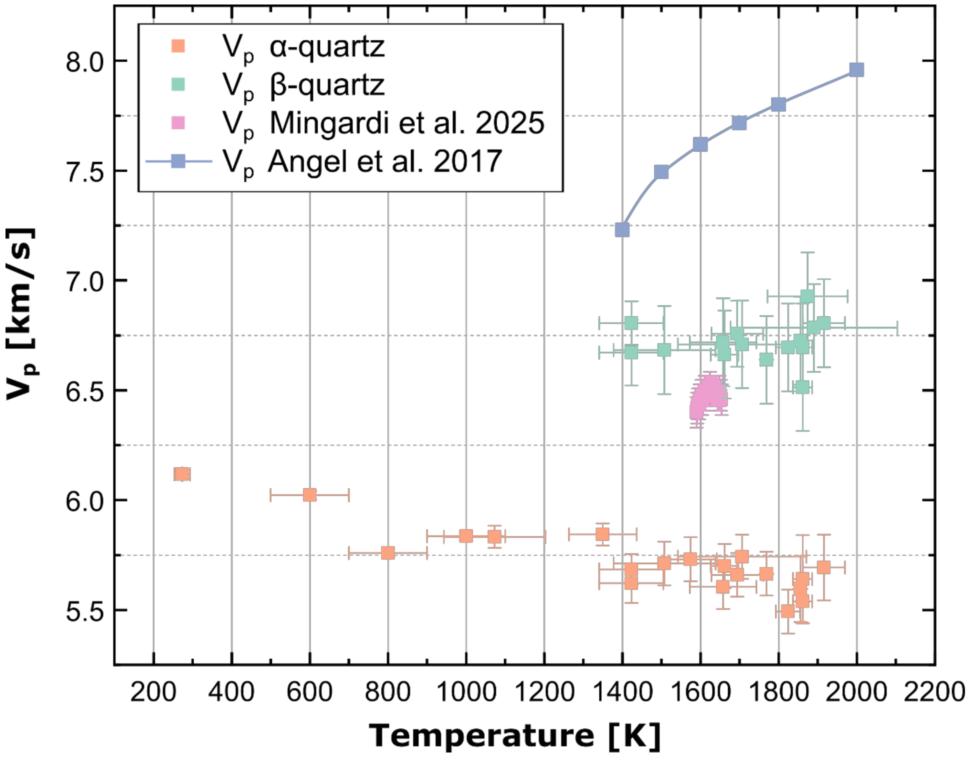

Fig. 3.4-7: Velocities in the α and β field of quartz obtained from Brillouin scattering and compared in the β-field with the EoS data from Angel *et al.*, 2017, CMP, 172, 29 and the synchrotron multianvil data reported in Mingardi *et al.*, 2025, CMP, 180, 21.

Given the difficulties of measurements at these pressure and temperature conditions and the importance of this result, we performed laser-heated diamond anvil cell experiments at ~ 2 GPa at the BGI. We collected single-crystal X-ray diffraction data and sound velocities from both α- and β-quartz using Brillouin scattering. We believe that these are the first Brillouin measurements made on any material at these low pressures and high temperatures. The preliminary data appear in agreement with the velocities and bulk moduli determined in synchrotron experiments. The elastic properties of α-quartz at simultaneous high pressure and high temperature appear to be close to published equations of state (EoS), but there is a large discrepancy with the velocities and the bulk modulus predicted by the current EoS for β-quartz (Fig. 3.4-7). The single crystal data indicate that at 2 GPa and 1800 K, in the β-field, the measured bulk modulus is 60 GPa against the 90 GPa predicted by the EoS of quartz at these conditions. These experiments have therefore provided important evidence that interpretations of seismic data based on the elastic properties of β-quartz in the lower crust, as well as entrapment condition estimates for quartz inclusions in the β-quartz stability field, may well be in error and should be approached with caution.

h. *Elasticity of Ti-bearing calcium silicate perovskite (Y. Wu/Wuhan, T. Boffa Ballaran, A. Kurnosov and D.J. Frost, in collaboration with T. Ishii/Misasa)*

Cubic perovskite-type $CaSiO_3$, also known as davemaoite, is considered the third most abundant phase in the Earth's lower mantle. As such, the structural stability and physical properties of davemaoite are critical for constraining the density and physical properties of mineralogical models of the lower mantle. However, davemaoite is unquenchable and cannot be recovered to ambient conditions, making direct experimental measurements of its physical properties technically challenging. To overcome this limitation, quenchable, perovskite-structured analogues in the $CaSiO_3$-$CaTiO_3$ system have gained increasing attention in the research community. Here we present the first single-crystal Brillouin scattering measurements of a Ti-bearing Ca silicate perovskite sample.

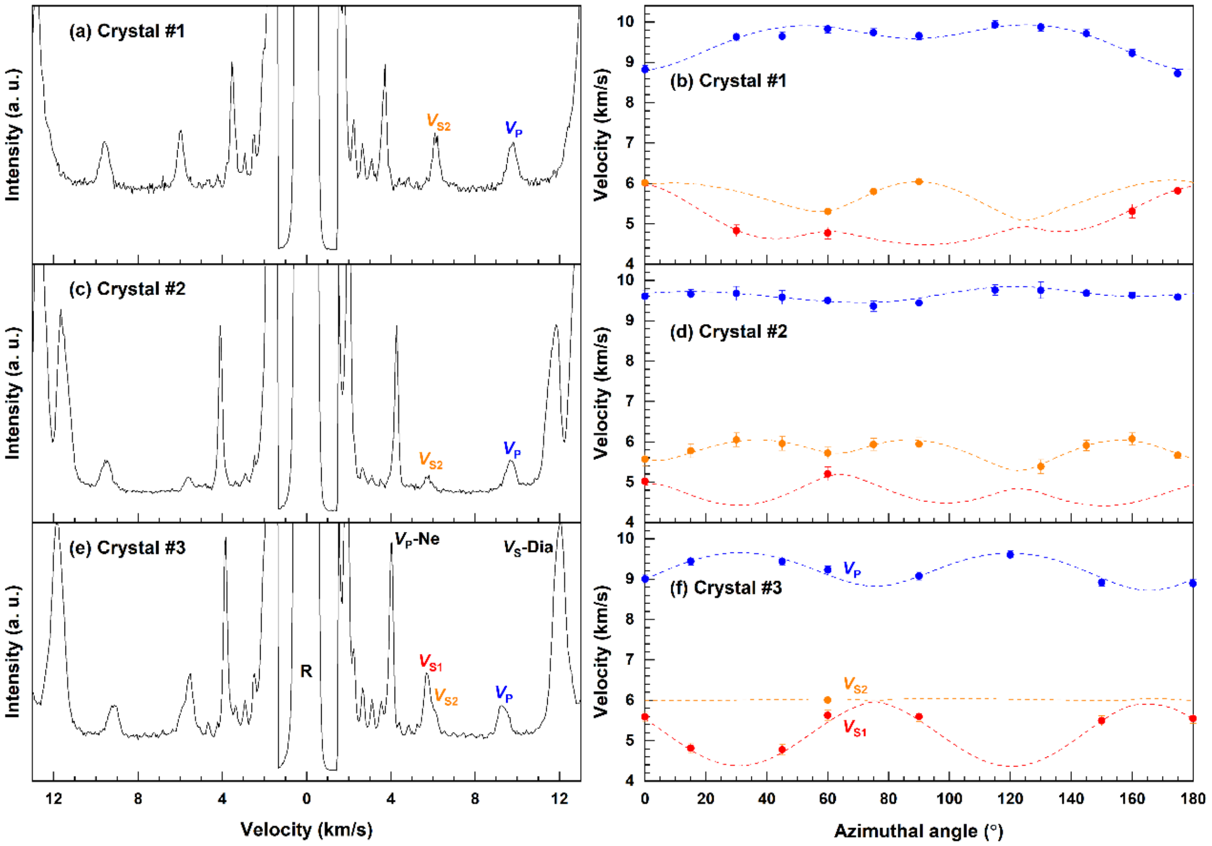

Fig. 3.4-8: Representative Brillouin light scattering spectra and sound velocities as a function of azimuthal angle of three single-crystal platelets for Ti-bearing calcium silicate perovskite ($CaSi_{0.53}Ti_{0.47}O_3$) at ~ 0.2 GPa and room temperature.

Three orthorhombic single-crystals with composition $CaSi_{0.53}Ti_{0.47}O_3$ were selected and double-polished down to a thickness of 10 µm in three different general orientations in order to constrain the nine independent elastic coefficients of the elastic tensor of this material. The crystals were loaded in a diamond anvil cell with helium as pressure-transmitting medium at a pressure of 0.2 GPa. X-ray diffraction was used to determine the unit-cell lattice parameters and volume of each crystal in order to determine their density. Brillouin scattering measurements were conducted at several chi angles in order to constrain the Ti-bearing calcium silicate perovskite anisotropy (Fig. 3.4-8). The full elastic tensor was obtained through the best fit of the measured acoustic velocities using the Christoffel equation. The adiabatic bulk and shear moduli, the aggregate longitudinal and shear velocities, and the sound velocity anisotropies of Ti-bearing calcium silicate perovskite were derived from the single-crystal elastic coefficients. Both bulk and shear moduli increase linearly with increasing mole fraction of $CaSiO_3$.

i. *Ultra-low-velocity disordered $CaCO_3$ may explain mid-lithospheric discontinuities (P. Zhang, L. Yuan, X. Wu and J. Zhang/Wuhan; L. Man)*

Cratons, the Earth's oldest continental nuclei, are underlain by thick, chemically buoyant mantle roots that extend hundreds of kilometres into the mantle. A defining seismic feature of the cratonic lithospheric mantle (CLM), which constitutes over 80 % of total craton thickness, is the mid-lithospheric discontinuity (MLD). MLDs are characterised by 2-7 % reductions in shear-wave velocity (V_S) across 15-30 km, typically occurring at depths of 80-120 km. This widespread feature – identified in 9 of 12 cratons globally – has long puzzled researchers and remains a key unsolved problem in understanding continental stability and evolution. As a major carbon reservoir, the CLM stores carbon primarily in the form of carbonates such as $CaCO_3$. Although phase transitions in $CaCO_3$ under high-pressure, high-temperature conditions have been investigated for decades, substantial discrepancies persist among reported phase boundaries. Further complexity arises from orientational disorder in $CaCO_3$, in which Ca and C atoms remain fixed while CO_3 groups rotate freely. This disordered behaviour, coupled with the mineral's unquenchable nature, obscures experimental characterization at ambient conditions. Consequently, the limited knowledge of $CaCO_3$ elasticity hampers efforts to link carbon storage in the CLM to observed seismic anomalies associated with MLDs.

Using density functional theory based, machine learning-accelerated molecular dynamics simulations that extend beyond conventional time and length scales, we identify a previously unrecognised phase transition in disordered $CaCO_3$ under MLD-relevant conditions (3-5 GPa and 1300-1500 K). This transition produces pronounced elastic softening – reducing the bulk and shear moduli by approximately 15 % and 45 %, respectively – and leads to exceptionally low sound velocities (*e.g.*, V_S = 2.04 km/s at 3.7 GPa and 1300 K), far lower than those of hydrous minerals, including H_2O ice (Fig. 3.4-9). Unlike hydrogen, which readily dissolves in peridotite and enhances electrical conductivity, carbon is insoluble in crystalline silicates and therefore exerts negligible influence on mantle conductivity as an isolated phase. Our results suggest that carbonated regions of the CLM containing small amounts of ultra-low-velocity disordered $CaCO_3$ provide a simple and self-consistent explanation for the origin of MLDs, particularly in dry mantle domains characterised by high resistivity in magnetotelluric surveys.

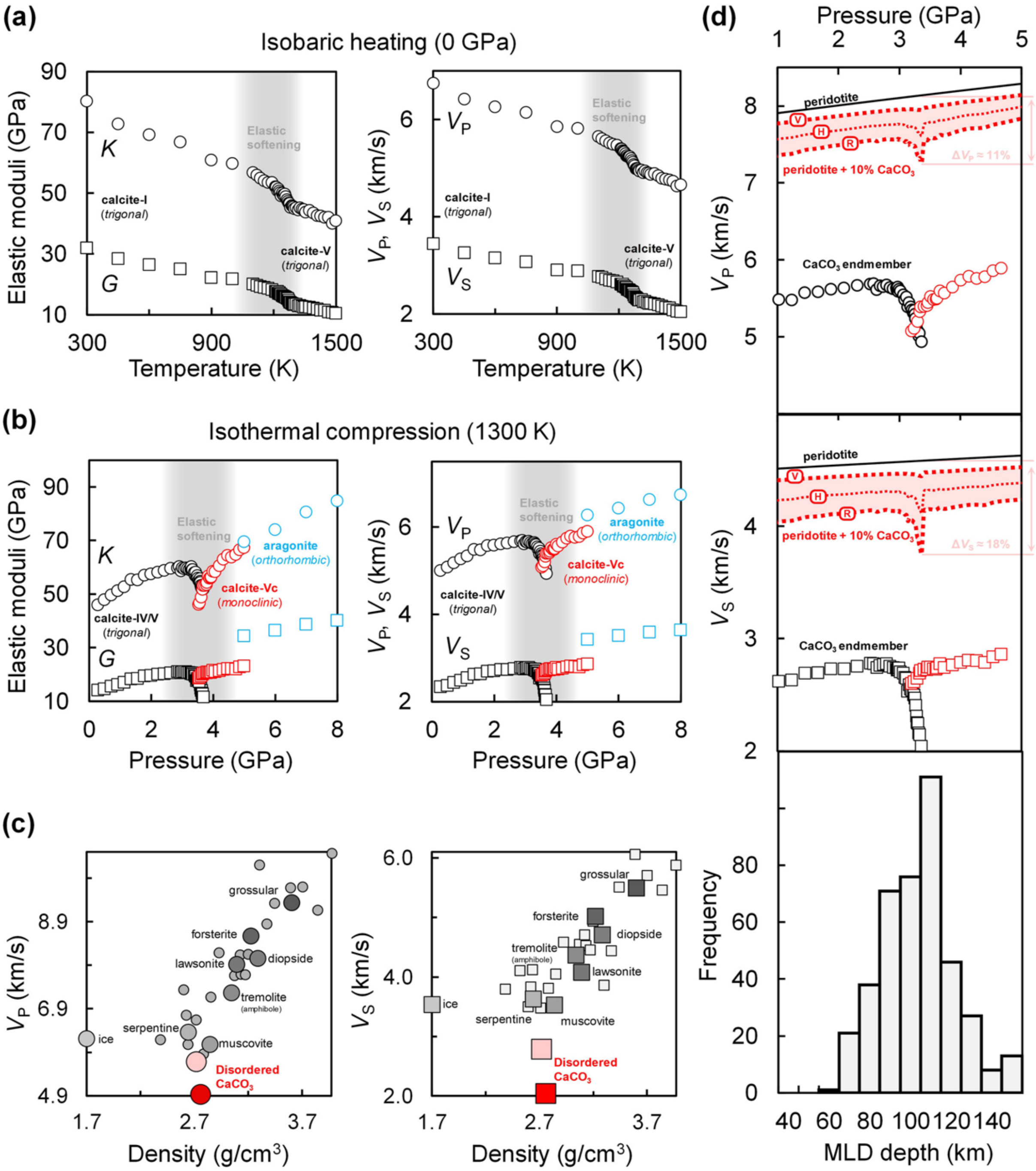

Fig. 3.4-9: Seismic properties of $CaCO_3$ aggregate and $CaCO_3$-bearing peridotite. (a) Left: Temperature-dependent adiabatic bulk (K) and shear (G) moduli. Right: Corresponding compressional (V_P) and shear (V_S) wave velocities. The shaded grey region indicates elastic precursor softening associated with the $CaCO_3$ order-to-disorder transition. (b) Left: Pressure-dependent K and G. Right: Corresponding V_P and V_S. The shaded grey region highlights elastic precursor softening linked to the trigonal-to-monoclinic transition. (c) Disordered $CaCO_3$ velocities are compared to those of major mantle silicates (*e.g.*, olivine, pyroxenes, garnet) and hydrous minerals (*e.g.*, serpentine, amphibole). (d) Upper and middle panels: V_P and V_S of $CaCO_3$-bearing peridotite as functions of depth and pressure (corrected by -0.33 GPa) at 1300 K. Lower panel: Observed depth distribution of the mid-lithospheric discontinuity.

3.5 Fluids, Melts and their Interaction with Minerals

The volatile elements carbon, nitrogen, and hydrogen largely determine the habitability of Earth's surface. However, the main reservoir of these elements in our planet may be the mantle and therefore, studying the storage of volatiles in the mantle and the processes that exchange them with the surface reservoirs is essential for understanding Earth's evolution. Among the volatile elements, nitrogen has always been particularly enigmatic. From abundances in near-surface reservoirs and upper mantle samples, it appears that nitrogen is depleted on Earth by about one order of magnitude relative to carbon and hydrogen. However, previous work at BGI had already suggested that maybe this apparent depletion is an artifact due to the preferential sequestration of nitrogen in a lower mantle reservoir that is poorly sampled. The first contribution in this section of the annual report lends further support to this idea. New experimental data show that nitrogen solubility in Fe and Al-bearing bridgmanite, the most abundant mineral of the lower mantle, is much higher than previously inferred from experiments in the pure $MgSiO_3$ system.

The subduction of oceanic crust continuously recycles volatiles from Earth's surface back into the mantle. However, the efficiency of this process is not yet fully constrained. Some previous studies had suggested that SiO_2 stishovite could be a main carrier of water deep into the lower mantle. However, new *in situ* X-ray diffraction experiments in a multianvil apparatus suggest that water solubility in stishovite strongly decreases with temperature, which limits its efficiency for transporting water into the lower mantle. The subduction of carbon is perhaps even more controversial than the recycling of water into the mantle. Recently, there have been suggestions that in addition to CO_2 and CH_4, organic carbon species may be stable in subduction zone fluids at high pressure. This was tested by piston cylinder experiments, which trapped high-pressure fluids as synthetic fluid inclusions in quartz. The results imply that at high-pressure and high-temperature conditions in stable equilibrium all carbon is present as CO_2, CH_4, or graphite. However, the experiments also show that organic carbon species may persist metastably to surprisingly high temperatures.

The remaining contributions in this section of the annual report all investigate the properties of magmas and their consequences for planetary evolution and volcanic activity. Water may reduce the viscosity of silicate melts by many orders of magnitude and it also has a drastic effect on many other properties. This is partially due to the fact that water chemically reacts with the melt according to the equilibrium $H_2O + O^{2-} = 2\ OH^-$. While this equilibrium is well studied for silicic melts, it is poorly constrained in basaltic systems. A new project attempts to constrain the temperature dependence of this equilibrium by long-term annealing experiments below the glass transformation temperature. Initial results suggest that this may be a promising strategy.

The two following contributions develop models for the viscosity of silicate melts. Magmas on Mars are more Fe-rich than their terrestrial analogues and *in situ* measurements of Martian peridotite melts confirm that their viscosity is lower than that of terrestrial analogues. These data will be used to constrain the early evolution of Mars. On Earth, hydrous andesitic magmas are a main source of volcanic risk. A new viscosity model suggests that for example the magmas of Sakurajima volcano in Japan are 45 times less viscous than previously thought.

The last two contributions in this section of the annual report describe experiments that directly simulate volcanic processes in the laboratory, in particular bubble nucleation in volcanic conduits and magma fragmentation during explosive eruptions. Technologically very impressive is the time-resolved, three-dimensional imaging of evolving bubbles using synchrotron radiation.

a. *Fe-bearing bridgmanite as a major host of nitrogen in the lower mantle (G. Rustioni, M. Wiedenbeck/Potsdam and H. Keppler)*

In contrast to Mars and Venus, Earth's atmosphere is dominated by nitrogen. Nitrogen concentrations in the accessible upper mantle reservoirs, however, are very low, such that in the bulk Earth, nitrogen may appear depleted relative to other volatiles such as carbon and hydrogen. The origin of this apparent nitrogen depletion on Earth has been a subject of intense debate. Research in the last years at BGI suggests that perhaps this depletion is not real, but an artifact of incomplete sampling of a nitrogen-rich reservoir deep in Earth's mantle. Indeed, minerals of the transition zone easily dissolve hundreds of ppm N by weight, and Fe-rich magnesiowüstite near the core-mantle boundary can even dissolve several wt. % of N. So far, however, nitrogen solubility in bridgmanite, the dominant mineral of the lower mantle and at the same time, the most abundant mineral in the entire planet Earth was only poorly constrained. Previous experiments in the pure $MgSiO_3$ system seemed to suggest very low solubilities in the order of a few ppm. In this project, we systematically studied nitrogen solubility in Fe and Al-bearing bridgmanite of realistic mantle composition from 24 to 33 GPa and from 1600 to 1800 °C. Oxygen fugacity was buffered near the Fe-FeO equilibrium.

Experiments were carried out in multianvil presses. Oxide mixtures were sealed with metallic iron into platinum capsules. As a source of nitrogen, ^{15}N-doped NH_4NO_3 was added. After the experiments, samples were sectioned and polished and nitrogen contents were measured by SIMS (secondary ion mass spectrometry) at GFZ Potsdam. ^{15}N-implanted single crystals of forsterite served as standards for quantification.

Figure 3.5-1 shows a typical run product with bridgmanite coexisting with magnesiowüstite and a metal phase. Due to some exchange with the capsule material, the metal is not pure Fe, but some Fe-Pt alloy, which causes some variations of oxygen fugacity between the experiments. Nitrogen solubility in bridgmanite as measured by SIMS is shown in Figure 3.5-2. Nitrogen solubility in Al-poor bridgmanite is very low, in the order of a few ppm, but increases to nearly 100 ppm for 3 wt. % Al_2O_3. At higher alumina contents in the bridgmanite, N solubility stays constant or maybe even slightly declines. The scatter in the data in Figure 3.5-2 is mostly due to variations in oxygen fugacity (see figure caption for further details).

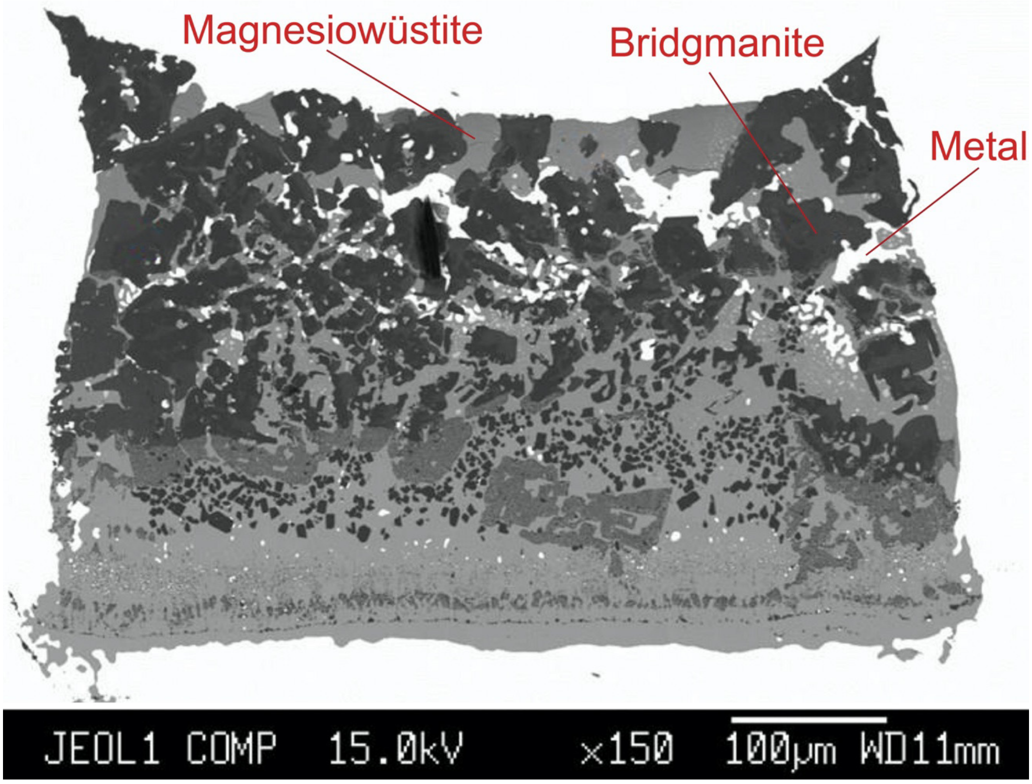

Fig. 3.5-1: Fe-bearing bridgmanite coexisting with magnesiowüstite and Fe-rich metal in the run product of an experiment quenched from 24 GPa and 1700 °C

The initial increase of nitrogen solubility with Al content and the levelling-off at high Al can likely be explained by a speciation model. Unfortunately, at the rather low N concentrations observed, it is difficult to infer the substitution mechanism of nitrogen by spectroscopic evidence. Possibilities include a coupled substitution of NH^{4+} + Al^{3+} for 2 Mg^{2+} or a substitution of N^{3-} for O^{2-} charge-compensated by Al^{3+} substituting for Mg^{2+}. Both mechanisms imply a molar 1:1 ratio of Al:N, which would predict a linear increase of N solubility with Al concentration. However, it is well established that at high Al concentrations in bridgmanite, most Al is incorporated by a charge coupled substitution mechanism of 2 Al^{3+} replacing Mg^{2+} + Si^{4+}. This substitution mechanism is expected to increase with the square of alumina activity and therefore dominates at high Al content, such that increasing Al does not further enhance nitrogen solubility.

The observed enhanced nitrogen solubility in Fe and Al-bearing bridgmanite provides further support for the idea that nitrogen may not be anomalously depleted on Earth, but rather it is concentrated in a deep mantle reservoir. 100 ppm N in bridgmanite throughout the entire lower mantle would correspond to 58 times the mass of nitrogen currently residing in Earth's atmosphere. While the lower mantle certainly is not nitrogen-saturated and the actual nitrogen concentrations almost certainly are below the maximum solubility level, it is still plausible that during magma ocean crystallization a large fraction of the bulk nitrogen in the Earth was sequestered by a deep reservoir that is poorly sampled by current geologic activity.

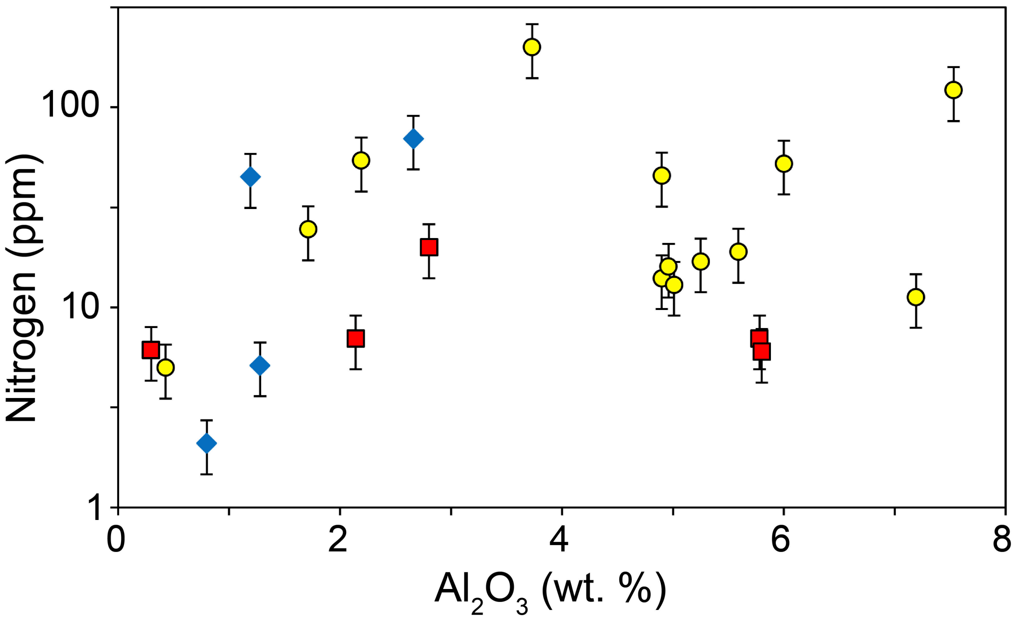

Fig. 3.5-2: Nitrogen solubility in Al and Fe-bearing bridgmanite close to Fe-FeO buffer conditions. Different colors correspond to variations in oxygen fugacity, as indicated by the composition of the coexisting Fe-alloy. Blue data points (> 50 wt. % Fe in the alloy) refer to the most reducing conditions, red data points (< 10 % Fe in the alloy) to the most oxidizing conditions, yellow data points are in between.

b. *Water storage in stishovite at deep mantle conditions (F. Wang, A. Chanyshev, L. Man, Y. Song, L. Wang, T. Ishii/Misasa, N. Tsujino/Sayo, S. Bhat/Hamburg, R. Farla/Hamburg and T. Katsura)*

Over geologic time, the long-term water cycle involving exchange between the surface and the deep mantle has played an important role in Earth's evolution. In this cycle, the amount of water in the mantle depends on how much water is transported downward by subducting slabs. However, this process remains poorly constrained, because most hydrous minerals break down near the top of the lower mantle, making the efficiency of deep water transport uncertain. Stishovite has been proposed as a major carrier of water into the lower mantle, but its role remains uncertain due to conflicting experimental data: Laser-heated diamond anvil cell experiments suggest very high-water solubility at high pressures, whereas multianvil experiments indicate much lower values.

To resolve this discrepancy, we investigated the water solubility in Al-free stishovite at 33-38 GPa and 700-1200 K using *in situ* X-ray diffraction in an advanced multianvil apparatus. In our experiments, hydrous stishovite formed at 34-38 GPa and 670-700 K. Observed excess volumes (ΔV), the differences between the unit cell volumes of hydrous and anhydrous stishovite at identical conditions, correspond to 1.8-3.6 wt. % H_2O (Fig. 3.5-3). However, ΔV decreased progressively with heating and became negligible above ~ 900-1000 K, at which point the unit-cell volumes matched the anhydrous equation of state. These results, reproduced in two independent runs, demonstrate that although stishovite can incorporate several wt. % H_2O at low temperatures (< 700 K), it rapidly dehydrates at higher temperatures. Thus, stishovite containing more than ~ 1 wt. % H_2O is strictly a low-temperature phase and cannot retain water at geophysically relevant conditions (> 1000 K). This suggests that pure SiO_2 stishovite is unlikely to serve as a major carrier of water into the deep lower mantle.

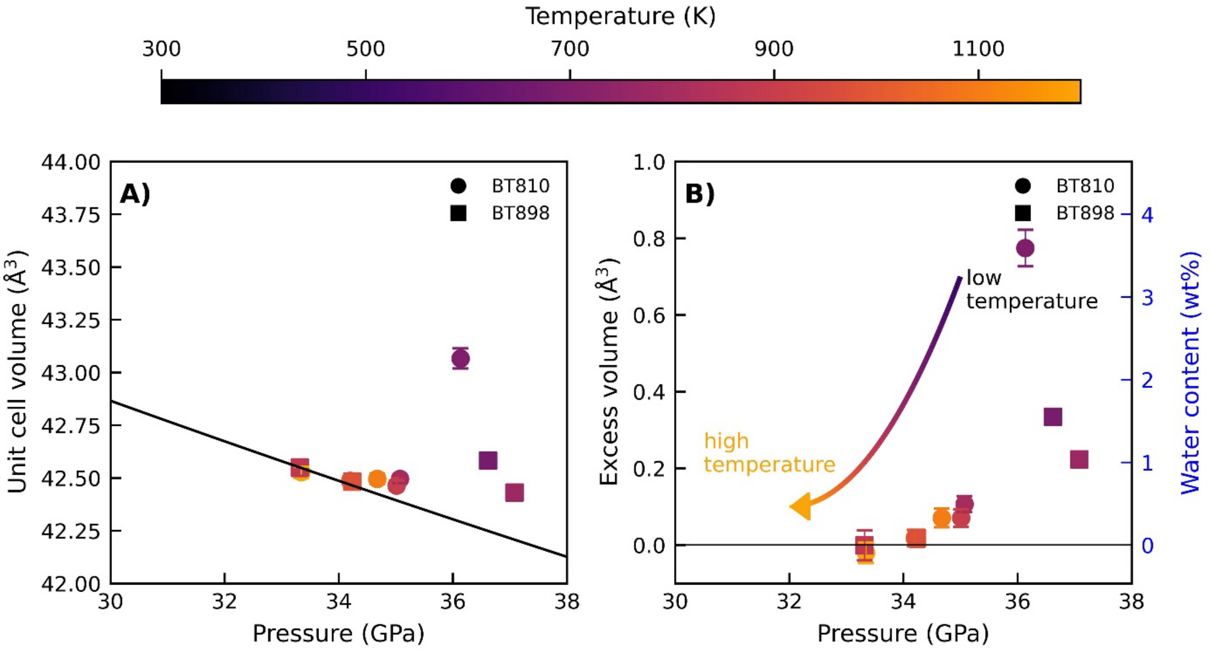

Fig. 3.5-3: (A) Measured unit cell volume of stishovite at high pressure and 300 K. Circles and squares show data from two separate experimental runs (BT810 and BT898) after quenching to room temperature. The symbol color shows the temperature to which the sample was heated prior to quenching. The solid black line is the equation of state of anhydrous stishovite parameter-fitted in this study. (B) Excess volume (left axis) of hydrous stishovite and its water content (right axis). The curved arrow shows the water solubility trend from low to high temperature. The symbol color shows the temperature, to which the sample was heated prior to quenching.

c. *Experiments on the stability of organic molecules in subduction zone fluids (P. Zampras and H. Keppler)*

Fluids released upon dehydration of the subducted slab are responsible for the formation of arc magmas and therefore, the growth of the continental crust. They may also contribute to the metal enrichment that leads to economically important porphyry deposits. The composition and properties of these fluids have therefore been intensely studied. Relatively recently, it was suggested that in addition to inorganic gas species and solutes, some organic molecules could also be stable at typical subduction zone conditions. In order to test this hypothesis, we carried out a series of piston cylinder experiments at 2-3 GPa and 500-600 °C in order to trap equilibrated fluids as synthetic fluid inclusions. Starting material was an aqueous solution containing 5 wt. % each of sodium acetate, sodium proprionate, and sodium benzoate. This mixture was chosen to test for the stability of a range of aliphatic and aromatic hydrocarbons. The solution was sealed into Pt capsules of 2 mm diameter together with pre-cracked cores of quartz or olivine. These inner capsules were then enclosed in outer capsules containing Co metal and water, in order to buffer oxygen fugacity near the Co-CoO equilibrium. Run durations lasted up to 11 days.

Figure 3.5-4 shows fluid inclusions in quartz from one experiment at 2 GPa and 600 °C. A curious observation here is that there are two different kinds of fluid inclusions: Dark ones and light-colored inclusions, coexisting within the same sample. Raman spectra (Fig. 3.5-5 and 3.5-6) also show the presence of very different molecular species in the two types of fluid inclusions. The light-colored inclusions contain abundant carbon monoxide (CO) and they show a Raman signal that suggests the persistence of some organic C-H species. In contrast to this, no evidence for organic species is seen in the dark inclusions, which appear to contain mostly H_2O, CH_4, and CO_2.

The presence of abundant carbon monoxide in the light-colored inclusions suggests incomplete equilibration, as the equilibrium $2\ CO = C + CO_2$ should be shifted far to the right-hand side at high pressure. We therefore argue that the light-colored inclusions preserve a metastable fluid composition, while in the dark-colored inclusions, full equilibrium was reached by precipitation of graphite. It therefore appears that under experimental conditions, organic species are not stable anymore. These results, however, do not preclude that organic species may become stable again at higher pressures or different oxygen fugacities. This will require further experimental studies.

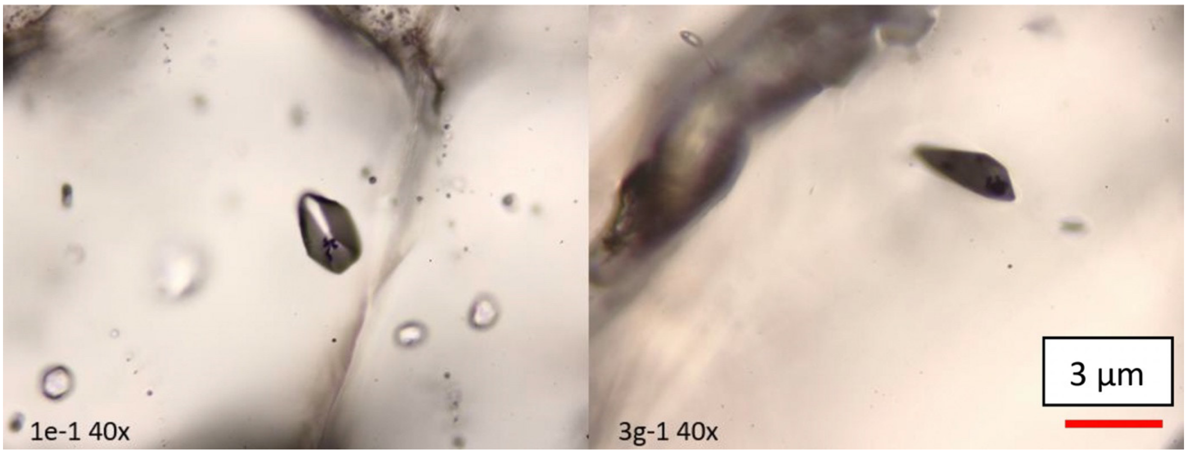

Fig. 3.5-4: Fluid inclusions in quartz formed in two experiments at 2 GPa and 600 °C. Larger dark fluid inclusions (left and right) coexist with smaller light-colored inclusions (left). The dark color is likely caused by the precipitation of graphite on the inner surface of the inclusion. Graphite failed to precipitate in the light-colored inclusions.

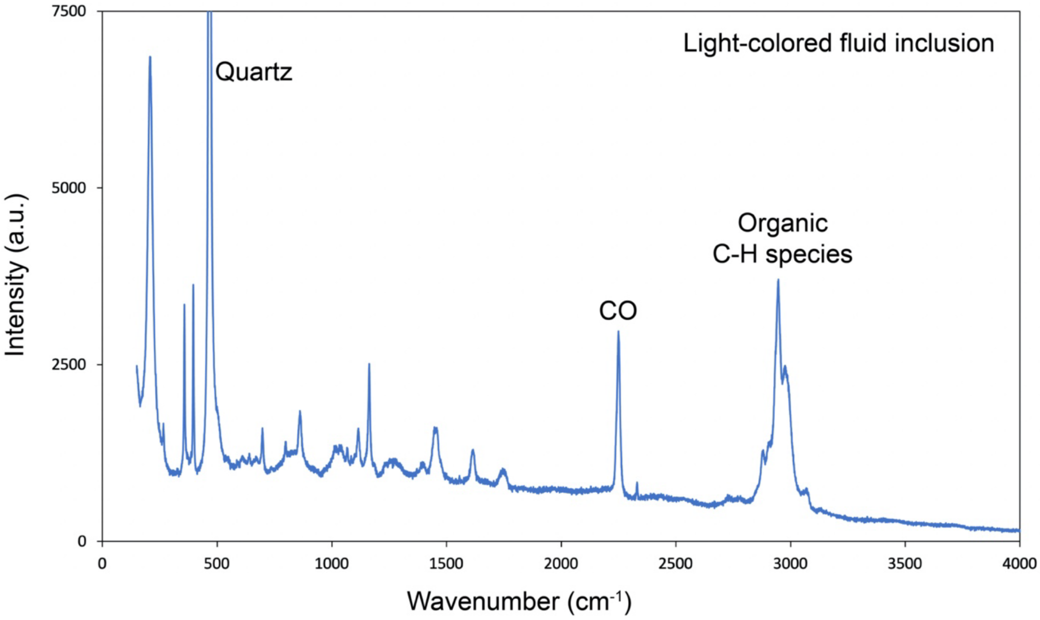

Fig. 3.5-5: Raman spectrum of a light-colored fluid inclusion in quartz from an experiment at 600 °C and 2 GPa. Prominent peaks are due to carbon monoxide (CO) and to metastable organic C-H species causing a signal with complicated fine structure near 3000 cm^{-1}. There are also Raman bands of organic species visible at lower frequency, notably bending vibrations of -CH_2 and -CH_3 groups just below 1500 cm^{-1}.

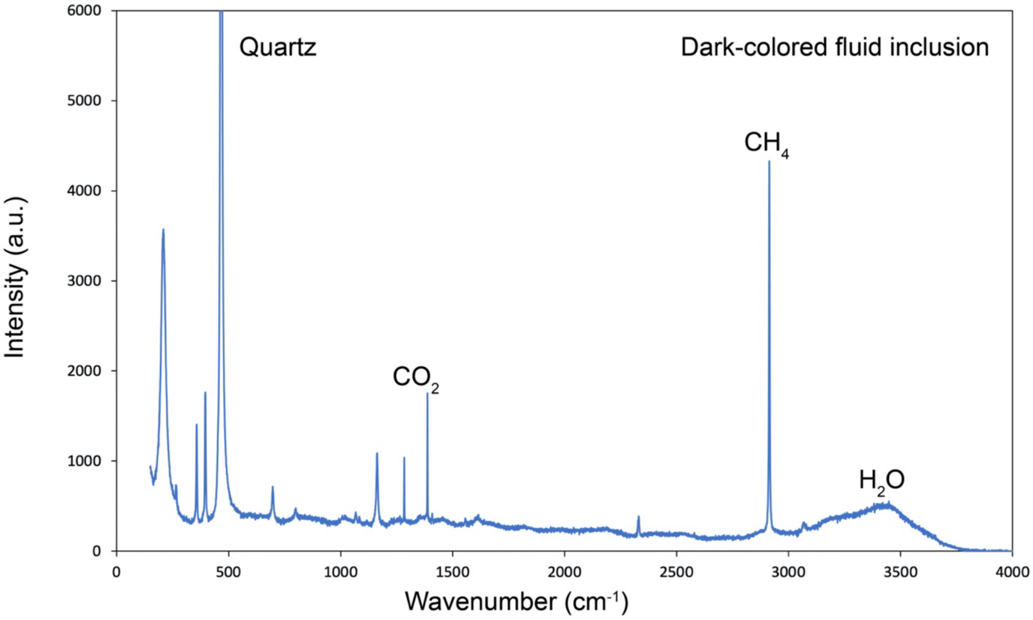

Fig. 3.5-6: Raman spectrum of a dark-colored fluid inclusion in quartz from an experiment at 600 °C and 2 GPa. Most prominent Raman feature are a sharp and intense CH_4 stretching vibration band near 2900 cm^{-1}, a broad band due to H_2O and the characteristic double band of the Fermi diade of CO_2. There is no indication for the persistence of organic species, they seem to have completely decomposed to CH_4, CO_2, and H_2O (plus some graphite that is not visible in the spectrum).

d. *The effect of temperature on the speciation of H_2O in a mid-ocean ridge basalt (A. Curtolo and H. Keppler)*

Water is the most abundant volatile species in the Earth's mantle and strongly influences the physical properties (*e.g.*, viscosity, electrical conductivity, melting temperature) of both minerals and melts. Moreover, water plays an important role in the generation and evolution of magmas at mantle depth as well as in the dynamics of volcanic systems.

Several spectroscopic studies in the past showed that water dissolves in silicate melts in the form of molecular H_2O and as OH groups produced by the reaction with bridging oxygen atoms. The formation of OH groups (which is described by the reaction $H_2O + O^{2-} = 2\ OH^-$) depolymerizes the melt by breaking the Si-O-Si bonds and drastically reduces its viscosity. Early studies assumed that the speciation of water observed in glasses quenched from high temperature reflects the speciation of water in the melt at the temperature at which the glass was quenched. This was later shown to be incorrect as structural relaxation of silicate melts above the glass transition temperature (T_g) is extremely fast and this prevents the speciation of water at temperature above T_g from being preserved upon quenching. However, the temperature dependence of water speciation can still be investigated experimentally by annealing glasses below T_g for a time long enough to allow structural relaxation. Rapid cooling after the annealing preserves the equilibrium speciation of water at the annealing temperature because of the longer relaxation timescales below T_g. In the current study, we use this approach to investigate water speciation in basaltic melts. While speciation is well studied in silicic systems, direct data on the temperature dependence of water speciation in basaltic melts are lacking. Such data are for example important to constrain the stability of small fractions of melt in the upper mantle.

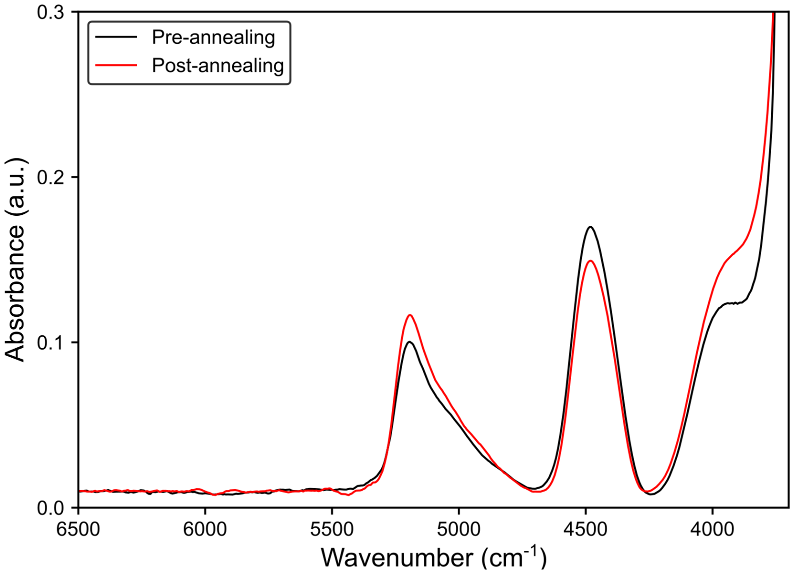

Fig. 3.5-7: Infrared spectra of a hydrous glass with about 2.2 wt. % of water before and after annealing at 415 °C for two weeks. Upon annealing, the OH band at 4500 cm^{-1} has decreased, while the H_2O band at 5200 cm^{-1} increased, indicating re-equilibration of water speciation.

Hydrous MORB (mid ocean ridge basalt) glasses were prepared in an internally heated pressure vessel at 2 kbar and 1250 °C. These glasses were subsequently annealed for up to two weeks run duration at temperatures below T_g using cold-seal pressure vessels. Water speciation was investigated before and after annealing by measuring FTIR spectra on doubly-polished samples. Figure 3.5-7 shows that the annealing clearly changed water speciation in the samples. Time-series experiments are currently being conducted to constrain equilibrium water speciation as a function of temperature. From the measured OH and H_2O concentrations, the equilibrium constant of the speciation reaction ($K = [OH^-]^2/\{[H_2O][O^{2-}]\}$) will be calculated.

e. In situ *viscosity measurements on iron-rich silicate melts under high pressure: Evaluating the solidification regime of the Martian magma ocean (R. Pierru, L. Man, J. Monteux/Clermont-Ferrand, S. Gréaux/Matsuyama, S. Kakizawa/Hyogo, Y. Kono/Osaka, L. Henry/Paris, D. Bondar, S. Gao/Leuven, R. Farla and X. Feng/Hamburg, G. Golabek, D. Antonangeli/Paris, and D.J. Frost)*

NASA's InSight mission has provided unprecedented seismic constraints on the interior of Mars, reinforcing the view that the planet once hosted a global magma ocean during its early differentiation. The crystallization and cooling of this primordial molten mantle likely shaped the planet's long-term thermochemical evolution, influencing heat transport, core formation, crustal extraction, and the present-day structure of the mantle. A key property governing the dynamics of a magma ocean is the viscosity of silicate liquids, which controls convective vigor, heat loss to space, chemical exchange between silicates and the metallic core, and the settling or suspension of crystals that drive fractional crystallization. The Martian mantle is richer in iron than Earth's mantle, and this elevated Fe content is expected to modify melt structure, to lower liquidus temperatures, and to reduce viscosity relative to terrestrial peridotitic compositions. However, experimental data on the viscosity of iron-rich silicate melts at high pressure remain scarce, especially under conditions relevant to the deep Martian interior. New viscosity constraints are therefore essential for developing realistic models of magma ocean evolution and for quantifying the timescales and mechanisms of early mantle differentiation on Mars. Such data are also required to assess whether the partially molten region inferred by InSight could represent a long-lived remnant of the ancient magma ocean, rather than a transient thermal anomaly at the core–mantle boundary.

We synthesized silicate powders representative of proposed Martian mantle compositions under controlled-atmosphere conditions (QFM–2). These starting materials were pressed into pellets and loaded into capsules for high-pressure viscosity experiments. Two synchrotron beamtimes were conducted in 2025, the first at Spring-8 (BL04B1) and the second at DESY (P61B), providing complementary constraints on melt behaviour at conditions relevant to the deep Martian mantle. To measure viscosity, small Re spheres (≈80-110 µm in diameter) were positioned at the top of the charge and tracked as they sank through the melt. Real-time X-ray radiography, recorded with a high-speed camera (100-1000 fps), allowed precise monitoring of their motion throughout the experiment. Sinking velocities were obtained from the linear portion of the displacement–time curves using least-squares regression.

Our high-pressure sinking-sphere experiments on Fe-rich silicate melts yield viscosities that plot slightly below the range of existing peridotite data obtained for terrestrial compositions (Fig. 3.5-8), consistent with the expected depolymerizing effect of iron on melt structure. By parameterizing these results with an Arrhenius-type formulation, we now can describe the viscosity of Martian liquids as a function of both pressure and temperature across the stability field of deep mantle melts. In addition to viscosity, our experimental campaign – combining synchrotron measurements (DESY P61B and Spring-8 BL04B1) with complementary high-pressure melting experiments at BGI – has enabled us to constrain the liquidus curve for Fe-rich Martian mantle analogues (Fig. 3.5-9). This liquidus parameterization will be integrated jointly with our viscosity model to ensure thermodynamically consistent treatment of melt mobility along the crystallization path of the magma ocean. We will apply our viscosity–liquidus model to construct a geodynamical model for the cooling of the Martian magma ocean. By integrating our experimental constraints with existing theoretical frameworks, we aim to investigate the role of iron in controlling melt viscosity and its implications for key planetary magmatic processes, including the lifetime of a magma ocean. This coupled liquidus–viscosity framework will provide a more reliable rheological description of Fe-rich magmatic systems and will be essential for improving models of thermochemical evolution of terrestrial planets.

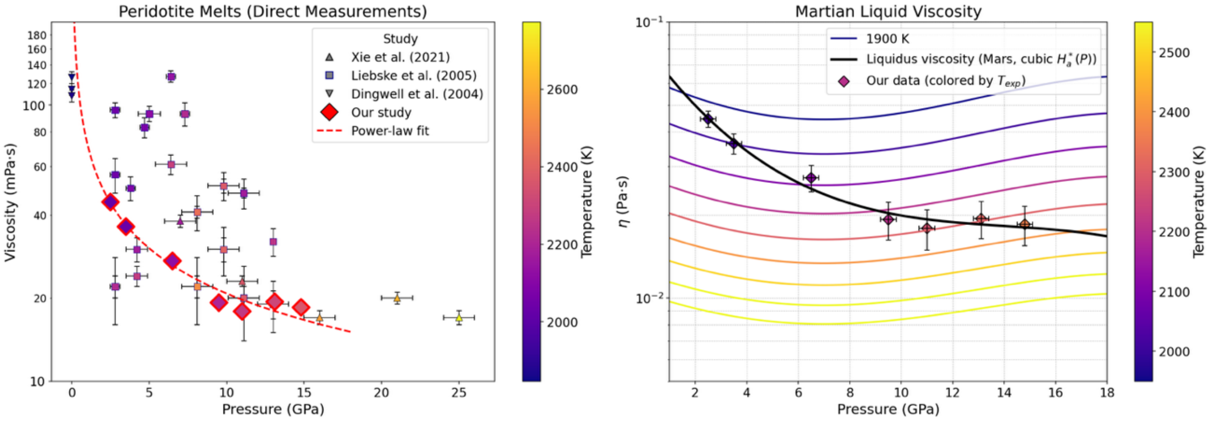

Fig. 3.5-8: Left: High-pressure viscosity measurements for Fe-rich Martian silicate melts (red diamonds) compared to terrestrial peridotite liquids. Iron-rich melts show lower viscosities than terrestrial peridotite, especially at low pressure. Right: Arrhenius viscosity model calibrated on our dataset, showing the pressure–temperature dependence of melt viscosity for implementation in magma ocean evolution models.

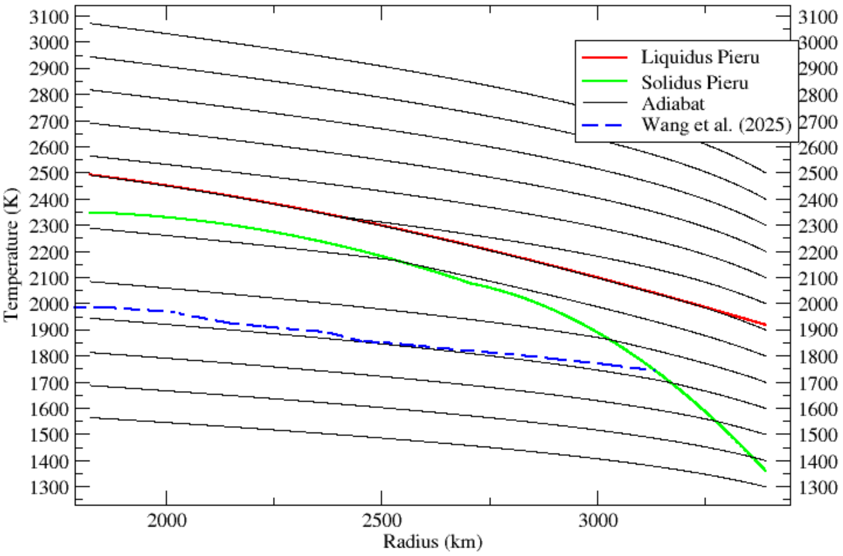

Fig. 3.5-9: Liquidus (red), solidus (green), and adiabatic temperature profiles (black) for a Fe-rich Martian mantle composition, including the effect of partial fusion on the adiabatic slope. The blue dashed curve shows the adiabat of Wang *et al.* (2025; Geophy Res Lett 52: e2024GL109666), in good agreement with our calculations. These results indicate that an initial near-adiabatic profile with T ≈ 1850 K at the top of the convecting layer is required to remain between the liquidus and solidus, providing a consistent thermal boundary condition for heat-flux and magma ocean cooling models.

f. *A viscosity model for hydrous andesitic magmas (P. Valdivia, J. Löschmann/Clausthal, D. Bondar, A. Zandonà/Clausthal, A. Kurnosov, J. Deubener/Clausthal, and D. Di Genova/Rome)*

Andesitic magmas are characterized by relatively high viscosities and elevated volatile contents, properties that exert first-order control on magma ascent, degassing efficiency, and the transition between effusive and explosive eruptive regimes. Accurately constraining the viscosity of hydrous andesitic melts is therefore fundamental for physically realistic modelling of volcanic processes and volcanic hazard assessment. However, widely used viscosity models systematically fail to reproduce the rheological behaviour of hydrous andesitic melts, particularly in iron-bearing systems, where nanoscale crystallization and water loss may occur during high-temperature viscosity measurements, thereby biasing experimental results. In this study, we present a new viscosity model for hydrous andesitic magmas that explicitly accounts for the influence of transition metal content, based on a comprehensive experimental dataset integrating viscometry, differential scanning calorimetry, and Brillouin spectroscopy, with a specific focus on andesitic compositions representative of Sakurajima volcano (Japan).

Two chemically related compositional endmembers were investigated: A natural Fe–Ti–Mn-bearing andesite (AND100) and an otherwise identical transition-metal-free analogue (AND0), both synthesized as hydrous glasses spanning water contents between ~ 0.6 and 5.6 wt. %. The amorphous and nanolite-free nature of the starting materials was verified prior to experiments using scanning electron microscopy and Raman spectroscopy. Total dissolved water contents were independently determined using Karl Fischer titration and Fourier-transform infrared spectroscopy.

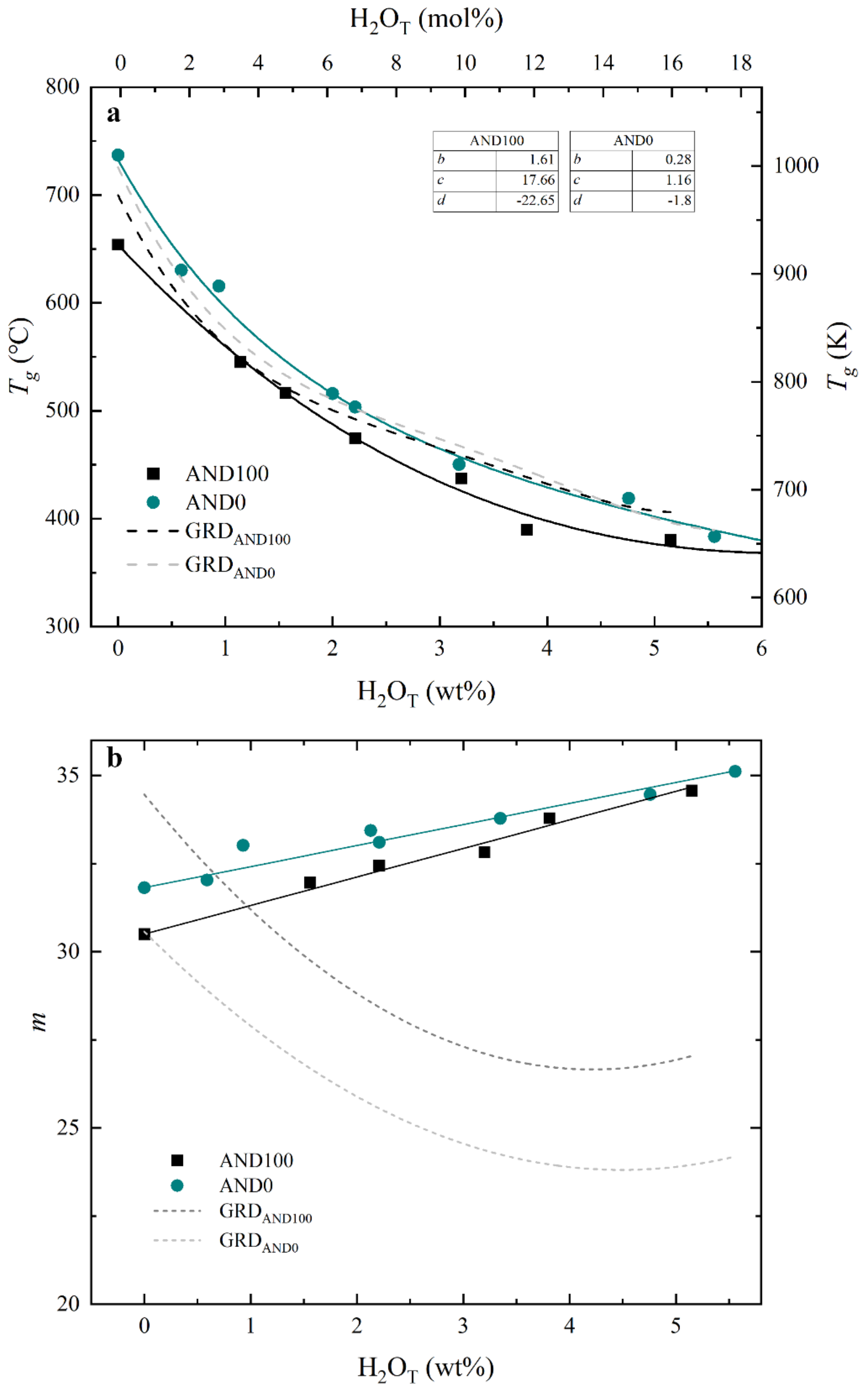

Fig. 3.5-10: **(a)** Glass transition temperature (T_g) as a function of water content (wt. %). Upper axis (H_2O in mol. %) refers to the andesite AND100 composition. Dashed lines correspond to values derived using the Giordano *et al.* (2008; Earth Planet Sci Lett 271: 123) model for AND100 (GRD_{AND100}) and AND0 (GRD_{AND0}) compositions. **(b)** Melt fragility (*m*) as a function of water content (wt. %). Values derived from new *K*/*G* calibration, plotted for hydrous andesite melts. Dashed lines correspond to values derived using the GRD model for AND100 (GRD_{AND100}) and AND0 (GRD_{AND0}) compositions.

Viscosity measurements and calorimetrically derived glass transition temperatures (T_g) reveal a systematic decrease in T_g with increasing water content in both compositional series, with a significantly stronger depolymerizing effect of water observed in the absence of transition metals (Fig. 3.5-10a). To model melt viscosity, we employed the Mauro–Yue–Ellison–Gupta–Allan (MYEGA) formalism, using T_g and the melt fragility index (m) as the primary input parameters. However, previously proposed correlations between elastic properties (*i.e.*, K/G ratios) and melt fragility do not adequately describe the behaviour of the investigated andesitic melts. We therefore derived two newly calibrated empirical relationships linking melt fragility to K/G, separately parameterized for transition-metal-bearing and transition-metal-free compositions. In contrast to previous viscosity parameterizations, our results demonstrate that melt fragility increases linearly with increasing water content in both systems (Fig. 3.5-10b). By combining the water dependence of T_g and m, we first parameterized the viscosity of the two endmember compositions, AND100 and AND0, as functions of temperature and water content (Fig. 3.5-11). These two endmembers were subsequently used to construct a generalized viscosity model applicable to intermediate andesitic compositions, which was successfully validated using an intermediate composition.

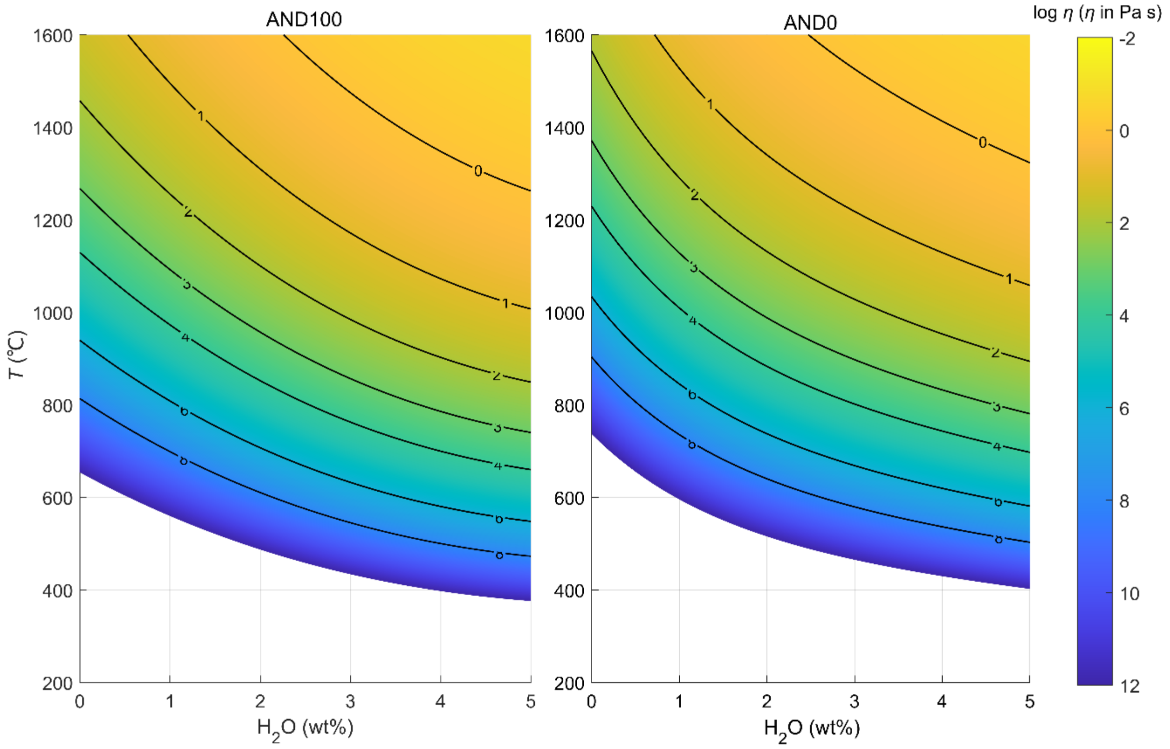

Fig. 3.5-11: Viscosity of andesite melts AND100 and AND0 as a function of water content (wt. %) and temperature (°C).

Finally, we applied the generalized model to pre-eruptive conditions relevant for Sakurajima andesite (1030 °C, ~ 3 wt. % H_2O). The resulting melt viscosities are approximately 45 times lower than those predicted by commonly used viscosity models, and similar viscosity reductions were obtained for other andesitic volcanic systems, indicating that previous models have systematically overestimated the viscosity of hydrous andesitic melts.

In conclusion, we present a physically consistent viscosity model for hydrous andesitic melts that captures the combined effects of water content, temperature, and transition metal concentration. By integrating Brillouin-derived elastic constraints with calorimetric data, the model provides substantially improved estimates of pre-eruptive melt viscosity, offering a robust framework for modelling magma ascent, degassing, and fragmentation in volatile-rich andesitic systems.

g. *4D quantification of vesiculation kinetics and simulation of conduit dynamics for magma ascent (F. Arzilli/Camerino, B. Cordonnier/Grenoble, S. Abeykoon/Camerino, E.C. Bamber/ Rome, D. Di Genova/Rome, G. La Spina/Catania, L. Calabrò/Rome, P. Valdivia and D. Bondar)*

Volcanic eruptions pose significant threats to both society and the environment. Explosive eruptions can release hazardous gases, volcanic ash, and fragmented solid material into the atmosphere, with eruption columns reaching heights of tens of kilometres and dispersing material over areas spanning hundreds of square kilometres. The magnitude of eruptive explosivity is primarily governed by the efficiency of magma fragmentation during ascent within volcanic conduits, which is controlled by the coupled processes of crystallisation and vesiculation.

During magma ascent, decompression promotes both crystal growth and volatile exsolution, leading to the formation and expansion of gas bubbles (vesicles). These processes strongly influence magma rheology, permeability, and ascent dynamics, and are therefore critical in controlling transitions in eruptive style and the degree of explosivity. Recent studies have highlighted the importance of nanolites – crystals with dimensions in the order of tens of nanometres – in regulating the crystallisation of micron-scale crystals and in modifying vesicle nucleation and growth. Through their influence on magma viscosity and degassing efficiency, nanolites may play a key role in magma ascent and fragmentation behaviour.

Despite growing recognition of their importance, the influence of nanolites on the kinetics of vesiculation remains poorly constrained. In particular, there is a lack of direct, *in situ* observations documenting how nanolites affect bubble nucleation, growth, and magma fragmentation at the micron scale under magmatic conditions. This knowledge gap is partially due to the rapid timescales over which these processes occur, often in the order of seconds to minutes, making them difficult to capture using conventional analytical approaches.

This study utilized synchrotron X-ray computed microtomography, combined with a customised three-dimensional conduit apparatus at the beamline BM18 of ESRF to directly observe and quantify the time-resolved, three-dimensional (4D) evolution and kinetics of vesiculation under magmatic conditions. Controlled, dynamic high-temperature experiments were conducted to investigate the nucleation and growth of crystals and gas bubbles as a function of three key parameters: Temperature, dissolved H_2O content, and the presence or absence of nanolites/microlites. This integrated experimental approach enabled high-resolution, time-resolved observations of vesiculation processes occurring on rapid timescales.

Starting materials were synthesised using piston–cylinder presses and rapid-quench TZM vessels at pressures of 2-5 kbar and temperatures between 1125 and 1250 °C. In selected experiments, partially crystalline starting materials were produced by reducing temperatures to 1050-850 °C. The compositions investigated span a broad range, including basalt, trachyte, phonotephrite, and rhyolite, representative of highly explosive volcanic eruptions worldwide. Anhydrous starting glasses were prepared by melting natural fragmented volcanic materials. These powdered glasses (< 250 µm) were loaded into AuPd capsules (5.0/4.6 mm outer/inner diameter), and distilled water was added to achieve hydration levels ranging from 0.45 to 2.70 wt. %. Capsules of 10 mm length were used for piston–cylinder experiments at 5 kbar and 1250 °C, using high-pressure assemblies made from MgO with a graphite heater. Longer capsules (20 mm) were used for TZM experiments conducted at 2 kbar and 1125 °C. After experimental run durations ranging from 12 to 24 hours, experiments were quenched rapidly, capsules were opened, and cylindrical hydrous glass samples were recovered for *in situ* vesiculation and crystallisation experiments.

In situ 4D (3D + time) X-ray computed microtomography (µCT) experiments were performed at the BM18 beamline at ESRF. We used a polychromatic X-ray beam with a peak around 60 keV and a resolution of around 3 µm at a scanning time of around 2 min per scan. These experiments were performed using an innovative X-ray transparent 3D conduit apparatus, which consists of a larger diameter hole at the bottom and narrower conduit on the top part.

By utilising the unique 3D conduit apparatus, we were able to observe the spatial evolution of vesiculation within the conduit in real time (Fig. 3.5-12). This allowed us to observe bubble nucleation and growth during magma ascent within the conduit. Bubble coalescence, connectivity evolution and the development of permeable pathways, which in turn promote outgassing, were directly observed.

We aim to integrate these results with a state-of-the-art numerical model to simulate and quantify the impact on the rheological behaviour of magmas under the dynamic conditions expected during magma ascent within volcanic conduits. This comprehensive, multidisciplinary study will be one of the first of its kind, which could highly benefit from *in situ* high resolution phase contrast tomography, as a powerful tool that could open new avenues for the study of magma ascent dynamics under high-temperature conditions within volcanic conduits. Furthermore, the outcomes of this study will provide important information for understanding the mechanisms behind highly explosive eruptions in general, important for hazard mitigation at active volcanic systems in highly populated areas.

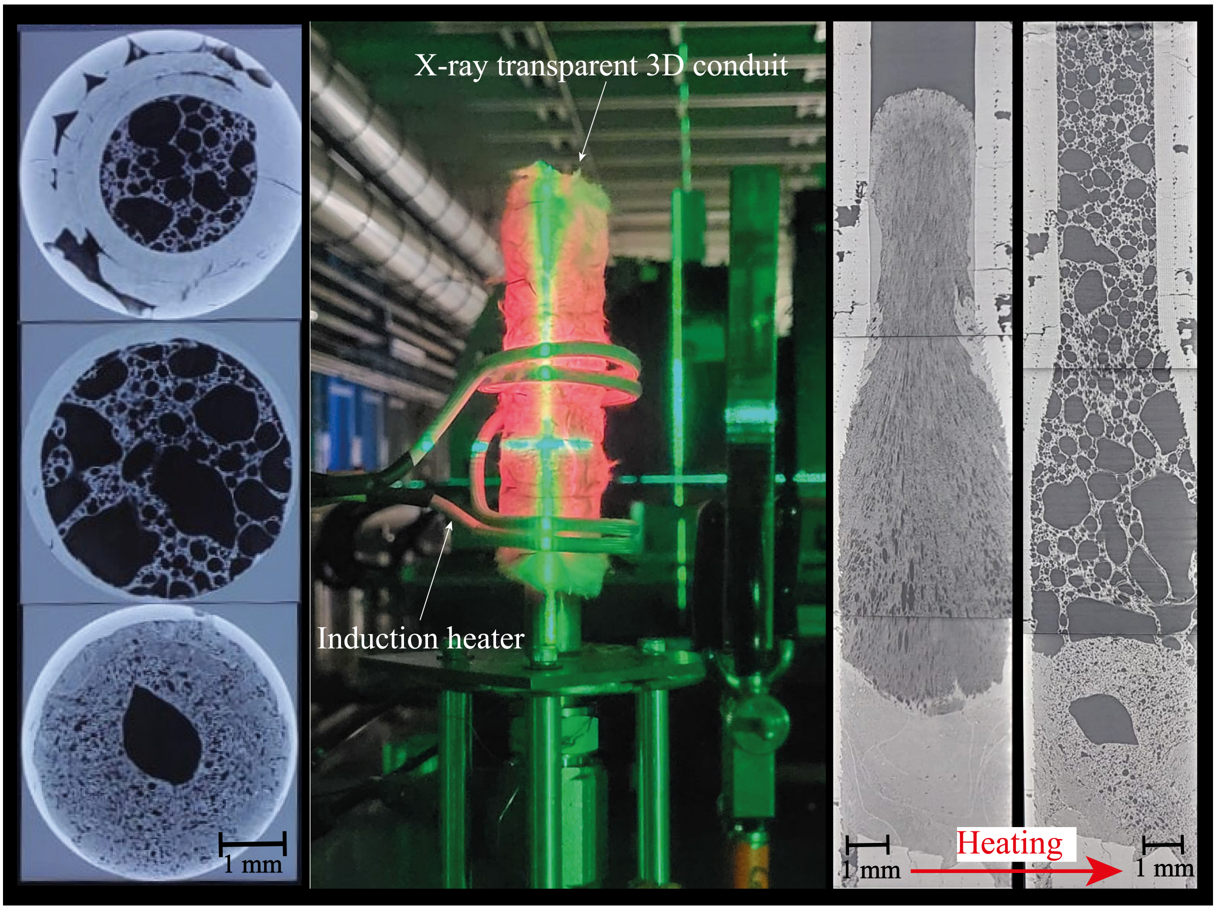

Fig. 3.5-12: *In situ* 4D (3D + time) X-ray computed microtomography (µCT) experiments of a model volcanic conduit carried out at the BM18 beamline at ESRF. Left: Horizontal cross sections of the conduit. Middle: X-ray transparent 3D conduit apparatus heated up by an induction furnace. Right: Vertical cross section showing the evolution of vesiculation within the conduit during heating.

h. *From melt to ash: Laboratory eruption under realistic magmatic P–T conditions using a novel fragmentation apparatus (D. Bondar, H. Keppler and D. Di Genova/Rome)*

Understanding magma fragmentation under realistic volcanic conditions is essential for constraining the processes driving explosive eruptions. Following the successful development of the new fragmentation apparatus at BGI – a high-temperature, high-pressure autoclave designed to overcome the limitations of previous shock-tube devices – we carried out the first test experiment under natural magmatic P-T conditions.

The new fragmentation apparatus extends the accessible experimental range to 1200 °C and 1500 bar, significantly exceeding the operational limits of earlier facilities (*ca.* 900 °C, 250 bar). This allows fragmentation studies on hotter and less silicic magmas, as well as controlled tests on nanolite formation and melt rheology prior to failure. The apparatus consists of a TZM-alloy autoclave inserted into a furnace and equipped with exchangeable rupture disks calibrated to fail at pre-defined pressures. During each run, the sample is inserted into the cold zone of the autoclave, pressurized with argon, heated under pressure, equilibrated in the hot zone, and then rapidly decompressed upon membrane failure, generating a small-scale laboratory eruption. Fragmented products are collected in an alumina tank at the top of the apparatus.

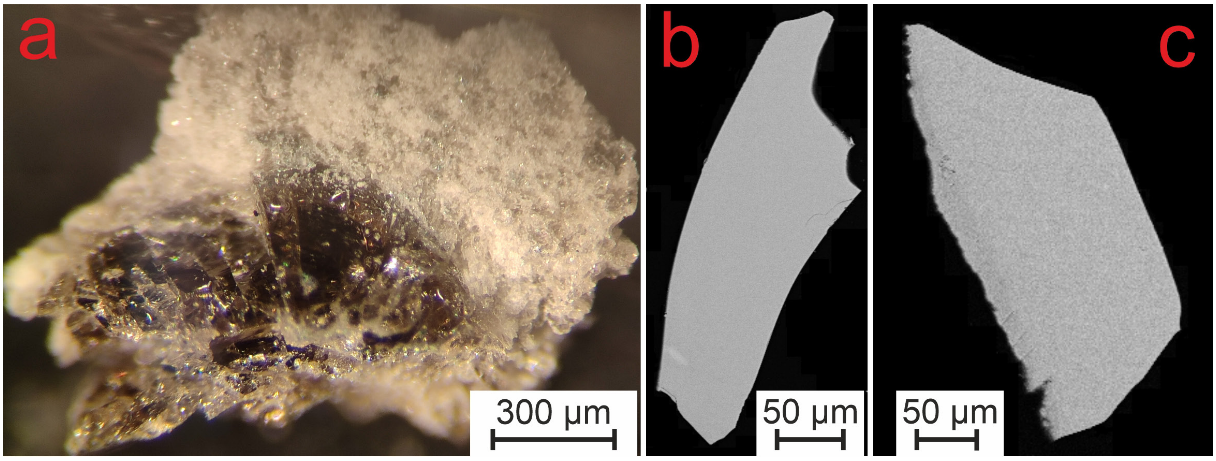

Fig. 3.5-13: (a) Optical image of a fragment of rhyolitic glass, and (b, c) EDS images of ash particles recovered after the test-fragmentation experiment.

A first test experiment was conducted using a microlite-poor rhyolitic obsidian. The starting material is an iron-rich glass (~ 3 wt. % FeO) containing < 1 vol. % Fe–Ti oxide microlites and ~ 0.15 wt. % initial water. The experiment was performed at 1000 °C with a 400 bar rupture membrane. After holding the sample for ten minutes in the hot zone to ensure complete melting, the failure of the membrane triggered rapid decompression and ejection of material into the collection system.

Post-run inspection showed that approximately 30 % of the sample remained as crushed glass fragments; most of these were clear, although a small fraction was found in contact with fragmented material (Fig. 3.5-13a). The remaining ~ 70 % fragmented into ash, which was mostly captured in the ambient-pressure receiver tank (Fig. 3.5-13b,c).

3.6 Rheology

Since its formation, Earth has been a dynamic planet such that the rheology of rocks has been an important factor in its development. The rheology describes the deformation (strain) of rocks due to deviatoric (shear) stresses. Both stress and strain have an influence on physical rock properties as well as effects on chemistry such as (metamorphic) mineral reactions. The latter effect, in particular, has been the aim of the first two experimental studies presented in this chapter. *Silva et al.* reproduced conditions in subducting oceanic plates where serpentinite undergoes a dehydration reaction to olivine, orthopyroxene and garnet with increasing temperature and pressure. The reaction is suspected to cause unusually deep earthquakes which are observed in subduction zones around the world. Results show that a network of reaction products is generated by concurrent deformation and that brittle (potentially seismic) deformation is induced only at high stresses and strain rates. *Sieber et al.* explored the carbonation of (ultra)mafic rocks at high pressure and temperature via a fluid driven reaction under deviatoric stresses. Concurrent deformation strongly enhanced the formation of carbonates by fracturing olivine and creating pathways for the fluid. Static carbonation caused a softening of the host rock such that subsequent deformation was mostly accommodated by the more ductile carbonates. These processes are also important for potential storage of atmospheric CO_2 in (ultra)mafic rocks.

Since deformation experiments are often challenging, computational approaches such as geodynamic modelling or a priori first principles calculations have been used to explore various aspects of rheological problems. The third contribution uses a computational modelling approach to explore the consequences of different rock rheologies in a subduction zone environment. *Weiler et al.* used a 2D model with a nonlinear visco-elasto-plastic rheology to simulate the potential source region of intermediate depth earthquakes in the Hindu Kush region which are thought to be related to slab detachment during subduction. Their results indicate that the viscosity ratio between lower continental crust and the oceanic lithosphere as well as the depth of the lower crust control the depth where seismicity and slab detachment occur. The last contribution by *Schulze & Steinle-Neumann* applies molecular dynamics calculations to determine the diffusion constant of oxygen vacancies in $CaSiO_3$ perovskite (davemaoite) under lower mantle p,T conditions which is a crucial factor for the plastic deformation of this mineral. Results show that davemaoite has the fastest oxygen vacancy diffusion among the minerals of the lower mantle which will make it relatively soft.

a. *Microstructural aspects of incipient serpentine dehydration (D. Silva Souza, M. Thielmann, F. Heidelbach and D.J. Frost)*

Deep-focus earthquakes offer insights into Earth's mantle and support plate tectonics. Since high pressures and temperatures hinder brittle failure, their mechanisms differ from shallow quakes. Dehydration embrittlement, dominant at 70-350 km depth, involves fluid release from minerals like serpentine, increasing pore pressure and triggering failure. However, serpentine dehydration decreases with pressure, requiring low-permeability layers to trap fluids for seismic failure. Experiments also show that serpentine dehydration often leads to ductile weakening without acoustic emissions.

To better understand the micro-mechanisms of serpentinite dehydration, particularly at its incipient stage, we conducted high-pressure, high-temperature experiments under static and deviatoric stress conditions. Serpentinite cores (2 mm diameter) were mounted in cubic assemblies (12 mm edge) and deformed in a 6-Ram multianvil press in pure shear geometry. Experiments at 3 GPa reached 46 % strain at strain rates of 1.04×10^{-4} s^{-1} to 1.28×10^{-6} s^{-1}. Temperature was constant: static experiments at ~ 560 °C and ~ 712 °C, non-isostatic at ~ 530 °C.

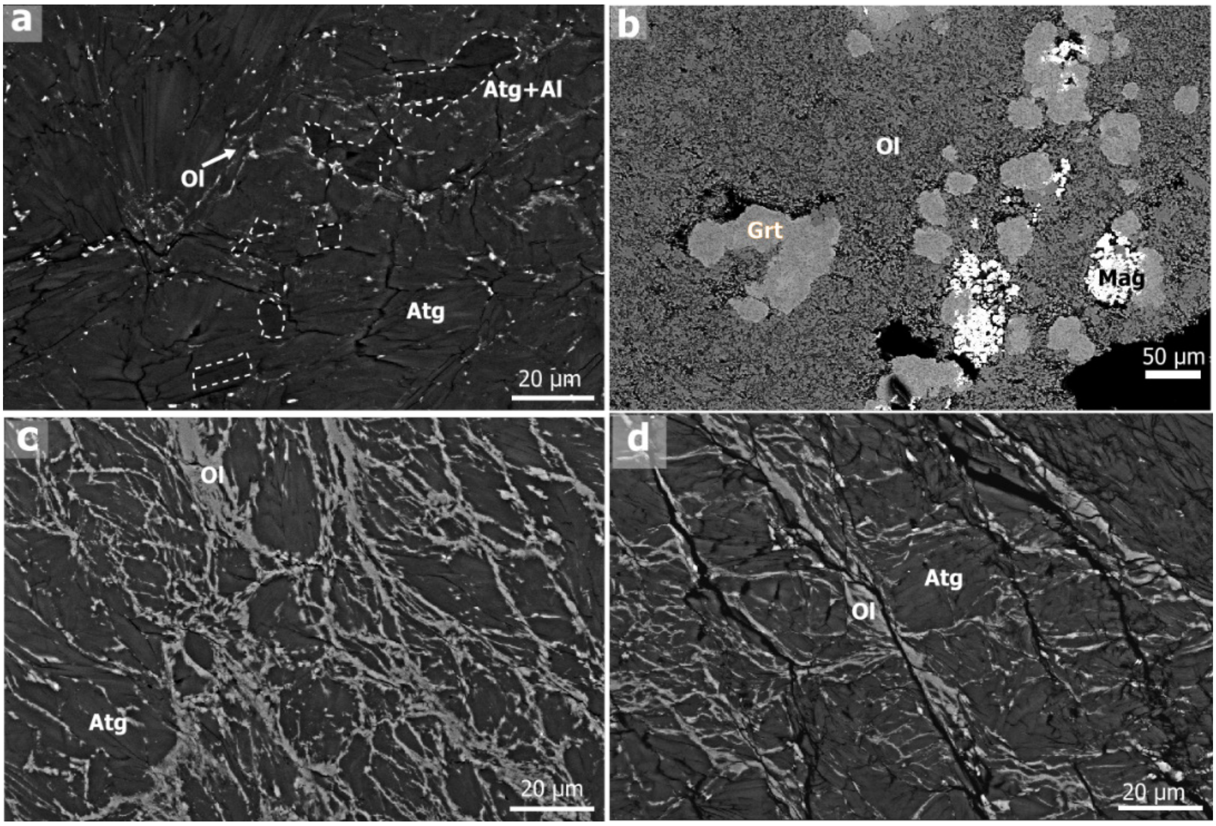

Fig. 3.6-1: Microstructures of antigorite dehydration experiments. a) Incipient dehydration of antigorite at static conditions, 3 GPa and 560 °C. Regions marked with the dotted line are richer in Al. Ol=Olivine, Atg=Antigorite and Mag=Magnetite. b) Antigorite after complete dehydration annealed for 2 h at 712 °C and 3 GPa. The fine matrix is composed of mostly olivine, the presence of enstatite is inferred. Poikilitic Garnet (Grt) is formed. c) Vein networks of polycrystalline olivine and orthopyroxene during slow (1.28×10^{-6} s^{-1}) deformation at 3 GPa and ~ 530 °C. d) Antigorite dehydration at fast deformation (1.04×10^{-4} s^{-1}) at 3 GPa and ~ 530 °C. Different from the other experiments as brittle failure microstructures are present near dehydration veins; compression and extension direction are vertical and horizontal in c) and d).

Results show that under static conditions of 3 GPa and ~ 560 °C, antigorite dehydrated and started to form polycrystalline clusters of olivine and orthopyroxene (Fig. 3.6-1a). At static conditions and higher temperature (~ 712 °C), antigorite is fully dehydrated and forms an aggregate of olivine, orthopyroxene and garnet (Fig. 3.6-1b). The early stage of incipient dehydration is marked by growth of clusters at antigorite grain boundaries, with a preferential shape orientation that possibly reflects antigorite shape orientation (Fig. 3.6-2A). Although the fully dehydrated sample is more porous than in the incipient stage, no evidence for dehydration embrittlement is present.

Under deviatoric stress conditions at 3 GPa and ~ 560 °C, dehydration clusters evolve into vein networks that are thicker after low strain rate deformation (Fig. 3.6-1c). At these conditions, the sample deforms without developing brittle fracture microstructures. At high strain rate deformation, dehydration clusters from thinner veins concentrated along sample diagonals and a major fracture develops, cutting through the sample from the top left to the bottom right corner (Fig. 3.6-1d). Shape orientation analysis of the clusters shows that deviatoric stress affects localization of dehydration fronts, since shape orientation changes under deviatoric stress (Fig. 3.6-2B,C).

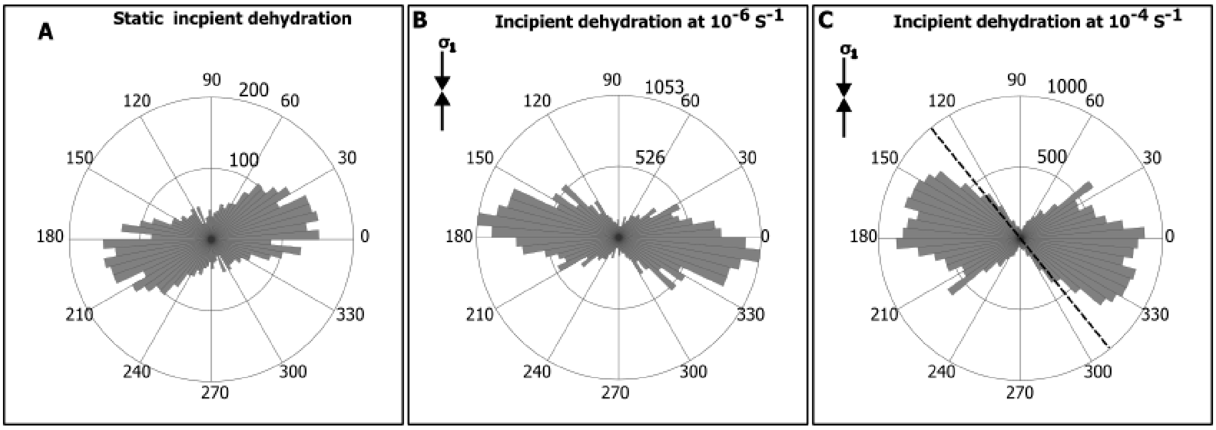

Fig. 3.6-2: Shape orientation of dehydration clusters in the static (A), low (B) and high (C) strain rate experiments conducted at incipient dehydration conditions (3 GPa; ~ 530-560 °C). The radius of the plot is the accumulated length of clusters analysed. Dotted line in C indicates orientation of sample fracture.

Our experiments demonstrate that antigorite dehydration embrittlement may not occur solely because of completed static dehydration. Formation of dehydration veins and networks is a dynamic process favored under deviatoric stress. At low strain rates, antigorite deforms in a ductile regime, which induces pore connectivity and formation of vein networks leading to uniform sample deformation without mechanical failure. At high strain rates, strain localization generates discrete dehydration bands, creating weaker regions relative to the surrounding antigorite matrix due to grain size contrast, ultimately leading to brittle failure. Future experiments will be carried out with *in situ* acoustic emission and synchrotron X-ray diffraction techniques to elucidate if the microstructures observed are seismogenic or not.

b. *Deformation of carbonated mafic and ultramafic rocks (M.J. Sieber/Berlin, D.J. Frost, D. Silva Souza and R. Farla/Hamburg)*

Fluid-driven carbonation of mafic and ultramafic lithologies likely plays an important role in Earth's long-term habitability by sequestering significant proportions of carbon within mantle rocks. Studying this process is also central to the development of engineered approaches for mitigating anthropogenic CO_2 emissions. This project examines how fluid-driven carbonation of partially hydrated (ultra)mafic lithologies in tectonically active settings, such as subduction zones, can proceed to completion despite the associated solid-volume expansion, which may reduce porosity and permeability. We aim to investigate how coupled thermo–hydro–mechanical–chemical feedbacks influence both the carbonation mechanism and overall carbonation efficiency. This also involves examining the role of deformation in facilitating fluid pathways, as well as assessing whether carbonation processes can lead to instabilities that may cause deep earthquakes.

Deformation experiments were carried out at beamline P61.B (DESY) and at BGI using cylindrical cores of natural serpentinite and actinolite, along with olivine powder, as the starting materials. Samples were enclosed with a mixture of oxalic acid and 5 wt. % $CaCO_3$, serving as a source of Ca-bearing COH fluids. The samples were deformed using 6-ram multianvil devices compressing cubic assemblies containing the sample within a cylindrical graphite furnace. During heating, oxalic acid decomposes, liberating a mostly CO_2-H_2O fluid that dissolves calcite. The Ca-bearing aqueous COH-fluid triggers the carbonation reaction. The incorporation of Ca into newly formed carbonates was used to monitor the reaction process over time.

At the P61.B beamline, acoustic emission (AE) signals could be recorded from the assembly using transducers attached within a cavity at the back of each of the six tungsten carbide anvils. X-ray radiography images were used to monitor sample strain, while energy-dispersive X-ray diffraction allowed the formation of reaction products such as carbonates, talc, and quartz to be identified. High fluid/rock ratios, intended to promote reaction progress, proved unfavorable for AE measurements. To address this, we modified the capsule design aiming to maintain the solid volume despite fluid loading. The fluid source was instead contained in a lower Ag housing that allowed the decomposed fluid to leak into the overlying sample through a small hole. This design was tested at the D-DIA press at BGI, albeit without AE monitoring.

Although the high fluid/rock ratios in the experiments conducted at P61.B inhibited the recording of AE, microstructural analyses of the recovered samples reveal distinct textural differences depending on the timing of deformation relative to carbonation. For instance, runs HH630 and HH631 were performed under identical conditions (~ 1 GPa, 350 °C, and similar fluid/olivine ratios), differing only in the onset of deformation. In HH630, deformation began immediately after reaching target temperature, resulting in extensive olivine fracturing during listvenite formation, *i.e.*, carbonation to a carbonate-quartz assemblage (Fig. 3.6-3). In contrast, deformation in HH631 was delayed by 2 h, allowing carbonation to nearly complete before deformation. In HH631, olivine grains remained largely unfractured, instead being replaced at their rims by serpentine and talc–magnesite (Fig. 3.6-4). These secondary assemblages accommodated strain in a more ductile fashion, preventing olivine fracturing. These observations suggest that deformation concurrent with carbonation enhances reaction progress by maintaining fluid pathways, whereas deformation following carbonation does not.

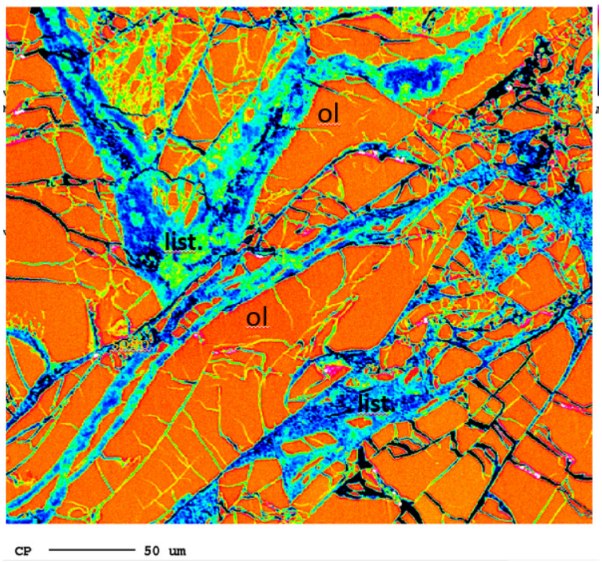

Fig. 3.6-3: Combined element maps (Si: yellow; Mg: red; Ca: blue) of HH630 showing the formation of quartz-magnesite mixtures (list.) and extensive fracturing of primary olivine (ol.) grains.

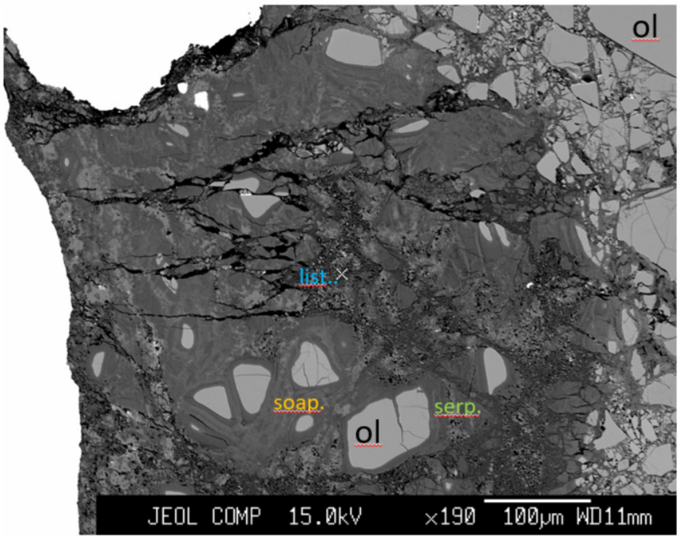

Fig. 3.6-4: BSE-images (HH631) showing reaction zones of serpentinization (serp.), talc-magnesite (soap.) and quartz-magnesite (list.) without significant fracturing of primary olivine (ol) grains.

c. *How does the lower crust affect slab detachment? (T. Weiler, A. Piccolo, A. Spang and M. Thielmann)*

Earthquake nests are defined as volumes of intense intermediate-depth seismicity which are isolated from any surrounding seismic activity. The high seismic activity within these earthquake nests occurs continuously and thus sets them apart from other seismic sequences such as earthquake swarms or aftershocks. These intermediate-depth and deep earthquakes cannot be explained by the same causes as shallow earthquakes. Instead, they appear often linked to slab detachment processes (*e.g.*, in the Hindu Kush region).

To constrain the conditions at which these large deep earthquakes occur, numerical models are required to better understand their tectonic environment. Here, we use two-dimensional models with a nonlinear visco-elasto-plastic rheology to determine the deformation state and the controlling mechanisms of the detachment process.

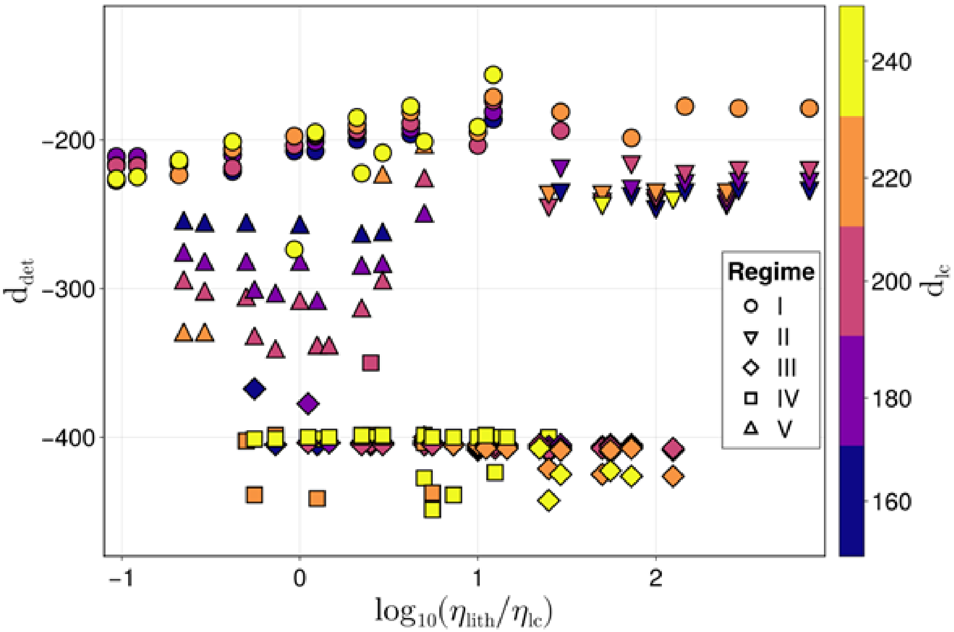

Fig. 3.6-5: Regimes of deformation behaviour. Detachment depth (d_{det}) of each model in dependency of its viscosity ratio (η_{lith}/η_{lc}) and lower crustal depth (d_{lc}). Symbols display the model types.

In this study, we focus on the question of how the viscosity ratio (η_{lith}/η_{lc}) between the lithosphere and the lower crust and the depth d_{lc} to which lower crust may have been subducted, influence the subduction process. Both parameters are poorly constrained for the Hindu Kush. To this end, we varied the viscosity ratio η_{lith}/η_{lc} between 0.01 and 1000 and the subduction depth of the lower crust d_{lc} between 160 km and 240 km. We obtained detachment depths ranging from 110 km to 470 km, which fall within the range of the Hindu Kush earthquake nest, extending up to 280 km. The deformation behaviour from the 264 models can be classified into five different regimes based on stress, strain rate, detachment depth, and coupling between subducting and overriding plate (Fig. 3.6-5). The five regimes represent the dependency of the detachment depth (d_{det}) to its viscosity ratio ($\eta_{\mathrm{lith}} / \eta_{\mathrm{lc}}$). Detachment in regime two is enhanced via shear heating and detachment in the other regimes occurs via necking. The relationship between lower crustal depth and detachment depth varies by model category. This variability reflects the complex influence of the "lubrication effect" of a weak lower crust and the limitation of subduction depth governed by its rheological properties.

d. *Oxygen-vacancy diffusion in davemaoite (M. Schulze and G. Steinle-Neumann)*

Perovskite-structured solids are known to facilitate rapid oxygen vacancy (OV) diffusion, resulting in high rates of chemical exchange and ionic conductivity. This property makes them attractive candidates for use as technical materials, such as oxygen-permeable membranes and solid oxide fuel cells. Here, we investigate whether this rapid OV diffusion behaviour can also be observed in davemaoite ($CaSiO_3$), a cubic perovskite and one of the main minerals of the ambient lower mantle and subducted oceanic crust and discuss its geochemical and geophysical implications. Experimental diffusion studies rely on the *ex situ* analysis of quenched samples synthesised at high pressures (*P*) and temperatures (*T*). However, preservation of the cubic davemaoite structure upon quenching has repeatedly proven to be difficult, posing a significant challenge in the study of OV diffusion. Therefore, we employ molecular dynamics (MD) simulations in conjunction with a machine learning potential (MLP) as a numerical alternative to laboratory diffusion experiments. The MLP approach enables MD simulations on the nanosecond timescale, while maintaining the quality of Kohn-Sham density functional theory-based MD at affordable computational cost. This allows long simulations to be repeated multiple times, which is crucial for obtaining statistically significant diffusivity results and reliable uncertainty estimates.

MLP-MD simulations were performed along five isobars from 25 to 125 GPa, *i.e.*, lower mantle conditions. The *T*-dependence of the OV diffusivity, D_v, is described excellently by the Arrhenius-type relation $\log D_v = \log D_v^0 - \frac{\Delta H_a}{\log k_B} \frac{1}{T}$, where D_v^0, ΔH_a, and k_B are the pre-exponential factor, the activation enthalpy, and the Boltzmann constant, respectively (Fig. 3.6-6A). We have utilised this observation as a physically sound basis to parameterise a model capable of predicting D_v over the entire *P*-*T* range of the Earth's lower mantle.

Considering geotherms representative of both the ambient mantle and subducted slabs, our model predicts values for D_v between 10^{-10} and 10^{-9} $m^2 \cdot s^{-1}$ at the top of the lower mantle. In both cases, these values decrease by roughly one order of magnitude toward the core–mantle boundary (CMB) (Fig. 3.6-6B). At shallow depths, the diffusivities are comparatively high, supporting the idea that davemaoite exhibits the elevated D_v expected for a perovskite-structured solid. Moreover, comparison with literature data indicates that davemaoite shows the lowest ΔH_a among the major minerals of the lower mantle. Since ΔH_a is the factor in the Arrhenius equation that most strongly governs the magnitude of D_v, it is likely that davemaoite also exhibits the fastest diffusivity. Even so, we argue that even this exceptionally high D_v is insufficient to bring the davemaoite fraction in subducted oceanic crust into complete redox equilibrium with the ambient mantle during its descent to the CMB. Finally, using davemaoite to explore an upper-limit scenario for ionic conduction, we conclude that its contribution to the electrical conductivity of the lower mantle is likely negligible across most regions.

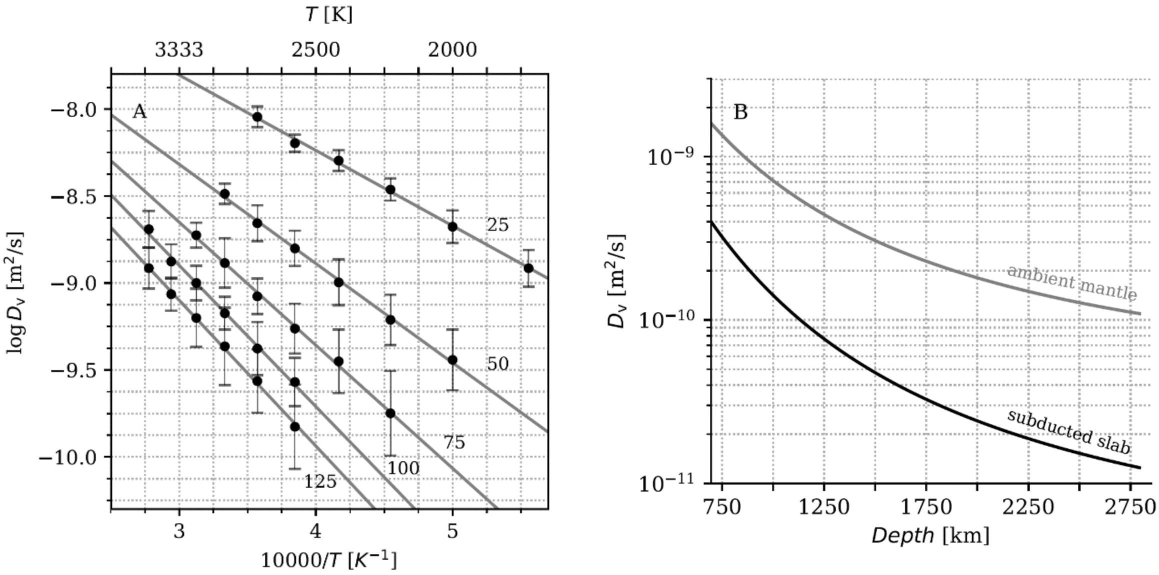

Fig. 3.6-6: Oxygen vacancy diffusivities D_v in davemaoite. (A) D_v as obtained from molecular dynamics simulations using a machine-learning potential along five isobars. Solid lines represent Arrhenius fits to the results. (B) D_v along geotherms representative for the ambient lower mantle and subducted slabs as predicted by a model parameterised based on the Arrhenius relation.

3.7 Material Science

For a long time, this section of the annual report was dominated by research on metal-based oxides, carbides and technical perovskites with relatively simple geometries, but advances in X-ray diffraction acquisition and data processing have made much more complex structures accessible and permit the study of elements with X-ray scattering factors that were considered too small for reliable structure determination a decade ago. This trend continues to be reflected in the contributions to this section, with almost all studies presented based on diamond anvil cell experiments to characterise high-pressure structures using a variety of X-ray sources.

One exception is the first project presented in the section which revisits a topic from last year's annual report, the behaviour of chiral halide perovskites with a hybrid organic-inorganic structure at high pressure in the multianvil press. Despite the high compressibility of the chiral perovskites and amorphization under compression to 15-20 GPa, the samples recovered are fully crystalline, although with subtle differences to the initial structures. Metal halides are also the topic of the second contribution, where iron chloride and iron bromide structures are presented that are based on an octahedral environment for Fe: for two chlorides with Fe^{3+} (Fe_4Cl_9 and Fe_3Cl_8) and for the bromide with Fe^{2+} ($FeBr_2$) at the centre of the halide octahedra. The differences between the structures formed via the octahedral framework are quite significant, more so than may be expected, and are related to an interplay of the structures with electronic and magnetic properties. In a further contribution on halides, the synthesis of Mg_3Cl_7 at high pressure is reported which is a rare case of a polar metal, in which the free electrons of the metal do not (fully) screen the structural dipole-dipole interactions.

The following two contributions revisit topics from the previous year, with the first one exploring the behaviour of aromatic hydrocarbons under compression. Naphthalene ($C_{10}H_8$) and anthracene ($C_{14}H_{10}$) show remarkable structural stability up to the maximum pressure reached in the experiments (~ 50 GPa). Over the past couple of years, researchers at the BGI have revealed a rich diversity of nitrogen-based compounds formed at high pressure, almost at the level of diversity for carbon-based structures. Here, a mixed compound with cyclo-N_5^- anions and N_2 dimers is synthesised that forms a crystal with perovskite topology.

For decades, the ruby pressure scale – based on the luminescence of Cr^{3+}-doped Al_2O_3 – has been used in the diamond anvil cell. However, under non-hydrostatic conditions, the two emission lines broaden and start to overlap, calling for alternative pressure scales. In the sixth contribution, luminescence in Al-oxonitridoborate AlB_4O_6N, also doped with Cr^{3+}, is explored as an alternative pressure calibrant, with promising results at low pressure, but splitting of the fluorescence peak near 75 GPa limits its applicability.

In the final contribution to this section, results from molecular dynamics simulations are presented that help to interpret one of the first experiments at the European XFEL in Schenefeld near Hamburg. The experiments suggest the formation of gold hydride at high pressure and temperature from gold loaded in a diamond anvil cell together with hydrocarbons used as a source for hydrogen. High pressure and temperatures at an X-ray free-electron laser facility are achieved through a train of ultra-short pulsed high-energy X-rays, also used to collect diffraction patterns. The simulations support the experimental hypothesis on the formation of gold hydride and the inferred hexagonal structure, and provide a plausible explanation on the stabilization of an entropy-driven high-temperature phase through superionic diffusivity of the hydrogen through the gold lattice.

a. *The effect of pressure on hybrid metal halides (A. Dibenedetto and L. Malavasi/Pavia, A.C. Withers and T. Boffa Ballaran)*

Chiral perovskites are hybrid organic-inorganic perovskites with excellent optoelectronic properties that make them important for several technological applications, for example in quantum computing and optical spintronics. Such properties are closely related to the packing of the organic molecules in the perovskite structure. Specifically, the electronic properties of the hybrid perovskites strongly depend on their organic-inorganic interactions and state of crystallinity. Due to the relatively high compressibility of these materials, an amorphization state is reached at relatively low pressures ($P < 10$ GPa). It has been observed, however, that the amorphization process is reversible. In order to understand whether this recovery depends on the timescale used to increase and decrease P, multianvil (MA) experiments have been conducted with controlled P ramps to investigate if the amorphous phase could be recovered at room P.

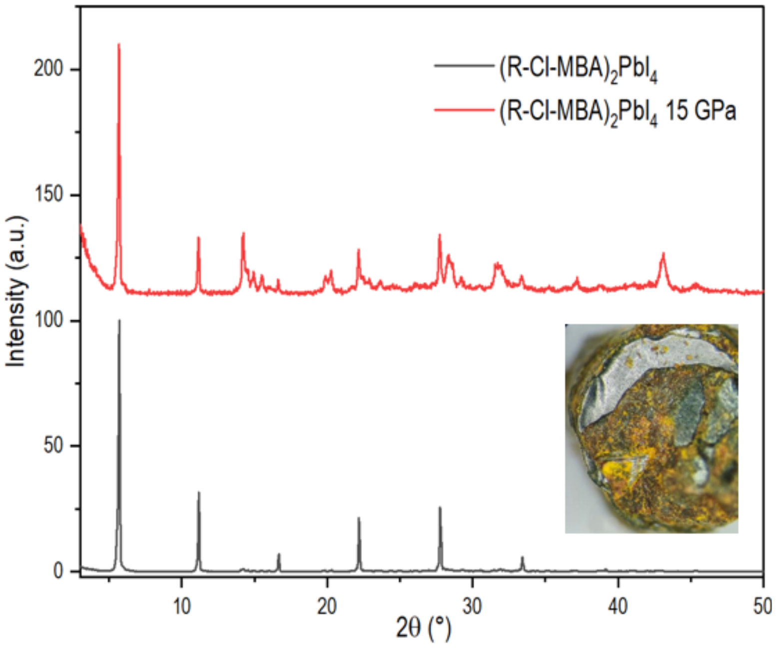

Fig. 3.7-1: Comparison of the X-ray diffraction patterns collected for $(R\text{-Cl-MBA})_2\text{PbI}_4$ before and after the 15 GPa experiment. The inset shows a microscope image of $(R\text{-Cl-MBA})_2\text{PbI}_4$ recovered from 15 GPa.

The materials chosen for the MA experiments are chiral hybrid metal halides with compositions (R-Cl-MBA)$_2$PbI$_4$, and (rac-Cl-MBA)$_2$PbI$_4$, where Cl-MBA stands for 1-(4-chlorophenyl)ethylamine, *R*- indicates the right-hand enantiomer of this material, and *rac*- indicates the racemic mixture. The synthesis of this material requires the dissolution of $(CH_3COO)_2Pb$ in an excess of hydroiodic acid, HI. The solution is heated to 90 °C in order to allow the complete dissolution of the lead precursor and then a stoichiometric amount of either *R*-Cl-MBA or *rac*-Cl-MBA is added. After a few minutes, the agitation and heating are turned off. The yellow/orange precipitate that forms is then filtered, washed with diethyl and dried in vacuum at 60 °C overnight. The powdered samples obtained are subsequently prepared for the MA experiment by pressing them to form two cylindrical pellets, 6 and 4 mm in diameter and 3 and 1.7 mm in length, respectively. Two MA experiments were carried out, one at 15 GPa and one at 20 GPa. For the experiment at 15 GPa, the *R* and *rac* samples were placed inside the same MgO octahedron separated by three sheets of Fe foil, and enclosed between two cylinders of MgO. In the experiment carried out at 20 GPa, the two samples were wrapped and separated by aluminium foil. The desired *P* was reached in 5 hours, maintained for 15 minutes and then lowered again for 10 hours without any heating cycle.

The recovered samples were analysed by X-ray diffraction at the Department of Chemistry of the University of Pavia. A comparison with the diffraction patterns of the starting materials (Fig. 3.7-1) indicates that the main peaks of the two (Cl-MBA)$_2$PbI$_4$ phases are still present even after subjecting them to pressures of 15 and 20 GPa, suggesting that their crystallinity is recovered even after these high-*P* conditions. However, some new peaks are clearly present in the diffraction patterns and further studies are under way to elucidate their nature.

b. *High-pressure synthesis of novel iron halides (A. Aslandukova, A. Aslandukov, Y. Yin, L.S. Dubrovinsky and N.A. Dubrovinskaia, in collaboration with G. Garbarino and A. Pakhomova/ Grenoble)*

Metal halides, and iron halides in particular, exhibit diverse correlated electronic and magnetic phenomena with potential technological applications. High pressure (*P*) is an effective tool to tune their structural, electronic, and magnetic properties. For instance, the prototypical Mott insulators FeI_2 and $FeCl_2$ undergo *P*-induced Mott transitions and high- to low-spin transitions with spin-flop behaviour. Beyond condensed-matter physics, iron halides may be geophysically relevant, potentially forming in the Earth's mantle. Understanding their *P*-dependent stability is therefore essential for both material science and deep-Earth modelling. In this work, we investigated the chemical reaction between iron and carbon tetrahalides (CCl_4 and CBr_4) in a laser-heated diamond anvil cell under high-*P* high-temperature conditions.

The reaction between iron and CCl_4 at ~ 52 GPa and ~ 3000 °C yields two mixed-valence iron chlorides: orthorhombic Fe_4Cl_9 (spacegroup *Cmcm*) and monoclinic Fe_3Cl_8 (spacegroup *C*2/*m*). Fe_4Cl_9 features a three-dimensional framework structure, whereas Fe_3Cl_8 adopts a layered topology (Figs. 3.7-2a and 3.7-2b). In both structures, there are two distinct iron sites, one consistently corresponds to Fe^{3+} in octahedral coordination. In Fe_4Cl_9, the second site is Fe^{2+} in a trigonal-prismatic coordination environment, while in Fe_3Cl_8, the second site exhibits capped trigonal-prismatic coordination and corresponds to a mixed-valence Fe^{2+}/Fe^{3+} state, also confirmed by Mössbauer spectroscopy. Notably, whereas mixed-valence iron oxides are well known, the compounds synthesised here represent the first mixed-valence iron halides.

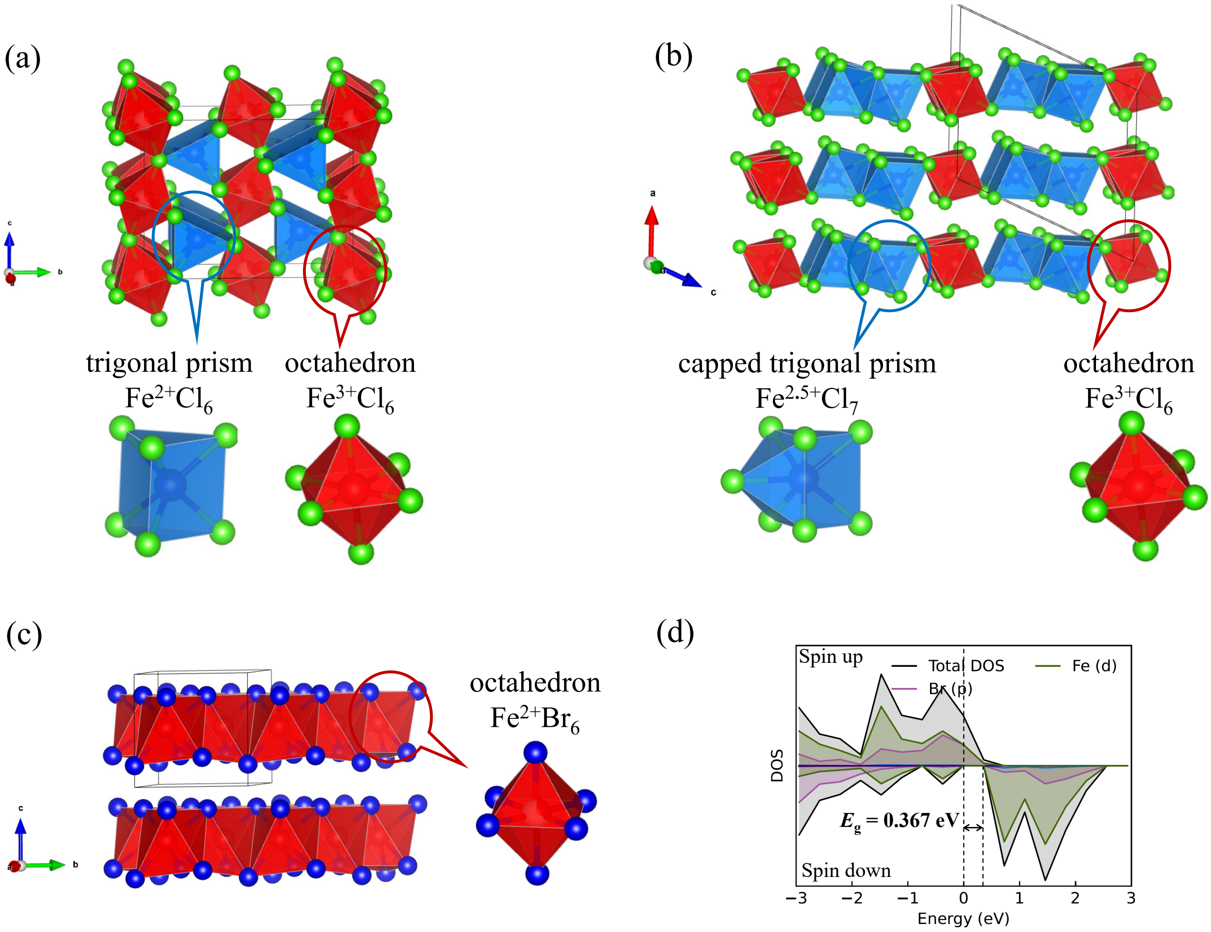

Fig. 3.7-2: Crystal structure of novel (a) Fe_4Cl_9 and (b) Fe_3Cl_8 at 52 GPa with the illustration of the Fe-Cl polyhedra – Fe^{3+} in octahedral, Fe^{2+} in trigonal prismatic, and $Fe^{2.5+}$ in a capped trigonal prismatic coordination. Fe^{3+}, $Fe^{2+}/Fe^{2.5+}$, and Cl atoms are shown as red, blue, and green balls, respectively. (c) Crystal structure of novel $FeBr_2$ polymorph at 40 GPa, with Fe and Br atoms shown as red and blue balls, respectively; (d) electronic density of states for $FeBr_2$ at 40 GPa, showing its half-metallicity. The Fermi energy level was set to 0 eV.

The reaction between iron and CBr_4 at ~ 40 GPa and ~ 3000 °C produced a novel layered trigonal polymorph of $FeBr_2$ (spacegroup $P31m$). In the crystal structure, iron exhibits octahedral coordination, and these $FeBr_6$ octahedra are connected via edges into layers (Fig. 3.7-2c). Complementary density functional theory calculations support experimental data and provide further insight into the stability and physical properties of the synthesised compounds. Phonon calculations confirm the dynamic stability of all phases at synthesis *P*. Interestingly, $FeBr_2$ exhibits notable half-metallic behaviour, acting as a normal metal for one spin channel and a semiconductor for the other, thus, the electrons near the Fermi level are distinctly spin-polarised (Fig. 3.7-2d).

These findings establish iron halides as a versatile platform for advanced electronic, spintronic, and functional materials. High-*P* synthesis thus provides a route to novel, tunable materials with both fundamental and technological significance.

c. *High-pressure Mg_3Cl_7 synthesised in a diamond anvil cell as a polar metal with second-harmonic generation (Y. Yin, L.S. Dubrovinsky and N.A. Dubrovinskaia, F. Tasnádi, F. Knoop and I.A. Abrikosov/Linköping, A. Aslandukov, A. Aslandukova and F.I. Akbar/Frankfurt a. M., W. Zhou/Beijing, D. Laniel/Edinburgh, A. Pakhomova, G. Garbarino and H. Fang/Grenoble, T. Fedotenko and K. Glazyrin/Hamburg)*

Polar metals represent an intriguing class of materials where polarity and metallicity coexist in the same phase, which may seem counterintuitive due to the screening effect of free carriers on long-range dipole-dipole interactions. In 1965, Anderson and Blount first proposed theoretically a route for the synthesis of polar metals through a second-order transition of a metallic phase, that might be accompanied by the appearance of a polar axis. Its experimental validation occurred in 2013 when a ferroelectric-like structural transition in the metallic perovskite $LiOsO_3$ was reported. The unique interplay of polarity and metallicity provides an opportunity to study unusual physical phenomena, which has led to increased research interest over the past decade.

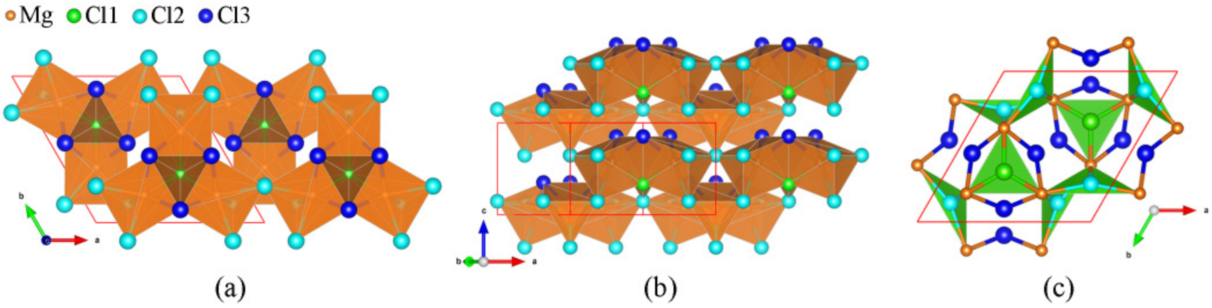

(a) (b) (c)

Fig. 3.7-3: The structure of the novel magnesium chloride Mg_3Cl_7 synthesised in this work. (a) Polyhedral model in $MgCl_6$ polyhedra (brown) as viewed along the *c* direction; the unit cell is outlined in red; (b) a view of the structure perpendicular to the *c* direction, highlighting the stacking of the triads, built of triangular prisms along the *c* direction; (c) a view along the *c* direction highlighting the coordination of Cl atoms with respect to magnesium; Mg atoms are shown in orange, Cl1 in green (coordination number on Mg, CN = 3), Cl2 in cyan (CN = 3), Cl3 in blue (CN = 2).

Despite notable progress, the synthesis of new polar metals remains a considerable challenge, and much remains to be learned about mechanisms of polar distortion in metallic materials. High-pressure (*P*) synthesis provides an opportunity for modifying chemical bonding and for stabilizing unconventional phases. Here, using single-crystal X-ray diffraction (SCXRD) for chemical and phase composition determination, and structural characterization of the materials, we have studied products of chemical reactions in the Mg-Cl system at *P* up to 93 GPa in laser-heated diamond anvil cells. We report the discovery of a novel polar metal, magnesium chloride Mg_3Cl_7, built on $MgCl_6$ octahedra, in which the metallicity of the polar structure is uniquely driven by attractive halogen interactions.

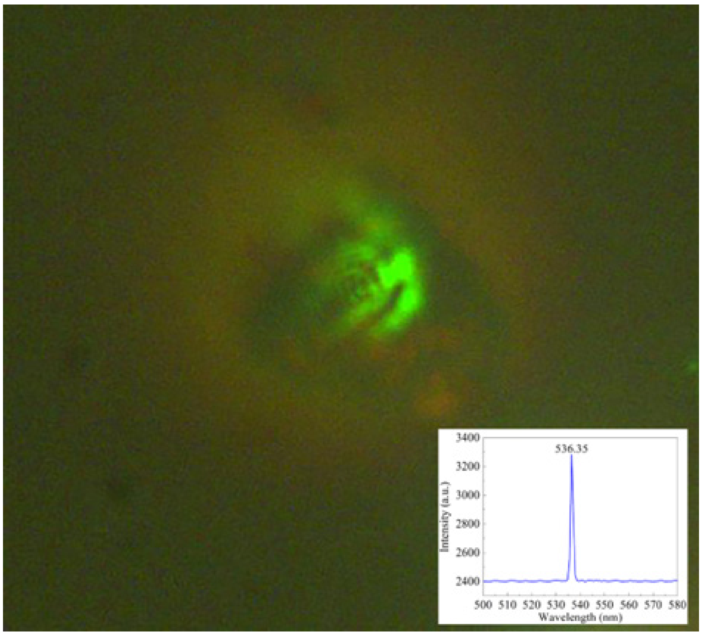

Fig. 3.7-4: Microphotograph of the *P* chamber in a DAC during laser heating. Green light is produced when irradiating the sample with the NIR laser (λ = 1070(2) nm). This is attributed to the non-linear optical properties of the compound formed, Mg_3Cl_7, producing photons of wavelength corresponding to the green color, through second-order harmonic generation (SHG). The inset shows the collected SHG signal.

Two BX90-type screw-driven DACs equipped with 250 µm and 120 µm culet diamond anvils were prepared to study the behaviour of the Mg-Cl system over a wide *P* range. The sample chambers were formed by pre-indenting rhenium gaskets to 30 or 20 µm thickness and laser-drilling a hole of 120 or 60 µm depending on the culet size. Both DACs were loaded with magnesium and carbon tetrachloride (Mg + CCl_4). Synchrotron SCXRD measurements were conducted at the European Synchrotron Radiation Facility (ESRF) and the Deutsches Elektronen-Synchrotron (DESY, PETRA III). The data obtained were analysed using the DAFi program for processing XRD from multi-grain multi-phase samples.

SCXRD revealed the formation of the Mg_3Cl_7 compound at *P* of 28(2)-93(3) GPa. The structure of the new compound has the polar hexagonal space group *P*6₃*mc* (Fig. 3.7-3), an example of a previously unknown anti-Th_7Fe_3 structure type. Measurements of the physical properties have shown that the material is a metallic conductor capable of emitting second-harmonic generation light (Fig. 3.7-4). Complementing *ab initio* calculations support the experimental findings.

d. *Compressional behaviour of naphthalene ($C_{10}H_8$) and anthracene ($C_{14}H_{10}$) (W. Zhou, L.S. Dubrovinsky and N.A. Dubrovinskaia, X. Li, A. Pakhomova and M. Hanfland/Grenoble, F.I. Akbar/Frankfurt a. M.)*

Naphthalene ($C_{10}H_8$) and anthracene ($C_{14}H_{10}$), the first and second members in a series of polycyclic aromatic hydrocarbons (PAHs), are among the representative compounds of this large class of organic materials and have long served as model solids. Their crystal structure, molecular packing, and the relative orientation of molecules within a molecular crystal can be significantly influenced by changes in temperature, pressure (*P*), and electric or magnetic fields. Due to the relatively weak intermolecular interactions in PAHs, the properties of these solids are highly responsive to applied *P*, but have not been sufficiently studied.

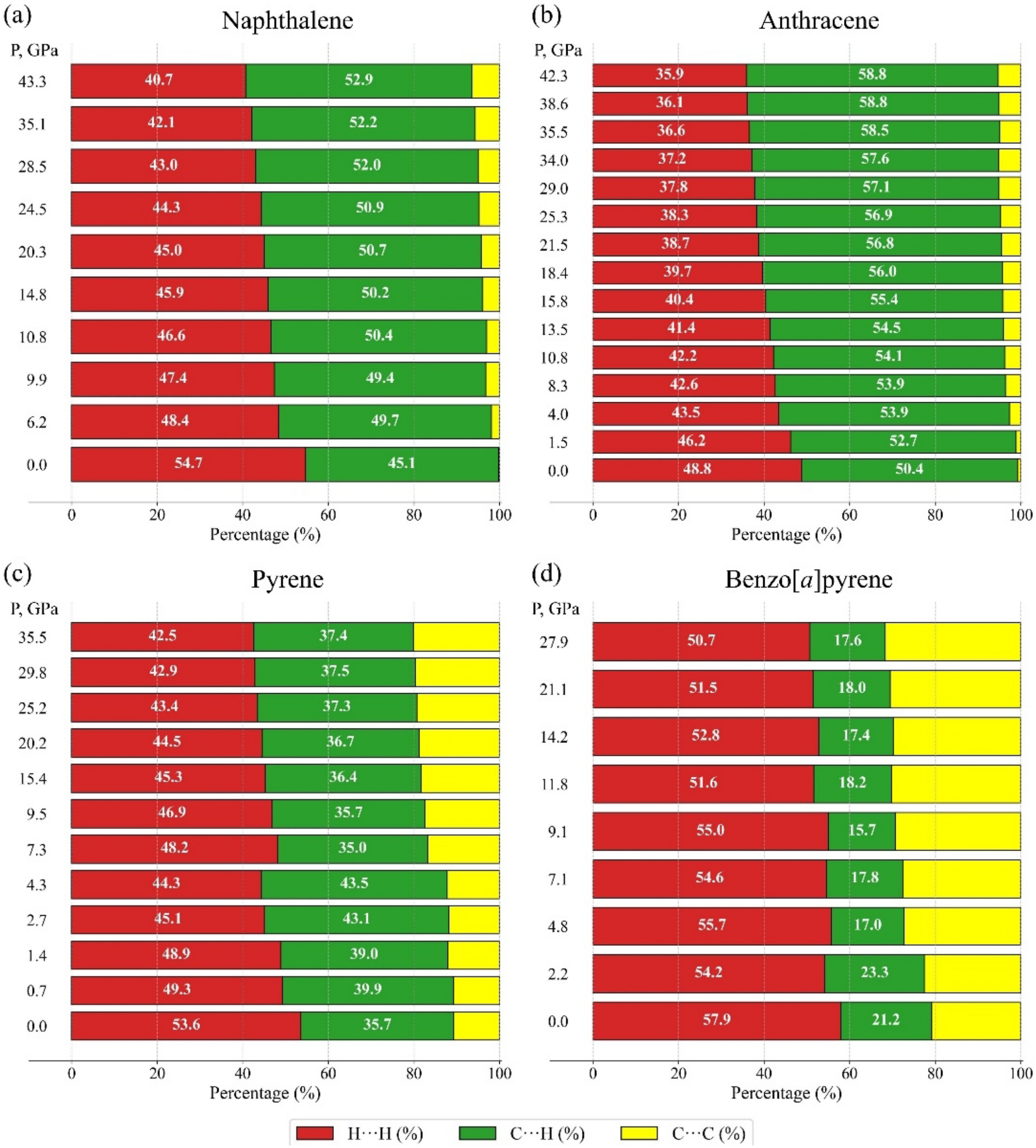

Fig. 3.7-5: Percentage contribution to the Hirschfeld surface area for the various close intermolecular contacts (H···H, C···H and C···C) as a function of pressure for molecules in (a) naphthalene, (b) anthracene, (c) pyrene and (d) benzo[*a*]pyrene.

In this work, we experimentally explored the compressional behaviour of naphthalene and anthracene up to 50 GPa and 43 GPa, respectively, using single crystal X-ray diffraction (SCXRD). At each *P* their crystal structures were refined. Our study reveals similar compressional behaviour of naphthalene and anthracene. With increasing *P*, the intermolecular angles decrease, resulting in significantly denser molecular packing. The unit cell volumes of both compounds decrease at similar rates, reaching approximately half their ambient values in the experimental *P* ranges. Specifically, the volume of naphthalene decreases from 364.3(4) Å^3 at ambient conditions to 171.2(8) Å^3 at 50.7 GPa, while that of anthracene decreases from 476.0(3) Å^3 at ambient *P* to 258.8(6) Å^3 at 42.3 GPa. The analysis of Hirshfeld surfaces and fingerprint plots for naphthalene and anthracene at ambient and high *P* show that the character of intermolecular interactions in both compounds does not change much (Fig. 3.7-5). Our experimental and computational investigations demonstrate that both compounds exhibit remarkable structural stability, as no phase transitions were observed, quite different from pyrene and benzo[*a*]pyrene (Fig. 3.7-5).

e. *High-pressure synthesis of nitrogen-rich $Y(N_5)_3{\cdot}N_2$ pentazolate with perovskite topology (A. Aslandukov, Y. Yin, A. Aslandukova, N.A. Dubrovinskaia and L.S. Dubrovinsky, F.I. Akbar and M. Bykov/Frankfurt a. M., E. Lawrence Bright/Grenoble and I.A. Abrikosov/Linköping)*

The discovery and stabilization of the cyclo-N_5^- anion has introduced a class of pentazolate compounds with significant potential as high-energy-density materials. This potential could be further enhanced by increasing the pentazolate-to-metal ratio. However, so far the pentazolate-to-metal ratio in known solvent-free metal-pentazolate compounds does not exceed 1:1.

Here we report the high-pressure high-temperature synthesis (at 125 GPa, 3000 K) and characterization of a novel yttrium pentazolate $Y(N_5)_3{\cdot}N_2$, which exhibits an exceptionally high nitrogen-to-metal ratio of 17:1. The crystal structure of $Y(N_5)_3{\cdot}N_2$ was solved based on synchrotron single-crystal X-ray diffraction collected at ID11 beamline at ESRF and corroborated by density functional theory calculations (Fig. 3.7-6). The crystal structure of $Y(N_5)_3{\cdot}N_2$ features pentazolate rings and neutral nitrogen dimers, representing a metal-pentazolate framework with perovskite topology. $Y(N_5)_3{\cdot}N_2$ cannot be recovered to ambient conditions due to the weakly-bonded N_2 molecule inclusions within its structure. $Y(N_5)_3{\cdot}N_2$ stabilises three pentazolate anions per metal cation, surpassing the previously achieved 1:1 ratio. This finding may pave the way for the discovery of high-energy-density nitrogen-inclusion-free metal-pentazolates frameworks with a 3:1 (or even higher) pentazolate-to-metal ratio at ambient conditions in the future.

In addition, we propose a centroid-based structure typification for solvent-free inorganic pentazolates. Our analysis reveals that the structure topology of these compounds is very diverse and comprises the motifs of previously known and newly discovered structure types. We believe that it is an important step for further structural classification of pentazolates and other oligo- and polynitrides.

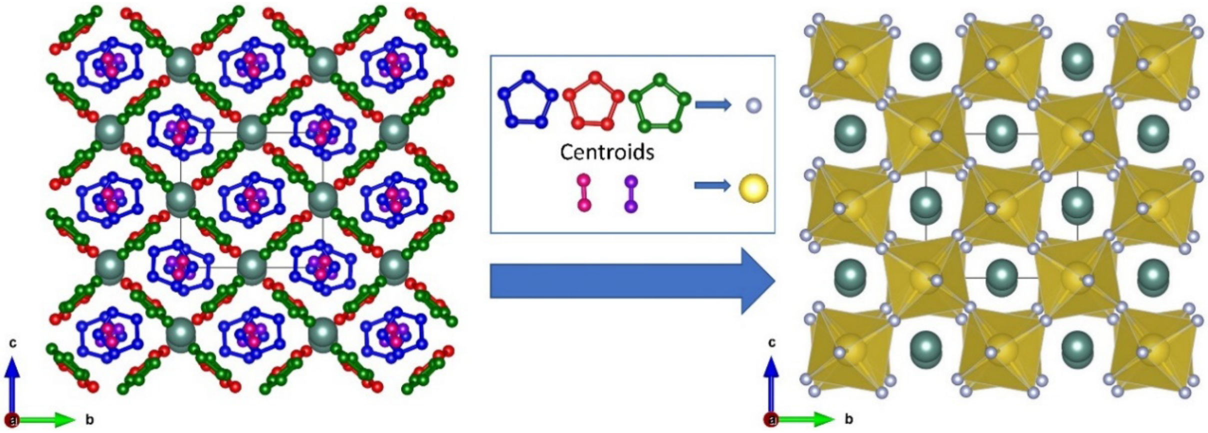

Fig. 3.7-6: Crystal structure of $Y(N_5)_3{\cdot}N_2$ at 125(2) GPa viewed along the *a*-direction (left) and its perovskite topology (right). Greenish big spheres correspond to yttrium atoms; small red, green and blue spheres correspond to nitrogen atoms of three distinct pentazolate rings; small purple and pink spheres correspond to nitrogen atoms of two distinct nitrogen dimers. Grey and yellow spheres represent centroids of pentazolate rings and nitrogen dimers, respectively.

f. *Extended investigations on the pressure stability of $AlB_4O_6N:Cr^{3+}$ (L.S. Dubrovinsky, in collaboration with I. Widmann and H. Huppertz/Innsbruck)*

The development of accurate and reliable pressure (*P*) calibration standards remains a central challenge in high-*P* science, especially as experiments in diamond anvil cells (DACs) routinely exceed tens of GPa and increasingly approach the megabar regime. For decades, ruby (Cr^{3+}-doped Al_2O_3) has served as the principal luminescent *P* gauge, capitalizing on the well-characterised *P*-induced shift of its R_1 and R_2 emission lines. However, the close spectral spacing of these lines and their progressive broadening under nonhydrostatic stress impose inherent limitations on calibration accuracy at elevated *P*. The search for alternative luminescent materials capable of maintaining sharp and well-resolved spectral features under extreme compression is therefore of considerable interest to the high-*P* community. Against this backdrop, the recently discovered aluminium oxonitridoborate $AlB_4O_6N:Cr^{3+}$ has emerged as a promising candidate. Unlike ruby, this compound exhibits only a single narrow R line at ambient conditions, a consequence of its nearly ideal octahedral coordination environment around Cr^{3+}. Earlier work demonstrated that this single-line luminescence persists up to at least 52 GPa, raising the prospect of improved *P* calibration at high compression. Here we extend the investigation of the structural and luminescence stability of $AlB_4O_6N:Cr^{3+}$ to 80 GPa.

To explore the behaviour of $AlB_4O_6N:Cr^{3+}$, a combination of optimised high-*P*/high-temperature multianvil synthesis, powder X-ray diffraction, synchrotron single-crystal diffraction, and DAC-based luminescence spectroscopy was employed. The $AlB_4O_6N:Cr^{3+}$ crystals were confirmed by Rietveld refinement to be structurally consistent with the known hexagonal $P6_3mc$ phase. For high-*P* optical measurements, micron-scale crystallites were loaded in a DAC with neon as a *P*-transmitting medium, and fluorescence spectra were recorded up to 78(1) GPa. Complementary single-crystal X-ray diffraction data were collected at synchrotron facilities (ESRF ID15B and PETRA III P02) under identical *P* conditions to examine potential structural modifications responsible for changes in luminescence behaviour.

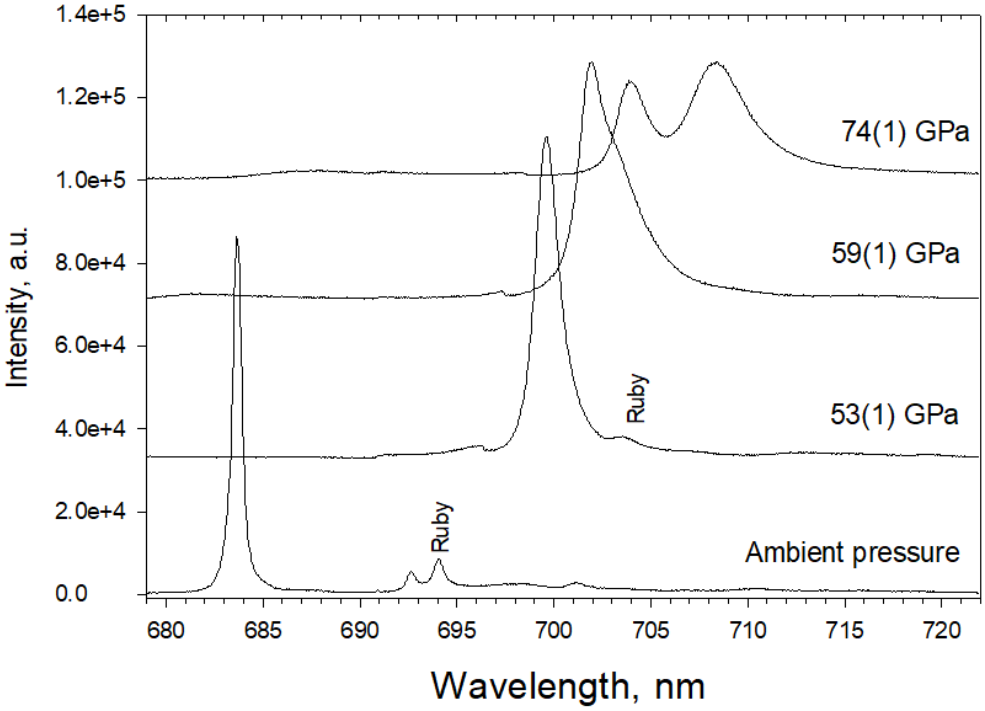

Fig. 3.7-7: Examples of fluorescence spectra of $AlB_4O_6N:Cr^{3+}$ (0.7 mol. % Cr^{3+}) collected upon compression using the pressure transmitting medium neon.

Luminescence measurements revealed that the single R line characteristic of $AlB_4O_6N:Cr^{3+}$ persists up to approximately 59(1) GPa (Fig. 3.7-7). Over this range, the line shifts linearly with *P* (dL/dp ≈ 0.302 nm/GPa), in agreement with previous reports. Beyond this threshold, however, the fluorescence peak becomes asymmetric, and clear splitting into two distinct lines appears by ~ 74 GPa. This splitting marks a significant deviation from the behaviour at lower *P* and necessitates structural investigation to determine its origin. By 78(1) GPa, where the separation of the two peaks is well pronounced, single-crystal diffraction data show that the compound retains its original hexagonal structure without any detectable phase transition or decomposition. The lattice parameters and interatomic bond lengths decrease substantially with *P*, as expected, but the crystal structure remains topologically unchanged. Analysis of the local coordination environments suggests that a subtle distortion of the $(Al/Cr)O_6$ octahedra—still within the limits of experimental uncertainty—likely accounts for the observed luminescence splitting. Although the distortion could not be quantified with high precision due to the intrinsic challenges of diffraction from light-element compounds at > 75 GPa, no alternative mechanism is supported by the data. Thus, the emergence of two R lines at very high P reflects the departure from the nearly perfect octahedral symmetry that enables single-line luminescence at lower P.

The findings demonstrate that $AlB_4O_6N:Cr^{3+}$ retains its structural integrity and general luminescence suitability well beyond 50 GPa, extending up to at least ~ 60 GPa before measurable symmetry-related changes begin to affect its optical response. Even above this threshold, the material remains structurally robust and its luminescence features remain sharp and resolvable up to 78(1) GPa, far exceeding the range where ruby lines become significantly broadened or merged. This makes $AlB_4O_6N:Cr^{3+}$ a highly promising luminescent P sensor material for high-precision measurements in the 0-60 GPa regime and potentially beyond, suggesting that it may outperform ruby in accuracy under certain conditions. Future work will aim to determine the maximum P this compound can withstand before structural breakdown, as well as to further refine calibration curves based on its P-dependent luminescence behaviour.

g. *Atomistic insight into the synthesis of gold hydride at high pressure and temperature at the X-ray free-electron laser (K. Abraham and R. Redmer/Rostock, M. Frost and S.H. Glenzer/Menlo Park, M. Schulze and G. Steinle-Neumann)*

Gold is considered an unreactive metal, but recent experiments at the European X-ray free electron laser facility (XFEL) report the formation of gold hydride at pressures (*P*) above 40 GPa and temperatures (*T*) of 2200 K and higher. Diamond anvil cells (DAC) were loaded with gold and hydrocarbons as H-precursors and exposed to pulsed high-intensity X-rays at the XFEL, used to both heat and probe the sample; as the XFEL pulse duration (< 50 fs) is shorter than the timescale of nuclear motions, diffraction occurs prior to heating the sample, a procedure that is repeated with a frequency of 4.5 MHz (222 ns). The high-*T* reaction product of Au and hydrogen has hexagonal symmetry, reminiscent of a Cu_2H phase, but with unknown stoichiometry. The high-*T* phase reverts back to fcc Au on cooling, suggesting that its stability is entropy-driven. As analytical tools for the *in situ* analysis of the sample are limited, Kohn-Sham density-functional theory (DFT) based molecular dynamics (MD) simulations were used to support the experiments. Simulations were performed for a range of stoichiometries from Au to Au_2H, with initial structures of the hydrides based on the Cu_2H phase over the *P*-range in which the experiments observe hydride formation (40-80 GPa), with a thermostat of 2500 K.

The DFT-MD simulations support the inference that a hexagonal phase is stable at high *P* and *T* for gold hydride, and find that H atoms disorder over the H-sites in the Cu_2H structure. Hydrogens move rapidly through the structure, with diffusivity exceeding 10^{-4} $cm^2 \cdot s^{-1}$, which provides a potential mechanism for the required entropy stabilizing the hexagonal hydride. The experimentally observed axial ratio of larger than close-packing (> 1.633) is confirmed by the DFT-MD results. Most interestingly, the excess volume of the hydrides over pure Au from the DFT-MD simulations can be used as an estimate for the hydrogen content in the experimentally synthesised hydrides (Fig. 3.7-8), with a general trend of increasing H incorporation with *P*.

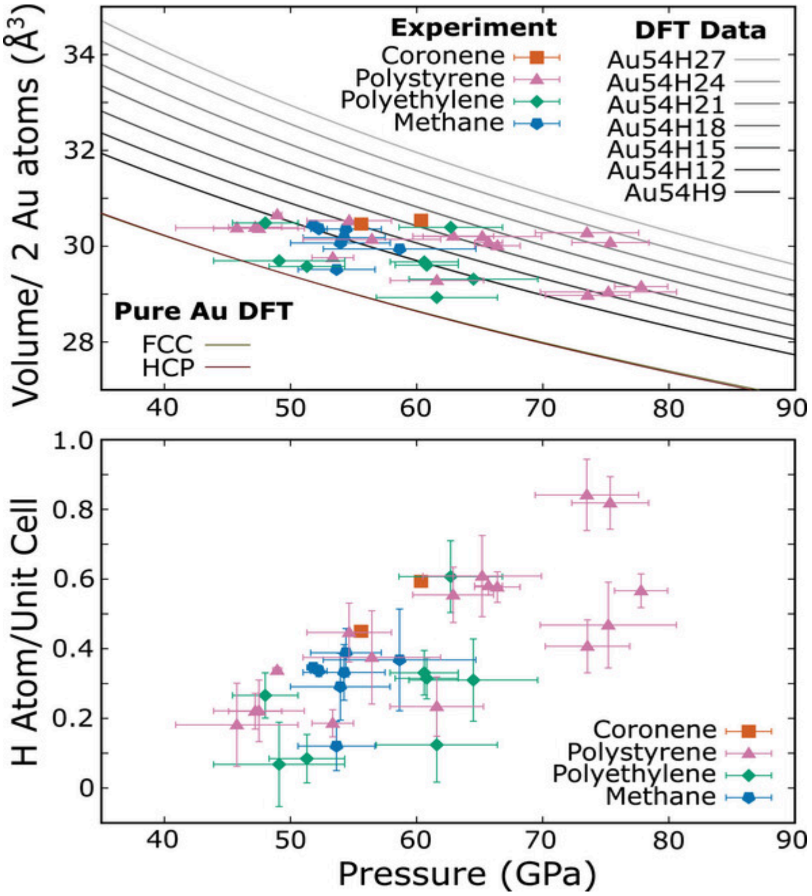

Fig. 3.7-8: Volumes for gold hydride formed in the experiments (symbols) and from computations with varying H content (lines). The *P*-dependence of experimental volumes imply increasing H content with *P*. The H-content in the experiments (bottom) is determined based on the molar volume of H from the DFT-MD simulations. Different colors for the symbols indicate different hydrogen precursor materials.

3.8 Methodological developments

The improvement of experimental and analytical techniques has been crucial to BGI's research since its beginnings. Experimental developments have focused on broadening the accessible parameter space for high-pressure, high-temperature experiments in order to reproduce the conditions of the deep Earth or the interiors of other planets. Since increasing pressures and temperatures in experiments tend to produce smaller and smaller samples, analytical techniques have to be adapted to smaller sample volumes and higher spatial resolution. This section includes four contributions that present methodological progress in widening the experimental parameter space and four projects that improve analytical possibilities, as well as progress in computational modelling.

Kurnosov *et al.* report the installation of a new laser that allows heating of small samples in the diamond anvil cell in a system capable of determining density (via X-ray diffraction) and elasticity (via Brillouin scattering) of a single crystal at pressures and temperatures pertaining to the entire lower mantle. Results from this type of measurement are urgently needed for the interpretation of seismic wave data to elucidate the structure of the deep Earth. Niu *et al.* present a significant expansion of the accessible pressure (depth) range in experiments with Kawai-type multianvil presses. Whereas standard presses of this type are limited to pressures of about 25 GPa, they managed to achieve pressures of up to 45 GPa in this new study while keeping a sample volume of about 10 mm^3.

The measurement of fluid overpressure in an experimental multianvil assembly at high pressure and temperature is demonstrated by Pöppelbaum *et al.* in the third report of this chapter. This phenomenon is rather common in the deep Earth, where fluids are released from crystal structures due to increasing pressure and temperature, causing a weakening of the surrounding rocks that may result in earthquakes at depths where brittle failure normally does not occur. Kubik *et al.* present a design of a multianvil assembly that allows heating of relatively large volumes of sample material with small temperature gradients. This is achieved by employing a box-shaped furnace instead of the commonly used furnace tube.

Among the analytical advancements, Minchenkova and Audétat introduce a strategy for measuring experimentally generated diffusion profiles with laser ablation ICP-MS, which requires a larger amount of material compared to other methods but provides a higher sensitivity. Instead of measuring along the profile vertically, they prepared their samples such that the profile is extended horizontally by a factor of 6-11, allowing for larger amounts of sample material per measurement point.

The next two contributions present advancements in the analysis of isotope ratios with high precision using a Neoma MC-ICP-MS/MS coupled with a 193 nm NWR nanosecond excimer laser. Zhu *et al.* optimised the analysis of Sn isotopes, which are widely used as tracers of metallogenesis, the characterisation of magmatic–hydrothermal evolution, and crustal geochemistry. Chen *et al.* developed an advanced protocol for determining the ages of lunar rocks using the Rb/Sr isotope system that overcomes earlier problems, particularly with the isobaric interference of ^{87}Rb on ^{87}Sr, which can compromise measurement accuracy.

In their numerical modelling of strain localization processes in rocks, Spang *et al.* encountered problems arising from strongly varying spatial and temporal scales during the simulation, which caused the model to be governed largely by the temporal and spatial resolution rather than by the actual physical processes. As a solution, they developed a time stepping algorithm that dynamically adjusts to the evolving time scale of the deformation process. They also explored different options to limit the model's variation in spatial scales.

a. *Development of the in-house system for simultaneous measurement of acoustic wave velocities and densities of materials during laser heating at high pressures (A. Kurnosov, T. Boffa Ballaran and L.S. Dubrovinsky)*

Simultaneous measurements of acoustic wave velocities and densities of minerals relevant to the Earth's and other planetary interiors are essential for interpreting seismic observations. Such combined measurements provide internally consistent data that are independent of external pressure calibrations. At BGI, an in-house system for these measurements has been available for several years and has successfully produced data over the entire pressure range of the Earth's lower mantle, at temperatures up to ~ 800 K achievable with resistively heated diamond anvil cells (DACs). However, realistic geotherms extend to several thousand Kelvin, temperatures that can only be reached by laser heating.

In recent years, a CO_2 laser-heating setup has been integrated into the in-house Brillouin spectroscopy (BS) system, enabling measurements during laser heating in the DAC at high pressures (see Annual Report 2023). Until now, density information for such experiments had to be obtained separately from thermal equations of state based either on limited experimental data or on modelling. The main technical obstacle to obtaining *in situ* unit-cell volumes or densities during laser heating of single crystals arises from refraction of the heating laser in the diamond anvils. While X-ray refraction in diamond is negligible – allowing rotation of the DAC within the opening angle without displacing the sample from the X-ray beam – visible and infrared radiation have a refractive index of ~ 2.4 in diamond. Consequently, even minor DAC rotations redirect the laser beam inside the diamond, preventing stable heating of the sample.

At synchrotron facilities, this challenge has been partially addressed using portable fibre-based laser-heating systems, in which flexible waveguides couple the laser to heating heads mounted directly on the rotational stage. This configuration ensures a constant beam incidence angle during cell rotation. However, such an approach is only feasible for near-infrared (1064 nm) lasers and micrometre-sized laser absorbing samples. For BS on transparent samples, typically tens of micrometres in size, these lasers are unsuitable. CO_2 lasers (10.6 μm), which are ideal for homogeneous heating of transparent materials, cannot be efficiently coupled through flexible waveguides due to their poor flexibility and limited power tolerance.

In this work, we implemented and successfully tested an alternative solution based on recently developed diamond anvils with a round table (DART, Fig. 3.8-1). These anvils feature a spherical diamond table whose surface curvature is geometrically centred on the culet. As a result, any laser directed toward the culet centre strikes the diamond surface orthogonally, independent of DAC rotation. This geometry enables stable laser heating throughout rotational scans within the DAC's opening angle. To reduce XRD acquisition times and minimize rotational movements, we replaced the previously used point detector with a MAR345 area detector (see Annual Report 2024). With this upgrade, both XRD and BS can now be performed on the same sample under identical pressure-temperature conditions, during laser heating, which was a primary objective of this development.

Additional advantages of the DART geometry were also identified. The curved diamond surface introduces an effective 2.4 × optical magnification, improving the focusing of both the CO_2 heating laser and the green BS probe laser. On the collection side of the BS system, the same magnification enhances imaging of the sample. For BS, this allows the use of significantly smaller samples: the minimum required lateral sample size has been reduced from ~ 50 µm to ~ 20 µm. Consequently, smaller culets can be employed, enabling access to higher pressures. Improved focusing of the CO_2 laser also increases heating efficiency, reducing the laser power required to achieve a given temperature and enhancing performance at high pressures. Overall, the upgraded system now covers the full pressure-temperature conditions of the Earth's lower mantle for combined acoustic-velocity and density measurements.

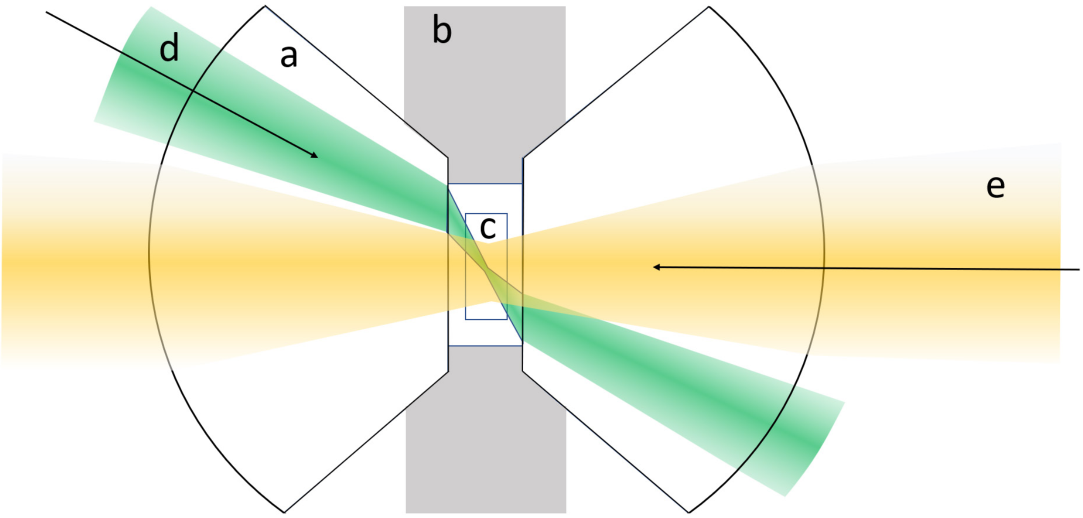

Fig. 3.8-1: a – diamond anvil with a spherical table (DART), b – gasket, c – sample, d – Brillouin scattering probe laser beam, e – CO_2 laser beam.

Further improvements have been observed, including higher BS resolution and improved separation of sample, diamond, and pressure-medium signals. These effects require additional investigation.

b. *High-pressure generation above 45 GPa over a 10 mm^3 volume with a multianvil press (G. Niu/Beijing, L. Man, A. Chakraborti, C. Qian, R. Pierru and H. Gou/Beijing)*

The multianvil press is a widely used device for generating high-pressure and high-temperature conditions in geoscience and materials science, offering sample volumes several orders of magnitude larger than those achievable with diamond anvil cells. However, conventional Kawai-type assemblies are limited to pressures below ~ 25 GPa when millimetre-scale samples are required. While recent studies have reached higher pressures by using smaller truncation edge lengths (TEL) of 1.5 or 1.0 mm, this comes at the expense of a ~ 90 % reduction in sample volume, making *in situ* measurements of bulk physical properties nearly impossible. This technical limitation hinders the exploration of fundamental questions, such as the direct measurement of mantle mineral moduli under lower-mantle conditions. Consequently, there is an urgent need to extend the pressure range of conventional 3 mm TEL assemblies without sacrificing sample volume or the anvil gap required for complex diagnostic techniques.

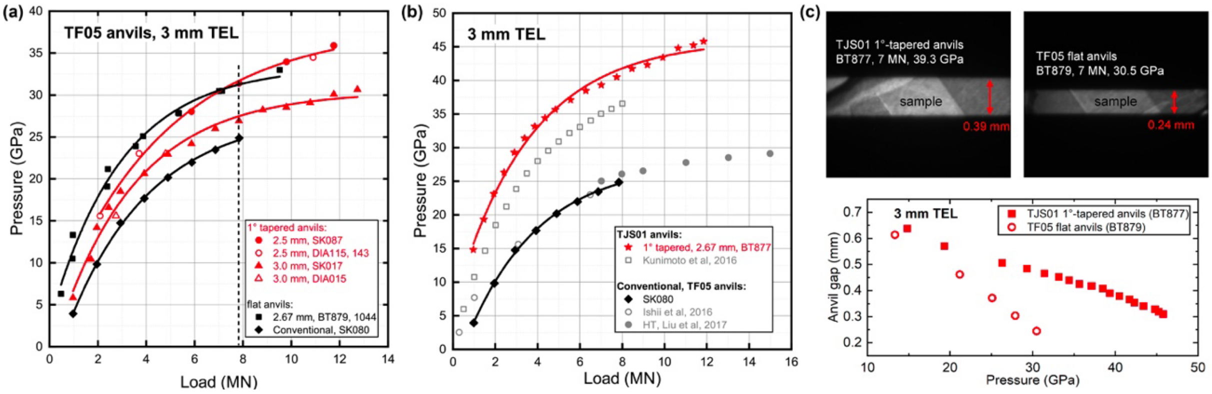

Fig. 3.8-2: (a) Pressure generation efficiency employing different gasket configurations with TF05 flat anvils; (b) pressure generation curves of the optimised assembly using 3 mm TEL TJS01 anvils, compared with previous studies; (c) anvil gaps observed using tapered and flat anvils. X-ray images were taken under 7 MN using different gasket and anvil configurations.

In this study, we systematically optimised the experimental setup for a Kawai assembly using tungsten carbide anvils with a TEL of 3 mm to extend the achievable pressure range. As shown in Figure 3.8-2 (a), reducing the gasket height from 3 mm to 2.67 or 2.5 mm significantly improved load transmission efficiency, enabling an approximately 33 % increase in pressure compared with conventional designs using the same type of anvils. Using the optimised gasket design together with ultra-hard tungsten carbide anvils with a 1° taper (TJS01, Fujilloy; TEL=3 mm), pressures of up to 45.8 GPa were achieved at room temperature (as shown in Figure 3.8-2 (b)), while maintaining a truncation-confined volume greater than 10 mm^3. Additionally, as shown in Figure 3.8-2 (c), 1° tapering effectively pre-compensates for anvil deformation under extreme loads, ensuring truncation faces remain nearly parallel and maintaining a substantial anvil gap greater than 0.3 mm. This technical breakthrough not only enables the synthesis of functional materials with large sample volumes at pressures above 45 GPa, but also opens access to unprecedentedly high pressures for precise physical property measurements that require large sample volumes and large anvil gaps, including ultrasonic interferometry, electrical impedance, and thermal conductivity measurements in a multianvil press. Furthermore, this high-efficiency strategy enables extreme pressure generation under moderate hydraulic loads, extending anvil fatigue life and making routine operations above 30 GPa more sustainable and economical.

c. *High-pressure* in situ *synchrotron measurements of fluid overpressures (M. Pöppelbaum, D.J. Frost, T. Boffa Ballaran and L. Man, in collaboration with R. Farla/Hamburg)*

The migration of supercritical fluids through Earth's mantle influences mantle metasomatism, the onset of volatile-mediated melting and possibly the generation of deep earthquakes. Fluid flow mechanisms under high-pressure and high-temperature conditions, however, are poorly understood, resulting in uncertainties in migration timescales. This is due to the difficulty of measuring the permeability of mantle assemblages to fluid flow. It should, in principle, be possible to determine the permeability, k, of an assemblage using Darcy's law,

$$q = -(k/\eta)(\Delta P/x),$$

which relates the fluid flux, q, across a distance x to the permeability, the fluid viscosity η and the pressure difference ΔP. Creating and determining pressure differences should be possible in high-pressure and -temperature experiments, as the dehydration of hydrous minerals is frequently invoked to generate a fluid overpressure, which could be used to drive a fluid through a mineral assemblage. However, it is also possible that in multianvil devices any overpressure becomes rapidly relaxed as a result of plastic flow of the assembly or gasket or due to adjustment of the confining oil pressure.

In this study we test whether it is possible to generate and measure an overpressure in a multianvil device under conditions equivalent to those in a sub-arc subducting slab. The overpressure is generated through the dehydration of serpentine (antigorite) according to the reaction,

$$\underset{\text{antigorite}}{\mathrm{Mg_{48}Si_{34}O_{85}(OH)_{62}}} = \underset{\text{fluid}}{\mathrm{31H_2O}} + \underset{\text{forsterite}}{\mathrm{14Mg_2SiO_4}} + \underset{\text{enstatite}}{\mathrm{10Mg_2Si_2O_6}}$$

If it is assumed that the multianvil maintains a constant rigid volume during the dehydration process, then, using equations of state for the solid and fluid phases, it is possible to calculate an overpressure generated upon dehydration. This overpressure depends on the P and T, but is calculated to reach values approaching 1 GPa at sub-arc pressures of ~3 GPa. To measure this overpressure, the capsule assemblage shown in Figure 3.8-3 was employed, where a lower fluid source of serpentine powder is mixed with a few percent of Au that acts as a pressure calibrant. The fluid released by dehydration then passes through a hot-pressed layer of olivine and is captured in an overlying layer of MgO, which is transformed to brucite. Au in the MgO layer also acts as a pressure calibrant and the overpressure is determined by comparing pressures measured by X-ray diffraction in the serpentine and MgO layers. The flux of H_2O through the olivine sample is determined after the experiment by measuring the thickness of the brucite layer produced at the boundary between the olivine and MgO.

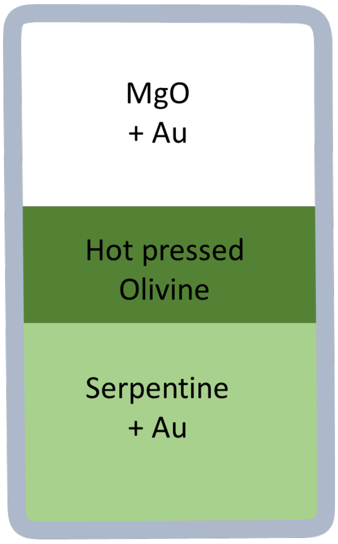

Fig. 3.8-3: Schematic of the 2 mm diameter cylindrical titanium metal capsule. The serpentinite fluid source was mixed with 5 wt. % Au powder. As the serpentine breaks down fluid is released which passes through the hot-pressed olivine core. H_2O passing through the olivine sample transforms the MgO material above the sample to brucite. The MgO layer also contains powdered Au as a pressure calibrant. The overpressure is determined as the difference in pressure recorded by the Au in the serpentine and MgO layers.

The experiments were conducted at the P61B beamline of the PETRA III Synchrotron (DESY) in Hamburg using 12/9 (cube edge length/anvil truncation length) cubic MgO assemblies in the 'Aster-15' six-ram press. In a previous attempt to measure the overpressure, single-crystal olivine capsules were employed. However, these were found to be too strong and shielded the capsule contents from the compressional environment until temperatures near 1000 K were reached and plastic deformation occurred. To avoid this problem, titanium foil capsules were used, which successfully sealed in the H_2O while still being transparent to X-rays.

Figure 3.8-4 shows the pressure differences calculated between Au in the serpentine layer and the MgO layer for an experiment performed at approximately 3 GPa. Serpentine dehydrates at temperatures of approximately 850 K. During the experimental run, the temperature was raised over 30 minutes to 1000 K and an overpressure of approximately 0.5 GPa was recorded in the serpentine layer relative to the MgO layer. This overpressure agrees very well with that predicted using equation-of-state data and implies that the multi-anvil retains a relatively constant sample volume upon dehydration at these temperatures. This pressure difference can be used in combination with Darcy's law to calculate the permeability of the olivine assemblage, using the fluid flux determined from a post-mortem examination of the amount of MgO transformed to brucite.

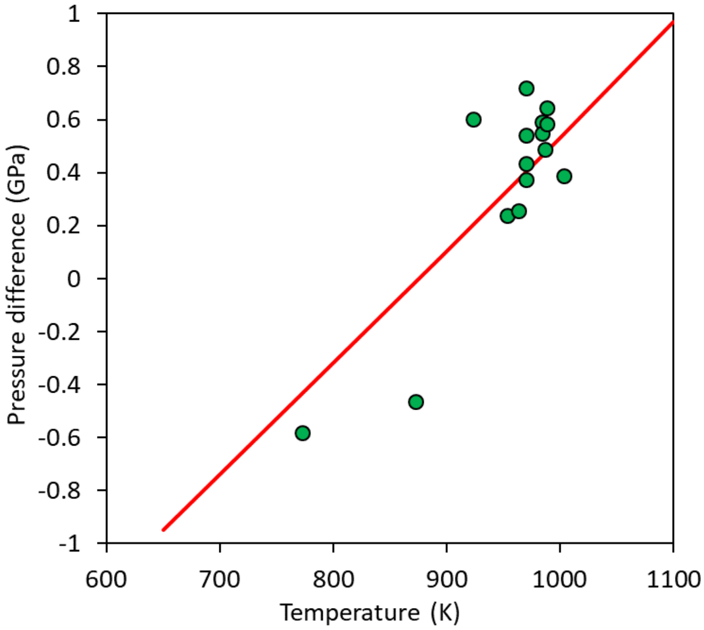

Fig. 3.8-4: The pressure difference determined using Au in the serpentine and MgO layers is plotted as a function of temperature for an experimental run performed at approximately 3 GPa (green circles). The red curve is calculated using equations of state for the solid and liquid phases, assuming that the volume of the serpentine reaction products remains constant upon dehydration.

d. *Thermal gradients in box furnace high-temperature high-volume assemblies determined by alumina solubility (E. Kubik, L. Man, A. Néri and A. Chakraborti, in collaboration with R. Hin/Milano)*

In this work, we measured thermal gradients in custom box furnace assemblies designed for high-temperature, high-pressure experiments in the multianvil press requiring large-volume samples. We used two techniques to characterise the gradients: spinel growth and alumina solubility.

Box furnace multianvil assemblies present a number of advantages including enhanced heating efficiency and a broadened range of possible experimental conditions, while maintaining a relatively homogeneous heating. Previous experimental work from the Bayerisches Geoinstitut also reported that this type of assembly design imposes remarkably low temperature gradients on the samples (< 2.4 °C/mm at 4 GPa and 1773 K). However, the custom assemblies in this work (Fig. 3.8-5a) were designed to maximise the sample volume to fit the experimental requirements of our study, leading to an extreme increase in sample volume compared to the standard assemblies (Fig. 3.8-5b), reaching up to 585 % in the case of the 18M assembly and 350 % for the 25M. Here, we investigate whether these unusually large samples for the multianvil technique, similar in size to those used in the piston cylinder technique, share the same feature of limited thermal gradients as previously reported for other box furnace designs.

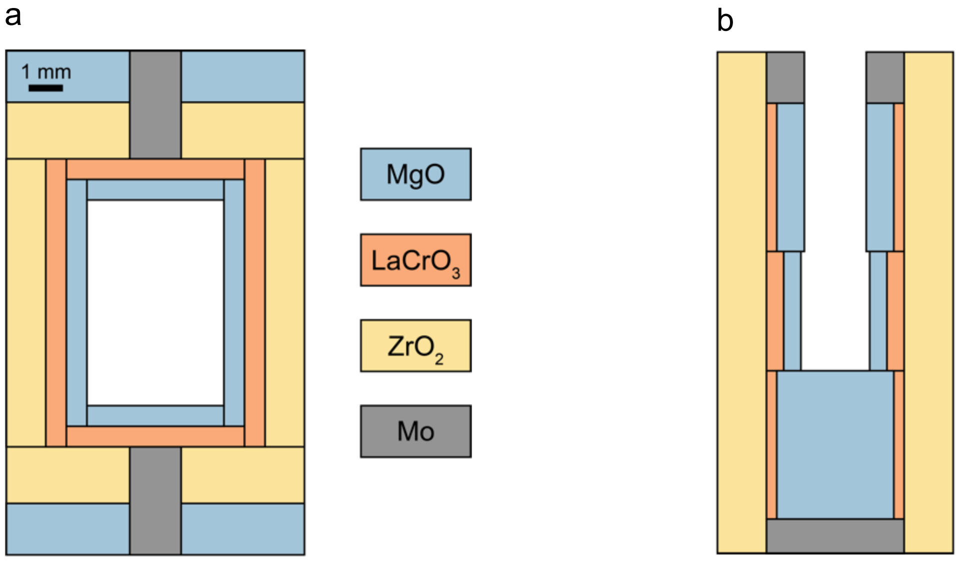

Fig. 3.8-5: a) Custom 25M box furnace multianvil assembly developed at the Bayerisches Geoinstitut. b) Standard 25M assembly, shown at the same scale as in (a).

Experiment Z2441 was performed at 14 GPa and 2173 K for 10 minutes using the 18/11 configuration. Its MgO capsule was packed with a mixture of MgO and Al_2O_3 powders. The temperatures in the experiment were calculated from alumina concentrations in MgO-rich phases, using a calibration established previously (Fig. 3.8-6a). These alumina concentrations were measured by EPMA on the pre-cut and polished run product (Fig. 3.8-6b).

Using the spinel layer growth kinetics technique, we conducted experiment Z2405 at 8 GPa and 2473 K in a 25/15 box furnace assembly. The MgO capsule was loaded with a pile of seven interposed discs of crushable MgO and Al_2O_3 directly inserted into the $LaCrO_3$ furnace. The experiment was left for 30 minutes at the target temperature of 2473 K to induce sufficient spinel growth. The thickness of the spinel layer, which could be directly linked to temperature via an empirical relation (Fig. 3.8-6c), was measured in different locations of the polished sample by SEM (Fig. 3.8-6d). For both experiments, the temperature was measured with a D-type thermocouple inserted vertically in the assembly directly above the experimental capsule, offset from the central axis where the upper molybdenum electrode is located (see Fig. 3.8-6d).

Both thermal gradient maps (Figs. 3.8-6a and c) present limited gradients, well below 100 K/mm and probably not higher than 40 K/mm in the experimental capsule centre, even at very high temperatures (Fig. 3.8-6c). We also note that both techniques yielded the same order of magnitude of gradients, although the gradients are lower in experiment Z2441, likely due to the lower experimental temperature. To conclude, these custom box furnace assemblies present the following advantages: (1) enhanced experimental temperature range, (2) significant sample volume increase with respect to the standard assembly, and (3) limited temperature gradients with stable heating for significant time durations at very high temperatures.

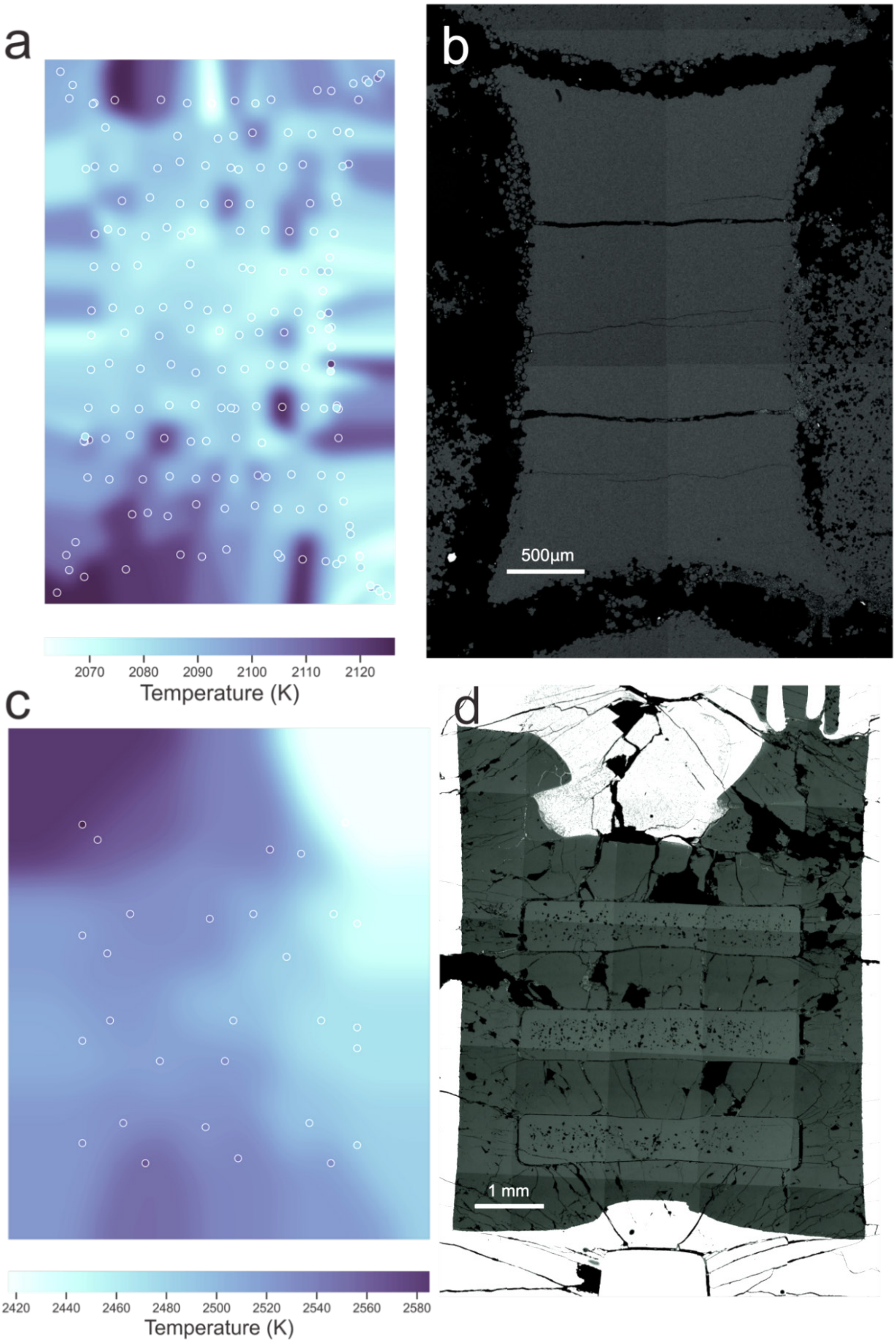

Fig. 3.8-6: Results of thermal gradient measurements represented on heat maps. (a) Heat map of experiment Z2441 interpolated from data collected using the alumina solubility technique. (b) Backscattered electron map of experiment Z2441, to scale relative to the heat map (a). (c) Heat map of experiment Z2405 interpolated from spinel growth data. (d) Backscattered electron map of experiment Z2405, to scale relative to the heat map (c).

e. *A method to analyse short diffusion profiles by LA-ICP-MS (A. Minchenkova and A. Audétat)*

Measuring trace elements in diffusion profiles of a few tens of micrometres length is challenging because this length is too short for conventional LA-ICP-MS analysis, and too long for SIMS depth profiling. In principle, the length would be suitable for depth profiling via LA-ICP-MS. However, since profiles usually have to be measured from high to low concentration, there is a high risk of contaminating the signals from deeper levels with material from higher levels, leading to profile distortion. We thus developed a method to analyse diffusion profiles of a few tens of micrometres in lengths by a (nearly) conventional LA-ICP-MS technique. Our specific application was to measure Zr diffusion profiles next to zircon crystals that were immersed at different temperatures and for different times in hydrous rhyolite melts, in order to obtain data on zircon solubility and Zr diffusivity.

The principle is very simple and certainly not new: instead of measuring concentration profiles perpendicular to the zircon–melt interface, they are measured on surfaces that are inclined by a small angle (~ 5-10 degrees) relative to the interface, resulting in a stretching of the profile by a factor of ~ 6-11. The main challenge of this approach was to obtain stable, long-enough LA-ICP-MS signals despite very shallow laser pits. Discs of natural, gem-quality zircon crystals were equilibrated in hydrous rhyolite melts at 800 °C, 2 kbar in rapid-quench cold-seal pressure vessels for durations of 4-5 days and then rapidly quenched to room temperature. Recovered samples were prepared as shown in Figures 3.8-7a, b. First, the sample was cut perpendicular to the zircon–glass interface into two halves (Fig. 3.8-7a). One half was then polished from the glass side until only a thin wedge of glass was left (left piece in Fig. 3.8-7b), whereas the other half was polished from the zircon side until only a small wedge of zircon was left (right piece in Fig. 3.8-7b). In piece "Z" the laser drilling direction at individual spots is *toward* the zircon, hence Zr concentrations increase with time, whereas in piece "G" the drilling direction is away from the zircon, and the Zr concentrations therefore decrease. A reflected-light photomicrograph of one of the pieces after the laser ablation analysis is shown in Figure 3.8-7c.

Laser ablation was performed in a sample chamber with a relatively slow washout time, using rectangular pits measuring 25 × 50 µm, a repetition rate of 1 Hz, and 20 shots per location. This analytical approach resulted in pits of ~ 3 µm depth and relatively flat, well-reproducible LA-ICP-MS signals.

The result of an experiment performed at 800 °C for 112 hours is shown in Figure 3.8-8. The distances in this figure refer to true, non-stretched distances from the zircon surface, calculated from the polishing angle and the distances measured on the sample surface, plus a correction of ±1.5 µm applied to account for pit depth. Although a 25 µm-wide laser pit was used on the sample surface in order to obtain sufficiently high Zr signals, the effective spatial resolution perpendicular to the zircon–glass interface is on the order of a few micrometres. The fact that the two measured profiles returned virtually identical fits and Zr intercept values suggests that convolution effects are negligible.

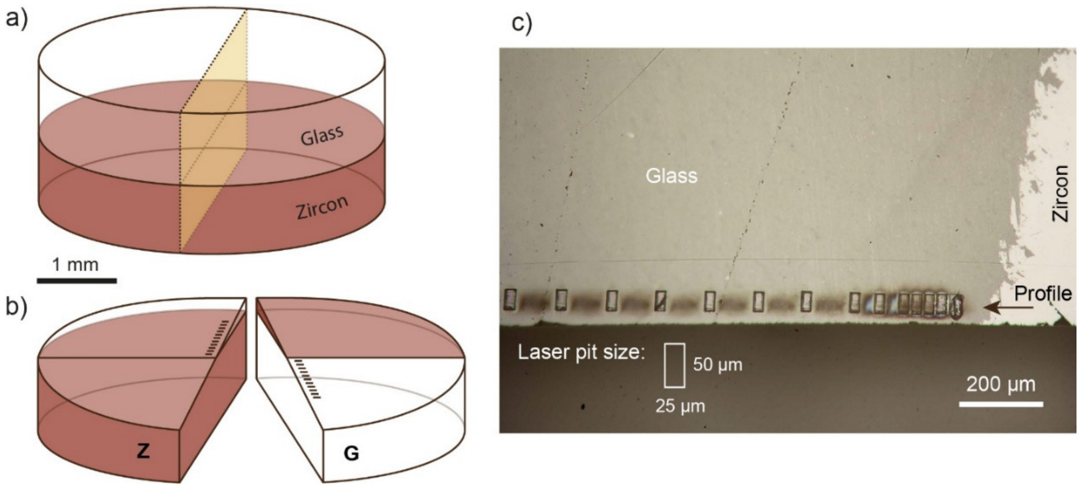

Fig. 3.8-7: (a, b) Schematic illustration of the sample preparation after the experiments. (c) Reflected-light photomicrograph of part of a LA-ICP-MS profile measured on one of the two sample halves.

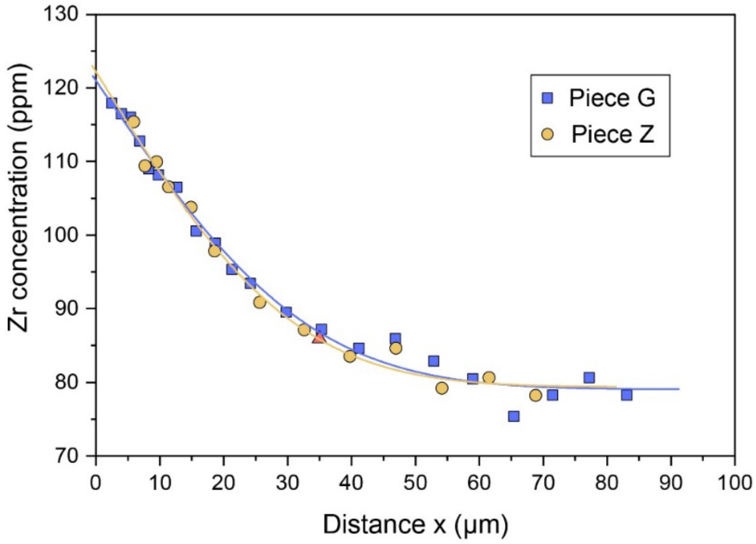

Fig. 3.8-8: Zr diffusion profiles measured next to a zircon crystal that was equilibrated in hydrous rhyolite melt at 800 °C, 2 kbar for 5 days. The ±identical nature of the two profiles suggests that convolution effects are negligible.

f. *Development of* in situ *Sn isotopic analysis in cassiterite using LA–MC–ICP–MS/MS and a synthesised standard material (D. Zhu, E. Kubik and A. Bouvier)*

Cassiterite (SnO_2) is the primary host of tin in magmatic-hydrothermal systems. Its Sn isotopic composition provides a sensitive tracer of redox evolution, fluid exsolution, and metal sources. However, conventional solution-based Sn isotope analysis requires hazardous dissolution procedures and yields only the average isotopic composition of crystals that have been pooled together, obscuring microscale heterogeneity. *In situ* analysis using Laser Ablation (LA) coupled with Multi-Collector Inductively Coupled Plasma Mass Spectrometry (MC-ICP-MS) offers a powerful alternative. Yet, routine application has been limited by matrix effects, laser-induced fractionation, and the absence of suitable isotopically homogeneous cassiterite standards.

This study presents a comprehensive methodological framework for high-precision *in situ* Sn isotope determination using a Neoma MC-ICP-MS/MS coupled with a 193 nm NWR nanosecond excimer laser. In the absence of reference materials for *in situ* Sn isotopic measurements in cassiterites, we synthesised and characterised a cassiterite reference material at BGI. A cassiterite from the Zinnwald deposit, Germany (with a known average Sn isotopic composition measured by a solution method) was powdered to < 5 µm as starting material, and loaded into a Pt capsule, which was then placed in a piston-cylinder apparatus at 800 °C and 1 GPa for 24 hours, producing a fully recrystallized and texturally homogeneous cassiterite. All Sn isotopic analyses were carried out at medium resolution ($m/\Delta m \approx 4000$), which effectively suppresses polyatomic interferences while maintaining high ion transmission–critical for precise Sn isotope measurements. Laser ablation parameters were optimised (Fig. 3.8-9) using a spot size of 20 µm, an energy fluence of 3 J cm^{-2}, and a repetition rate of 6 Hz, which yielded the most stable signals and the smallest isotope offsets. Additionally, a 500 ppb Sb solution (^{121}Sb/^{123}Sb = 1.33699) was added for internal mass-bias correction using an APEX Omega desolvation system and subsequently mixed with the laser-generated aerosol inside a custom-made dual-inlet spray chamber.

Self-bracketing of the piston-cylinder-synthesised cassiterite yields a mean $\delta^{122/118}\text{Sn}_{404}$ value of -0.009 ± 0.017 ‰ (2SD, n = 102). This synthesised cassiterite was subsequently applied as the bracketing standard to analyse the same cassiterite that was used as starting material for the experiment. The resulting triple-isotope plots (Fig. 3.8-10) demonstrate that the mass-bias-corrected Sn isotope ratios fall tightly along the expected mass-dependent fractionation line, with $\delta^{122/118}\text{Sn}_{3161a}$ values also lying well within the global cassiterite range (-1.24 to +1.28 ‰). This confirms that the Sb-based internal normalisation combined with matrix-matched bracketing effectively corrects for instrumental mass bias and is consistent with mass-dependent isotopic variations. In addition, isotope measurements along Lines 1 and 2 (Fig. 3.8-11) reveal a systematic decline in $\delta^{122/118}\text{Sn}_{3161a}$ toward the crystal margins, reflecting preferential incorporation of heavier Sn isotopes during the earliest stages of cassiterite growth and progressive enrichment of lighter isotopes in coexisting fluids. This isotopic zoning provides valuable insight into magmatic pulsing, subsequent hydrothermal fluid exsolution, and even the potential involvement of late-stage meteoric water during the formation of Sn deposits.

Together, this work establishes one of the most comprehensive and reproducible protocols for *in situ* Sn isotopic analysis using a nanosecond laser ablation system. The integration of a homogeneous cassiterite reference material, optimised laser conditions, and internal normalisation using Sb addition significantly enhances analytical reliability and expands the potential of Sn isotopic variations in cassiterite as tracers of metallogenesis, magmatic–hydrothermal evolution, and crustal geochemistry.

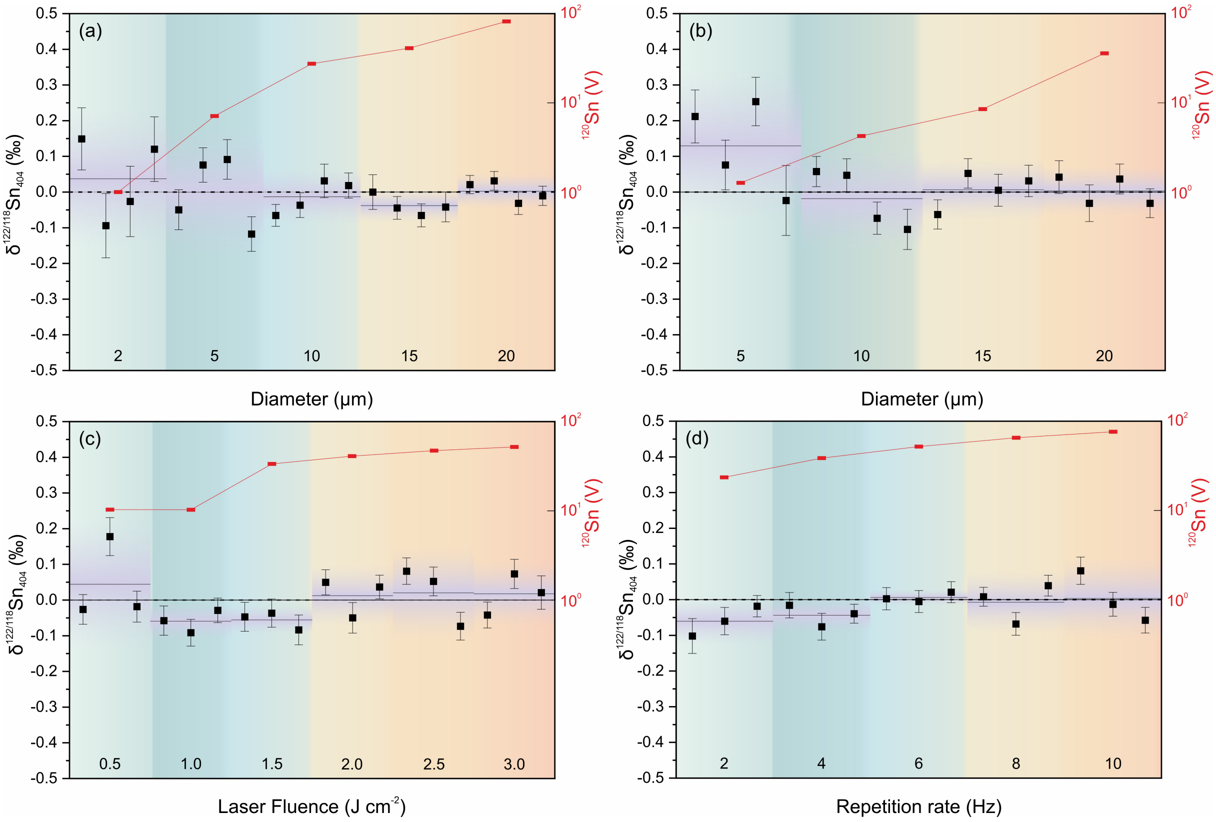

Fig. 3.8-9: Effects of laser ablation parameters on *in situ* Sn isotope analysis. (a) Line-scan analysis performed using different diameters (2 to 20 μm); (b) Spot analysis using different laser spot sizes (5 to 20 μm); (c) Laser fluence test ranging from 0.5 to 3.0 J cm^{-2}; (d) Repetition-rate test conducted between 2 and 10 Hz. The vertical error bars denote the 2SE of each measurement. The solid black line indicates the mean isotopic composition for each experiment session, and the purple shaded band represents the associated ± 2SD.

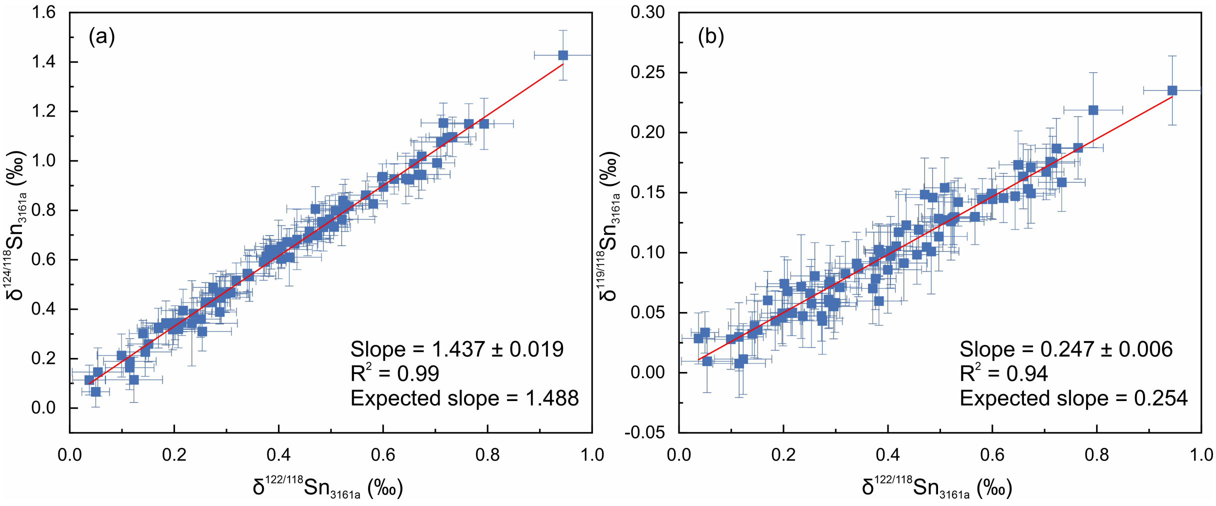

Fig. 3.8-10: Sn triple-isotope correlations of cassiterite measured against the synthesised in-house reference material (Cst_{404}) and normalised to NIST SRM 3161a. (a) $\delta^{124/118}Sn_{3161a}$ vs. $\delta^{122/118}Sn_{3161a}$; (b) $\delta^{119/118}Sn_{3161a}$ vs. $\delta^{122/118}Sn_{3161a}$. Error bars for individual analysis represent 2SE analytical uncertainties of the corrected average ratios.

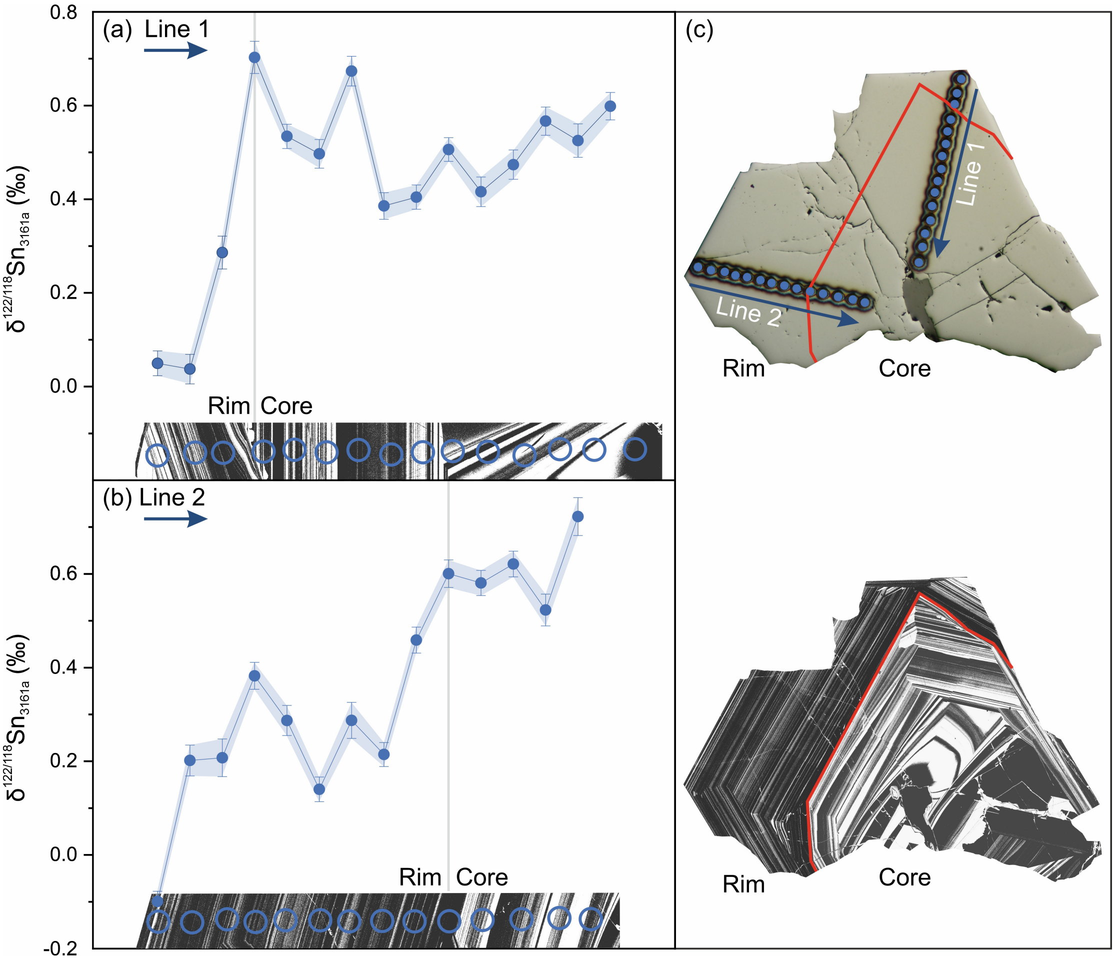

Fig. 3.8-11: Integrated isotopic and imaging characterisation of cassiterite (starting material). Left panels show $\delta^{122/118}Sn_{3161a}$ profiles along Line 1 (a) and Line 2 (b). (c) Corresponding sampling lines on reflected-light (top) and CL (bottom) images, with the red line marking the core-rim boundary.

g. In situ *Rb-Sr analyses by LA-MC-ICPMS/MS: Method development and applications to lunar rocks (T.-W. Chen and B. Zhang/Houston, P.H. Warren/Los Angeles, R. Zhao, D. Zhu and A. Bouvier)*

The BGI is equipped with a Thermo Scientific Neoma multi-collector inductively coupled plasma mass spectrometer with a pre-cell mass filter and a collision reaction cell (MC-ICP-MS/MS) coupled to an ESL NWR 193 nm excimer laser ablation system. This instrumentation enables *in situ* ^{87}Rb-^{87}Sr geochronology, a widely applied radiometric dating technique for ancient terrestrial and extraterrestrial materials based on the long half-life of ^{87}Rb (49.6 Ga). Compared with conventional solution-based methods that provide high-precision bulk analyses, *in situ* measurements preserve spatial resolution, allowing chronological investigations of individual mineral phases and domains. This capability is particularly valuable for petrologically complex samples such as lunar rocks, where different lithologies may record distinct formation or thermal events.

A major analytical challenge for *in situ* Rb-Sr dating is the isobaric interference of ^{87}Rb on ^{87}Sr, which can compromise measurement accuracy. The prefiltering system that consists of a double-Wien filter and a collision reaction cell in Neoma addresses this limitation by using SF_6 (mixed with He) as a reaction gas. This approach selectively converts Sr into molecular SrF ions while leaving Rb unreacted, effectively separating the two elements and eliminating the interference. Our analytical protocol utilises NIST 610 glass to correct for ^{87}Rb/^{86}Sr fractionation, and AMNH 107160 labradorite as the ^{87}Sr/^{86}Sr reference material. Secondary corrections to isochron slopes are then applied offline by analysing granites or meteorites with known ages.

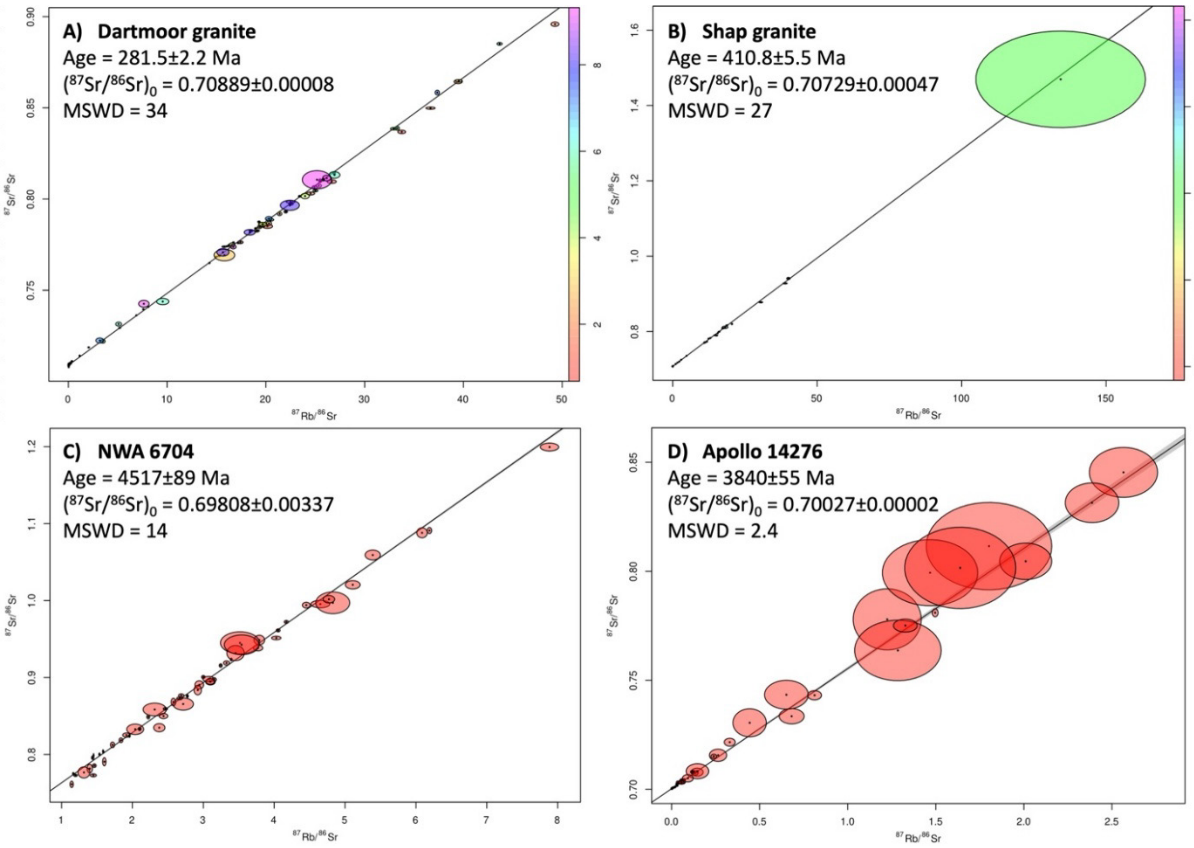

Fig. 3.8-12: *In situ* Rb-Sr analyses of the (A) Dartmoor granite, (B) Shap granite, (C) NWA 6704 (achondrite meteorite), and (D) Apollo 14276 (lunar KREEP mare basalt-like impact melt rock). The color scale in panels (A) and (B) indicates the number of different analytical sessions.

We first validated our method using the Dartmoor (DG) and Shap (SG) granite standards that are commonly employed for isochron calibration in previous studies. Cross-calibration between these standards yielded a slope correction factor of 0.77 for DG and 0.78 for SG, with corrected ages and initial ^{87}Sr/^{86}Sr (Figs. 3.8-12A and B) consistent with reference values determined by thermal ionization mass spectrometry (TIMS). Analysis of the ungrouped achondrite meteorite, Erg Chech 002, yielded a slope correction factor of 0.84, distinct from the terrestrial granite values. Applying this slope correction factor to another achondrite meteorite, NWA 6704, yielded an isochron age and an initial isotopic ratio (Fig. 3.8-12C) that are consistent with values determined by solution-based methods. In contrast, analyses of the lunar gabbro meteorite (NWA 6950) and Apollo samples (*e.g.*, 14276, Fig. 3.8-12D) required no slope correction factor, with both ages and initial isotopic values consistent with reference values. This suggests that planetary materials may have compositional characteristics for Rb/Sr fractionation, possibly related to Sr fluorination efficiency, requiring further investigation. These results demonstrate the potential of *in situ* Rb-Sr analysis by laser-probe for lunar sample applications while highlighting the importance of matrix-matched slope-correction standards. Future measurements of additional meteorites and returned samples will refine this methodology and establish a robust framework for extraterrestrial sample applications.

h. *Overcoming the numerical challenges owing to rapid ductile strain localization (A. Spang, M. Thielmann/Bonn, C. Pranger/Munich, A. de Montserrat/Zürich and L. Räss/Lausanne)*

Strain localization describes the concentration of deformation into a narrow zone that allows relatively stiff blocks to move past each other without significant internal deformation. This process plays a crucial role in tectonic processes such as subduction and mountain building, as well as geohazards like landslides and earthquakes. It can occur by brittle failure, or in the ductile regime due to thermal runaway. Numerical modelling of strain localization remains challenging due to the large differences in spatial and temporal scales. Models have to cover the kilometre scale of the geological setting which evolves on timescales of Myr as well as the millimetre scale of the shear zone which may evolve on timescales of seconds. Another issue is the self-feeding nature of strain localization which commonly results in localization onto a single grid cell. At this point, the model results no longer depend on the physics of the problem and are instead governed by numerical resolution.

To overcome these challenges, we employ a number of strategies including adaptive time stepping, adaptive rescaling, viscosity regularization, and gradient regularization. To accurately capture the slow increase of stress and temperature, the spontaneous onset of localization, and the rapid stress drop during thermal runaway, we employ an adaptive time stepping scheme that adjusts the time step based on changes in stress and temperature (Fig. 3.8-13a). With this scheme, we achieve time step reductions of more than 10 orders of magnitude without destabilizing the numerical solver. Such large changes in timescale can introduce significant round-off errors due to numerical precision which we prevent by adaptively rescaling our model parameters between time steps.

To avoid mesh-dependent results, we test two regularization techniques. Viscosity regularization introduces a lower viscosity cutoff in the system which limits localization and results in a finite shear zone width (Fig. 3.8-13b). Gradient regularization introduces a diffusion term for viscous dissipation, which smooths the temperature increase and results in larger shear zones as well. Both methods can mitigate mesh-dependency in different ways and with different side effects. While viscosity regularization limits the maximum slip velocity, gradient regularization limits the maximum temperature. Viscosity regularization is computationally cheaper.

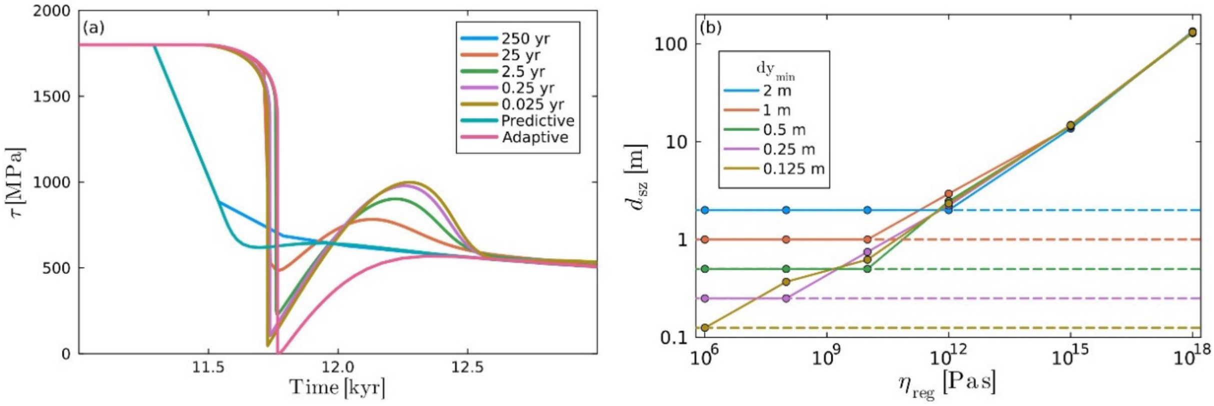

Fig. 3.8-13: (a) Temporal evolution of deviatoric stress (τ) for different constant time steps and two variable time stepping schemes. Only adaptive time stepping can accurately resolve the stress drop due to strain localization. (b) Effect of regularization viscosity (η_{reg}) on shear zone width (d_{SZ}). Colors denote different resolutions, and dashed lines show the corresponding size of a single cell.

4. Publications, Conference Presentations, Seminars

4.1 Publications (published)

2025

Refereed international journals

ASLANDUKOV, A.; YIN, Y.; BYKOV, M.; ASLANDUKOVA, A.; AKBAR, F.I.; BRIGHT, E.L.; ABRIKOSOV, I.A.; DUBROVINSKAIA, N.; DUBROVINSKY, L. (2025): High-pressure synthesis of nitrogen-rich $Y(N_5)_3 \cdot N_2$ pentazolate with perovskite topology. Angew. Chem. Int. Ed., e202506334, https://doi.org/10.1002/anie.202506334

ASLANDUKOVA, A.; ASLANDUKOV, A.; YIN, Y.; BYKOV, M.; CERANTOLA, V.; PAKHOMOVA, A.; DUBROVINSKAIA, N.; DUBROVINSKY, L. (2025): High-pressure yttrium borate $oC20$-YBO_3 and yttrium orthocarbonate $hR39$-$Y_3(CO_4)_2$ synthesized at megabar pressures. Inorg. Chem. 64(10), 5098-5104, https://doi.org/10.1021/acs.inorgchem.4c05308

AUDÉTAT, A.; CHANG, J.; GAYNOR, S.P. (2025): Widespread occurrence of former anhydrite phenocrysts in Laramide-age magmas related to porphyry-skarn Cu mineralization at Santa Rita and Hanover-Fierro, New Mexico, USA. J. Petrol. 66(2), egaf002, https://doi.org/10.1093/petrology/egaf002

AUDÉTAT, A.; CHANG, J.; GAYNOR, S.P. (2025): Depth of magma crystallization and fluid exsolution beneath the porphyry-skarn Cu deposits at Santa Rita and Hanover-Fierro, New Mexico, USA. Econ. Geol. 120(7), 1679-1699, https://doi.org/10.5382/econgeo.5197

BAMBER, E.C.; ARZILLI, F.; CIPICCIA, S.; BATEY, D.J.; LA SPINA, G.; POLACCI, M.; GHOLINIA, A.; BAGSHAW, H.; DI GENOVA, D.; BROOKER, R.; GIORDANO, D.; VALDIVIA, P.; BURTON, M.R. (2025): 3D quantification of nanolites using X-ray ptychography reveals syn-eruptive nanocrystallisation impacts magma rheology. Nat. Commun. 16, 7083, https://doi.org/10.1038/s41467-025-62444-z

BARATELLI, L.; MURRI, M.; ALVARO, M.; MIHAILOVA, B.; BOFFA BALLARAN, T.; DOMENEGHETTI, M.C.; CÁMARA, F. (2025): The effect of cation ordering in omphacite on the phonon compressibility: A step towards Raman elastic geothermobarometry. Chem. Geol. 678, 122650; https://doi.org/10.1016/j.chemgeo.2025.122650

BARBUY, B.; FERNÁNDEZ-TRINCADO, J.; CAMARGO, M.S.; GEISLER, D.; BRAUNER, M.; VILLANOVA, S.; MINNITI, D.; GARCÍA-HERNÁNDEZ, D.A.; SOUZA, S.O.; ERNANDES, H.; FRIAÇA, A.; PIGNATARI, M. (2025): Investigating phosphorus abundances in a sample of APOGEE-2 bulge globular clusters. Astron. J. 170(4), 245, https://doi.org/10.3847/1538-3881/ae046b

BERMINGHAM, K.R.; TORNABENE, H.A.; WALKER, R.J.; GODFREY, L.V.; MEYER, B.S.; PICCOLI, P.; MOJZSIS, S.J. (2025): The non-carbonaceous nature of Earth's late-stage accretion. Geochim. Cosmochim. Acta 392, 38-51, https://doi.org/10.1016/j.gca.2024.11.005

BLANCHARD, I.; SIEBERT, J.; KUBIK, E.; MINCHENKOVA, A.; CALVO, L.M. (2025): Earth's deep magma ocean never reached sulfide saturation. Geochem. Perspect. Lett. 34, 6-10, https://doi.org/10.7185/geochemlet.2506

BOFFA BALLARAN, T.; KULARATNE, K.; TRØNNES, R.G. (2025): High-pressure behaviour of a $CaIrO_3$ perovskite-type structure. Eur. J. Mineral. 37, 699-708, https://doi.org/10.5194/ejm-37-699-2025

BONDAR, D.; CANIZARÈS, A.; BILARDELLO, D.; VALDIVIA, P.; ZANDONÀ, A.; ROMANO, C.; ALLIX, M.; DI GENOVA, D. (2025): Nanolite crystallization in volcanic glasses: Insights from high-temperature raman spectroscopy and low-temperature rock-magnetic analysis. Geochem. Geophys. Geosyst. 26(1), e2024GC011846, https://doi.org/10.1029/2024GC011846

BOUVIER, A.; BERMINGHAM, K.R.; FÜRI, E. (2025): Planetary materials: A record of early solar system events to planetary processes. – In: Treatise on Geochemistry 7 (3rd Edition), (Eds. Anbar, A.D.; Weis, D.), Elsevier, 203-256, https://doi.org/10.1016/B978-0-323-99762-1.00137-6

BUCHEN, J.; PARDO, O.S.; DOBROSAVLJEVIC, V.V.; STURHAHN, W.; ISHII, T.; CHARITON, S.; GREENBERG, E.; TOELLNER, T.S.; JACKSON, J.M. (2025): Linking the spin transition of ferric iron in δ-(Al,Fe)OOH to water storage in the lower mantle. JGR Solid Earth 130, e2025JB031715, https://doi.org/10.1029/2025JB031715

CASSETTA, M.; SZEWCZYK, D.; GIULIANI, G.; DOMINIJANNI, S.; VETERE, F.; IEZZÌ, G.; RADICA, F.; BONDAR, D.; DI FIORE, F.; PONTESILLI, A.; KARACASULU, L.; DALDOSSO, N.; MIZUNO, H.; DI GENOVA, D. (2025): Chemically driven nano-elastic heterogeneities control fragility in volcanic melts. Adv. Sci. 13(5), e12063, https://doi.org/10.1002/advs.202512063

CHANG, J.; AUDÉTAT, A.; PETTKE, T. (2025): Ten kilometers ascent of porphyry Cu (Au, Mo)-forming fluids in the Sanjiang region, China. Nat. Commun. 16, 2330, https://doi.org/10.1038/s41467-025-57710-z

CHANYSHEV, A.; PUREVJAV, N.; BONDAR, D.; TANG, H.; FEI, H.; WANG, L.; WANG, F.; KIM, E.-J.; LIU, D.; ISHII, T.; BHAT, S.; FARLA, R.; KATSURA, T. (2025): Phase relations in the $MgSiO_3$ system associated with hot mantle upwelling across the 660 km depth. Geophys. Res. Lett. 52(17), e2025GL115385, https://doi.org/10.1029/2025GL115385

CHAUDHARI, A.; MASOTTA, M.; SHCHEKA, S.; KEPPLER, H. (2025): The solubility of molecular hydrogen in silicate melts and the origin of hydrogen in the interiors of terrestrial planets. Contrib. Mineral. Petrol. 180, 84, https://doi.org/10.1007/s00410-025-02272-y

CRINITI, G.; BOFFA BALLARAN, T.; KURNOSOV, A.; ISHII, T.; ROGMANN, E.-M.; GLAZYRIN, K.; FEDOTENKO, T.; FROST, D.J. (2025): Effect of chemistry on the compressibility and high-pressure structural evolution of the $CaFe_2O_4$-type aluminous silicate phase. Phys. Earth Planet. Inter. 361, 107331, https://doi.org/10.1016/j.pepi.2025.107331

DALE, K.I.; MORBIDELLI, A.; RUBIE, D.C.; NESVORNÝ, D. (2025): Compositional outcomes of Earth formation from a narrow ring. Earth Planet. Sci. Lett. 658, 119334, https://doi.org/10.1016/j.epsl.2025.119334

DI FIORE, F.; VONA, A.; DI GENOVA, D.; CARACCIOLO, A.; PONTESILLI, A.; CALABRÒ, L.; GIULIANI, G.; MOLLO, S.; BONDAR, D.; NAZZARI, M.; ROMANO, C. (2025): Impact of cooling rate on rheology and emplacement dynamics of basaltic lavas: Insights from the January 2024 Sundhnúksgígar eruption (Iceland). J. Volcanol. Geotherm. Res. 466, 108400, https://doi.org/10.1016/j.jvolgeores.2025.108400

DI GENOVA, D.; GIULIANI, G.; ABEYKOON, S.; DADWAL, K.; SHARMA, S.; KHANNA, A.; ZANDONÀ, A.; BONDAR, D.; MEYER, S.; CALABRÒ, L.; DOMINIJANNI, S.; DEUBENER J. (2025): Intralaboratory calibration of the DSC shift-factor approach for melt viscosity determination: A case study on lead metasilicate glass. J. Non-Cryst. Solids 666, 123709; https://doi.org/10.1016/j.jnoncrysol.2025.123709

DORN, C.; GOLABEK, G.J.; BOWER, D.J. (2025): Interior-atmosphere interactions for terrestrial Solar System objects, Super-Earths and Sub-Neptunes. – In: Handbook of Exoplanets 2nd ed., (Eds. Deeg, H.J., Belmonte, J.A.), Springer, https://doi.org/10.1007/978-3-319-30648-3_66-2

FANESI, E.; DI GENOVA, D.; VALDIVIA, P.; BONDAR, D.; DOMINIJANNI, S.; ABEYKOON, S.; GIULIANI, G.; KURNOSOV, A.; GIORDANO, G.; CASSETTA, M.; VONA, A.; ROMANO, C.; ARZILLI, F. (2025): A review of the differential scanning calorimetry shift-factor approach: Application to Colli Albani melt viscosity and implications for mafic Plinian eruptions. J. Volcanol. Geotherm. Res. 461, 108276, https://doi.org/10.1016/j.jvolgeores.2025.108276

FANG, J.; AUDÉTAT, A.; DOLEJS, D. (2025): Molybdenum speciation in magmatic-hydrothermal fluids: Constraints from molybdenite solubility experiments and thermodynamic modeling. Geochim. Cosmochim. Acta 395, 95-111, https://doi.org/10.1016/j.gca.2025.01.032

FEI, H.; CHEN, J.; WANG, F.; ZHANG, B.; XIA, Q.; KATSURA, T. (2025): Gravitationally unstable hydrous melt at the bottom of the upper mantle. JGR Solid Earth 130, e2024JB030737, https://doi.org/10.1029/2024JB030737

FROST, M.; ABRAHAM, K.; GONCHAROV, A.F.; MCWILLIAMS, R.S.; HUSBAND, R.J.; BROWN, D.; BYKOVA, E.; CELESTE, A.; EDMUND, E.; HARTLEY, N.J.; GLAZYRIN, K.; JAISLE, N.; ANDRZEJEWSKI, M.; APPEL, K.; BAEHTZ, C.; KONÔPKOVÁ, Z.; STROHM, C.; LAURUS, T.; GRAAFSMA, H.; TANG, M.; LIN, Y.; MASSANI, B.; SCHÖRNER, M.; BERGERMANN, A.; SCHULZE, M.; YOUNES, Z.; STEINLE-NEUMANN, G.; REDMER, R.; GLENZER, S.H. (2025): Synthesis of gold hydride at high pressure and high temperature, Angew. Chem. Int. Ed. 64(38), e202505811, https://doi.org/10.1002/anie.202505811

GAUTIER, A.; BOLFAN-CASANOVA, N.; MOINE, B.; BUREAU, H.; KHODJA, H.; WITHERS, A.C.; PIANI, L. (2025): H and D/H analysis in olivine and wadsleyite with a multianalytical approach combining Raman spectroscopy, ion and nuclear probes. Eur. J. Mineral. 37, 305-318, https://doi.org/10.5194/ejm-37-305-2025

GILLMANN, C.; ARNEY, G.N.; AVICE, G.; DYAR, M.D.; GOLABEK, G.J.; GÜLCHER, A.J.P.; JOHNSON, N.M.; LEFEVRE, M.; WIDEMANN, T. (2025): Venus. – In: Treatise on Geochemistry 7 (3rd Edition), (Eds. Anbar, A.D.; Weis, D.), Elsevier, 289-323, https://doi.org/10.1016/B978-0-323-99762-1.00099-1

GIULIANI, G.; CALABRÒ, L.; STOPPONI, V.; BONDAR, D.; ABEYKOON, S.; ROMANO, C.; DINGWELL, D.B.; DI GENOVA, D. (2025): Aluminum control on viscosity and structure of haplogranitic melts: Implications for rhyolitic melt viscosity determination. Chem. Geol. 698, 123127, https://doi.org/10.1016/j.chemgeo.2025.123127

HAMANO, K.; GILLMANN, C.; GOLABEK, G.J.; LOURENÇO, D.; WESTALL, F. (2025): The evolutionary divergence of Mars, Venus and Earth. – In: Treatise on Geochemistry 7 (3rd Edition), (Eds. Anbar, A.D.; Weis, D.), Elsevier, 541-574, https://doi.org/10.1016/B978-0-323-99762-1.00104-2

HSIEH, W.P.; DESCHAMPS, F.; TSAO, Y.C.; PEASE, A.; DORFMAN, S.M.; BAUSCH, H.J.; WANG, F. (2025): Spin transition in magnesiowüstite and ultralow thermal conduction in ultralow velocity zones. Nat. Commun. 16, 10431, https://doi.org/10.1038/s41467-025-65430-7

IIZUKA, I. *et al.* with the Hayabusa2 Initial Analysis Chemistry Team (including BOUVIER, A.) (2025): The fate of water on carbonaceous asteroids inferred from hafnium isotopes in Ryugu samples. Nature 646, 62-67, https://doi.org/10.1038/s41586-025-09483-0

KATSURA, T. (2025): Phase relations of bridgmanite, the most abundant mineral in the Earth's lower mantle. Commun. Chem. 8, 28, https://doi.org/10.1038/s42004-024-01389-8

KEPPLER, H.; AUDETAT, A. (2025): The redox dependence of the fluid/melt partitioning of tin. Geochim. Cosmochim. Acta 394, 182-193, https://doi.org/10.1016/j.gca.2025.02.007

KOVALEV, V.; SPAHR, D.; WINKLER, B.; BAYARJARGAL, L.; WEDEK, L.; ASLANDUKOVA, A.; PAKHOMOVA, A.; GARBARINO, G.; BYKOVA, E. (2025): High-pressure synthesis and crystal structure of iron sp^3-carbonate ($Fe_2[C_4O_{10}]$) featuring pyramidal $[C_4O_{10}]^{4-}$ anions. Commun Chem 8, 66, https://doi.org/10.1038/s42004-025-01450-0

LANIEL, D.; TRYBEL, F.; ZHOU, W.; ASLANDUKOV, A.; SPENDER, J.; TASNÁDI, F.; FEDOTENKO, T.; RANIERI, U.; LIANG, A.; ASLANDUKOVA, AKBAR, F.I.; YIN, Y.; CHARITON, S.; PAKHOMOVA, A.; GARBARINO, G.; MEZOUAR, M.; HANFLAND, M.; PRAKAPENKA, V.; ABRIKOSOV, I.A.; DUBROVINSKY, L.; DUBROVINSKAIA, N. (2025): High-pressure synthesis of oP28-C_3N_4 recoverable to ambient conditions. Adv. Funct. Mater. 35(11), 2416892, https://doi.org/10.1002/adfm.202416892

LI, T.; FALCH, K.V.; GARREVOET, J.; DUBROVINSKY, L.; LYUBOMIRSKIY, M. (2025): High-resolution ptychographic nanoimaging under high pressure with X-ray beam scanning. PNAS 122, e2514163122, https://doi.org/10.1073/pnas.2514163122

LIU, Z.; LI, Y. (2025): The partitioning of selenium and tellurium between sulfide liquid and silicate melt and their abundances in the silicate Earth. Earth Planet. Sci. Lett. 656, 119277, https://doi.org/10.1016/j.epsl.2025.119277

LU, W.; YANG, Y.-N.; LONG, T.; XIAN, H.; LI, Y.; DU, Z. (2025): Substantial water retained early in Earth's deep mantle. Science 390, 1177-1180, https://doi.org/10.1126/science.adx5883

MAN, L.; LI, X.; BOFFA BALLARAN, T.; ZHOU, W.; CHANTEL, J.; NÉRI, A.; KUPENKO, I.; APRILIS, G.; KURNOSOV, A.; NAMUR, O.; HANFLAND, M.; GUIGNOT, N.; HENRY, L.; DUBROVINSKY, L.; FROST, D.J. (2025): The structure and stability of $Fe_{4+x}S_3$ and its potential to form a Martian inner core. Nat. Commun. 16, 1710, https://doi.org/10.1038/s41467-025-56220-2

MARRAS, G.; MIKHAILENKO, D.; MCCAMMON, C.; LOGVINOVA, A.; HANžEL, D.; DALLAI, L.; STAGNO, V. (2025): Oxy-thermobarometry of grospydite and high-Ca eclogite xenoliths from Zagadochnaya kimberlite pipe (Yakutia, Siberian craton). Miner. Petrol. 119, 649-667, https://doi.org/10.1007/s00710-025-00910-8

MCGREGOR, N.J.; NIMMO, F.; GILLMANN, C.; GOLABEK, G.J.; PLATTNER, A.M.; CONRAD, J.W. (2025): Probing the viscosity of Venus's mantle from dynamic topography at Baltis Vallis. JGR Planets 130, e2024JE008581, https://doi.org/10.1029/2024JE008581

MIKHAILOVA, D.; AVDOSHENKO, S.M.; AVDEEV, M.; HANFLAND, M.; SCHWARZ, U.; PROTS, Y.; SARAPULOVA, A.; GLAZYRIN, K.; DUBROVINSKY, L.; SENYSHYN, A.; ENGEL, J.; EHRENBERG, H.; TSIRLIN, A.A. (2025): Metallization without charge transfer in $CuReO_4$ perrhenate under pressure. Inorg. Chem. 64, 6010-6022, https://doi.org/10.1021/acs.inorgchem.4c05051

MIYAJIMA, N.; WANG, L.; KATSURA, T. (2025): First observation of quenched davemaoite to ambient conditions: its electron diffraction pattern. Geophys. Res. Lett. 52(19), e2025GL115280, https://doi.org/10.1029/2025GL115280

NIU, G.; CAO, S.; YAN, B.; GOU, H.; KATSURA, T.; MAO, H-k. (2025): MASTer: A high-performance stable temperature controller for high-pressure multi-anvil presses. Matter Radiat. Extremes 10, 057802, https://doi.org/10.1063/5.0277958

O'CONNELL, D.; MCCAMMON, C.; BYRNE, J.; JAKOBSEN, R.; JENSEN, M.M.; THAMDRUP, B.; BRUUN HANSEN, H.C.; POSTMA, D. (2025): Isotopic exchange between aqueous Fe(II) and solid Fe(III) in lake sediment – a kinetic assemblage approach. Environ. Sci. Technol. 59, 5534-5544, https://doi.org/10.1021/acs.est.4c07369

OHASHI, T.; SAKAMAKI, T.; FUNAKOSHI, K.-i.; STEINLE-NEUMANN, G.; HATTORI, T.; YUAN, L.; SUZUKI, A. (2025): Pressure-induced elongation of hydrogen-oxygen bond in sodium silicate melts, J. Mineral. Petrol. Sci. 120, 240926a, https://doi.org/10.2465/jmps.240926a

PAKHOMOVA, A.; JOURNAUX, B.; KURNOSOV, A.; BOFFA BALLARAN, T.; TOBIE, G.; HANFLAND, M. (2025): Methanol storage in high-pressure clathrate hydrates as a prolonged source of methane in large ocean worlds. Earth Planet. Sci. Lett. 666, 119478, https://doi.org/10.1016/j.epsl.2025.119478

PAUL, J.; SPANG, A.; PICCOLO, A. (2025): Hydration weakening and destruction of the North China Craton. Tectonophysics 908, 230756, https://doi.org/10.1016/j.tecto.2025.230756

PIGNATARI ,M.; AMARI, S.; HOPPE, P.; FRYER, C.; JONES, S.; PSALTIS, A.; LAIRD, A.M.; HERWIG, F.; ROBERTI, L.; SIEGERT, T.; LUGARO, M. (2025): Production of radioactive ^{22}Na in core-collapse supernovae: The Ne-E(L) component in presolar grains and its possible consequences on supernova observations. Astrophys. J. 990, 19, https://doi.org/10.3847/1538-4357/adef4c

ROHITH KOTLA, S.; NOOHINEJAD, L.; POKHRIYAL, P.; TOLKIEHN, M.; AGARWAL, H.; RAMAKRISHNAN, S.; VAN SMAALEN, S. (2025): Broken inversion symmetry in the charge density wave phase in $EuAl_4$. Phys. Rev. B 112, 064113, https://doi.org/10.1103/kl2z-brms

RUBIE, D.C.; DALE, K.I.; NATHAN, G.; NAKAJIMA, M.; JENNINGS, E.S.; GOLABEK, G.J.; JACOBSON, S.A.; MORBIDELLI, A. (2025): Tungsten isotope evolution during Earth's formation and new constraints on the viability of accretion simulations. Earth Planet. Sci. Lett. 651, 119139, https://doi.org/10.1016/j.epsl.2024.119139

SATTA, N.; CRINITI, G.; BOFFA BALLARAN, T.; KURNOSOV, A.; ISHII, T.; BUCHEN, J.; MARQUARDT, H. (2025): The effect of Fe incorporation on the single-crystal elasticity of δ-AlOOH. Phys. Chem. Minerals 52, 18, https://doi.org/10.1007/s00269-025-01319-7

SAWA, S.; GASC, J.; MIYAJIMA, N.; SCHUBNEL, A.; BAISSET, M.; MUTO, J. (2025): Magnitude distribution during transformational faulting: Implication for deep-focus earthquakes. JGR Solid Earth, 130(8), e2025JB031779, https://doi.org/10.1029/2025JB031779

SCHÖNBÄCHLER, M.; BOUVIER, A.; KITA, N.T.; KRUIJER, T.S. (2025): Initial conditions of planet formation: Time constraints from small bodies and the lifetime of reservoirs in the solar protoplanetary disk. Space Sci. Rev. 221, 97, https://doi.org/10.1007/s11214-025-01216-z

SERGHIOU, G.; REICHMANN, H.J.; JI, G.; NIGAY, L.; WRIGHT, J.P.; FROST, D.J.; CALDER, G. (2025): High pressure and compositionally directed route to a hexagonal GeSn alloy class. J. Am. Chem. Soc. 147(42), 38413-38418, https://doi.org/10.1021/jacs.5c11716

SHI, C.; HOU, W.; DENG, H.; PATRA, B.; ROHITH KOTLA, S.; LIU, Y.; RAMAKRISHNAN, S.; EISELE, C.; AGARWAL, H.; NOOHINEJAD, L.; LIU, J.-Y.; YANG, T.; LIU, G.; BARAN MAITY, B.; WANG, Q.; LIN, Z.; KANG, B.; YANG, W.; LI, Y.; YANG, Z.; CHEN, Y.; LI, X.; LI, Y.; QI, Y.; THAMIZHAVEL, A.; REN, W.; CAO, G.-H.; YIN, J.-X.; SINGH, B.; LIU, X.; SINGH, B.; LIU, X.; VAN SMAALEN, S.; CAO, S.; Bao, J.-K. (2025): Charge density wave with suppressed long-range structural modulation in canted antiferromagnetic kagome FeGe. Commun. Phys. 8, 405, https://doi.org/10.1038/s42005-025-02316-6

SOLDAVINI, B.C.; MERLINI, M.; GEMMI, M.; PARLANTI, P.; FUMAGALLI, P.; MILANI, S.; JOSEPH, B.; BAIS, G.; POLENTARUTTI, M.; KURNOSOV, A.; POLI, S. (2025): Crystal structure and elastic properties of parabreyite: a new high-pressure ring silicate in the $CaSiO_3$ system. Eur. J. Mineral. 37, 13-24, https://doi.org/10.5194/ejm-37-13-2025

SPANG, A.; THIELMANN, M.; DE MONTSERRAT, A.; DURETZ, T. (2025): Transient propagation of ductile ruptures by thermal runaway. JGR Solid Earth, 130(6), e2025JB031240, https://doi.org/10.1029/2025JB031240

SPARGAAREN, R.J.; HERBORT, O.; WANG, H.S.; MOJZSIS, S.J.; SOSSI, P. (2025): A statistical approach to nebular composition-dependent element volatility in a rocky planet formation context. Astron. Astrophys. 703, A218, https://doi.org/10.1051/0004-6361/202556011

STROZEWSKI, B.T.; RAUTELA, O.; BUCHEN, J.; STURHAHN, W.; ISHII, T.; OHIRA, I.; PARDO, O.; ZHAO, J.; TOELLNER, T.S.; JACKSON, J.M. (2025): Sound velocities of (Al,Fe)-phase H and the seismic visibility of dense oxyhydroxides in Earth's lower mantle. Phys. Earth Planet. Inter. 369, 107466, https://doi.org/10.1016/j.pepi.2025.107466

SU, X.; LIU, J.; ZHOU, Y.; MAN, L.; HOU, M. (2025): Inner core composition of the Moon and Ganymede constrained by thermal equation of state of $Fe_{0.99}C_{0.01}$. JGR Planets 130(1), e2024JE008612, https://doi.org/10.1029/2024JE008612

VALDIVIA, P.; ZANDONÀ, A.; LÖSCHMANN, J.; BONDAR, D.; GENEVOIS, C.; CANIZARÈS, A.; ALLIX, M.; MIYAJIMA, N.; KURNOSOV, A.; BOFFA BALLARAN, T.; ET AL. (2025): Nanoscale chemical heterogeneities control the viscosity of andesitic magmas. Commun. Earth Environ. 6(1), 455, https://doi.org/10.1038/s43247-025-02424-9

WANG, F.; BAUSCH, H.J.; GARDNER, L.L.; ZHANG, D.; ARMSTRONG, K.; BELL, A.S.; ZHAO, J.; ALP, E.E.; JACOBSEN, S.D. (2025): Thermoelastic properties of iron-rich ringwoodite and the deep mantle aerotherm of Mars. Geophys. Res. Lett. 52(3), e2024GL109666, https://doi.org/10.1029/2024GL109666

WANG, F.; WANG, L.; FEI, H.; MIYAJIMA, N.; MCCAMMON, C.; FROST, D.J.; KATSURA, T. (2025): Bridgmanite's ferric iron content determined Earth's redox state. Nat. Geosci. 18, 670-674, https://doi.org/10.1038/s41561-025-01725-0

WANG, L.; KATSURA, T. (2025): Davemaoite is present throughout the Earth's lower mantle, Nat. Geosci. 18, 283-284, https://doi.org/10.1038/s41561-025-01658-8

WANG, L.; MIYAJIMA, N.; WANG, F.; KATSURA, T. (2025): Persistence of davemaoite at lower mantle conditions. Nat. Geosci. 18(4), 365-369, https://doi.org/10.1038/s41561-025-01657-9

WEGNER, L.; BURTON, E.D.; MCCAMMON, C.; SCHEINOST, A.C.; PLANER-FRIEDRICH, B.; PEIFFER, S.; HOCKMANNN, K. (2025): Ferrous iron oxidation in the presence of antimonate: Mutual effects on iron mineral products and antimony sequestration. J. Hazard. Mater. 488, 137380, https://doi.org/10.1016/j.jhazmat.2025.137380

WHITNEY, D.L.; WILKE, M.; HANEL, S.; HEIDELBACH, F.; ROSA, A. (2025): $Fe^{3+}/\Sigma Fe$ variation in lawsonite and epidote in subducted oceanic crust. Eur. J. Mineral. 37, 143-149, https://doi.org/10.5194/ejm-37-143-2025

WIDMANN, I.; DUBROVINSKY, L.; HUPPERTZ, H. (2025): Extended investigations on the pressure stability of $ALB_4O_6N{:}CR^{3+}$. Z. Naturforsch. 80(6-7)b: 277-283, https://doi.org/10.1515/znb-2025-0024

WU, G.; HUANG, Y.; NAKAMURA, M.; TSUJIMORI, T.; LI, Y. (2025): Sequestration of carbon in the forearc mantle wedge. Geochim. Cosmochim. Acta 404, 93-114, https://doi.org/10.1016/j.gca.2025.07.002

XIE, L.; KATSURA, T.; MIYAJIMA, N.; QU, T.; MAO, H.-K. (2025): Water-rich incipient melt of the deep upper mantle indicates locally-preserved low-velocity zones above 410-km discontinuity. PNAS 122, e2500017122, https://doi.org/10.1073/pnas.2500017122

XUE, S.; LI, Y. (2025): The partitioning of chalcophile and siderophile elements (CSEs) between sulfide liquid and carbonated melt. Geochim. Cosmochim. Acta 388, 94-113, https://doi.org/10.1016/j.gca.2024.11.019

YIN, Y.; DUBROVINSKY, L.; TASNADI, F.; ABRIKOSOV, I.A.; ASLANDUKOV, A.; ASLANDUKOVA, A.; AKBAR, F.I.; ZHOU, W.; KNOOP, F.; LANIEL, D.; PAKHOMOVA, A.; FEDOTENKO, T.; GLAZYRIN, K.; GARBARINO, G.; FANG, H.; DUBROVINSKAIA, N. (2025): High-pressure Mg_3Cl_7 synthesized in a diamond anvil cell as a polar metal with second-harmonic generation. J. Am. Chem. Soc. 147(36), 32591-32599, https://doi.org/10.1021/jacs.5c07812

ZAWASKI, M.J.; MARIN-CARBONNE, J.; BOUVIER, A.-S.; KELLY, N.M.; MOJZSIS, S.J. (2025): Marine sedimentary protoliths of ca. 3700 Ma Eoarchean calc-silicates and quartzites of the Snowpatch Formation (Isua supracrustal belt, West Greenland). Geochim. Cosmochim. Acta 398, 99-118, https://doi.org/10.1016/j.gca.2025.03.029

ZHANG, M.; LI, Y. (2025): Chalcophile and siderophile element (CSE) partitioning between sulfide liquid and silicate melt and the role of the "Hadean matte". Chem. Geol. 679, 122671, https://doi.org/10.1016/j.chemgeo.2025.122671

ZHANG, P.; MAN, L.; YUAN, L.; WU, X.; ZHANG, J. (2025): Ultra-low-velocity disordered $CaCO_3$ may explain mid-lithospheric discontinuities. JGR Solid Earth, 130(9), e2025JB031906, https://doi.org/10.1029/2025JB031906

ZHOU, W.; ASLANDUKOV, A.; MINCHENKOVA, A.; HANFLAND, M.; DUBROVINSKY, L.; DUBROVINSKAIA, N. (2025): Structural transformations and stability of benzo[*a*]pyrene under high pressure. JUCrJ, 12(1), 16-22, https://doi.org/10.1107/S2052252524010455

ZHOU, W.-Y.; HAO, M.; SU, W.; KIM, T.; CHEN, S.; SHIM, S.H.; ZHANG, D.; NGUYEN, P.Q.; ARMSTRONG, K.; ZHANG, J.S. (2025): Elasticity of davemaoite as a primary contributor to lower-mantle heterogeneities. Science 390(6776), 935-939, https://doi.org/10.1126/science.adx8356

ZHU, K.; YAMAGUCHI, A.; SOSSI, P.A.; BOUVIER, A.; CHEN, L.; NI, P. (2025): High-energy impact and vapor recondensation history of the angrite parent body revealed by nickel isotopes. PNAS 122(46), e2519759122, https://doi.org/10.1073/pnas.2519759122

ZORZANO, M.-P. *et al.* with the Mars Sample Return Campaign Science Group (including BOUVIER, A.) (2025): Sample Science Traceability Matrix (SSTM) for perseverance's Mars sample return collection. Astrobiology 25(10), 725-741, https://doi.org/10.1177/15311074251382585

ZUCCHINI, A.; BOFFA BALLARAN, T.; FASTELLI, M.; COMBONI, D.; HANFLAND, M.; FRONDINI, F.; COMODI, P. (2025): Influence of cation disorder on the mineral physics of ankerite. Am. Mineral. 110, 908-918, https://doi.org/10.2138/am-2024-9495

4.2 Publications (submitted, in press)

ABRAMOV, O.; MEDVEGY, A.; KREMER, B.; MOJZSIS, S.J.: A timeline for the origin of life on Hadean Earth. PNAS (submitted)

AKBAR, F.I.; ASLANDUKOVA, A.; ASLANDUKOV, A.; YIN, Y.; BYKOVA, E.; BYKOV, M.; LANIEL, D.; MILKIN, P.; LIERMANN, H.P.; WRIGHT, J.; PAKHOMOVA, A.; GARBARINO, G.; MEZOUAR, M.; HANFLAND, M.; DUBROVINSKAIA, N.; DUBROVINSKY, L.: High-pressure synthesis and structural studies of La, Dy, Sm, and Gd chlorides and chloride carbides, ACS Omega (in press), https://doi.org/10.1021/acsomega.5c09373

AUDÉTAT, A.; CHANG, J.; GAYNOR, S.P.: Widespread anhydrite saturation in Laramide-age arc magmas of the southwestern USA. Geology (in press), https://doi.org/10.1130/G53661.1

BONDAR, D.; WITHERS, A.C.; DI GENOVA, D.; ZANDONÀ, A.; BUREAU, H.; KHODJA, H.; KURNOSOV, A.; FEI, H.; KATSURA T.: Compositional dependence of molar absorptivities for infrared absorption bands of H_2O in rhyolitic to peridotitic glasses. Chem. Geol. (submitted)

BUCHEN, J.; WANG, B.; SATTA, N.; TRAUTNER, V.; CRINITI, G.; SAN JOSÉ MÉNDEZ, A.; LIERMANN, H.-P.; MARQUARDT, H.: Cyclic loading experiments at high pressures: oscillating elastic strains and stresses in polycrystalline MgO at seismic frequencies. Geophys. J. Int. (submitted)

CALVO, L.M.; CHANYSHEV, A.; WANG, F.; WANG, L.; ISHII, T.; MCCAMMON, C.; KATSURA, T.: Chemistry of bridgmanite in the $MgO–SiO_2–Al_2O_3–Fe_2O_3–FeO$ system at 27 GPa and 1700-2300 K. Am. Mineral. (in press), https://doi.org/10.2138/am-2025-9935

CASSATA, W.S.; LUGARO, M.; PIGNATARI, M.; WEHNMEYER, B.; MOJZSIS, S.J.; TRAPPITSCH, R.: The astrophysical birth environment of the Solar System inferred from cometary noble gases. Astrophys. J. (in press), https://doi.org/10.3847/1538-4357/ae27c1

CHAKRABORTI, A.; FEI, H.; NISHIHARA, Y.; THIELMANN, M.; HEIDELBACH, F.; TSUJINO, N.; CHANYSHEV, A.; KURNOSOV, A.; MAN, L.; DOLINSCHI, J.; WU, W.; CAO, W.; HIGO, Y.; DABROWSKI, M.; KATSURA, T.: Bridgmanite-ferropericlase interface energy controls lower mantle viscosity. Nat. Geosci. (submitted)

CHANYSHEV, A.; BONDAR, D.; WANG, L.; FEI, H.; TSUJINO, N.; SONG, Y.; MARTIROSYAN, N.; CHAKRABORTI, A.; KIM, E.-J.; TANG, H.; BHAT, S.; FARLA, R.; KATSURA, T.: Olivine-ahrensite phase relations in the Mg_2SiO_4-Fe_2SiO_4 system as a function of temperature. J. Geophys. Res. Solid Earth (submitted)

COLOMBIER, M.; CÁCERES, F.; BIRNBAUM, J.; DEGRAFFENRIED, R.; LAVALLÉE, Y.; KENDRICK, J.E.; SCHEU, B.; THIVET, S.; VALDIVIA, P.; RUHEKENYA, R.M.; SCHLEPÜTZ, C.M.; CASTRO, J.M.; HESS K.-U.; DINGWELL, D.B. (2025): Inherent duality of vesiculation kinematics revealed through 4D imaging. J. Volcanol. Geotherm. Res. (in press): https://doi.org/10.1016/j.jvolgeores.2025.108505

DALE, K.I.; MORBIDELLI, A.; NATHAN, G.; WOO, J.; NESVORNÝ, D.; RUBIE, D.C.: Oxidation constraints on terrestrial planet formation from a ring. Icarus (submitted)

DEMÉNY, A.; NÉMETH, P.; MOJZSIS, S.; PÉCZ, B.; ZAJZON, N.; CORA, I.; BAJNÓCZI, B.; SILVEIRA, F.V.: A formation model for carbonado diamond from impact-induced subduction and subsequent metamorphic resorption. Gondwana Res. (submitted)

DEVI, M.; GRECU, S.-C.; TÓTH, Zs.-R.; CONSTANTIN, D.; BREZEANU, D.; BARLA, A.; NESTEROVSCHI, I.; CINTA-PINZARU, S.; DUCEA, M.N.; MOJZSIS, S.J.; TIMAR-GABOR, A.: Sensitization of OSL signals in quartz grains: Insights from multi-spectroscopic techniques for rock samples from diverse regions worldwide. JGR Earth Surf. (in press)

DOMINIJANNI, S.; FROST, D.J.; DUBROVINSKY, L.S.; MIYAJIMA, N.; KOEMETS, E.; APRILIS, G.; CHARITON, S.; FEDOTENKO, T.; KHANDARKHAEVA, S.; MELAI, C.; KOEMETS, I.; LIU, Z.; CERANTOLA, V.; CHUMAKOV, A.; HANFLAND, M.; SVITLYK, V.; ROSA, A.; MCCAMMON, C.A.: Calibration of the Fe-Ir redox sensor at high pressure and the oxygen fugacity of laser heated diamond anvil cell experiments. Contrib. Mineral. Petrol. (submitted)

DOMINIJANNI, S.; CALABRÒ, L.; BAMBER, E.C.; GIULIANI, G.; BONDAR, D.; VALDIVIA, P.; ARZILLI, F.; LA SPINA, G.; KURNOSOV, A.; VONA, A.; LONGO, A.; DI GENOVA, D.: Modelling magma viscosity and ascent dynamics of the 472 CE sub-Plinian eruption of Somma-Vesuvius (Italy). Earth Planet. Sci. Lett. (in press), https://doi.org/10.1016/j.epsl.2025.119714

DURETZ, T.; DE MONTSERRAT, A.; SEVILLA, R.; RÄSS, L.; UTKIN, I.; SPANG, A.: Automatic tuning of iterative pseudo-transient solvers for modelling the deformation of heterogeneous media. Geoscientific Model Development (in press), https://doi.org/10.5194/egusphere-2025-5641

FUKUSHIMA, R.; TSUJIMORI, T.; MIYAJIMA, N.; INOUÉ, S.; BOFFA BALLARAN, T.; CRINITI, G.: Melting of lawsonite eclogite xenolith in the Colorado Plateau: Micropetrological constraints on the Oligocene thermal pulse. J. Petrol. (submitted)

HAN, K.; ÖZAYDIN, S.; FEI, H.; MAN, L.; WANG, F.; CHANYSHEV, A.; WITHERS, A.C.; GRAYVER, A.; KATSURA, T.: Lower-mantle iron heterogeneity constrained by the electrical conductivity of Al-bearing bridgmanite. Sci. Adv. (submitted)

HECKEL, C.; WITHERS, A.C.; WOODLAND, A.B.; GIBSON, S.A.; LUDWIG, T.: The H_2O component of sheared mantle peridotites from the Kaapvaal craton: evidence for hydrous deformation with implications for the stability of cratons. Contrib. Mineral. Petrol. (in press), https://doi.org/10.1007/s00410-025-02295-5

ISSA, J.; HERWIG, G.; MOJZSIS, S.J.; PIGNATARI, M.: 3D macro physics and Light Odd-Z Element Production in O-C Shell Mergers: Implications for 40K production and radiogenic heating inventories of rocky exoplanets. Astrophys. J. (in press), https://doi.org/10.3847/1538-4357/ae2ad1

KAWASAKI, N., *et al.* with the Hayabusa2 Initial Analysis Chemistry Team (including BOUVIER, A.): Early generation of carbonaceous planetesimals predating chondrules in carbonaceous chondrites. Science (submitted)

KOTAR, E.; OTA, S.; DEWEY, A.; MILLMAN, J.; ROBERTI, L.; PIGNATARI, M.: Impact of the latest ^{22}Ne+α reaction rates on nucleosynthesis in massive stars and galactic chemical evolution. Astrophys. J. (in press), https://doi.org/10.3847/1538-4357/ae0ad3

MARRAS, G.; MIKHAILENKO, D.; MCCAMMON, C.; AULBACH, S.; LU, Y.; TAO, R.; LOGVINOVA, A.; ZEDGENIZOV, D.; STAGNO, V.: Oxygen fugacity, temperature and pressure for the origin of Siberian lithospheric diamonds with implications for the Archaean convecting mantle redox state. Science Advances (submitted)

MEDVEGY, A.; ABRAMOV, O.; KREMER, B.; MOJZSIS, S.J.: Whence the demise and fall of the RNA World? Sci. Adv. (submitted)

MEIER, T.G.; PIERREHUMBERT, R.T.; BIRKBY, J.; CHATTERJEE, R.D.; FISHER, C.E.; GUIMOND, C.M.; GOLABEK, G.J.; HAMMOND, M.; KOMACEK, T.D.; LICHTENBERG, T.; MCGINTY, A.; MEIER VALDES, E.; NICHOLLS, H.; PARKER, L.T.; SPAARGAREN, R.J.; TACKLEY, P.J.: Mantle convection and nightside volcanism on Lava World K2-141 b. Mon. Not. R. Astron. Soc. (submitted)

MELAI, C.; FROST, D.J.; BOFFA BALLARAN, T.; MCCAMMON, C.; NERI, A.; APRILIS, G.; ASLANDUKOVA, A.; MIYAJIMA, N.: The ferropericlase stability field and the exsolution of coherent nano-crystalline spinel ferrite at one atmosphere. Am. Mineral. (submitted)

MELAI, C.; WITHERS, A.C.; GUYETT, P.C.; TOMLINSON, E.T.: Experimental investigation of the role of komatiite-peridotite interaction in generating silica enrichment in the cratonic lithosphere. Mineral. Mag. (submitted)

MOJZSIS, S.J.: From early Earth biogeodynamics to exoplanet geoastronomy. Geochem. Perspect. (in press)

MÜLLER, A.; AUDÉTAT, A.; MONECKE, T.; BREITER, K.; LARSEN, R.B.: The narrative of quartz and silica in the Earth and other planetary bodies. Elements (submitted)

PICCOLO, A.; SPANG, A.; ESKENS, L.H.; ANDRIĆ-TOMAŠEVIĆ, N.; EIZENHOEFER, P.; LE BRETON, E.; THIELMANN, M.: The dynamics and surface signal of slab break-off in continental settings: Insights from 3D numerical modelling. JGR Solid Earth (submitted)

PIERRU, R.; BONNET-GIBET, V.; FRANÇOISE, M.; DOMINIJANNI, S.; PARISIADES, P.; ANDRIAMBARIARIJAONA, L.; ZHAO, B.; PANDOLFI, S.; BOCCATO, S.; BLANCHARD, I.; WEHR, N.; MAN, L.; GUIGNOT, N.; HENRY, L.; KING, A.; BADRO, J.; MICHAUT, C.; ANTONANGELI, D.: Melting properties and melting phase relations of the Martian mantle from *in situ* measurements on iron-rich mineralogical assemblages. Phys. Earth Planet. Inter. (submitted)

QIAO, Y.-B.; AUDÉTAT, A.: Scapolite as a major fractionating mineral phase in deep-seated arc magmas. Geology (submitted)

ROBERTI, L.; PIGNATARI, M.: The SPAr burning: proton captures powering carbon–oxygen shell mergers in massive stars. Astron. Astrophys. 703, L15 (in press), https://doi.org/10.1051/0004-6361/202556941

RUSSO, P.J.; DAY, J.M.D.; MOJZSIS, S.J.: Evidence for Paleoarchean subduction from Jack Hills detrital Cr-spinel. Nat. Commun. (submitted)

SAHA, P.; MURAKAMI, M.; MIYAJIMA, N.: Earth's lower mantle predominated by ferric iron-rich Bridgmanite. Geophys. Res. Lett. (submitted)

SCHULZE, M.; STEINLE-NEUMANN, G.: Oxygen vacancy diffusion in davemaoite ($CaSiO_3$ perovskite): Implications for the redox equilibrium and the electrical conductivity of Earth's lower mantle. Earth Planet. Sci. Lett. (submitted)

SPANG, A.; THIELMANN, M.; PRANGER, C.; DE MONTSERRAT, A.; RÄSS, L.: Overcoming the numerical challenges owing to rapid ductile localization with DEDLoc (version 1.0.0). Geosci. Model Dev. (in press), https://doi.org/10.5194/gmd-19-369-2026

STROZEWSKI, B.; LIU, Z.; ROSSMAN, G.R.; STURHAHN, W.; BUCHEN, J.; JACKSON, J.M.: Vibrational spectroscopy of dense oxyhydroxides: hydrogen bond disorder and symmetrization at high pressure. Am. Mineral. (submitted)

TRAUTNER V.E.; KOEMETS, E.; WANG, B.; SATTA, N.; BUCHEN, J.; HUGHES, G.M.; LEDOUX, E.E.; MARQUARDT, K.; FEI, H.; GIORDANO, N.; KATSURA, T.; MARQUARDT, H.: Shielding of ferropericlase by bridgmanite during compression of a polycrystalline mantle assemblage. Am. Mineral. (submitted)

TRUBOWITZ, C.; MURAKAMI, M.; MUNCH, F.; GRAYVER, A.; LIEBSKE, C.; KHAN, A.; MIYAJIMA, N.; SAHA, P.; OKUDA, Y.; SPIEKERMANN, G.; MORALES, L.G.: The electrical conductivity of the lower mantle from high-pressure/high-temperature measurements of pyrolite and ten years of geomagnetic observations. JGR Solid Earth (submitted)

TRUEMAN, T.C.L.; YAGÜE LÓPEZ, A.; LUGARO, M.; PIGNATARI, M.: Galactic chemical evolution of short-lived radioactive isotopes produced by explosive nucleosynthesis: ^{60}Fe and ^{53}Mn. Astrophys. J. (in press), https://doi.org/10.48550/arXiv.2509.20956

VALDIVIA, P.; et al.: A viscosity model for hydrous andesitic magmas. Earth Planet. Sci. Lett. (submitted)

VORBERGER, J.; GRAZIANI, F.; RILEY, D.; BACZEWSKI, A.D.; BARAFFE, I.; BETHKENHAGEN, M.; BLOUIN, S.; BÖHME, M.P.; BONITZ, M.; BUSSMANN, M.; CASNER, A.; CAYZAC, W.; CELLIERS, P.; CHABRIER, G.; CHAMEL, N.; CHAPMAN, D.; CHEN, M.; CLÉROUIN, J.; COLLINS, G.; COPPARI, F.; DÖPPNER, T.; DORNHEIM, T.; FLETCHER, L.B.; GERICKE, D.O.; GLENZER, S.; GONCHAROV, A.F.; GREGORI, G.; HAMEL, S.; HANSEN, S.B.; HARTLEY, N.J.; HU, S.; HURRICANE, O.A.; KARASIEV, V.V.; KAS, J.J.; KETTLE, B.; KLUGE, T.; KNUDSON, M.D.; KONONOV, A.; KONÔPKOVÁ, Z.; KRAUS, D.; KRITCHER, A.; MALKO, S.; MASSACRIER, G.; MILITZER, B.; MOLDABEKOV, Z.A.; MURILLO, M.S.; NAGLER, B.; NETTELMANN, N.; NEUMAYER, P.; OFORI-OKAI, B.K.; OLEYNIK, I.I.; PREISING, M.; PRIBRAM-JONES, A.; RAMAZANOV, T.; RAVASIO, A.; REDMER, R.; RETHFELD, B.; ROBINSON, A.P.L.; RÖPKE, G.; SOUBIRAN, F.; STARRETT, C.E.; STEINLE-NEUMANN, G.; STERNE, P.A.; TANAKA, S.; THOMPSON, A.P.; TRICKEY, S.B.; VINCI, T.; VINKO, S.M.; WANG, L.; WHITE, A.J.; WHITE, T.G.; ZASTRAU, U.; ZUREK, E.; TOLIAS, P.: Roadmap for warm dense matter physics. Plasma Phys. Controlled Fusion (submitted)

WANG B.; SATTA, N.; KOEMETS, E.; BUCHEN, J.; TRAUTNER V.; SAN JOSÉ MÉNDEZ, A.; CRINITI, G.; GLAZYRIN, K.; LIERMANN, H.-P.; MARQUARDT, H.: Dynamic compression and pressure cycling in dynamic diamond-anvil cells: MgO and neon studied by time-resolved XRD. Phys. Rev. B (submitted)

WANG, F.; CHANYSHEV, A.; MAN, L.; SONG, Y.; WANG, L.; ISHII, T.; TSUJINO, N.; BHAT, S.; FARLA, R.; KATSURA, T.: Limits of water storage in stishovite at deep mantle conditions. Geophys. Res. Lett. (submitted)

YAO, J.; CIOBANU, C.L.; COOK, N.J.; EHRIG, K.; SLATTERY, A.D.; ILTON, E.S.; MIYAJIMA, N.; STEINLE-NEUMANN, G.: Long-range modulation in uranium-bearing hematite superstructure constrained from STEM analysis and ab initio calculations. Am. Mineral. (in press), https://doi.org/10.2138/am-2025-9794

ZAWASKI, M.J.; HAGADORN, J.W.; WHITE, K.R.; LONGMAND, M.; YUSAS, M.; LAHEY, B.L.; PHILLIPS, A.A.; SHEN, J.; ALGEO, T.J.; HASS, J.; LIU, Z.; MOJZSIS, S.J.: Tracing paleoenvironmental change across the Permian-Triassic transition in a marginal-marine setting focusing on Colorado's Front Range. Gondwana Res. 153, 150-169 (in press), https://doi.org/10.1016/j.gr.2025.11.010

ZHANG, Z.; WITHERS, A.C.; LIU, X.; ZHANG, L.: Revisiting quantitative infrared analysis of absorbing species in anisotropic media. Am. Mineral. (submitted)

ZHOU, C.; BUCHEN, J.; DOBROSAVLJEVIC, V.V.; STROZEWSKI, B.; PARDO, O.S.; STURHAHN, W.; ISHII, T.; TOELLNER, T.; WILDING, J.D.; CHARITON, S.; KALKAN, B.; KUNZ, M.; JACKSON, J.M.: Equation of state of a low-sulfur iron-nickel alloy up to 143 GPa. Phys. Earth Planet. Inter. (submitted)

ZHU, K.; CHEN, Q.; YOKOYAMA, T.; YAMAGUCHI, A.; BOUVIER, A.; CHEN, L.: When wet meets dry: Ivuna-like impactor triggered volatile loss on the angrite parent body. Sci. Adv. (submitted)

4.3 Presentations at scientific institutions and at congresses

ABRAHAM, K.; STEINLE-NEUMANN, G.; REDMER, R.: 12th Workshop on High Pressure, Planetary and Plasma Physics (12HP4), European XFEL, Schenefeld, Germany: "Equation of state and transport properties of iron hydrides at outer core conditions via ab-initio and machine learning methods"

AUDÉTAT, A.; CHANG, J.; QIAO, Y.-B.: 16.06.2025, SEG Student Chapter, Friedrich-Alexander-University, Erlangen, Germany: "Recent advances in deciphering the magmatic controls on porphyry copper formation"

AUDÉTAT, A.; CHANG, J.; QIAO, Y.-B.: 17.10.2025, China University of Geosciences, Wuhan, P.R. China: "Magmatic controls on porphyry copper formation"

BOFFA BALLARAN, T.: 13.06.2025, Université Clermont Auvergne, Clermont-Ferrand, France: "What can the elasticity of minerals tell us about the composition of the Earth's mantle"

BOFFA BALLARAN, T.; KULARATNE, K.; TRØNNES, R.G.: 25.-29.08.2025, European Crystallographic Meeting ECM35, Lviv-Poznań, Poland: "Influence of cation substitution on the compressibility of Ca perovskites"

BOFFA BALLARAN, T.; CRINITI, G.; HUANG, R.; KURNOSOV, A.: 16.-18.09.2025, SIMP-SGI Joint Congress 'Geosciences and the Challenges of the 21st Century', Padova, Italy: "Relationship between the crystal chemistry of mantle minerals and their elastic properties"

BOUVIER, A.: 11.02.2025, Workshop ESA F3 call – fast NEO sample return mission, online (*invited*): "Requirements for the chemical and isotopic analyses of returned samples"

BOUVIER, A.: 03.-07.03.2025, 3rd International Team Meeting, International Space Science Institute, Bern, Switzerland: "Timing and processes of planetesimal formation and evolution"

BOUVIER, A.: 17.03.2025, University College London, Department of Earth Sciences, London, U.K. (*invited*): "Meteorite records of early planetary crust formation"

BOUVIER, A.; HU, X.-J.; WITHERS, A.C.; VERVOORT, J.F.: 05.-11.07.2025, Goldschmidt 2025, Prague, Czech Republic: "Calibrating mixed Sm-Nd and Lu-Hf isotope spikes for use in Earth and planetary materials"

BOUVIER, A.: 27.10.2025, Paneth Kolloquium, Nördlingen, Germany: "Dating early solar system processes and the search for a robust short-lived radionuclide anchor"

BUCHEN, J.; WANG, B.; SATTA, N.; TRAUTNER, V.; CRINITI, G.; SAN JOSÉ MÉNDEZ, A.; LIERMANN, H.-P.; MARQUARDT, H.: 21.-23.07.2025, 'Two Decades of Rapid Compression Diamond Anvil Cell Research: Present and Future Developments', Hamburg, Germany: "Cyclic loading experiments in the dynamic DAC: strains and stresses in polycrystalline MgO"

BUCHEN, J.; WANG, B.; SATTA, N.; TRAUTNER, V.; CRINITI, G.; SAN JOSÉ MÉNDEZ, A.; LIERMANN, H.-P.; MARQUARDT, H.: 16.-19.06.2025, EMPG 2025, Orléans, France: "Stresses and strains in polycrystalline MgO at high pressures and seismic frequencies"

CALVO, L.M.; LABIDI, J.; SHAHAR, A.; KUBIK, E.; SIEBERT, J.: 16.-19.06.2025, EMPG 2025, Orléans, France: "Experimental tracing of the origin of volatile elements on Earth through sulfur isotopes"

CALVO, L.M.; SIEBERT, J.; HUANG, D.; BLANCHARD, I.; KUBIK, E.; BONINO, V.; SCHREIBER, A.; LABIDI, J.: 16.-19.06.2025, EMPG 2025, Orléans, France: "Volatile element accretion on Earth: no late veneer required"

CALVO; L.M.; LABIDI, J.; SHAHAR, A.; KUBIK, E.; SIEBERT, J.: 05.-11.07.2025, Goldschmidt 2025, Prague, Czech Republic: "Experimental constraints on sulfur isotopic fractionation during planetary differentiation"

CHAKRABORTI, A.; FEI, H.; NISHIHARA, Y.; THIELMANN, M.; HEIDELBACH, F.; TSUJINO, N.; CHANYSHEV, A.; KURNOSOV, A.; MAN, A.; DOLINSCHI, J.; WU, W.; CAO, W.; HIGO, Y.; DABROWSKI, M.; KATSURA, T.: 28.09.-03.10.2025, 29th International Conference on High Pressure Science and Technology (AIRAPT-29), Matsuyama, Japan: "Bridgmanite-ferropericlase interface energy controls lower mantle viscosity"

CHANYSHEV, A.; FEI, H.; BONDAR, D.; WANG, B.; LIU, Z.; ISHII, T.; FARLA, R.; MCCAMMON, C.; KATSURA, T.: 21.-26.09.2025, IUCr High Pressure Workshop, Shanghai, P.R. China: "High-pressure chemistry of bridgmanite under Fe_2O_3 and SiO_2-saturated conditions"

CHANYSHEV, A.; MARTIROSYAN, N.; FEI, H.; KATSURA, T.: 28.09.-03.10.2025, 29th International Conference on High Pressure Science and Technology (AIRAPT-29), Matsuyama, Japan: "Melting relations of dry KLB-1 peridotite to 33 GPa"

CHANYSHEV, A.; FEI, H.; BONDAR, D.; WANG, B.; LIU, Z.; ISHII, T.; FARLA, R.; MCCAMMON, C.; KATSURA, T.: 28.09.-03.10.2025, 29th International Conference on High Pressure Science and Technology (AIRAPT-29), Matsuyama, Japan: "Fe^{3+} substitution mechanism in bridgmanite under SiO_2-saturated conditions as function of pressure and temperature"

COLLINGS, I.E.; JOURNAUX, B.; PAKHOMOVA, A.; BOFFA BALLARAN, T.; KURNOSOV, A.: 07.-12.09.2025, EPSC-DPS Joint Meeting 2025, Helsinki, Finland: "Salt hydrate mineralogy at the conditions of icy moon interiors and surfaces"

COMODI, P.; ZUCCHINI, A.; PENNACCHIONI, L.; MASOTTA, M.; FASTELLI, M.; BOFFA BALLARAN, T.; FIGUEIREDO EOARES RODRIGUES, J.E.; GARBARINO, G.: 16.-19.06.2025, EMPG 2025, Orléans, France: "Influence of Fe content on the mineral physics of ordered and disordered ankerites"

DEBAILLE, V.; MOJZSIS, S.; PIGNATARI, M.; HENG, K.; GAILLARD, F.: 11.09.2025, Europlanet Science Conference, Helsinki, Finland: "Having cold feet: The fate of extrasolar systems starting with less 26Al"

FARLA, R.; BHAT, S.; SPEKTOR, K.; FENG, X.; NÉRI, A.; MAN, A.; CHANYSHEV, A.; LATHE, C.; SONNTAG, S.; HAEUSSERMANN, U.; KATSURA, T.: 28.09.-03.10.2025, 29th International Conference on High Pressure Science and Technology (AIRAPT-29), Matsuyama, Japan: "P61B: A dedicated station for *in situ* X-ray diffraction and imaging on materials at HPHT in the Large Volume Press"

FROST, D.: 14.-15.01.2025, FORCE 3rd Winter Workshop on Recent Advances in High Pressure Research, virtual: "Investigating planetary interiors using a large-large volume multianvil press"

FROST, D.; MAN, L.; PIERRU, R.: 05.-11.07.2025, Goldschmidt 2025, Prague, Czech Republic: "Phase relations of iron-oxygen liquids and the effect of oxygen on the elastic properties of planetary cores"

FUKUSHIMA, R.; TSUJIMORI, T.; MIYAJIMA, N.: 19.-23.06.2025, The 15th International Eclogite Conference (IEC-15), Rohnert Park, California, USA: "Antiphase domains in omphacite: Potential archives of slab eclogitization kinetics"

FUKUSHIMA, R.; TSUJIMORI, T.; MIYAJIMA, N.: 19.-23.06.2025, The 15th International Eclogite Conference (IEC-15), Rohnert Park, California, USA: "Dehydration melting of lawsonite eclogite xenolith in the Colorado Plateau: Micropetrological constraints on plume–slab interaction"

GAILLARD, F.; HENG, K.; MOJZSIS, S.J.; TIAN, M.; ROGERIE, G.; PIGNATARI, M.; DEBAILLE, V.: 11.09.2025, Europlanet Science Conference, Helsinki, Finland: "On the impact of Nebular H2 capture on the internal geochemistry of Sub-Neptune exoplanets"

GOLABEK, G.J.; MEIER, T.G.; LICHTENBERG, T.; SPAARGAREN, R.J.; GUIMOND, C.M.; HAMMOND, M.; STUITJE, K.; DANG, L.; TACKLEY, P.J.: 24.-27.08.2025, German-Swiss Geodynamics Workshop, Bartholomä, Germany: "Magma oceanography of the dense, ultrashort-period sub-Earth GJ 367 b"

GOLABEK, G.J.; RADUCAN, S.D.; ZIPPOLI, M.; JUTZI, M.: 27.04.-02.05.2025, EGU General Assembly 2025, Vienna, Austria: "Post-impact thermal evolution of iron-rich planetesimals", Abstract EGU25-17777

GOLABEK, G.J.; GILLMANN, C.: 17.03.2025, Université de Lille, France: "Outgassing and atmosphere formation on terrestrial bodies"

KATSURA, T.; WANG, L.; MIYAJIMA, N.; WANG, F.: 14.-15.01.2025, FORCE 3rd Winter Workshop on Recent Advances in High Pressure Research, Arizona State University, Tempe, USA, virtual (*invited*): "The $CaSiO_3$ solubility in bridgmanite as a function of pressure, temperature and composition"

KATSURA, T.; FEI, H.: 04.03.2025, HPSTAR, Beijing, P.R. China: "Grain growth kinetics of bridgmanite coexisting with ferropericlase as a function of pressure"

KATSURA, T.; FEI, H.: 06.03.2025, Yanshan University, Qinghuangdao, P.R. China: "Grain growth kinetics of bridgmanite coexisting with ferropericlase as a function of pressure"

KATSURA, T.: 10.03.2025, Institute of Geology IGCAGS, Beijing, P.R. China: "Unveiling water storage in bridgmanite"

KATSURA, T.; WANG, L.; MIYAJIMA, N.; WANG, F.: 17.03.2025, China University of Geoscience, Wuhan, P.R. China: "Davemaoite does exist in the lower mantle"

KATSURA, T.; FEI, H.: 21.03.2025, Chengdu University of Technology, Chengdu, P.R. China: "Grain growth kinetics of bridgmanite coexisting with ferropericlase as a function of pressure"

KATSURA, T.; WANG, L.; MIYAJIMA, N.; WANG, F.: 24.03.2025, Zhejiang University, Hangzhou, P.R. China: "Davemaoite does exist in the lower mantle"

KATSURA, T.; FEI, H.: 27.03.2025, China University of Geoscience, Beijing, P.R. China: "Grain growth kinetics of bridgmanite coexisting with ferropericlase as a function of pressure: the origin of LLSVP and mid-mantle slab stagnation"

KATSURA, T.; FEI, H.: 09.04.2025, Indian Institute of Science Education and Research, Kolkata, India: "Grain growth kinetics of bridgmanite coexisting with ferropericlase as a function of pressure: the origin of LLSVP and mid-mantle slab stagnation"

KATSURA, T.; FEI, H.: 16.-19.06.2025, EMPG 2025, Orléans, France (*invited*): "Grain growth kinetics of bridgmanite coexisting with ferropericlase as a function of pressure"

KATSURA, T.; FEI, H.: 25.-29.07.2025, 'From Atom to Earth', Peking University, Beijing, P.R. China (*invited*): "Grain growth kinetics of bridgmanite coexisting with ferropericlase as a function of pressure: the origin of LLSVP and mid-mantle slab stagnation"

KATSURA, T.: 28.09.2025, Pre-AIRAPT Workshop on High-Temperature Pressure Calibration, Matsuyama, Japan: "Towards establishment of high-temperature pressure scales"

KATSURA, T.; FEI, H.: 28.09.-03.10.2025, 29th International Conference on High Pressure Science and Technology (AIRAPT-29), Matsuyama, Japan: "Grain growth kinetics of bridgmanite and implications for slab stagnation and the origin of LLSVPs"

KATSURA, T.; SONG, Y.; CHANYSHEV, A.; WANG, F.; LIU, D.; ISHII, T.; GUO, X.: 28.09.-03.10.2025, 29th International Conference on High Pressure Science and Technology (AIRAPT-29), Matsuyama, Japan: "Phase relations in the Al_2O_3–SiO_2–H_2O system at lower mantle conditions: Implications for deep water transport via subduction"

KEPPLER, H.: 05.-11.07.2025, Goldschmidt 2025, Prague, Czech Republic: "H_2 solubility in silicate melts and the origin of hydrogen in planetary interiors"

KUBIK, E.: 22.01.2025, Nantes Université, Laboratoire de Planétologie et Géosciences, Nantes, France (*invited*): "Core–mantle isotopic fractionation in large terrestrial planets"

KUBIK, E.; MAKHATADZE, G.; SCHULZE, M.: 16.-19.06.2025, EMPG 2025, Orléans, France: "Nickel isotope fractionation during core formation on large terrestrial planets"

KUBIK E.: 02.12.2025, University of Cambridge, Department of Earth Sciences, Cambridge, U.K. (*invited*): "Core–mantle isotopic fractionation in terrestrial planets"

KUBIK E.: 18.12.2025, Queen's University, Belfast, Ireland (*invited*): "Making planets in the laboratory"

KUBIK, E.; MAKHATADZE, G.; SCHULZE, M.: 05.-11.07.2025, Goldschmidt 2025, Prague, Czech Republic (*invited*): "Nickel isotope fractionation during core formation on large terrestrial planets"

KURNOSOV, A.; BOFFA BALLARAN, T.: 16.-19.06.2025, EMPG 2025, Orléans, France: "Self-consistent acoustic wave velocity measurements at simultaneous high pressure and high temperature"

MAN, L.; FROST, D.J.; DUBROVINSKY, L.S.: 05.-11.07.2025, Goldschmidt 2025, Prague, Czech Republic: "Updated Fe-FeS phase diagram under high pressure"

MELAI, C.; WITHERS, A.C.; GUYETT, P.; TOMLINSON, E.L.: 05.-11.07.2025, Goldschmidt 2025, Prague, Czech Republic: "Experimental investigation of the role of komatiite-peridotite interaction in generating silica enrichment in the cratonic lithosphere"

MIYAJIMA, N.; WANG, L.; KATSURA, T.: 16.-19.06.2025, EMPG 2025, Orléans, France: "Direct view of ferric iron distribution in an iron and aluminium-bearing bridgmanite by scanning transmission electron microscopy"

MOJZSIS, S.J.: 04.06.2025, COST Action – Planets, Leeds, U.K.: "Thermal consequences of impact bombardements to the silicate crusts of terrestrial-type exoplanetes"

MOJZSIS, S.J.; KREMER, B.; MARIN-CARBONNE, J.; TACKLEY, C.; MASON, P.: 15.06.2025, COST Action – Biogeodynamics, Bratislava, Slovakia: "Biogeosphere"

MOJZSIS, S.; ABRAMOV, O.: 11.09.2025, Europlanet Science Conference, Helsinki, Finland: "Thermal consequences of impact bombardments to the silicate crusts of rocky exoplanets"

MOJZSIS, S.; ARP, T.B.; GABOR, N.; KREMER, B. 11.09.2025, Europlanet Science Conference, Helsinki, Finland: "Rainbow edges: Light-harvesting by photosynthetic systems as a function of stellar mass and metallicity"

MOJZSIS, S.; ROBERTI, L.; SCHERF, M.; PIGNATARI, M.: 11.09.2025, Europlanet Science Conference, Helsinki, Finland: "Luminosity recipes for Solar-type stars as a function of mass, rotation, metallicity and age"

MOJZSIS, S.J.: 01.10.2025, University of Groningen, Kapetyn Astronomical Institute, Groningen, The Netherlands: "With a grain of salt: Variably fractionated volatile lithophile alkali metals and alkali earths in (exo)planetary contexts"

MOJZSIS, S.J.: 27.-28.10.2025, PANETH Kolloquium, Nördlingen, Germany: "Variably fractionated volatile lithophile alkali metals and alkali earths in (exo)planetary contexts"

MOJZSIS, S.J.: 04.11.2025, InterCAT Seminar, Aarhus University, Denmark: "Rocky differentiated planets and the Lavoisier-Lomonosov bridge from non-life to life"

MOJZSIS, S.J.: 21.11.2025, Frontiers Seminar LMU, München, Germany: "After the Moon"

NÉRI, A.; KUBIK, E.; GOLABEK, G.J.; BOUVIER, A.; WALTE, N.P.: 16.-19.06.2025, EMPG 2025, Orléans, France: "Reproducing iron-rich phase textures in acapulcoites: overcoming surface tension in solids"

NOVAIS-RODRIGUES, E.; NESTOLA, F.; BOFFA BALLARAN, T.; WITHERS, A.C.: 16.-18.09.2025, SIMP-SGI Joint Congress 'Geosciences and the Challenges of the 21st Century', Padova, Italy: "The high-pressure conversion of merrillite to tuite in the upper mantle"

PIERRU, R.; MAN, L.; MONTEUX, J.; GRÉAUX, S.; KAKIZAWA, S.; KONO, Y.; HENRY, L.; FARLA, R.; FENG, X.; GOLABEK, G.; ANTONANGELI, D.; FROST, D.: 05.-11.07.2025, Goldschmidt 2025, Prague, Czech Republic: "*In situ* viscosity measurements on iron-rich silicate melts under high pressure: Evaluating the solidification regime of the Martian magma ocean"

SAKURAI, M.; TSUJINO, N.; NISHIHARA, Y.; WITHERS, A.C.; BOFFA BALLARAN, T.; KATSURA, T.: 28.09.-03.10.2025, 29th International Conference on High Pressure Science and Technology (AIRAPT-29), Matsuyama, Japan: "Water partitioning between wadsleyite and garnet under water-unsaturated conditions"

SILVA SOUZA, D.; THIELMANN, M.; FROST, D.; HEIDELBACH, F.; GASC, J.: 27.04.-02.05.2025, EGU General Assembly 2025, Vienna, Austria: "Microscale processes in experimental serpentine dehydration: implications for deep earthquake mechanisms", Abstract EGU25-6058

SILVA SOUZA, D.; THIELMANN, M.; FROST, D.; HEIDELBACH, F.; GASC, J.: 16.-19.06.2025, EMPG 2025, Orléans, France: "Microstructural aspects of incipient serpentine dehydration"

SPANG, A.; THIELMANN, M.; DE MONTSERRAT, A.; DURETZ, T.: 27.04.-02.05.2025, EGU General Assembly 2025, Vienna, Austria: "2D numerical models of ductile rupture propagation", Abstract EGU25-4156

SPANG, A.; THIELMANN, M.; DE MONTSERRAT, A.; DURETZ, T.; KISS, D.; RÄSS, L.: 04.07.2025, DGGV-TSK-Webinar, online: "Ductile strain localization and transient rupture propagation by thermal runaway"

SPANG, A.; THIELMANN, M.; DE MONTSERRAT, A.; DURETZ, T.: 07.-12.09.2025, GeoMOD 2025, Lisbon, Portugal: "Transient propagation of ductile ruptures by thermal runaway"

SPANG, A.; THIELMANN, M.; DE MONTSERRAT, A.; DURETZ, T.; KISS, D.; RÄSS, L.: 08.10.2025, ETH Zurich, Switzerland: "Ductile strain localization and transient rupture propagation by thermal runaway"

SPANG, A.; THIELMANN, M.; DE MONTSERRAT, A.; DURETZ, T.; KISS, D.; RÄSS, L.: 04.12.2025, Universität Bonn, Germany: "Understanding the physics of thermal runaway and ductile rupture propagation"

STEINLE-NEUMANN, G.; ABRAHAM, K.; SCHULZE, M.; BERGERMANN, A.; SCHÖRNER, M.; REDMER, R.; FROST, M.; GONCHAROV, A.F.; MCWILLIAMS, R.S.; HUSBAND, R.J.; BROWN, D.; BYKOVA, E.; CELESTE, A.; EDMUND, E.; HARTLEY, N.J.; GLAZYRIN, K.; JAISLE, N.; ANDRZEJEWSKI, M.; APPEL, K.; BAEHTZ, C.; KONÔPKOVÁ, Z.; STROHM, C.; LAURUS, T.; GRAAFSMA, H.; TANG, M.; LIN, Y.; MASSANI, B.; YOUNES, Z.; GLENZER, S.H.: 22.-24.09.2025, 12th Workshop on High Pressure, Planetary and Plasma Physics (12HP4), European XFEL, Schenefeld, Germany: "Atomistic insight into the synthesis of gold hydride at high P and T at the XFEL"

STEINLE-NEUMANN, G.; SCHULZE, M.: 22.-24.09.2025, 12th Workshop on High Pressure, Planetary and Plasma Physics (12HP4), European XFEL, Schenefeld, Germany: "Oxygen diffusivity in davemaoite and its geophysical and geochemical implications"

STEINLE-NEUMANN, G.: 07.-10.10.2025, 4th Onsen Workshop on Formation and Chemical Composition of Cores, Yunishigawa, Nikko, Tochigi, Japan: "Hydrogen in Earth's core – a computational perspective"

STEINLE-NEUMANN, G.: 25.-28.11.2025, Annual Meeting of DFG SPP 2024 (DeepDyn), Wernigerode, Germany: "Atomistic insight into the synthesis of gold hydride at high P and T at the XFEL"

STEINLE-NEUMANN, G.: 08.12.2025, Seminar series of DFG SPP 2404 (DeepDyn), online: "Hydrogen in Earth's core. Does it get in and what does it do?"

TROPPER, P.; PEINE, J.; SCHMITT, A.K.; MOJZSIS, S.J.; MANNING, C.E.: 05.-11.07.2025, Goldschmidt 2025, Prague, Czech Republic: "Geothermobarometry and rutile petrochronology of Neo-Archaean metamorphism in the Eo-Archaean metasediments from Akila and Innersuartuut (SW Greenland) and the southern Inukjuak domain, Québec (Canada)"

WEILER, T.; PICCOLO, A.; SPANG, A.; THIELMANN, M.: 27.04.-02.05.2025, EGU General Assembly 2025, Vienna, Austria: "How to generate deep earthquakes in the Hindu Kush", Abstract EGU25-6856

WEILER, T.; PICCOLO, A.; SPANG, A.; THIELMANN, M.: 07.-12.09.2025, GeoMOD 2025, Lisbon, Portugal: "Deep earthquakes in the Hindu Kush – A data driven modelling approach"

WITHERS, A.C.: 05.-11.07.2025, Goldschmidt 2025, Prague, Czech Republic: "Fingerprints for coupled substitutions of H and trivalent elements in olivine from polarized infrared spectroscopy"

ZHAO, R.; BOUVIER, A.; BRASSER R.: 05.-11.07.2025, Goldschmidt 2025, Prague, Czech Republic: "Origin of metal in lunar impactites using siderophile element abundance analysis"

ZHU, D.; KUBIK, E.; BOUVIER, A.: 05.-11.07.2025, Goldschmidt 2025, Prague, Czech Republic: "High precision Sn isotope analysis using MC-ICP-MS/MS with double-spike technique"

4.4 Lectures and seminars at Bayerisches Geoinstitut

APPEL, Karen, European XFEL, Schenefeld, Germany: "Using time resolved FELs to access high pressure states and properties of deep Earth materials", 26.06.2025

ARZILLI, Fabio, Università di Camerino, Scuola di Scienze e Tecnologie, Camerino, Italy: "In situ 4D crystallization and vesiculation in basaltic magmas: Implications for magma mobility within the Earth's crust, fragmentation and eruptive style", 27.03.2025

BUSEMANN, Henner, ETH Zurich, Departement Erd- und Planetenwissenschaften, Zurich, Switzerland: "Comparative noble gas cosmochemistry with carbonaceous chondrites and samples returned from asteroids Ryugu and Bennu", 16.01.2025

CARO, Guillaume, Université de Lorraine, Centre de Recherches Pétrographiques et Géochimiques, Vandoeuvre-lès-Nancy, France: "Tracing the onset of volatile cycling at subduction zones: Insights from multiple sulfur isotopes in Eoarchean arc lavas", 04.12.2025

CHEN, Jun-Feng, Chengdu University of Technology, Chengdu, P.R. China: "Redox evolution of the Martian mantle – Insights from Shergottite Meteorites", 30.04.2025

CHUVASHOVA SHAPOREVA, Irina, Florida State University, Miami, USA: "Advancing high-pressure chemistry: Exploring structure-property relationships in complex rare-earth-containing materials", 28.05.2025

COLLINET, Max, Université de Namur, Institut of Life, Earth and Environment, Namur, Belgium: "Crustal recycling and the formation of intermediate to felsic crustal plateaus on Venus", 30.01.2025

CURTOLO, Andrea, Università degli Studi di Padova, Istituto di Geoscienze e Georisorse, Padova, Italy: "The distribution of volatile elements in the Earth's mantle", 22.04.2025

DAI, Wei, University of Copenhagen, Centre for Star and Planet Formation (StarPlan), Copenhagen, Denmark: "Calcium isotope fractionation during Ca-perovskite crystallization in the deep terrestrial magma ocean", 23.04.2025

DALE, Katherine, Observatoire de la Côte d'Azur, Nice, France: "A recipe for the Earth: Models of metal-silicate equilibration during Earth's formation", 20.08.2025

DENG, Jie, Princeton University, Department of Geosciences, Princeton, USA: "Mantle heterogeneities originated from the Earth's core: A new model", 25.09.2025

DIAS, Maria, Universität Bochum, Institut für Geowissenschaften, Bochum, Germany: "Experimental constraints on the diffusion rates and mechanisms in orthopyroxene: Novel methods and applications", 16.10.2025

EDMUND, Eric, Universität Münster, Germany: "Optical investigations of the melting point of bridgmanite at lower mantle pressures", 30.10.2025

FARSANG, Stefan, Université de Genève, Section of Earth and Environmental Sciences, Genève, Switzerland: "Sulphur species and gold transport in magmatic fluids", 05.12.2025

HAMMOUDA, Tahar, Université Clermont Auvergne, Laboratoire Magmas et Volcans, Aubière, France: "Enstatite chondrites, rare-earth elements and the Solar Nebula", 15.05.2025

HENG, Kevin, LMU München, Fakultät für Physik, Universitätssternwarte München, Germany: "The geoastronomy of sub-neptunes", 10.12.2025

KACZMAREK, Mary-Alix, Université de Toulouse, Géosciences Environment Toulouse (GET), France: "Magmatic processes and plastic deformation in planetesimals through the microstructural study of brachinite-type meteorites, and comparison with Martian and terrestrial ultramafic rocks", 05.06.2025

KUFNER, Sofia-Katerina, Universität Erlangen, GeoZentrum Nordbayern, Erlangen, Germany: "Intermediate-depth seismicity in oceanic-to-continental slabs – examples from Hindu Kush, Pamir, and Myanmar, plus notes on the 28th March M7.7 Myanmar earthquake", 03.07.2025

MAGALI, John, Universität Münster, Institut für Geophysik, Münster, Germany: "From mineral deformation to mantle flow: Using laboratory-constrained textures to explain the observed anisotropy from seismic tomography", 17.07.2025

MARXER, Felix, Leibniz Universität Hannover, Institut für Erdsystemwissenschaften, Hannover, Germany: "Characterisation and quantification of crustal phase equilibria systematics in arc magmas", 13.11.2025

MEIER, Tobias, University of Oxford, Atmospheric, Oceanic and Planetary Physics, Oxford, U.K.: "Interior dynamics of tidally locked super-Earths", 24.07.2025

MOULAS, Evangelos, Johannes Gutenberg-Universität Mainz, Institut für Geowissenschaften, Mainz, Germany: "Stress gradients in multiphase rocks: Thermodynamic and rheologic implications", 06.11.2025

PIERRU, Rémy, Bayerisches Geoinstitut, Bayreuth, Germany: "Melting and physical properties of Martian magmas: Implications for the presence of a basal melt layer at the core-mantle boundary", *Academy Commission Business Meeting*, 24.04.2025

SANCHEZ-VALLE, Carmen, Universität Münster, Institut für Mineralogie, Münster, Germany: "Lab experiments supporting the exploration of Solar and extra-Solar icy worlds", 20.11.2025

SAURETY, Adrien, Institut de Physique du Globe de Paris, France: "Thermodynamic and chemical properties of silicate melt under shock", 12.06.2025

VACI, Zoltan, Charles University, Institute of Petrology and Structural Geology, Prague, Czech Republic: "Impact-driven symplectite formation in ultramafic achondrites", 23.01.2025

VACI, Zoltan, Charles University, Institute of Petrology and Structural Geology, Prague, Czech Republic: "The timing and nature of planetesimal differentiation as told by ungrouped achondrites", 18.12.2025

VALDIVIA, Pedro: Bayerisches Geoinstitut, Bayreuth, Germany: "Nanoscale crystallization in natural magmas: Influence on melt viscosity and impact on volcanic eruptions", *Academy Commission Business Meeting*, 24.04.2025

WANG, Fei, Bayerisches Geoinstitut, Bayreuth, Germany: "Bridgmanite's ferric iron content determined Earth's redox state", *Academy Commission Business Meeting*, 24.04.2025

ZHANG, Yanyao, Stanford University, Earth and Planetary Sciences, Stanford, USA (online): "Exploring planetary interiors in the laboratory", 27.01.2025

4.5 Conference organisation

27.04.-02.05.2025, EGU General Assembly 2025, Vienna, Austria: "Venus: models, observations, (ancient) Earth- and exoplanet analogue" (G. GOLABEK, Co-convenor)

27.04.-02.05.2025, EGU General Assembly 2025, Vienna, Austria: "Dynamics, tectonics and evolution of rocky planets from formation to the present day" (G. GOLABEK, Co-convenor)

05.-11.07.2025, Goldschmidt 2025, Prague, Czech Republic: Theme 1 "From Dust to Planets" (A. BOUVIER, Co-chair)

05.-11.07.2025, Goldschmidt 2025, Prague, Czech Republic: 02f "Experimental and theoretical calibration of isotope fractionation: from core to crust formation" (E KUBIK, Co-convenor)

04.-06.09.2025, Geoastronomy Workshop, Helsinki, Finland (S. MOJZSIS)

28.09.2025, Pre-AIRAPT Workshop on High-Temperature Pressure Calibration, Matsuyama, Japan (T. KATSURA)

14.-17.10.2025, Short course at the China University of Geosciences Wuhan, P.R. China: "Practical application of fluid inclusions" (A. AUDÉTAT)

5. Visiting Scientists

5.1 Visiting scientists funded by the Bayerisches Geoinstitut

APPEL, Karen, European XFEL, Schenefeld, Germany: 25.-27.06.2025

ARZILLI, Fabio, Università di Camerino, Scuola di Scienze e Tecnologie, Camerino, Italy: 16.-18.10.2025

BRASSER, Ramon, Konkoly Observatory, Research Centre for Astronomy and Earth Sciences, Budapest, Hungary: 16.-22.02.2025

BUSEMANN, Henner, ETH Zurich, Departement Erd- und Planetenwissenschaften, Zurich, Switzerland: 15.-17.01.2025

CARO, Guillaume, Université de Lorraine, Centre de Recherches Pétrographiques et Géochimiques, Vandoeuvre-lès-Nancy, France: 03.-05.12.2025

CHEN, Jun-Feng, Chengdu University of Technology, Chengdu, P.R. China: 27.04.-01.05.2025

COLLINET, Max, Université de Namur, Institut of Life, Earth and Environment, Namur, Belgium: 29.-31.01.2025

CURTOLO, Andrea, Università degli Studi di Padova, Istituto di Geoscienze e Georisorse, Padova, Italy: 21.-24.04.2025

DIAS, Maria, Universität Bochum, Institut für Geowissenschaften, Bochum, Germany: 15.-17.10.2025

DOLEJŠ, David, Universität Freiburg, Institut für Geo- und Umweltnaturwissenschaften, Freiburg, Germany: 16.-20.02.2025

EDMUND, Eric, Universität Münster, Institut für Mineralogie, Münster, Germany: 29.-31.10.2025

FARSANG, Stefan, Université de Genève, Section of Earth and Environmental Sciences, Genève, Switzerland: 03.-06.12.2025

HAMMOUDA, Tahar, Université Clermont Auvergne, Laboratoire Magmas et Volcans, Aubière, France: 14.-17.05.2025

KACZMAREK, Mary-Alix, Université de Toulouse, Géosciences Environment Toulouse (GET), France: 01.-06.06.2025

MAGALI, John, Universität Münster, Institut für Geophysik, Münster, Germany: 16.-18.07.2025

MAGÈRE, Alice, Université Clermont Auvergne, Laboratoire Magmas et Volcans, Aubière, France: 15.04.-15.06.2025

MARXER, Felix, Leibniz Universität Hannover, Institut für Erdsystemwissenschaften, Hannover, Germany: 05.-07.11.2025

MASOTTA, Matteo, Università di Pisa, Dipartimento di Scienze della Terra, Pisa, Italy: 16.-20.02.2025

MEIER, Tobias, University of Oxford, Atmospheric, Oceanic and Planetary Physics, Oxford, U.K.: 23.-26.07.2025

SANCHEZ-VALLE, Carmen, Universität Münster, Institut für Mineralogie, Münster, Germany: 19.-21.11.2025
SAURETY, Adrien, Institut de Physique du Globe de Paris, France: 11.-13.06.2025
WALTE, Nico, TU München, Forschungs-Neutronenquelle Heinz Maier-Leibnitz (FRM II), Garching, Germany: 01.-03.09.2025
VACI, Zoltan, Charles University, Institute of Petrology and Structural Geology, Prague, Czech Republic: 22.-24.01.2025, 17.-19.12.2025
ZAMPRAS, Pavlos, University of Athens, Greece: 13.01.-28.02.2025

5.2 Visiting scientists supported by other externally funded BGI projects

DALE, Katherine, Observatoire de la Côte d'Azur, Nice, France: 19.-21.08.2025 (ERC[*B])
DENG, Jie, Princeton University, Department of Geosciences, Princeton, USA: 21.09.-25.09.2025 (DFG[*A])

[*A] DFG: Deutsche Forschungsgemeinschaft
[*B] ERC: European Research Council

5.3 Visitors (externally funded)

ABEYKOON, Sumith, Università di Camerino, Scuola di Scienze e Tecnologie, Camerino, Italy: 17.-29.03.2025
ABRAHAM, Kilian, Universität Rostock, Institut für Physik, Rostock, Germany: 11.-12.03.2025
AKBAR, Fariia, Goethe-Universität Frankfurt a. M., Geozentrum, Frankfurt a. M., Germany: 11.-12.02.2025
ANGEL, Ross, Università degli Studi di Padova, Istituto di Geoscienze e Georisorse, Padova, Italy: 14.-22.03.2025
ARZILLI, Fabio, Università di Camerino, Scuola di Scienze e Tecnologie, Camerino, Italy: 23.-28.03.2025
CAVALLERA, Rebecca, Università di Camerino, Scuola di Scienze e Tecnologie, Camerino, Italy: 15.10.-19.12.2025
CHEN, Tsai-Wei, Rice University, Department of Earth, Environmental and Planetary Sciences, Houston, USA: 24.06.-04.07.2025, 06.-19.10.2025
CHENG, Haoming, Center for High Pressure Science & Technology Advanced Research (HPSTAR), Beijing, P.R. China: 23.03.-06.04.2025
CHUVASHOVA SHAPOREVA, Irina, Florida State University, Miami, USA: 26.-29.05.2025
COLLE, Fabio, Università di Pisa, Dipartimento di Scienze della Terra, Pisa, Italy: 16.-21.02.2025
CRINITI, Giacomo, Earth & Planets Laboratory, Washington D.C., USA: 14.-16.04.2025

DAI, Wei, University of Copenhagen, Centre for Star and Planet Formation (StarPlan), Copenhagen, Denmark: 22.-24.04.2025

DI GENOVA, Danilo, CNR – ISSMC Faenza, Italy: 29.07.-06.08.2025, 15.-19.10.2025

DIBENEDETTO, Andrea, Università di Pavia, Dipartimento di Chimica, Pavia, Italy: 26.03.-05.04.2025

FENG, Xiaokang, Deutsches Elektronen-Synchrotron DESY, Hamburg, Germany: 23.03.-06.04.2025

FRANZÈ, Sara, Università degli Studi di Padova, Dipartimento di Geoscienze, Padova, Italy: 23.-26.09.2025

GILLMANN, Cédric, ETH Zurich, Departement Erd- und Planetenwissenschaften, Zurich, Switzerland: 28.-31.10.2025

HAUPT, Cordula, Institut des Sciences de la Terre d'Orléans (ISTO), France: 22.-25.04.2025

HENG, Kevin, Ludwig-Maximilians-Universität München, Universitätssternwarte, München, Germany: 09.-11.12.2025

HUSSEIN, Zain, Florida State University, Miami, USA: 26.-29.05.2025

ISMAIL-ZADEH, Alik, Karlsruhe Institute of Technology (KIT), Institute of Applied Geosciences, Karlsruhe, Germany: 10.12.2025

JURZICK, Pascal, Goethe-Universität Frankfurt a. M., Institut für Geowissenschaften, Frankfurt a. M., Germany: 25.-26.11.2025

KIM, Eun Jeong, Kongju National University, Department of Geo-Environmental Sciences, Gongju, South Korea: 01.-05.07.2025

KOVALEV, Valentin, Goethe-Universität Frankfurt a. M., Institut für Geowissenschaften, Frankfurt a. M., Germany: 08.-11.07.2025

KUFNER, Sofia-Katerina, Universität Erlangen, GeoZentrum Nordbayern, Erlangen, Germany: 03.07.2025

LIU, Zhiwei, Guangzhou Institute of Geochemistry, Chinese Academy of Sciences, Guangzhou, P.R. China: 01.01.-01.03.2025

MAN, Lianjie, ETH Zurich, Departement Erd- und Planetenwissenschaften, Zurich, Switzerland: 08.-12.12.2025

MELAI, Caterina, Trinity College Dublin, Department of Geology, Dublin, Ireland: 01.01.-01.08.2025

MINGARDI, Giulia, Università di Pavia, Dipartimento di Scienze della Terra e dell'Ambiente, Pavia, Italy: 17.-29.03.2025

MOULAS, Evangelos, Johannes Gutenberg-Universität Mainz, Institut für Geowissenschaften, Mainz, Germany: 05.-07.11.2025

NARDONI, Chiara, Università di Bologna, Dipartimento di Fisica e Astronomia "Augusto Righi", Bologna, Italy: 08.-11.07.2025

NÉRI, Adrien, Université de Lille, Unité Matériaux et Transformations, Lille, France: 02.-04.07.2025

REDMER, Ronald, Universität Rostock, Institut für Physik, Rostock, Germany: 11.-12.03.2025

SHAPOREV, Aleksey, Florida State University, Miami, USA: 26.-29.05.2025

SHARAPOVA, Ninel, Goethe-Universität Frankfurt a. M., Institut für Geowissenschaften, Frankfurt a. M., Germany: 08.-11.07.2025, 17.-19.11.2025

SIEBER, Melanie, Universität Potsdam, Institut für Geowissenschaften, Potsdam, Germany: 11.-14.08.2025

STOLZ, Ronny, Leibniz-Institut für Photonische Technologien e.V. (Leibniz-IPHT), Jena, Germany: 16.05.2025

VAZQUEZ, James, Florida State University, Miami, USA: 26.-29.05.2025

WALTE, Nico, TU München, Forschungs-Neutronenquelle Heinz Maier-Leibnitz (FRM II), Garching, Germany: 13.-17.01.2025, 30.01.2025

WILLEMYNS, Soetkin, Katholieke Universiteit Leuven, Department of Earth and Environmental Sciences, Leuven, Belgium: 07.-10.12.2025

YAN, Han, University of Science and Technology of China, Hefei, P.R. China: 20.09.-20.12.2025

YOKOYAMA, Hiroaki, Tohoku University, Department of Earth Sciences, Sendai, Japan: 21.06.-12.07.2025

YUAN, Hongsheng, Center for High Pressure Science & Technology Advanced Research (HPSTAR), Shanghai, P.R. China: 11.-18.02.2025

6. Additional scientific activities

6.1 Theses

Ph.D. theses

ASLANDUKOV, Andrii: High-pressure synthesis, structure, and properties of rare-earth (poly-) nitrides and carbonitrides.
ASLANDUKOVA, Alena: The diverse high-pressure chemistry of Y–ammonia borane and Y–paraffin oil systems.
MAN, Lianjie: Experimental constraints on the compositions and thermal regimes of terrestrial planetary interiors.

M.Sc. theses

MINCHENKOVA, Anastasiia: Zircon solubility in felsic silicate melts.
ZIPPOLI, Matteo: Constraints on the petrogenesis of mesosiderite meteorites.

6.2 Editorship of scientific journals

AUDÉTAT, Andreas	Associate Editor "Economic Geology"
BOFFA BALLARAN, Tiziana	Associate Editor "European Journal of Mineralogy"
BOUVIER, Audrey	Associate Editor "Geochimica et Cosmochimica Acta"
DUBROVINSKY, Leonid	Member, Editorial Board "High Pressure Research" Member, Advisory Board "Minerals" Editor-in-Chief, "Minerals"
FROST, Dan	Member, Executive Committee for "Elements"
KEPPLER, Hans	Editorial Board "Contributions to Mineralogy and Petrology" Editorial Board "ACS Earth and Space Chemistry"
LI, Yuan	Associate Editor "Geochimica et Comochimica Acta" Advisory Board "Earth and Planetary Science Letters" Advisory Board "Acta Geochimica" Advisory Board "Matter and Radiation at Extremes"

MIYAJIMA, Nobuyoshi	Associate Editor "European Journal of Mineralogy"
MOJZSIS, Steven	Editorial Board "Annales Geophysicae" Editorial Board "Earth and Planetary Science Letters" Editor Board "Central European Geology (formerly Acta Geologica Hungarica)"
STEINLE-NEUMANN, Gerd	Editor "Geodynamica"

6.3 Membership of scientific advisory bodies

AUDÉTAT, ANDREAS	Member, Review Board of the German Science Foundation (DFG)
BOUVIER, Audrey	Co-Chair, Section Geochemistry, Deutsche Mineralogische Gesellschaft (DMG) Member, Leonard medal, Nier prize and Fellows committee, Meteoritical Society Member, European Space Agency, Science Working Team for Early Solar System Evolution and Sample Analysis Working Team, Martian Moons eXploration (MMX) mission led by the Japanese Aerospace Exploration Agency Member, European Space Agency, Mars Sample Return (MSR) Campaign Science Group
DUBROVINSKY, Leonid	Member, Review Panel of Canadian Light Source Chair Member, Subcommission on Spectroscopy, Diffraction, and new Instrumentations in Mineral Physics of the International Mineralogical Association Member, Review Panel of PETRA III Lithuanian Research Council, Head of Evaluation Committee in Civil Engineering Lithuanian Research Council, Head of Evaluation Committee in Natural Sciences
FROST, Dan	Member, Royal Society Member, Bavarian Academy of Sciences Member, German National Academy of Sciences (Leopoldina) Member, Scientific Advisory Committee of the GeoForschungsZentrum Potsdam President of the European Association of Geochemistry

KATSURA, Tomoo	Japan Association of Mineralogical Sciences Award Committee Chair
KEPPLER, Hans	Member, German National Academy of Sciences (Leopoldina) Member, Bavarian Academy of Sciences Member, Leibniz Prize selection committee, DFG
MCCAMMON, Catherine	Member, Mediation Committee, International Mineralogical Association
MOJZSIS, Steven	Voting/Participating Member, International Commission on Stratigraphy, Sub-commission on Precambrian Stratigraphy International Board Member, European Astrobiology Institute, Topical Events Chair, EGU Member, COST Action GEOBiG Biogeodynamics Council Chair

7. Scientific and Technical Personnel

Name		Position	Duration in 2025	Funding source
ABRAMOV, Oleg	Dr.	Wiss. Mitarbeiter	from 01.11.	EU
ANTUNES, Anaelle Coralie	B.Sc.	Student. Hilfskraft		DFG
ASLANDUKOV, Andrii	M.Sc.	Wiss. Mitarbeiter		DFG
ASLANDUKOVA, Alena	M.Sc.	Wiss. Mitarbeiterin		DFG
AUDÉTAT, Andreas	Dr.	Akad. Oberrat		BGI
BAUER, Gerald	Dipl.-Ing. (FH)	Techn. Angestellter		BGI
BOFFA BALLARAN, Tiziana	Dr.	Akad. Oberrätin		BGI
BONDAR, Dmitry	Dr.	Wiss. Mitarbeiter		EU
BOUVIER, Audrey	Prof. Dr.	Professorin		BGI
BUBMANN, Daniela		Techn. Angestellte		BGI
BUCHEN, Johannes	Dr.	Juniorprofessor		BGI
BUCHERT, Petra		Fremdsprachen-Sekretärin		BGI
CHANYSHEV, Artem	Dr.	Wiss. Mitarbeiter		DFG
CHATTOPADHYAY, Aritro	M.Sc.	Stipendiat	from 01.10.	DAAD
CURTOLO, Andrea	Dr.	Wiss. Mitarbeiter	from 18.08.	BGI/VP
CZEKAY, Laura	Dr.	Wiss. Mitarbeiterin		DFG
DELL, Serghius		Elektrotechniker		BGI
DUBROVINSKAIA, Natalia	Prof. Dr.	Professorin		BGI
DUBROVINSKY, Leonid	Apl. Prof. Dr.	Akad. Direktor		BGI
EBERT, Kathleen		O&M Koordinatorin	from 01.08.	EU
FISCHER, Heinz		Mechaniker		DFG
FROST, Daniel	Prof. Dr.	Stellvertr. Leiter		BGI
GASPERT, Olga		Verwaltungsreferentin		BGI
GOLABEK, Gregor	Prof. Dr.	Professor		BGI
HAHN, Laura		Sekretärin	from 20.05.	BGI
HAO, Xiaoshu	M.Sc.	Stipendiatin	to 25.11.	CSC
HE, Guoqiang	B.Sc.	Student. Hilfskraft	from 01.10.	DFG
HEIDELBACH, Florian	Dr.	Wiss. Mitarbeiter		BGI
HLEDE, Matej	M.Sc.	Wiss. Mitarbeiter		DFG
HU, Xiao-Jun	M.Sc.	Stipendiatin		CSC
HU, Yedan	M.Sc.	Stipendiatin	from 15.09.	CSC
JEMAL, Ibrahim Jibril	B.Sc.	Student. Hilfskraft	to 30.11.	DFG
KATSURA, Tomoo	Prof. Dr.	Professor		BGI

KELK-HUTH, Denise		Sekretärin		BGI
KEPPLER, Hans	Prof. Dr.	Leiter		BGI
KONRAD, Erik		Präparator		BGI
KRAUßE, Detlef	Dipl.-Inform. (FH)	Techn. Angestellter		BGI
KREEGER, Laurence	B.Sc.	Student. Hilfskraft	01.04.-12.08.	UBT
			from 13.08.	DFG
KRIEGL, Holger		Haustechniker		BGI
KUBIK, Edith	Dr.	Stipendiatin	to 28.02.	AvH
		Wiss. Mitarbeiterin	01.03.-31.07.	BGI/VP
KURNOSOV, Alexander	Dr.	Wiss. Mitarbeiter		BGI
LI, Yuan	Dr.	Akad. Rat		BGI
LINHARDT, Sven		Elektrotechniker		BGI
LIU, Zhiwei	Dr.	Stipendiat	to 31.03.	CSC
MAN, Lianjie	M.Sc.	Wiss. Mitarbeiter	to 30.09.	DFG
MATTHÄUS, Rebecka		Chem.-Techn. Assistentin		BGI
MCCAMMON, Catherine	PD Dr.	Wiss. Mitarbeiterin		DFG
MIYAJIMA, Nobuyoshi	Dr.	Akad. Oberrat		BGI
MINCHENKOVA, Anastasiia	B.Sc.	Student. Hilfskraft	to 31.03.	DFG
MOJZSIS, Stephen	Dr.	Wiss. Mitarbeiter	from 01.06.	EU
NJUL, Raphael		Präparator		BGI
OVSYANNIKOV, Sergey	Dr.	Wiss. Mitarbeiter	to 31.10.	DFG
PIERRU, Rémy Alfred	Dr.	Wiss. Mitarbeiter		BGI
PIGNATARI, Marco	Dr.	Wiss. Mitarbeiter	from 01.07.	EU
PÖPPELBAUM, Melanie	M.Sc.	Wiss. Mitarbeiterin		DFG
POTZEL, Anke		Chem.-Techn. Assistentin		BGI
PUCHTLER, Toni		Werkzeugmechaniker	from 01.04.	BGI
QIAN, Cheng	M.Sc.	Stipendiatin		CSC
QIAO, Yibo	M.Sc.	Wiss. Mitarbeiter		DFG
RAUSCH, Oliver		Mechaniker		BGI
SAMAL, Sanket	M.Sc.	Stipendiat	from 01.10.	DAAD
SCHULZE, Maximilian	Dr.	Wiss. Mitarbeiter		DFG
SEKIYA, Natsuko	B.Sc.	Student. Hilfskraft	from 01.10.	DFG
SHU, Sha	M.Sc.	Wiss. Mitarbeiterin	from 09.10.	DFG
SIKDAR, Jinia	Dr.	Wiss. Mitarbeiterin	to 31.07.	EU
SILVA SOUZA, Danielle	M.Sc.	Wiss. Mitarbeiterin		DFG
SONG, Yunke	M.Sc.	Stipendiat	to 31.10.	CSC
SPANG, Arne	Dr.	Wiss. Mitarbeiter		DFG

STEINLE-NEUMANN, Gerd	Privatdozent Dr.	Akad. Oberrat		BGI
THIELMANN, Marcel	Dr.	Wiss. Mitarbeiter	to 28.02	DFG
TRENZ, Ulrike		Biol.-Techn. Assistentin		BGI
TRUEMAN, Thomas	Dr.	Wiss. Mitarbeiter	from 01.09.	EU
ÜBELHACK, Stefan		Mechaniker		BGI
VALDIVIA MUNOZ, Pedro Antonio	M.Sc.	Wiss. Mitarbeiter	to 30.09.	EU
WANG, Fei	Dr.	Wiss. Mitarbeiter	to 03.07.	DFG
			03.07.-29.11.	BGI
			from 30.11.	DFG
WANG, Lin	Dr.	Wiss. Mitarbeiter	to 31.03.	BGI
WEILER, Tatjana	M.Sc.	Wiss. Mitarbeiterin		DFG
WETZEL, Stephanie		Sekretärin	to 28.02.	BGI
WIESNER, Dorothea		Techn. Assistentin		BGI
WITHERS, Antony	Dr.	Wiss. Mitarbeiter		BGI
WU, Ye	Dr.	Stipendiatin	01.02.-26.09.	CSC
WU, Zhen	M.Sc.	Stipendiat	from 15.10.	CSC
YAN, Han	M.Sc.	Stipendiatin	20.09.-20.12.	CSC
YIN, Yuqing	Dr.	Wiss. Mitarbeiterin		DFG
YORDANOV, Simeon	B.Sc.	Student. Hilfskraft	from 1.10.	DFG
ZAMPRAS, Pavlos	B.Sc.	Student. Hilfskraft	01.04.-18.09.	UBT
			from 19.09.	DFG
ZHAO, Ran	M.Sc.	Stipendiat		CSC
ZHOU, Kai	B.Sc.	Student. Hilfskraft	01.10.-27.12.	UBT
			from 28.12.	DFG
ZHOU, Shan	M.Sc.	Stipendiatin	to 31.03.	CSC
ZHOU, Wenyi	Dr.	Wiss. Mitarbeiterin	to 31.05.	BGI/VP
			from 01.06	BGI
ZHU, Da-Peng	M.Sc.	Stipendiat		CSC
ZIPPOLI, Matteo	B.Sc.	Student. Hilfskraft	to 30.09.	DFG

Abbreviations/explanations:

AvH	Alexander von Humboldt Foundation
BGI	Staff Position of Bayerisches Geoinstitut
BGI/VP	Visiting Scientists' Program of Bayerisches Geoinstitut
CSC	China Scholarship Council
DAAD	Deutscher Akademischer Auslandsdienst
DFG	German Science Foundation
EU	European Union
UBT	Universität Bayreuth

Index